Electronic Theses and Dissertations

Theses, Dissertations, and Major Papers

2009

Shallow wake in open channel flow - a look into the vertical variability

Arindam Singha
University of Windsor

SHALLOW WAKE IN OPEN CHANNEL FLOW
- A LOOK INTO THE VERTICAL VARIABILITY

by

Arindam Singha

A Dissertation

Submitted to the Faculty of Graduate Studies

through Mechanical, Automotive and Materials Engineering

in Partial Fulfillment of the Requirements for

the Degree of Doctor of Philosophy at the

University of Windsor

Windsor, Ontario, Canada

2009

Shallow wake in Open Channel Flow – A look into the Vertical Variability

by

Arindam Singha

APPROVED BY:

_____
V. Chu, External Examiner
McGill University

_____
S. Cheng
Department of Civil & Environmental Engineering

_____
R. Barron
Department of Mechanical, Automotive & Materials Engineering
and Department of Mathematics & Statistics

_____
G. Rankin
Department of Mechanical, Automotive & Materials Engineering

_____
R. Balachandar, Advisor
Department of Mechanical, Automotive & Materials Engineering

_____
T. Bolisetti, Chair of Defense
Department of Civil & Environmental Engineering

21 May 2009

Declaration of Co-Authorship / Previous Publication

I. Co-Authorship Declaration

I hereby declare that this thesis incorporates material that is result of joint research, as follows:

This thesis incorporates outcome of a research undertaken under the supervision of Dr. Ram Balachandar. The collaboration is covered in chapter 2, 4, 5 and 6 of the thesis. In all cases, the key ideas, primary contributions, experimental designs, data analysis and interpretation, were performed by the author, and the contributions of the co-authors was primarily through the provision of supervision.

I am aware of the University of Windsor Senate Policy on Authorship and I certify that I have properly acknowledged the contribution of other researchers to my thesis, and have obtained written permission from each of the co-author(s) to include the above material(s) in my thesis.

I certify that, with the above qualification, this thesis, and the research to which it refers, is the product of my own work.

II. Declaration of Previous Publication

This thesis includes 3 original papers that have been previously published/submitted for publication in peer reviewed journals, as follows:

Thesis Chapter	Publication title/full citation	Publication status
Chapter 4	*PIV-POD investigation of the wake of of a sharp-edged bluff body immersed in shallow channel flow, J. Fluids Engg.*	*Published*
Chapter 5	*Vertical variability of the wake of a sharp-edged bluff body immersed in a shallow*	*Under review*

	channel flow, Phy. Fluids	
Chapter 5	*Coherent structure statistics in the wake of a sharp-edged bluff body placed vertically in a shallow channel flow, Phys. Fluids*	*Submitted*

I certify that I have obtained a written permission from the copyright owner(s) to include the above published material(s) in my thesis. I certify that the above material describes work completed during my registration as graduate student at the University of Windsor.

I declare that, to the best of my knowledge, my thesis does not infringe upon anyone's copyright nor violate any proprietary rights and that any ideas, techniques, quotations, or any other material from the work of other people included in my thesis, published or otherwise, are fully acknowledged in accordance with the standard referencing practices. Furthermore, to the extent that I have included copyrighted material that surpasses the bounds of fair dealing within the meaning of the Canada Copyright Act, I certify that I have obtained a written permission from the copyright owner(s) to include such material(s) in my thesis.

I declare that this is a true copy of my thesis, including any final revisions, as approved by my thesis committee and the Graduate Studies office, and that this thesis has not been submitted for a higher degree to any other University of Institution.

Abstract

The vertical variability of a typical wake behind a bluff body in an open channel flow has been investigated. The focus of the study was to explore the variability of the flow structures in terms of mean velocity profiles, turbulent parameters and coherent structures. A sharp-edged bluff body was chosen to minimize the effect of Reynolds number and ensure fixed flow separation points in the vertical direction. Velocity measurement was performed using particle image velocimetry at three vertical locations: near-bed, mid-depth and near the free surface. In the streamwise direction, three different fields-of-view were considered to cover a distance 10 times the width of the body. At all locations, 2000 image pairs of 2048×2048 pixel resolution were acquired at a sampling frequency of 1 Hz. Proper orthogonal decomposition (POD) was used as a tool to educe information about the coherent structures in the flow. A robust closed-streamline based coherent structure identification algorithm was developed to systematically detect the presence of the coherent structures in the flow. This step was followed by a statistical study of the location, size and strength of the coherent structures.

The results show that the bed and the free surface, as well as the approaching vertically sheared flow have a significant effect on the structure of the wake. The bed was found to restrict the transverse growth of the wake, whereas the free surface enhances the turbulent energy redistribution at the free surface. The size, shape and the development of the recirculation zone behind the bluff body also indicates vertical variability. Analysis based on signed swirling strength indicates rapid dissipation of vorticity at the near-bed region, compared to other vertical locations. The maximum size of the detected coherent

structures was found to be largest at the mid-depth location, and smallest at the near-bed location. Also, the strength of the structures was found to be smaller at the near-bed location, compared to other vertical locations. Indirect evidence of the merging of the coherent structures has also been demonstrated in the present study.

Dedication

To

My Motherland, India,

and

My wife Riya

Acknowledgements

I am indebted to my supervisor, Dr. Ram Balachandar, for his distinguishing supervision and support. In addition to encouraging independence in work and providing excellent facilities, Dr. Balachandar's thought provoking quaries and suggestions have been instrumental for the timely completion of the present work.

I sincerely acknowledge my gratitude to my committee members Dr. R. Barron, Dr. G. Rankin and Dr. S. Cheng for their valuable time and suggestions for the study. A special thanks to Dr. Barron for meticulously proof reading the document.

Next only in importance in the contribution to the current dissertation is Dr. A Shinneeb, who has been kind enough to teach me the fundamentals of experimentation and programming. Additional thanks to Vesselina for her help and the endless discussions we have to come up with new ideas. Last but not the least, thanks go to my friends at the University of Windsor; Arjun, Anirban, Faruqubhai, Barsha, Ben, Tian, Anupam, Sanjib, Sarmistha, Miltonbhai. Special thanks to Matt St. Louis, for letting me borrow everything from his workshop in aid of my expriments. Heart-felt acknowledgement goes to Tim Horton's for endless medium double-double and Winamp for playing all those mp3s!!

Table of Contents

List of Figures

List of Tables

Nomenclature

2DCS	Two-dimensional coherent structures
CCD	Charge coupled device
C_f	Skin friction coefficient
D	Diameter of the bluff body
DNS	Direct numerical simulation
FFT	Fast fourier transform
f	Frequency of vortex shedding
FOV	Field-of-view
Fr	Froude number
H	Depth of flow
K(x,x')	Correlation function
L	Length scale after which coherent structures dissipates
l_{3D}, l_{2D}	Length scale of two-dimensional and three-dimensional structures, respectively.
l_v	Viscous length scale
LES	Large eddy simulation

N_{cw}, N_{ccw}	Number of clockwise and counterclockwise structures
N_f	Fraction of the number of structures of each group
P_{island}	Island wake parameter
PIV	Particle image velocimetry
POD	Proper orthogonal decomposition
R	Velocity deficit parameter
Re_d, Re_H	Reynolds numbers
R_{ij}	Absolute difference of the variables at grid point i and j
S, S_{near}, S_{far}	Stability number
St	Stanton number
SB	Steady bubble
S_{ij}	Sum of weight fucntion between grid points i and j
T_{ij}	Threshold between grid points i and j
$T_{\lambda+}, T_{\lambda-}$	Fraction of time of positive swirl
U_c, V_c, W_c	Velocity in x-, y- and z- directions associated with the coherent structures
U_∞	Freestream velocity
$u_{POD}, v_{POD}, w_{POD}$	POD reconstructed velocity in x-, y- and z- directions

$u_{rms}, v_{rms}, w_{rms}$	Root-mean-square velocity in x-, y- and z- directions, respectively
u_T	Terminal velocity of seeding particle
UB	Unsteady bubble
U_{defect}	Defect velocity
VS	Vortex street
W_{ij}	Weight function between grid-points i and j.
$z_{0.5}$	Half-width of wake

Greek symbols

α	Entrainment coefficient
δ	Local thickness of shear layer
Γ	Circulation
λ	Eigenvalue
τ_w	Wall shear stress
φ	Fluctuation of the measured flow velocity
μ	Dynamic viscosity
ρ	Density of medium
$\omega_x, \omega_y, \omega_z$	Vorticity in x-, y- and z- directions

Chapter 1
INTRODUCTION

1.1 Shallow flows

Numerous flows occurring in nature can be regarded as shallow. In these types of flows, the length scale in the horizontal direction is much greater than the vertical length scale. Examples of shallow flow include flow in rivers, headlands, estuaries, stratified lakes and coastal seas (Vriend, 2004). Dissipated heat from the earth may induce density variation in the vertical direction and this density stratification may induce shallow wake flow over mountains and hills (Scorer, 1978). A proper understanding of the shallow flow and their transport capacity is crucial since this will help in predicting as well as modelling flows in riverbeds and coastal zones. This would also help in analyzing the dispersion of heat, pollutants, and biological species in the flow. Moreover, it would add to our efforts in modelling weather since the waterbeds and marshlands play crucial role in controlling the local weather conditions (Jirka & Uijttewaal, 2004).

The present study is concerned with the shallow wake generated by the insertion of a bluff body in an open channel. The incoming flow is of boundary layer type, and therefore sheared in the vertical direction. This boundary layer type of flow can be destabilized by a sudden change of topology, introduction of horizontal shear or deceleration of the flow. In the present case, the destabilizing mechanism is horizontal shear, introduced by the presence of the body in the flow. As a result, large predominantly two-dimensional eddies are shed alternatively from both sides of the body

and are advected downstream. For the case of the deep wake (where the approaching flow is uniform, i.e., zero vertical shear) the flow is always inviscidly unstable. However, the additional vertical shear in the shallow wake helps to stabilize the flow and dissipate the kinetic energy of the two-dimensional eddies. The characteristics of a shallow wake will depend on the comparative influence of two effects – the destabilizing effect of the lateral shear layer and the stabilizing effect of the vertical bed-induced shear.

1.2 Practical occurrences of shallow wake

Shallow wakes can be seen to occur in nature as well as in engineered flows. Some phenomenological examples are illustrated below.

*Atmospheric flow: T*he interaction between the atmospheric boundary layer with physical structures located on the ground (e.g., mountains), can result in large-scale vortex formation. Figure 1.1 shows the image of the cloud shed from the Juan Fernandez Islands (also called Robinson Crusoe Island) off the Chilean coast in September, 1999. The island is about 1.5 km in diameter, and rises 1.6 km into a layer of marine stratocumulus clouds. The flow pattern resembles the classical von Karman vortex street. The vortices are seen to be shed from both sides of the island and advect with the ambient wind. In the downstream direction, the length scale of the wake is several hundred kilometres, amplifying the fractal nature of the wake flow. This type of flow is particularly important in cooling the earth and counteracting greenhouse gas effects.

Stratified water body: Stratified flows like flow around islands, oceans and lakes exhibit shallow flow characteristics, mainly due to their limited vertical depth. Various types of instabilities (to be discussed later) will lead to the formation and development of fluid structures unique to shallow flows. An interesting case in this category is the crude oil spill from the oil tanker Argo Merchant southeast of Nantuket Shoals, Massachusetts in December, 1976 (Van Dyke, 1982). The shallow wake generated by the dispersion of the crude oil in the sea water is observed clearly in the picture shown in Figure 1.2.

Tidal waves in shallow flow: In addition to atmospheric flows, the wake flow shed from solid obstacles like bridge piers may be dangerous in some instances. One of these instances is the tidal wake of Naruto Strait, which connects the Awaji and Shikoku islands in Japan. The left picture in Figure 1.3 shows a freighter stranded in the tidal wave below the bridge. The freighter got stranded in the whirlpool at around 11:00 AM and remained so till the next high tide arrived. In the left picture, a whirlpool of diameter approximately 15 m can be seen in the lower right corner. On the right picture, the whirlpool can be seen very clearly.

Miscellaneous flows: Shallow flows can also be observed in air conditioning applications (Kanda & Linden, 2003), plate heat exchangers and liquid metal sheet casting process. An extreme and almost exact representation of shallow flow can be found in experiments of falling soapfilms (Goldberg et al., 1997) where the bounding surface is almost shear-free, neglecting the air friction. Therefore, this flow is completely free from any three-

dimensional structures and will contain only two-dimensional turbulent motions and hence represent shallow flow.

1.3 Motivation

Since the early days of Prandtl, there has been an enormous amount of research dedicated to the study of flows around bluff-bodies. The mechanism of vortex formation, flow separation and fluid-structure interaction constitutes the greatest part of the literature. Considering the overwhelming number of publications and research hours dedicated to this topic, any new investigation seems to be redundant. But, given the enormous importance of these flow features, it generates new challenges that require better understanding of the fundamental principles that govern them. Additionally, the continuous evolution of computational and experimental techniques provides new perspectives to the same problem. One of the major developments in the area of experimental fluid mechanics is the development of the particle imaging techniques, which enables one to perform measurements in the spatial domain, therefore presenting an unprecedented wealth of information. The combination of computational resources with the development of the charged-coupled-device (CCD) makes the future of fluid mechanics research more promising, especially for flows in which fluid-structures of different scales co-exist.

The major contribution of the present study is to combine the available hardware, software and mathematical tools for the exploration of the characteristics of a typical shallow wake generated in an open channel flow. The complete methodology involves

use of the state-of-the-art particle image velocimetry technique to measure the spatial characteristics of the shallow wake, use of modern techniques to evaluate and process the measurements, development and application of recent mathematical techniques to educe coherent structures in the flow.

Finally, one last paragraph is necessary to define the author's motivation and drive throughout the research. It is not only the complexity of the nature itself, but complexity of the fluid mechanics that this work is intended to address. But what makes our life far more complex is the human nature, our human curiosity that continuously drives us to seek new challenges to overcome, new questions to answer and new obstacle to overcome. We have reached a tremendous level of understanding of the nature surrounding us, still it is highly appropriate to quote the great philosopher Aristotle *"....the more I understand, the more I realize the little I know"*. Any scientific investigation will end up posing new set of questions and obstacles to overcome. There is no doubt that a dissertation is expected to resolve an issue in considerable depth so that it can address almost all questions in mind. However, it will be arrogant to claim or expect that the present investigation will come up with a complete solution of the problem we are examining. In this circumstance, the major objective and personal ambition is to develop versatility, problem solving ability and a broard understanding of the relevant physics and the problem solving abilities. This is, of course, an endless process, but laying the ground and the foundation upon which one can build and evolve these skills is an indisputable part of the dissertation.

1.4 Scope

A typical shallow wake was generated by immersing a sharp-edged bluff body in a shallow open channel flow. The depth of flow was maintained nominally at 100 mm and the aspect ratio of the flow was 12. The flow was subcritical and in turbulent state. According to previous literature, the stability number of the wake implies negligible effect of the bed. Particle image velocimetry measurement was carried out at near-bed, mid-depth and near-surface locations ranging in the streamwise direction extending to ten times the body width.

A general review of the available literature on shallow wake flow is presented in Chapter 2. Following a brief introduction of turbulent flow, the source of uniqueness of the shallow wake is explored. The literature is loosely classified based on the effect of bed, free surface and the approaching flow. In light of the available literature, the relevance of the present study is stressed at the end of this chapter. Chapter 3 contains the description of the particle image velocimetry system used in the measurement. Since particle image velocimetry is a recent technique, a brief introduction of the measurement principle is illustrated and then the configuration of the present series of experiment is discussed. Chapter 4 contains the discussion about the vertical variability of the wake flow in terms of the mean velocity profiles and turbulence parameters at specific streamwise locations at the near-wake region. The presence and effect of coherent structures at the near-bed and near-surface region has been highlighted, but no quantitative information is provided. Chapter 5 covers the vertical variability of the shallow flow, covering near- and intermediate- wake regions in terms of the contours of

time mean velocity, vorticity and turbulence parameters. The effect of the bed and the free surface on the vorticity distribution is highlighted and a phenomenological picture of the flow field is reconstructed. Chapter 6 concerns the application of the proper orthogonal decomposition technique to decompose the flow field into coherent and incoherent parts. The large-scale coherent structures are identified by a novel closed-streamline based vortex identification scheme. Following the identification, a statistical description of the location, size, sense of rotation and circulation of these structures are documented as a step towards quantification of the shallowness effect on the large-scale coherent structures. Lastly, the thesis ends by summarizing the conclusions and recommending a possible path for future study. The related Matlab® scripts used for the present work are included in the Appendices.
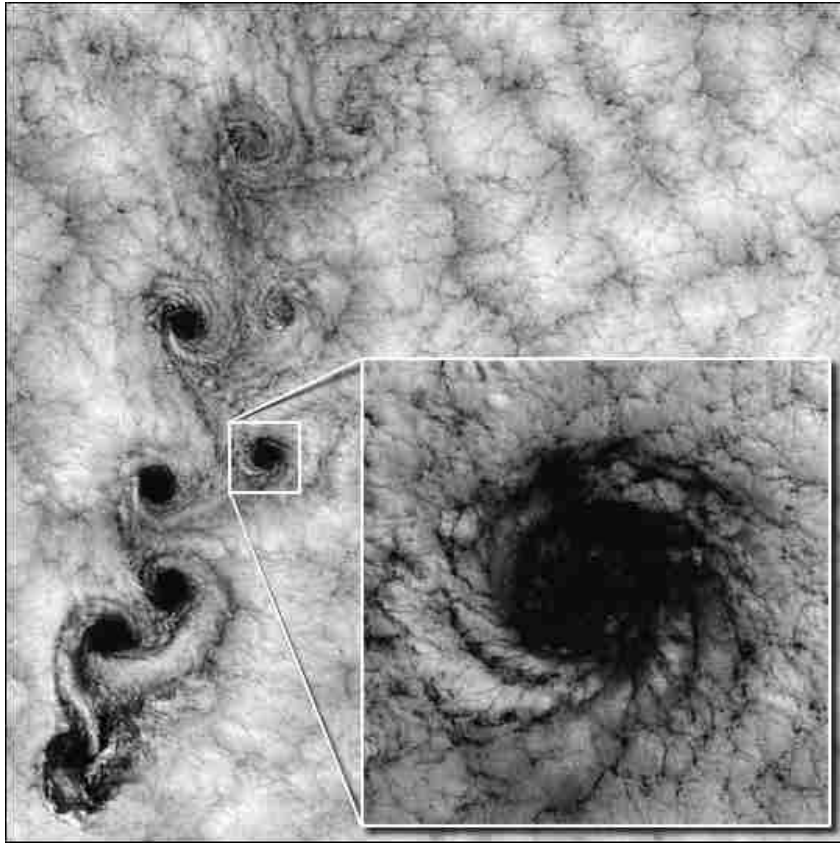
Figure 1.1: Vortex street of the Juan Fernandez Islands [1]
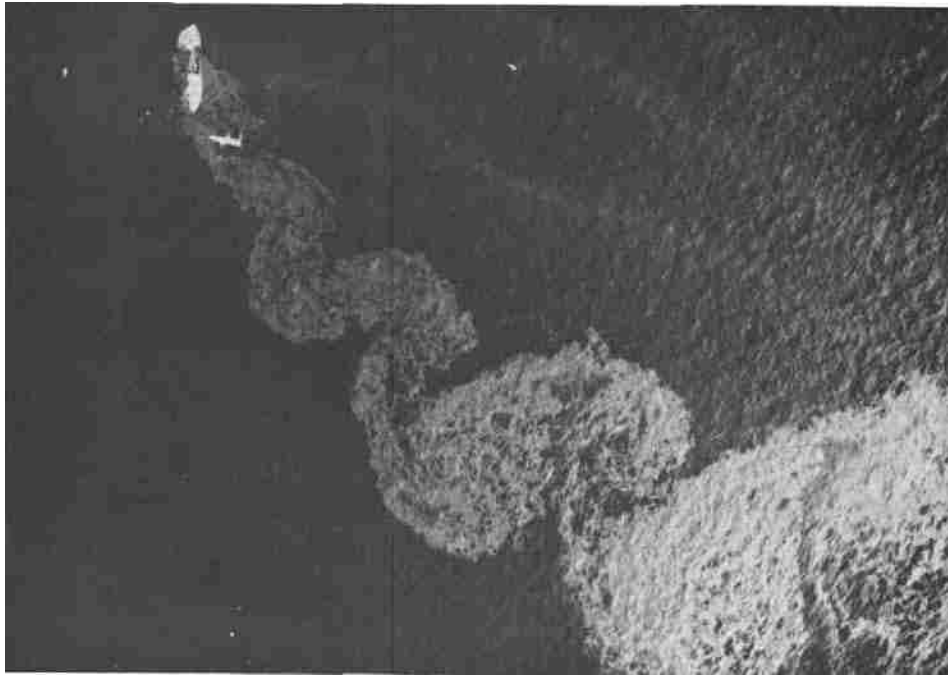
Figure 1.2: Shallow wake behind Argo Merchant (Van Dyke, 1982).
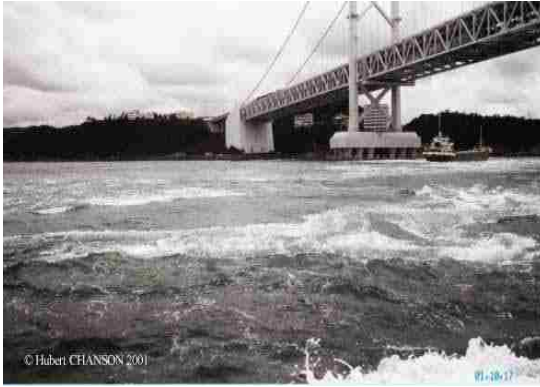
Figure 1.3: Shallow wake in Naruto Strait and the ship stranded in the whirlpool[2]

Chapter 2

LITERATURE REVIEW

2.1 General remarks

This chapter discusses the current state of development in the investigation of shallow wake in open channel flow. Open channel flow itself has several unique features and differs considerably from the conventional boundary layer like flows. Herein, open channel flow is first discussed in brief, to provide the required details of the background flow. According to the existing literature, the uniqueness of a shallow wake is determined by three factors: the effect of bed, the effect of the free surface and the effect of the nonuniform vertically sheared approaching flow. A major portion of the relevant literature is discussed under these three subheadings. Some of the investigations that can not be categorized under these headings are discussed in a separate subsection. The chapter concludes by highlighting the importance of the present study.

2.2 Introduction

Numerous flows occurring in nature can be regarded as shallow (Vriend, 2004). In these flows, the length scale in the horizontal direction is much greater than that in the vertical direction (Jirka & Uijttewaal, 2004). Examples of shallow flow can be found in rivers, headlands, estuaries, stratified lakes and coastal seas (Vriend, 2004). Heat dissipated from the earth can bring forth density variation in the vertical direction which can induce shallow flow over mountains and hills (Scorer, 1978). Knowledge of the characteristics of shallow flow and its transport capacity is crucial in modelling and

predicting the flow, besides assisting in analyzing the dispersion of heat, pollutants and biological species. Furthermore, it would also aid in weather modelling as the waterbeds and marshlands play a crucial role in controlling the local weather condition (Jirka & Uijttewaal, 2004).

From the perspective of fluid dynamics, shallow flow has important features due to the presence of the bounding surfaces in the form of the bed and the free surface. The bed imparts vertical shear while the free surface acts as a stress-free weak boundary. A typical shallow wake can be generated by introducing a disturbance in the form of a bluff-body in an otherwise plane flow. The resulting separation of flow from the sides of the body, though similar to a deep wake, would be modified due to the effect of the background flow conditions. As a first step, a brief discussion of a shallow channel flow is necessary, as this constitutes the background flow condition for the shallow wake.

2.3 Shallow channel flow

The simplest example of shallow flow is the plane uniform open channel flow. This type of flow is unique because it developes under a confinement bounded by the side walls of the channel and by the free surface which is subject to atmospheric pressure. The flow is driven along the slope of the channel by the component of the weight of the liquid, and the shear force on the channel boundaries is the main resisting force. Open channel flows can be classified as shallow when the vertical length scale of the flow (usually the depth, H) is significantly smaller than the horizontal/transverse length scales (Jirka & Uijttewaal, 2004). While in the limit of infinite depth, flow in open channels could be described by the theory of classical turbulent boundary layers, in many practical

applications and hydraulic engineering practice, this approximation is violated due to the finite shallow depth of the flow.

2.3.1 Near-bed region

The shallow open channel flow is governed mostly by the wall turbulence. An example of a velocity field in open channel flow obtained with the particle image velocimetry (PIV) technique is shown in (a). This figure shows a typical time-averaged velocity in a viewing window 100 mm long and 92 mm high. Averaging is done over 2000 PIV images. The mean velocity profiles conform to the typical pattern of the streamwise velocity in wall-bounded flows. In many situations, the mean velocity can still be characterized by the logarithmic law of the wall. However, recent experiments by Pokrajac et al., (2007) in shallow open channel flows over rough beds have shown that the logarithmic layer will form only if there is enough space between the top of the roughness and the free surface. If this is not the case, the velocity profile may still have a logarithmic shape, but the parameters of the corresponding logarithmic law may not have the same physical meaning as the parameters of the universal logarithmic law of the wall.

One of the disadvantages of the time–averaging is that it hides much of the unsteady features of the flow. In contrast, the instantaneous and fluctuating velocity fields obtained at a particular instance. While the instantaneous velocity field ((b)) provides little evidence for the presence of vortical structures, the fluctuating velocity field reveals well-defined patterns. In (c), a small vortex (highlighted by a circle) and a typical signature of an ejection event (highlighted by a square) in the bottom-left corner

of the same field can be seen. During the ejection event, fluid particles are lifted away from the wall by the positive wall-normal fluctuations.

The structure of the turbulence in shallow open channel flows is three-dimensional, dominated by ejection and sweep events. Near the bed, shallow open channel flow is mainly occupied by fluid structures similar to these observed in the turbulent boundary layer. Numerous studies have been devoted towards exploration of the effect of the boundary layer in an effort to understand the associated dynamics of the near-bed mechanisms (e.g., Falco, 1977; Head & Bandyopadhyay, 1981; Robinson, 1991; Adrian, 2007). Mainly, the bed region is dominated by the negative streamwise fluctuations with fluid particles being lifted away from the bed by positive bed-normal fluctuations (ejection) and positive streamwise fluctuations moving towards the bed (sweep). Above this region, turbulent bulges with a length scale of the order of two-to-three wall units can be observed (Blackwelder & Kovasznay, 1972). In addition, structures inclined about 45° to the bed, resembling a horseshoe, appear in the flow. They are commonly known as hairpin vortices (Theodorsen, 1955). According to Kline & Robinson (1989), the near-bed region is mainly occupied by the following structures: low speed streamwise streaks in the viscous sublayer, events corresponding to ejection and sweep, vortical structures of various forms, three-dimensional turbulent bulges and hairpin vortices. Recent PIV measurements (Roussinova et al., 2008) in open channel flow at shallow depth ($H = 0.10$ m) confirmed the presence of the hairpin vortices near the bed. A simple way to visualize the vortical structures is to apply Galilean decomposition via removal of a fixed advection velocity from the instantaneous velocity

14

field. This method is suitable for to uncovering vortices advecting at similar speeds. However, in wall-bounded flows, vortices advect with different speeds at different wall-normal locations and, in order to reveal all embedded structures in the flow, one must remove a broad range of advecting velocities. In Figure 2.2(a) and Figure 2.2(b), Galilean decompositions of the instantaneous velocity field shown in Figure 2.1 are presented. By removing different advection velocities from the instantaneous velocity field, different structures can be seen. In Figure 2.2(a), several heads of the hairpin vortices are visible with the circles moving in a frame convecting with $U_C = 0.9U_0$. These vortices cannot be identified from the fluctuating velocity field shown in Figure 2.2. Figure 2.2(b) reveals the result of the Galilean transformation for a convection velocity $U_C = 0.8U_0$. As the convection velocity becomes smaller than the maximum velocity U_0, the vortices near the solid wall become visible. More information related to the existence of large-scale structures in the flow was presented by Roussinova et al., (2008) who applied the proper orthogonal decomposition (POD) technique to expose the structures. Their POD results revealed the existence of hairpin vortices of different sizes and energy levels. Further analysis of the POD reconstructed velocity maps was performed using different combinations of modes to expose the energetic large-scale structures, and less energetic small-scale structures. The first set of POD modes recovered 50% of the turbulent kinetic energy while the second group of modes recovered 33% of the kinetic energy. An example of a POD reconstructed velocity field of recovering 50% of the energy is shown in Figure 2.3(a) where most of the large eddies are elongated and inclined towards the boundaries in the streamwise direction. The

results also revealed patterns of strong ejection (Q2) and sweep (Q4) events which are common features in wall-bounded flows. Close to the free surface, existence of hairpin vortices was observed with legs possibly extended upwards towards the free surface. Near the free surface, the induced flows from the large scale-structures contribute to the increase of the quadrant 3 events. In Figure 2.3(b), POD reconstructed velocity field from a second set of the POD modes recovering 33% of the energy is shown. By combining the higher order POD modes (13-100), structures are exposed which appear to be more circular. Hairpin vortices with length scales smaller or in the order of the flow depth have been also found in shallow open channel flows (Nezu & Nakagawa, 1993).

Because of the shallow depth, most of the low speed fluid parcels often reach the water surface, while at times still being attached to the bed. Nikora et al., (2007) speculate that these low speed parcels can be viewed as clusters of fluid-made 'cylinders' randomly distributed in space and embedded into the faster moving surrounding flow. These attached eddies can be responsible for weakening the horizontal eddies present in the flow, providing for a very different mechanism of energy transfer.

2.3.2 Near free surface region

Based on evidences put forward in the literature (e.g., Komori et al.; 1982, Willart & Gharib, 1994, Maheo, 1999), close to the free surface the turbulent kinetic energy in the vertical direction has been shown to be redistributed to the horizontal directions (both streamwise and transverse). The redistribution of kinetic energy occurs in two separate fluid layers close to the free surface (Hunt & Graham, 1978). The first layer is where the turbulent kinetic energy in the vertical direction decreases and the surface parallel

component is enhanced. The second layer corresponds to a very thin viscous layer, where the turbulent fluctuation of the vertical velocity rapidly diminishes to zero. Walker et al. (1996) determined the thickness of the former and later layers to be approximately one and one-tenth of the turbulent length scale, respectively. The energy redistribution is limited to only large-scale structures of the flow, whereas the small-scale structures maintain their universality. Based on these observations, Shen et al. (2000) proposed a computational model for large-eddy simulation (LES) of free surface turbulence.

Close to the surface, mainly two types of structures can be observed; surface-normal vortex tubes with predominantly vertical vorticity component and surface-parallel vortex tubes buried inside the surface layer. Physically speaking, one would assume the surface-normal vorticity would induce 'pressure' and control the deformation of the free surface. But, Dommermuth (1994) concluded the presence of a weak correlation between the free surface deformation and surface-normal vorticity by comparing the initial and the final state of the vorticity induced pressure and the free surface deformation. The lack of correlation is also supported by the findings of Zheng et al. (1999). However, Weigard & Gharib (1995) performed simultaneous shadowgraph and PIV experiments to show that the vertical vorticity location and strength correlate fairly well with the appearance of the free surface deformation.

Due to the computational difficulty of modeling a free surface, very little computational work was carried out until recently. The first direct numerical simulation (DNS) of the free surface, utilizing the rigid lid assumption, was reported by Lam & Banerjee (1992). Worth mentioning are the studies of Komori et al. (1993) and Handler et

17

al., (1993) who utilized a full free surface computational model in the direct numerical simulation. Pan & Banerjee (1995) performed DNS of open channel flow to explore the large-scale structures appearing at the free surface. They broadly classified the structures into three groups: 'vortices', 'upwelling' and 'downdraft'. These types of structures have also been reported by Gupta et al. (1994) based on experimental observations. 'Vortices' is the region of cluster of surface-normal vorticity where the ratio of surface-normal to the surface-parallel velocity is close to zero, i.e., the vertical velocity towards the free surface is negligible. 'Upwelling' is a region of divergence of streamlines with large surface-normal velocity. The 'downdraft' region exhibits strong downward velocity component originating from the free surface. It should be noted that the surface normal velocity has to be zero exactly at the free surface, but these velocities mentioned above are at a location of 10-20 wall units beneath the free surface, inside the surface layer. When a typical upwelling reaches the free surface, a near circular vorticity pattern (donut shaped) is generated. This pattern interacts with the free surface and generates vorticity which connect with the free surface and form a number of short-lived vortices around the edge of the upwelling. At the end of this cycle, downdraft takes place. The energy spectra of the velocity close to the free surface shows $k^{-5/3}$ and $k^{-3.5}$ regions, which is characteristic of two-dimensional turbulence, where k is the characteristic wave number. The turbulent kinetic energy transfer spectra indicate flow of turbulent kinetic energy from smaller to larger scales at the near-surface region. But at a considerable distance from the free surface, deep within the flow, the usual three-dimensional turbulence persists.

18

Nikora et al. (2007) used particle tracking velocimetry to explore the near-surface structure of an open channel flow for both subcritical and supercritical flow conditions (Froude number Fr = 5.64, 3.49 and 0.31; corresponding Reynolds number Re_d = 6437, 6397, 2736, respectively). Following the velocity measurement, the probability density function, correlation function and structure function of the streamwise and transverse velocity components close to the free surface were examined. These indicate the existence of the large-scale structures of lateral extent larger then the flow depth at the near free-surface location. The structures have characteristics that resemble two-dimensional turbulence and depict inverse energy cascade. They postulated two possible hypotheses regarding the appearance of the large-scale structures in shallow channel flow. Any turbulent channel flow is characterized by sweep events and ejection of fluid packets from the bed due to the associated dynamics of the turbulent boundary layer - like region (Adrian, 2007). Due to the limited depth of shallow channel flow, these fluid packets eventually arrive at the free surface while also being attached to the bed. One can view these structures as a cluster of 'fluid cylinders' resembling tornadoes immersed in the background flow. These structures interact with the instability associated with the inflexion point of the transverse velocity distribution and generate horizontal structures with two-dimensional turbulence characteristics. Another possible mechanism of generation of these structures was put forward by Shen et al. (1999). The hairpin eddies which are generated near the bed reach the free surface due to the limited depth of the flow. In that situation, the head of the eddy quickly dissipates or is advected by the flow and the remaining legs contribute to the formation of the two-dimensional structures.

19

It should be noted that a typical shallow turbulent channel flow contains two-dimensional as well as three-dimensional structures. The length scale of the three-dimensional structures (l_{3D}) is in the order of, or less than, the depth of flow. But the two-dimensional structures of length scale (l_{2D}) greater than the flow depth, with predominantly vertical vorticity is unique to shallow channel flow (Chen & Jirka, 1995). Jirka & Uijttewaal (2004) has aptly summarized the following: "*Shallow flows are largely unidirectional, turbulent shear flows driven by piezometric gradient and occurring in a confined layer of depth. This confinement leads to the separation of turbulent motions between small scale, three-dimensional turbulence $l_{3D} \leq H$, and large scale two-dimensional turbulent motion, $l_{2D} \geq H$, with some mutual interaction.*"

2.4 Shallow wake

Before embarking upon the discussion of the shallow wake characteristics, a convenient starting point may be a brief discussion of the deep wake. In this context, the deep wake is defined as the wake produced when the body is immersed in a flow of 'theoretically' infinite depth, i.e., the approaching flow is uniform in nature and there are no boundary effects. When any unbounded flow goes past a bluff body, four distinct regions can be observed upstream and downstream of the bluff-body as mentioned by Zdravkovich (1997). He broadly divided the field around the bluff body into four regions. Region I is a very thin region of retarded flow directly upstream of the body. As the flow impinges upon the body, a stagnation point is formed and a boundary layer is generated around the surface of the body. This region is referred as Region II. Region III is the

region on the sides of the body, where the flow velocity is higher than the mean incoming flow. This region is also called as accelerated flow region. Region IV is the region directly downstream of the body and contains the recirculation region. Several aspects of the deep wake including velocity defect profiles have been studied in detail (for example, see Williamson, 1995, 1996). Usually, the incoming flow interacts with the boundary layer formed on the body and the separated shear layer is shed as vortices in the streamwise direction. Although, the vortex shedding process appears two-dimensional in nature, there is considerable three-dimensionality in the flow (Wei & Smith, 1986). The three-dimensionality mainly originates from the end condition (Ramberg, 1983) and may induce spanwise disturbance and oblique vortex shedding (Hammache & Gharib, 1991). In all cases, the separating boundary layer rolls up on both sides of the body and is advected downstream as the von Karman vortex street. The periodic vortex shedding is characterized by a nearly constant Strouhal number ($St = fD/U \sim 0.2$) for $1000 \leq \mathrm{Re}_D \leq 100{,}000$. Important in the present context is the achievement of self-similarity at far-wake streamwise locations (Pope, 2000).

When a body is immersed in an open channel flow of finite flow depth, a shallow wake is generated. The presence of the bounding surfaces (bed and free surface) has two different effects on the development of a shallow wake as mentioned by Chen & Jirka (1995). First, the limited depth restricts the onset of the three-dimensional breakdown of the vortex street. As a result, the von Karman vortex street can be observed for a larger range of Reynolds numbers in a shallow wake. For example, the pattern of crude oil spillage from the ship Argo Merchant stranded at Nantuket Shoals in Massachusetts

21

shows a clear vortex street pattern at a very high Reynolds number $\mathrm{Re} \approx 10^7$ (Van Dyke, 1982). Secondly, the bed friction tends to arrest the transverse growth of the disturbances associated with a typical vortex street pattern and stabilize the wake. This may occur either in the near-wake, or in the far-wake region. For the case of a shallow wake, the stability number, as will be shown later, determines the effect of the bed friction and the subsequent wake stability. In the near-wake region, if the stability number $S_{near} = C_f D / H$ exceeds a certain critical value, wake stabilization takes place. In the far-wake region, stability number is defined as $S_{far} = C_f 2b / H$, where b is the local wake width. Similar wake stabilization takes place at the far-wake region if S_{far} exceeds a certain critical value.

2.4.1 Stability number

Crucial to the development of the shallow wake is the mutual interaction of the vertical shear due to the approaching flow with the horizontal (transverse) shear due to the variation of momentum deficit in the transverse direction. Therefore, the spatio-temporal growth of the shallow wake is controlled by their mutual interaction. The shallow wake is maintained in an equilibrium state as a balance of two different effects: on the one hand, turbulent kinetic energy is extracted from the mean flow and is fed to the large-scale coherent structures by interaction with the lateral shear layer. On the other hand, in the bottom boundary layer, the turbulent kinetic energy is extracted from the large-scale structures and dissipated through the small-scale structures according to Kolmogorov theory of local isotropy. Thus, one can balance the loss of the turbulent

energy due to the bottom friction by the production of the turbulent kinetic energy by the lateral shear layer. The energy fed into the large-scale coherent structures can be computed as the product of the coherent velocity fluctuations and the transverse mean streamwise velocity gradient as (Babarutsi & Chu, 1985),

$$P = \langle u_c w_c \rangle \frac{\partial U}{\partial z} ; \tag{2.1}$$

where, the subscript 'c' denotes the velocity associated with the coherent motions only. u and w indicate the instantaneous velocity in streamwise (x) and transverse (z) directions, respectively. The produced energy is dissipated through the small-scale fluctuations at the bottom boundary layer. Babarutsi and Chu (1985) showed that if the velocity associated with the coherent structure is small compared to the mean flow, then the dissipation can be approximated as:

$$F_b = \frac{C_f}{2H} U (2\langle u_c u_c \rangle + \langle w_c w_c \rangle), \tag{2.2}$$

where C_f is the skin friction coefficient and H is the depth of flow.

Equating the above two equations, the flux stability number can be approximated as

$$S_{flux} = \frac{P}{F_b} = \frac{C_f U}{2H \frac{\partial U}{\partial z}} \frac{2(\langle u_c u_c \rangle + \langle w_c w_c \rangle)}{\langle u_c u_c \rangle}. \tag{2.3}$$

The ratio on the extreme right represents the ratio of the coherent Reynolds normal and shear stress. Chu et al. (1983) proposed a gradient stability number for shallow flow, which has an inflexion point in the transverse distribution of the streamwise velocity, i.e.,

$\dfrac{\partial^2 U}{\partial y^2} = 0$. Without affecting the calculation, the term at the extreme right can be dropped

safely and the velocity gradient can be expressed as $\Delta U = U_1 - U_2$, where U_1 and U_2 are

characteristic velocity at each side of the shear layer of local thickness δ. Thus, the

gradient stability number is

$$S_{grad} = \frac{C_f}{H} \frac{U}{\dfrac{\partial U}{\partial y}}\Bigg|_{Inflexion} \approx C_f \frac{\delta}{H} \frac{U_{avg}}{\Delta U} = \frac{C_f}{2R} \frac{\delta}{H}; \qquad (2.4)$$

where $R = \dfrac{U_1 - U_2}{U_1 + U_2} = \dfrac{\Delta U}{2U_{avg}}$.

This equation is applicable for any general shear layer. For the case of a shallow wake, it

can be applied at the lee of the recirculation bubble. Since $U_2 \approx 0$, $R = 1$ and the width of

the shear layer is approximated to be half of the diameter of the cylinder (D/2), the wake

gradient stability number can be found as,

$$S_{grad} = \frac{1}{4} C_f \frac{D}{H}. \qquad (2.5)$$

The wake stability number (S) is four times the gradient stability number,

$$S = 4S_{grad} = C_f \frac{D}{H}. \qquad (2.6)$$

Unlike the gradient stability number, wake stability number (S) is a global parameter,

and it does not depend on the choice of local coordinate system. Therefore, it is a more

universally accepted number and mentioned profusely in shallow wake literature.

2.4.2 Effect of the bed

As mentioned earlier, the uniqueness of a shallow wake depends on the combined effect of the bed and the free surface. Although these two effects are closely interrelated, it may be possible to view them independently. Wolonski et al. (1984) defined an island wake parameter, $P_{island} = U_a H^2 / k_z D$, where U_a is the ambient flow velocity, H is the flow depth, k_z is the vertical eddy viscosity and D is the characteristic dimension in the transverse direction. The vertical eddy viscosity was approximated as $k_z = 0.15 H U_\tau = 0.15 H U (C_f / 2)^{\frac{1}{2}}$, where U_τ is the friction velocity. They have suggested that a critical value of P_{island} of the order of unity exists, and a vortex street type of wake is not possible for $P_{island} < P_{c,island}$. Their classification is somewhat incomplete and lacks descriptive information, as it is based on satellite imaging and temperature mapping of the island wake and no direct measurements were conducted to support the classification.

An important investigation in shallow wake was performed by Ingram & Chu (1987) by observing the oceanic shallow wake behind island in Rupert Bay, Ontario. Initially, they formulated an analytical description of the effect of the bed on the shallow flow. To complement the formulation, they performed flow visualization in the laboratory. A total of six laboratory observations and 26 events of oceanic shallow wakes at Reynolds numbers (Re = $4HU/\gamma$) ranging from 4,700 to 11,000, and stability numbers ranging from 0.03 to 0.65 have been reported. They introduced the stability number as a measure of the bottom friction effect on the shallow wake. Based on a series

of observations, they postulated a critical stability number of 0.48, above which the oscillating characteristic of the wake gets stabilized due to the bottom friction. Below the critical stability number, the effect of bed friction is not strong enough to stabilize the wake and a vortex street type of wake can be observed. Figure 2.4 is adopted from their paper and depicts three different cases; (a) $Re = 11,000$, $S_w = 0.031$, (b) $Re = 11,000$, $S_w = 0.013$ and (c) $Re = 4,700$, $S_w = 0.054$. Clearly seen in this figure is the suppression of the wake oscillation with change in the Reynolds number and stability number. The frictional effect of the bed is also shown to affect the entrainment coefficient of the wake. However, the range of Reynolds number and stability number for the investigation is not large enough to draw firm conclusions about the state of the wake.

Along the same lines, extensive laboratory experiments (57 with circular cylinder, 54 with solid plate and 34 with porous plate) and visualization of shallow wake was performed by Chen & Jirka (1995) covering a wide range of Reynolds number and stability number ($Re_h = 570\text{-}7300$, $Re_d = 3000\text{-}414000$, $S = 0.01\text{-}0.94$). Based on visual observations, they divided the shallow wake into three different categories: vortex street type (VS), unsteady bubble wake (UB) and steady bubble wake (SB). If the perturbation due to the separating shear layer is dominant, the shallow wake resembles the well-known von Karman vortex street as seen in a conventional deep wake. Although qualitatively similar, the vortex street of the shallow wake and the conventional von Karman vortex street have significant differences. The vortex street (VS) shows a streaky and fuzzy appearance due to the presence of the small-scale structures arising from the bed frictional effect. This fuzziness sometimes causes blurring out of the well observed

roll up of the vortices. This type of wake is visible for $S \leq 0.2$. If the stability number is increased ($0.2 \leq S \leq 0.5$), the bed friction effect increases and the flow separates from both sides of the body simultaneously, not alternatively. A nearly steady bubble is formed immediately downstream of the body. But the end of the bubble oscillates alternatively and this leads to periodic breakdown of the vortices. This is called the unsteady bubble (UB) wake. The steady bubble (SB) mode can be observed when the bed friction effect decreases the momentum to such an extent that the recirculation bubble stays almost stable at the lee of the body and no shedding is observed. By analytical approximation of the wake momentum deficit, Chen & Jirka (1995) defined a length scale L beyond which the wake momentum deficit disappears,

$$L = 2h / C_f = 2D / S.$$

Unstable shallow wakes get stabilized after a streamwise distance of the order of L, mainly due to the increasing momentum deficit, and subsequent increase in the stability parameter. They also observed that the width of the shallow wake greatly exceeds the depth of the flow, and as a result the flow structures are mainly two-dimensional in nature. They suggested that the majority of the effect of the bed friction is agglomerated at the bottom boundary layer and may not contribute towards the three-dimensionality of shallow flow. The bed friction effect is averaged over the full depth of flow and is manifested in the form of the wake stability number.

Nagretti et al. (2005) mounted artificial roughness mats on the bed of a shallow wake flow to investigate the effect of the increased roughness. Two series of experiments were conducted; for the first series, roughness elements were placed in the lateral shear

layer region and for the second series, the roughness elements were placed at the end of the re-circulating bubble. For the first case, roughness was found to decrease the magnitude of the Reynolds stress in addition to narrowing the wake width. Also, the wake behaved very similar to a stable bubble wake, since the introduced roughness reduces the momentum exchange with the ambient flow. When the roughness element was placed at the back of the re-circulating bubble, the usual wake behaviour was observed till the flow reached the roughness and the fluid structures were destroyed while flowing over the roughness. This study explicitly indicates that the bed roughness has the ability to alter the near-wake as well as the far-wake structure.

2.4.3 Effect of the free surface

Not many studies have been conducted on the free surface effect, mainly because of numerical (mathematical representation of the free surface) and experimental (measurements close to the corrugated free surface) constraints. Interaction of the free surface with shallow flows (jet, wake, mixing layer) shows the development of the surface deformation as a function of the anisotropy between the vertical and transverse turbulent fluctuations (Walker and Johnston, 1991; Anthony and Willmarth, 1992; Walker et al, 1996; Logory et al., 1996; Maheo, 1999).

Logory et al., (1996) used LDV and PIV to investigate the effect of free surface on an otherwise deep wake. Due to the large water depth, the effect of the bed is expected to be confined close to the bed and not penetrate beyond a certain vertical distance from the bed. As a result, close to the free surface, the sole effect of free surface will be realized with reduced contamination arising from bed friction. In fact, LDV measurement

of the wake flow behind the bluff body, measured at half-depth, matches well with the published data for the deep wake. But close to the free surface ($\sim$ 12-13 mm below) the wake width was found to be doubled, while the centerline velocity remained almost constant. The contour of the mean streamwise velocity in the streamwise plane downstream of the body, adopted from Logory et al. (1996) is shown in Figure 2.5. The self-similar behavior of the mean and root-mean-square velocity is also lost at the free-surface location. PIV measurements at a depth $\sim$ 20 mm below the free surface showed evidence of 'upwelling' and 'downdraft' as seen in a shallow flow, in addition to the large-scale structures originating due to the presence of the body. At the near-surface layer, opposite signed streamwise vorticity was found to exist in pairs at both sides of the wake centreline, which induces flow from the centreline towards the ambient flow region. In the deep wake, vortex structures are predominantly two-dimensional, but close to the surface, the vortex structures tend to re-orient themselves in either surface-normal or surface-parallel direction. The magnitude of the surface-normal vorticity was found to be smaller compared to the deep wake region. The origin of these structures is believed to be the quasi-streamwise rollers originating from the turbulent boundary layer on the bluff body. The existence of these surface-normal structures was also confirmed by the LIF (laser induced fluorescence) flow visualization. Histogram of the vorticity of these surface-parallel structures revealed that they are inclined at 45-50° angles from the wake centreline and induce a velocity away from the wake centreline directed to the upstream direction. The resulting motion from this complex vorticity distribution causes the wake

widening at the near-surface region as the surface-parallel structures carrie low momentum fluid towards the ambient flow region.

Based on the available literature and his own analysis, Maheo (1999) summarized the near-surface dynamics of a typical shallow flow, for the case of turbulent jet and wake. Maheo (1999) found that the free surface only affects the velocity components in a thin layer close to the surface. The thickness of the surface layer was approximately one-half of the local width or the vorticity thickness of the wake or jet, respectively. Inside this layer, the fluctuation in the vertical direction gets retarded and the turbulent kinetic energy in the vertical direction was redistributed to the horizontal velocity components in the streamwise and transverse directions. The streamwise vorticity tubes buried inside the surface layer were found to generate surface currents which affect the dynamics of the flow. Figure 2.6 shows a typical signature of the surface currents close to the free surface. The motions of these structures contribute towards widening of the surface shear flows, compared to the deep flow case. He found the widening of the turbulent shear layer at the near-surface can be as much as 20% for a turbulent wake and 25% for a turbulent jet.

2.4.4 Effect of the approaching velocity

The incoming open channel flow approaches and senses the presence of the body. When the approaching flow meets the body, a stagnation point is generated and the total flow divides along the upstream sides of the body. The resultant stagnation pressure at the body at a certain elevation is higher than at an elevation closer to the bed due to the nonuniform incoming velocity profile. Consequently, a vortex tube is generated and elongated along the sides of the body, due to the accelerating flow region (Region III) at

the sides of the body. This particular system of vortex tubes is called a horseshoe vortex, and it plays a crucial role in the development of a shallow wake.

Rao et al. (2004) investigated the effect of the approaching velocity on the bed-structure interaction for a typical shallow wake by a qualitative dye visualization study for flow depths of 150, 200 and 250 mm, respectively. The maximum streamwise velocity and Reynolds number ranges were $U = 0.08 - 0.21$ m/s and $Re_d = 1500\text{-}4400$, respectively. Dyes of different colors were injected into the flow through ports situated at different elevations on the cylinder. Amongst their conclusions, they found a vertical oscillation of the shear layer at the sides of the body. The source for this was tracked back to the horseshoe vortex wrapping around the body. As mentioned earlier, they connected the dynamics of the horseshoe vortex as the possible source of the three-dimensionality of the shallow wake. Figure 2.7 shows the side view of a circular cylinder, immersed in a shallow channel flow of 100 mm depth. Red and blue dyes were injected through ports located at 14.3 mm and 63.5 mm from the bed. The red dye from the lower port became entrapped into the horseshoe vortex and followes the same closely. The blue dye follows the vortex shedding from the side of the body. A distinguishing feature of the horseshoe vortex is the upward three-dimensional rollup of the horseshoe vortex and the subsequent interaction with the vortex street emanating from the sides of the body. This interaction leads to the three-dimensionality and vertical variability of the shallow wake.

Wang et al. (2006) investigated the effect of variable momentum thickness of the approaching boundary layer on different aspects of the downstream wake flow. The momentum thickness of the approaching boundary layer was adjusted to be $0.07D$, $0.13D$

and 0.245D, where D (= 20 mm) is the characteristic width of the body. The Reynolds number of the flow was Re_D = 11,500. In this experiment the flow was allowed to move over the top of the body, i.e., the body did not pierce the free surface. This does not really comply with the standard definition of a shallow wake, but some of the conclusions may be worth mentioning. With increasing momentum thickness of the approaching boundary layer, an upward flow originating from the bed and towards the free surface was noticed. This upward flow contributed towards the reduction of the reverse flow region close to the bed. At the same time, the magnitude of the Reynolds stress decreased close to the bed. Also, the variable thickness of the approaching flow was found to alter the nature of the vortex shedding from the body (symmetric/anti-symmetric). These studies indicate that the approaching flow has a significant influence on the shallow wake flow.

2.4.5 Two-dimensional coherent structures

The turbulent open channel flow can be disturbed at any time by a sudden change of the flow geometry, for example, presence of an obstacle mounted in the channel floor. These initial disturbances extract the turbulent kinetic energy of the flow and grow in size in the form of eddies. During the process of growth, sometime, the transverse size of these eddies may exceed the vertical flow depth. Due to purely kinematic reason, the vorticity vector of these eddies, termed as two-dimensional coherent structures (2DCS), must be perpendicular to the bed or the free surface. The appearance of the 2DCS is consistently reported by a number of researchers (Dracos, 1992; Chen & Jirka, 1995; Uijttewaal & Tukker, 1998; Singha et al., 2009)

Holmes et al. (1996) and Bonnet et al. (1998) reviewed the recent literature on the importance and the characteristics of coherent structures in different kinds of turbulent flow. Although there is no general consensus about the definition of a coherent structure, Hussain (1983) formed a working definition as follows: "*A coherent structure is a connected (large-scale) turbulent fluid mass with an instantaneously phase-correlated vorticity over its spatial extent*". Carmer & Jirka (2001) showed that the transport capacity of these large-scale structures is about two orders of magnitude higher than the small-scale structures. Therefore, characterization of the large-scale coherent structures will lead to a better modeling of discharge and dispersion of pollutants released in shallow rivers or lakes.

Jirka (2001) has indicated three different type of forcing mechanisms for the generation of the large-scale coherent structures:

Topological forcing (Type A): Presence of a body (i.e., island, headlands, jetties etc.) in a shallow flow represents the strongest mechanism for generation of 2DCS. With development of these eddies, the interaction between them and the bed increases. As a result, more energy is extracted from the mean flow and is fed to the rotational energy of the eddy. In this case, turbulent kinetic energy flows from the smaller to the larger scale, and therefore exhibit inverse energy cascade. An example of this type of instability is the shallow wake past Guadalupe Island off the coast of California, as shown in Figure 2.8(a).

Internal shear flow instability (Type B): Varying momentum flux (deficit or excess) due to the velocity gradient in the lateral direction may trigger this type of instability.

Such triggering action can be caused by the presence of a source flow such as a shallow jet, wake or mixing layer. Figure 2.8(b) shows one example of this type of instability at the joining of two rivers along the mixing layer.

Secondary instability of the base flow (Type C): This is the weakest type of instability and experimental evidence is sparse (except for Nikora et al., 2007). Consider the case of a shallow channel flow containing a vertically sheared boundary layer and 3D turbulent coherent structures. This flow is maintained in equilibrium by the bed friction. However, slight imbalance in the flow may lead to the redistribution of the turbulent kinetic energy in the entire range of wave numbers. The distortion of the vortex line caused by the secondary instability will lead to the formation of 2DCS provided the disturbance does not die down.

Following the work of Dracos et al. (1992) and Uijttewall & Tukker (1998), the generation and development of the 2DCS can be divided into a number of stages in time and space. The 'near-field' of any shallow flow is characterized mainly by the two-dimensional transverse shear layers and contains small-scale three-dimensional structures. The 'middle-field' has strong three-dimensionality because of the interaction of the bed and free surface. At the 'far-field', the structures generated earlier grow in size greater than the depth of flow. To preserve the kinematic condition, these eddies must have two-dimensional character and will have vorticity perpendicular to the free surface. Also, the mean flow, whose transverse scale is of the same order as the large turbulent eddies, became two-dimensional.

Following the generation, the 2DCS grow and develop by entraining outside ambient fluid. In addition to this, two or more 2DCS may merge together to generate a larger 2DCS (Dracos et al., 1992). It must be mentioned here that the limited depth restricts the mechanism of vortex stretching that is present in three-dimensional turbulent flow. Merging of 2DCS to form larger 2DCS leads to the flow of turbulent kinetic energy from the high to the small wavenumber range and therefore exhibits inverse energy cascade (Kraichnan, 1967). The possible existence of the two-dimensional turbulence in shallow flow was demonstrated by Dracos et al. (1992) and Chen & Jirka (1998) by computing the velocity spectra. The 2DCS lose their energy owing to the effect of the bed friction. Dimensionally, it can be shown that an eddy of size $2H/C_f$ will loose all its energy in one rotation due to bed friction.

2.4.6 Related literatures and vertical variability of shallow wake

There are other studies in the literature related to the shallow wake. These include, for example, searching for suitable scale to absorb the effect of bounding surfaces, and investigation of the variation of the flow characteristics as a function of the vertical elevation from the bed. Balachandar et al. (1999) classified the shallow wake into shallow-shallow and deep-shallow wake based on visual observation and video-imaging of dye concentration injected in a shallow wake. The depth of flow, mean freestream velocity and Reynolds number were varied between 10 - 40 mm, 76 - 157 mm/s and 1570 - 4810, respectively. If the stability number was lower than a critical value ($S_w < 0.008$) then the von Karman type vortex street was observed. For stability numbers greater than the critical value, either an intermittent vortex street was observed or it was completely

annihilated. This classification is more like that of Wolosnksi (1984) for island wake as discussed earlier. Figure 2.9, adapted from Tachie (1997), shows an example of the deep-shallow and shallow-shallow wake, respectively. The left figure corresponds to higher depth of flow ($H/D = 2.00$), and the right figure corresponds to lower depth of flow ($H/D = 0.25$). The vortex street can be seen for the case of higher depth of flow, but it was completely annihilated for lower flow depth due to increased bed friction effect. In a later study to characterize turbulent shallow wakes, Balachandar et al. (2000) performed velocity measurements downstream of a flat plate immersed in a shallow channel flow. Measurements were carried out at three different vertical locations, $H/4$, $H/2$ and $3H/4$. Several normalizing parameters were attempted in an effort to collapse the mean streamwise velocity defect at different streamwise locations and depth of flow. $C_d \delta_v$ was identified as one of the proper normalizing length scales, where C_d and δ_v are the drag coefficient and the half-width of the wake, respectively. At a given distance from the bed, the approaching velocity upstream was found to be one of the normalizing scales for streamwise velocity deficit, for which the data collapses fairly well for all streamwise and vertical measurement locations. It should be mentioned here that for the deep wake, the approaching velocity is constant with vertical distance from the bed, whereas for shallow flow, it is a function of the vertical distance. A parameter β was proposed to represent the relative effect of the bed friction and transverse shear. Above a critical value, $\beta_c = 0.2$, the organized motion of the vortices began to disappear.

   To quantify the effect of the bed roughness, Balachandar & Tachie (2001) measured velocity distribution of a shallow wake generated on a smooth and a rough

wall. The roughness was found to affect both the mean and turbulence parameters of the of the wake flow. For approximately the same value of Reynolds number, the width of the wake was found to be much smaller for the rough bed compared to the smooth bed. Also, the ratio of the transverse shear to the bed friction was found to be smaller for the case of the rough bed. Shallowness of the flow was also found to enhance the turbulent fluctuations in the flow.

In a series of papers, the general features, stability and control of the shallow wake have been further addressed (Akilli & Rockwell, 2002; Fu & Rockwell, 2005a; Fu & Rockwell, 2005b) using PIV. The experimental procedure for all these investigations is more or less similar; a circular cylinder is placed in a shallow channel flow. In the first paper, the focus was on the spatio-temporal evolution of the vortex formation process. In the second and third investigations, they addressed the effect of Reynolds number on the flow and explored different possible ways to stabilize the wake, respectively. The shallow wake was found to be characterized by large-scale vertical structures (or 2DCS) emanating from the body downstream of the cylinder. However, their investigation discovered an axial flow from the bed towards the free surface through the core of these structures, supporting the finding of Cohn & Koochesfahani (1993). This flow was believed to contribute significantly to the three-dimensionality of the shallow wake structure. The instantaneous streamline topology and vorticity contours at different elevations from the bed compare well, in a general sense, with a conventional deep wake, but a signature of three-dimensionality was also observed. The location of the saddle point in the instantaneous streamline topology was found to be a function of the distance

from the bed. With increasing distance from the bed, the spanwise extent of the instantaneous vorticity contour as well as the streamline topology grows in the transverse direction, probably due to the diminishing effect of the bed. Close to the bed, a unique structure of the instantaneous streamline was observed, called as owl face of the first kind (Perry & Steiner, 1987), which has a very well-defined pair of foci and saddle points. With increasing distance from the bed, the organization of the foci as well as the saddle points gets lost. At the near-bed location, the vorticity contour was found to be tilted toward the central region, but with increasing distance from the bed, the tendency of tilt decreases. Additionally, the peak magnitude of vorticity was found to be dissipated rapidly close to the bed, compared to some locations far from the bed. The contour of the time-mean Reynolds stress was found to be very well-defined in accordance with the shear layer separation, except close to the bed. In the near-bed region, additional cluster of Reynolds stress was noticed which explains the interaction of the horseshoe vortex with the shear layer at the sides of the cylinder. Unlike the vorticity, the peak magnitude of the Reynolds stress remains almost the same and does not change with the distance from the bed. The stability number of the shallow wake was found to play an important role in the resulting mode of the wake. For example, increasing the stability number leads to the attenuation of the appearance of the large-scale coherent structures in the wake. Despite this, a well-defined varicose instability was observed. The reason of this particular instability can be attributed to the dynamics of horseshoe vortex wrapping of the body. At an even higher stability number, the wake was completely stabilized, but smaller amplitude rotational motions were noticed to set off now and then in the near-

wake region. In the third investigation of the aforementioned series, Fu & Rockwell (2005b) introduced a variable width streamwise slot cut through the cylinder. For smaller slot size, the cluster of vorticity preserved their shape, but appeared downstream compared to the case of no slot. Also, the frequency of undulation of the emanating jet from the slot may affect the shedding frequency of the vertical structures.

2.5 Objective of the present study revisited

Although the study of shallow wake started not long ago, the field is rapidly maturing because of the state-of-the-art resources available computationally and experimentally. As implied from the present chapter, the presence of the boundaries has a drastic effect on the dynamics of a shallow wake, and the characteristic of the shallow wake may differ greatly with distance from either boundaries. In other words, the shallow wake may exhibit variability in its characteristics with the vertical distance. This may be termed 'vertical variability'. Until now, no major study has been carried out to expose the vertical variability of the shallow wake. In the present study, a typical shallow wake was formed by placing a sharp-edged bluff body in an open channel flow. The sharp-edge of the body ensures that the boundary layer on the body separates at the sharp-edge of the body consistently at all vertical locations. This is a crucial criterion, since the shape of the body eliminates any possible vertical variability due to the flow separation. One may note that in the case of a circular cylinder the location of the flow separation points can vary with the vertical distance. Further, the geometric nature of the body permits no Reynolds number dependence on the location of the separation points.

39

The refined specific objectives of the present study can be summarized as follows.

- Examination of the mean streamwise and transverse velocity profiles at selected axial stations at different vertical locations to assess the vertical variability of the shallow wake. Also to be examined are the distributions of the turbulence parameters (root-mean-square velocity, Reynolds stress) at selected axial distances are also to be examined.

- Quantification of the effect of the bed and free-surface layer by using the proper orthogonal decomposition (POD) technique, and their effect on the vertical variability of the wake.

- Investigation of the distribution of the turbulent kinetic energy over the entire flow depth, due to the presence of the vertical confinement.

- Quantification of the effect of the shallowness on the distribution of the predominant vorticity at different vertical locations using swirling strength analysis.

- Use of POD as a viable path to educe large-scale coherent structures of shallow wake flows.

- Development and application of a coherent structure identification scheme. The coherent structures play an important role in the dynamics of the shallow flow, and successful extraction of information of the coherent structures will help to assess the effect of the dynamics of these on the vertical variability of the shallow wake flow.
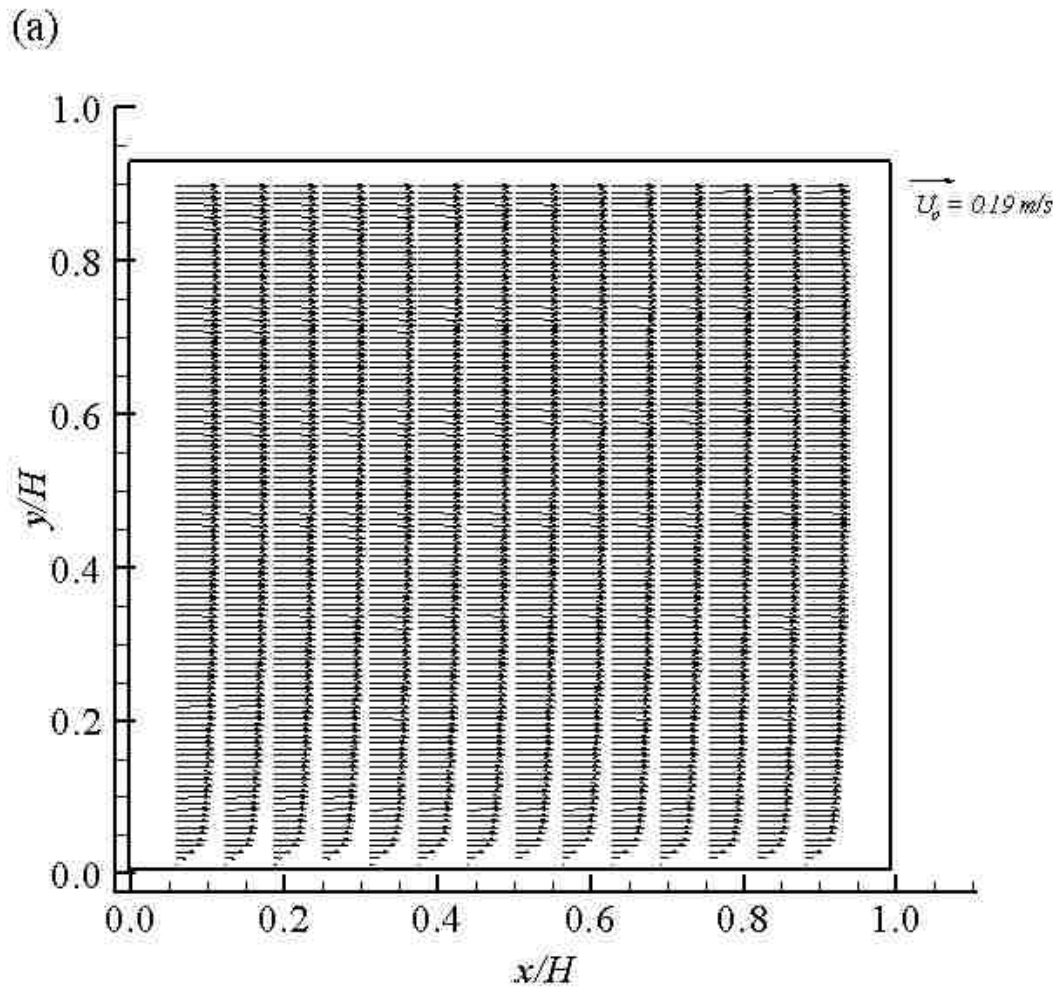
Figure 2.1: Velocity field of open channel flow at H = 0.10 m, a) mean velocity field from 2000 images, b) instantaneous velocity field, and c) corresponding fluctuating velocity field. The flow direction is from left to right.

(b)

$\overrightarrow{U_o} = 0.19\,m/s$

42

(c)

$\overline{U}_o = 0.01$
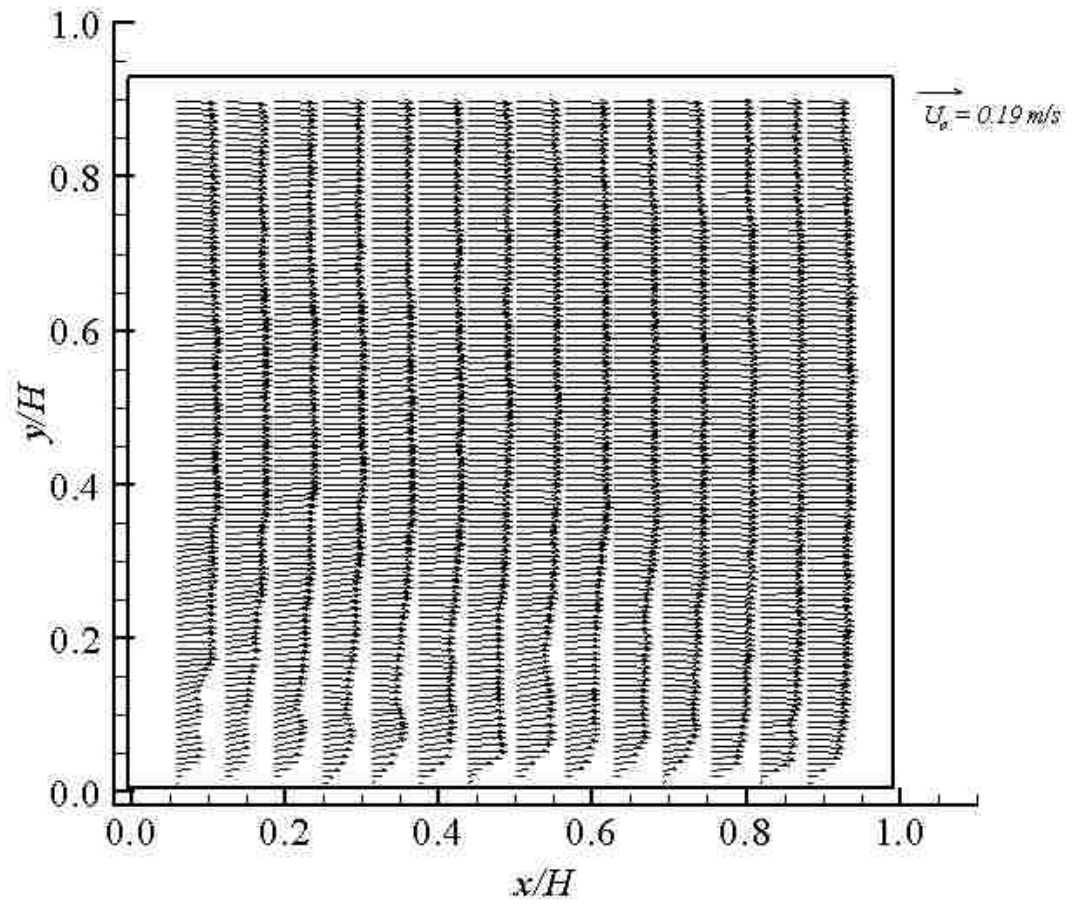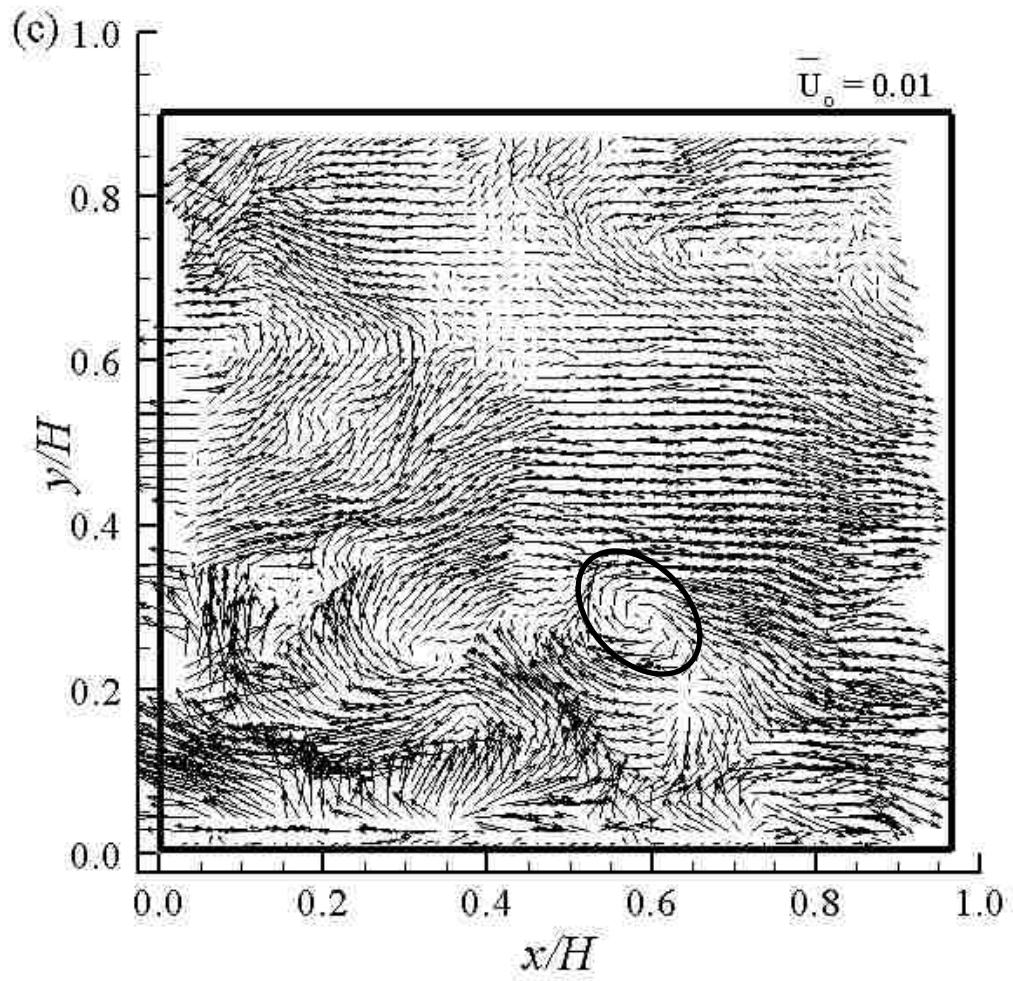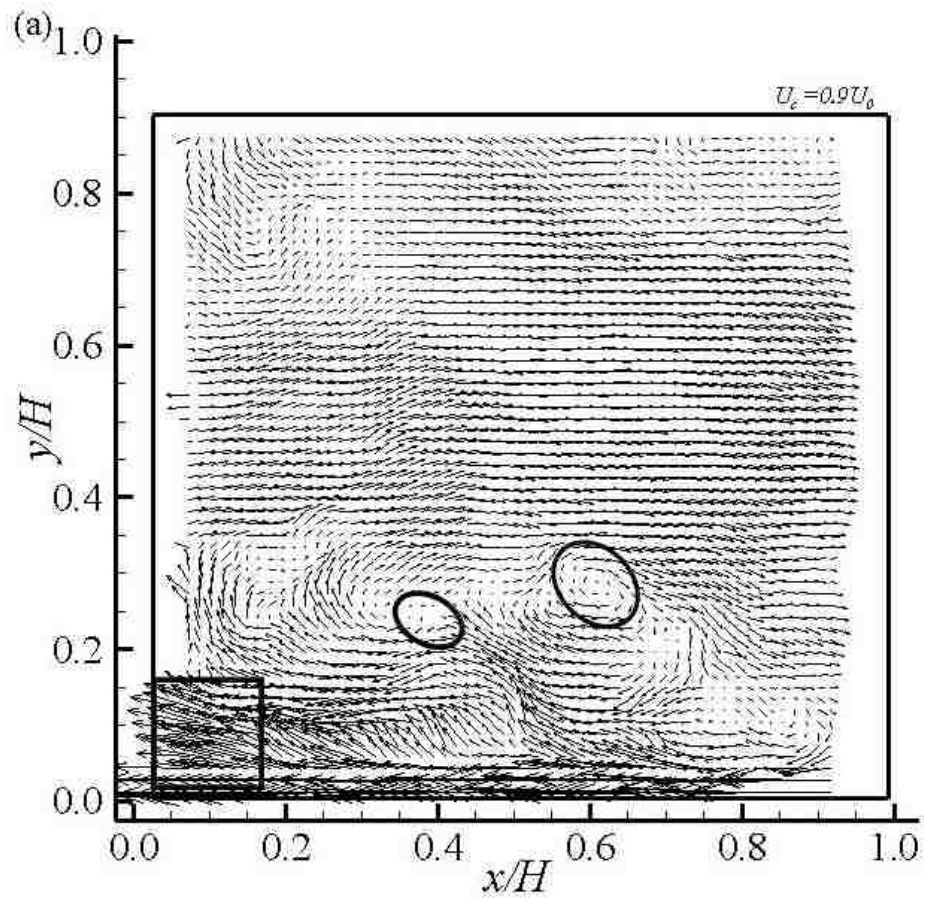
Figure 2.2: Galilean decomposed velocity fields in (*x, y*) plane at Re_d = 2100 at (a) U_C = 0.9U_0 and (b) U_C = 0.8U_0 .

(b)
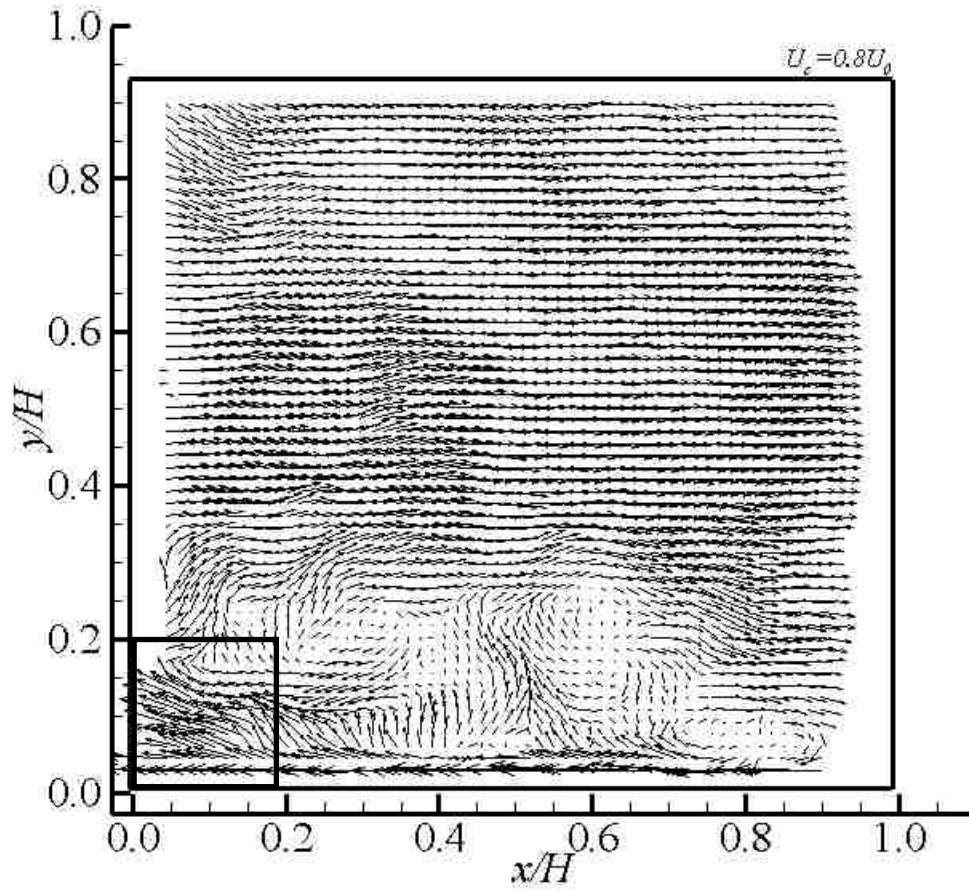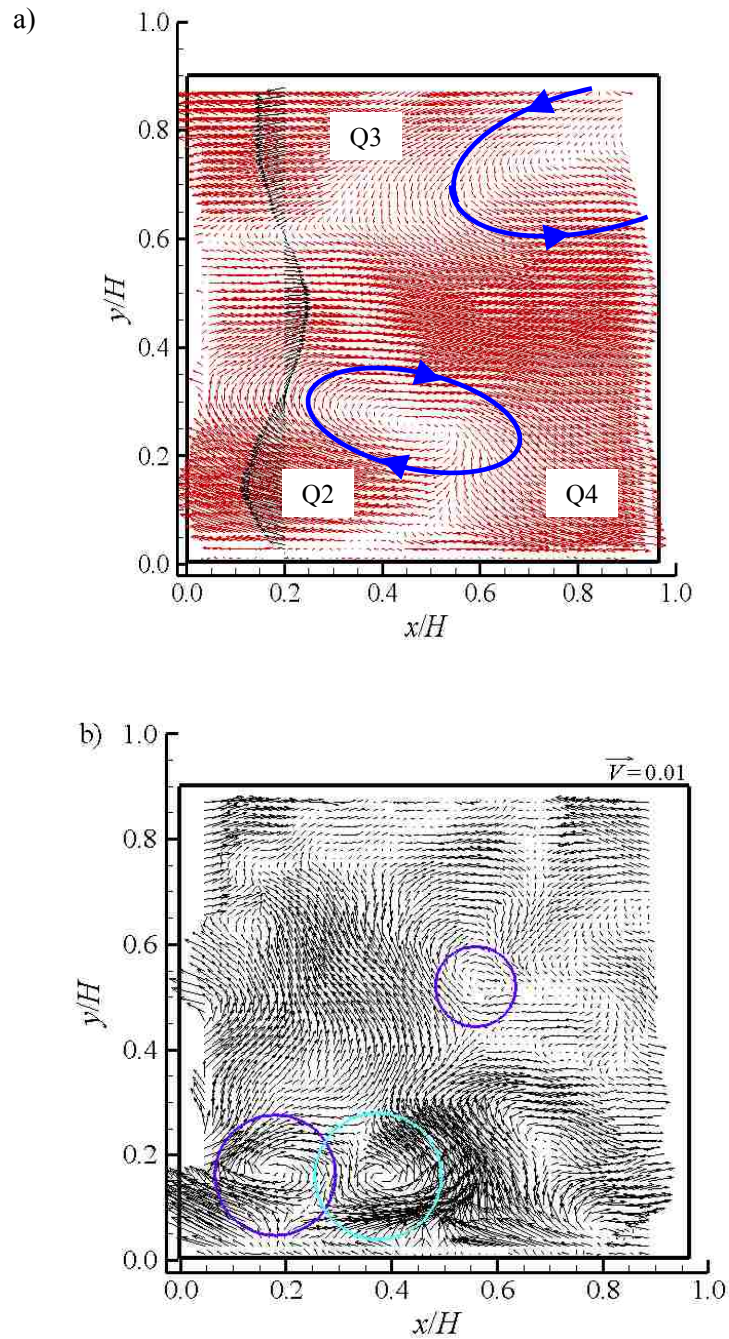
Figure 2.3: Examples of POD reconstructed velocity fields (a) using the first twelve POD modes and (b) from POD modes 13 to 100. Note that only every second vector is shown to avoid cluttering.
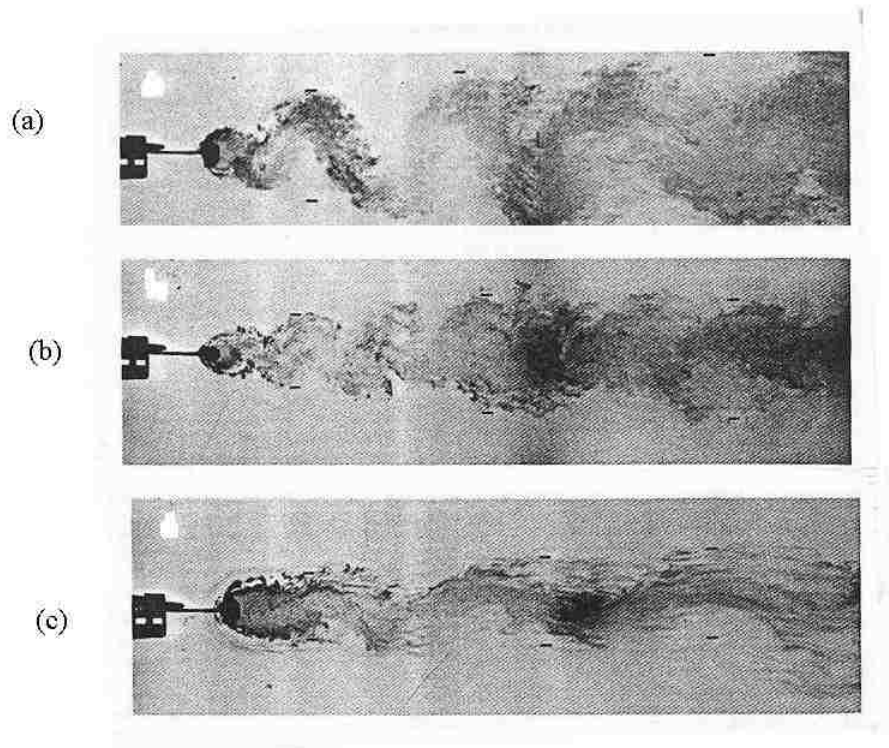
Figure 2.4: Qualitative demonstration of the effect of the bed on the development of shallow wake (Reproduced with the permission of American Geophysical Union).
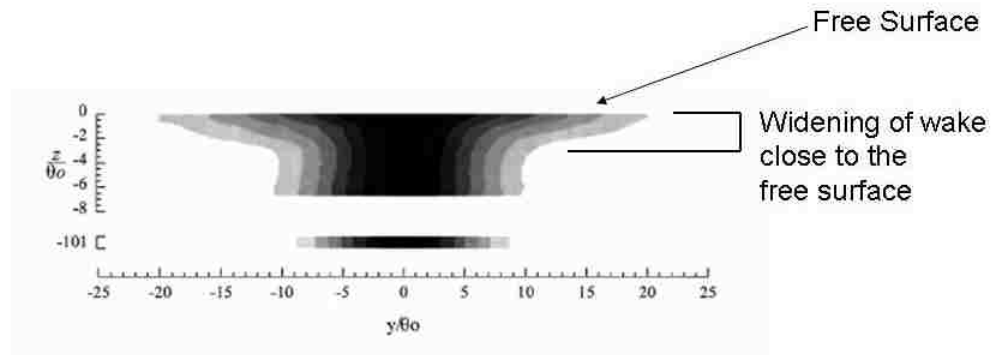
Figure 2.5: Widening of the wake close to the free-surface (Adopted from Logory et al. 1996). The contour levels represents mean velocity, white to dark shade represents higher to lower range of streamwise velocity. θ_0 (= 3.1 mm) is the half-momentum thickness of the wake (Reproduced with the permission of American Institute of Physics).
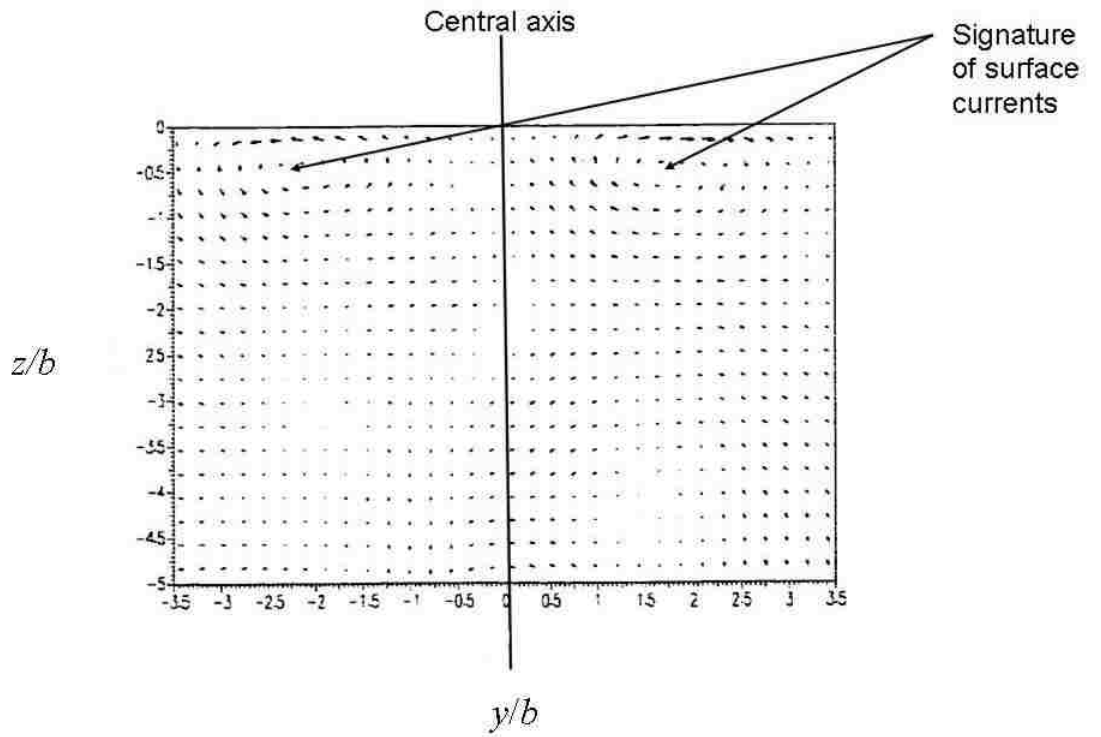
Figure 2.6: Signature of the surface currents as seen in a streamwise plane downstream of a bluff body. (Reproduced by permission from P Maheo).
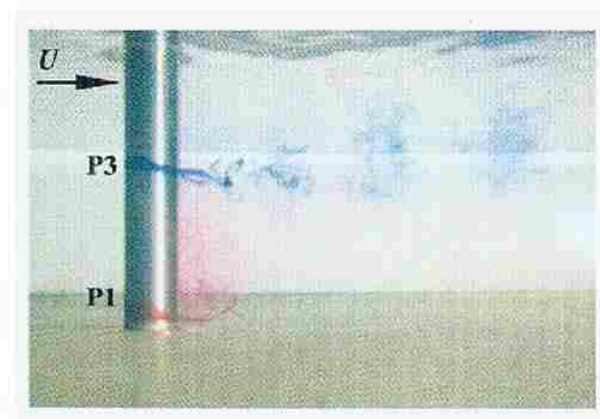
Figure 2.7: Qualitative demonstration of the dynamics of the horseshoe vortex around a circular cylinder as the source of three-dimensionality of shallow wake (Rao et al., 2004; Reproduced by permission from Visualization Society of Japan).

(a)

(a) Type A Instability: Oceanic wake at Guadalupe Island, California (Reproduced according to the general terms of use, NASA Visible Earth Repository).

(b) Type B Instability: The confluence point of two rivers in Salzburg, Austria. The large-scale structures can be seen along the mixing layer.

Figure 2.8: Examples of the instability mechanisms of shallow flows

$t_o + 4\,s$

$t_o + 4\,s$
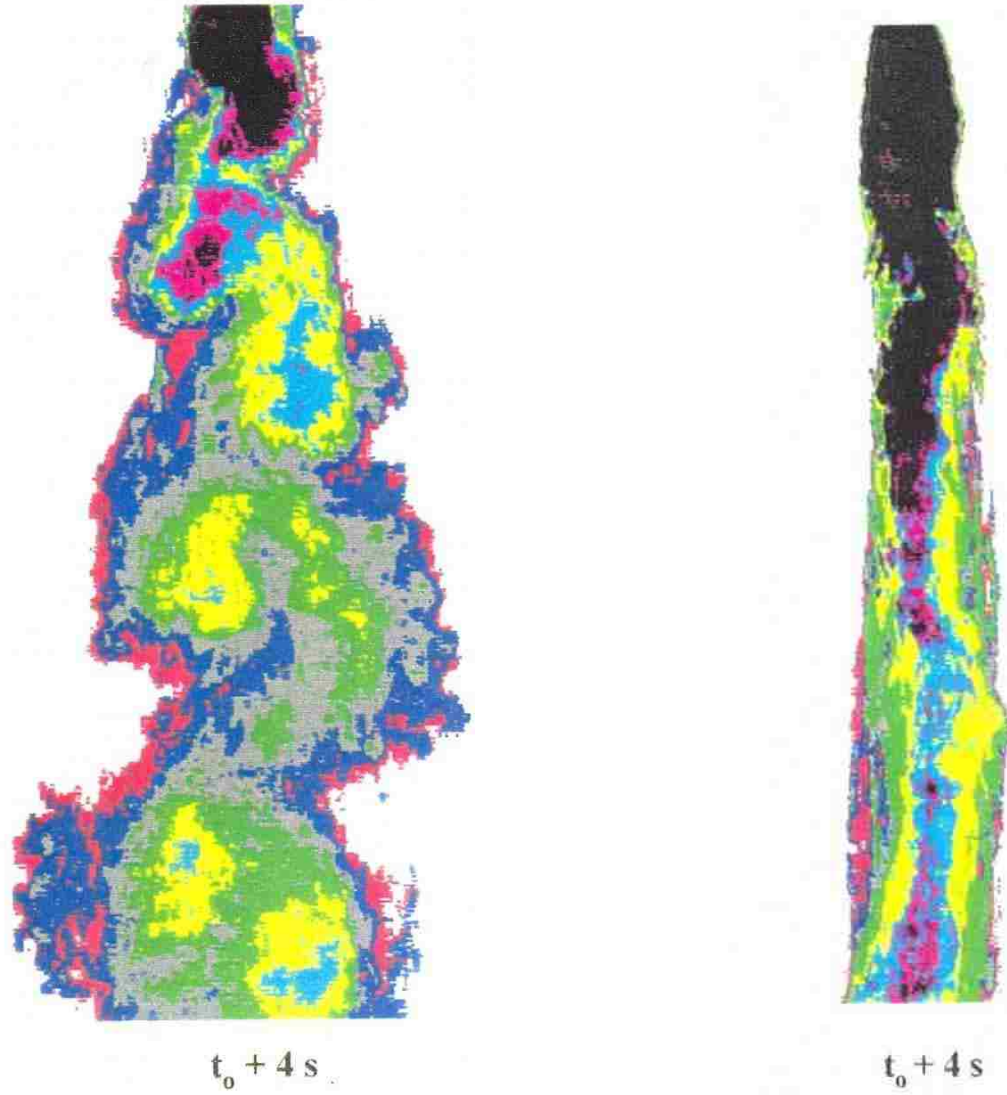
Figure 2.9: Example of deep-shallow and shallow-shallow wake (Reproduced by permission from M. Tachie)

Chapter 3
EXPERIMENTAL DETAILS

3.1 General comments

This chapter presents the details of the experimental setup and procedures used in the study. A detailed description of the Particle Image Velocimeter used in the study along with typical uncertainty estimates is also presented. A description of the various algorithms used in the data analysis (variable threshold outlier rejection technique, proper orthogonal decomposition and the coherent structure identification) are presented.

3.2 Experimental setup

3.2.1 Open channel recirculating flume

A 9.5 m long and 1.2 m wide open channel recirculating flume was used in this study. The flume was constructed of Plexiglas to ensure optical access from the bottom as well as from the sides. The water supply system consisted of a reservoir located below the flume, a pump and flow control valves. In addition, a sluice gate located at the exit section of the flume was used to control the depth of flow. In the present study, the inclination of the sluice gate was adjusted to maintain the flow depth nominally at 100 mm in the test section region which is located at 6.3 m from the start of the flume. The aspect ratio of the flume was 12 and can be considered to be large enough to have reduced secondary flow effects (Nezu & Nakagawa, 1993). Tap water, filtered through a 5 μm filter, was used as the working fluid. A flow conditioner made of plastic straws and

wire mesh was placed at the inlet of the channel to reduce the turbulence levels in the flow. The flow was tripped using a 25 mm sand-trip located 3 m from the entrance to ensure the formation of fully developed flow conditions at the measurement section.

3.2.2 Bluff body

A sharp-edged bluff body of height 110 mm was placed 3 m downstream of the sand-trip. The width at the upstream face of the body was 30 mm and was chamfered towards the downstream side. The bluff body was oriented to be vertical and affixed to the bed. A picture of the bluff body is shown in Figure 3.1. The origin of the coordinate axes is located at the point where the centre of the body touches the bed of the flume.

3.2.3 Measurement locations and details

For the present study, two different series of experiments were performed. The first set of experiments was performed at a lower freestream velocity of 0.19 m/s with corresponding Reynolds number, based on the depth of flow, $Re_H = 19,000$. The stability number of the shallow wake was 0.0015. Measurements were performed at three vertical positions, near-bed ($y/H = 0.10$), mid-depth ($y/H = 0.51$) and near-surface ($y/H = 0.76$). The measurement fields-of-views were roughly between $1.5 \leq x/D \leq 3.5$ in the axial direction. This set of experiments enables us to demonstrate the effect of the bed, free-surface and approaching flow on the shallow wake. The detail of this series of experiment is tabulated in Table 3.1. In this Table, 'location along x-axis' refers to the location of the starting edge of the field-of-view (FOV) for each case.

The second set of experiments was done at a higher freestream velocity of 0.45 m/s, and the corresponding Reynolds number, based on the depth of flow, $Re_H = 45,000$. The stability number was higher, 0.025. The vertical location of the measurements were moved closer to the boundary, at near-bed ($y/H = 0.10$), mid-depth ($y/H = 0.50$) and near-surface ($y/H = 0.80$). Close to the bed, excessive reflections from the Plexiglas rendered the measurements impossible at any locations closer than $y/H = 0.10$. Similarly, the downdraft of the free surface and the movement of the bubbles originating from the free surface, made it impossible to move to locations higher than $y/H = 0.80$. In the axial direction, a distance from 0-10D was covered, where D is the width of the bluff body. Following the first experiment, it was deemed necessary to raise the stability number to the extent possible within the constraints of the setup and measurement conditions. As will be shown later, the second set of experiments enabled us to perform statistical population of the coherent structures in the flow, which was not possible with the first set of experiments. More details about this aspect can be found in the appropriate chapters of the dissertation. Table 3.2 summarizes the experimental parameters for second series of experiment.

3.3 Particle image velocimetry

In summer of 1984, teams at University of Oldenburg and DLR (German Aerospace Lab) carried out particle image velocimetry (PIV) measurement in the DLR wind tunnel for the first time, using a photographic plate to acquire the image of the tracer particles. At that time, the evaluation of the displacement of the particles in the flow was done optically. A few months later, DLR devised the first Nd:YAG double

pulsed laser and hence started the journey of PIV. In 1995, the first digital camera that would allow capturing the image of the flow field at a short interval of time was available. After this major breakthrough, the PIV technique spread widely and differentiated in many distinct applications ranging from microscale flow to combustion and supersonic flow, both in academic and industrial settings. This was made possible due to the technological advancement in the area of video techniques, laser and software for image evaluation.

Particle image velocimetry is a non-intrusive technique to measure the flow velocity at multiple points simultaneously. A typical PIV system usually consists of several subsystems – a laser, a camera, and a synchronizer. Specifications of the PIV subsystems used in the present case are tabulated in Table 3.3. Figure 3.3 briefly explains a typical setup for PIV measurement. Some specific tracer particles are added to the flow, and these are illuminated at a particular location twice within a short time-interval by a laser sheet. The light scattered by each of these particles is recorded either in a single frame, or in several frames depending on the type of application. Once the displacement of tracer particles within the time interval of the laser pulse is determined by some appropriate technique (for example, cross-correlation calculation), the velocity of each of the particles can be found by simply dividing the displacement vector by the already known time interval. Of course, each of these processes requires sophisticated instruments and methodologies. The next subsections discuss the steps involved in a successful PIV experiment.

3.3.1 Flow seeding with tracer particles

The PIV technique does not measure the fluid velocity directly rather it measures the velocity of the tracer particles. So, the properties of the tracer particle must be such that it would represent the fluid velocity in a satisfactory way. The particle should be big enough so that it can reflect enough light to be captured by the camera. On the other hand, it has to be small enough so that it can follow the flow velocity faithfully. Large particle size can cause drop out of data from critical flow area, for example, vortex core, boundary layer or shear layer. The density of the tracer particle may also influence the particle's ability to follow the flow feature. Lastly, the terminal velocity of the particle should be as small as possible.

Clearly, the choice of the tracer particle is an important step towards successful PIV experimentation. In the present experiment, hollow glass-beads manufactured by Potters Industries were used as the tracer particles. Two different types of particles of diameter 12 μm and 17 μm were used. According to the criterion of Raffel et al. (1993), the minimum size of the particle has to be 2 pixels to ensure minimal error due to the sub-pixel interpolation. The particle sizes chosen satisfy this minimum size criterion, and therefore are assumed to induce negligible error due to the sub-pixel interpolation procedure.

Assuming a spherical particle, the terminal velocity of the particle can be estimated as (Clift et al. 1978),

$$u_T = \frac{gd_p^2(\rho_p - \rho)}{18\mu}$$ (3.1)

Here d_p is the particle diameter, ρ_p is the particle density and μ is the dynamic viscosity of the working fluid. Using this equation, the settling velocities were approximated as 0.0078 m/s and 0.015 m/s, respectively, for the two particles chosen in this study. These values are small enough to assume that the particles are capable of following the flow faithfully.

In addition to this, accurate measurement needs at least 15-20 tracer particles in the interrogation area (Adrian, 1991). Once the FOV size was determined, the approximate amount of tracer particles needed to satisfy this criterion was estimated and was mixed well with a small amount of water to prepare a high density stock solution. This stock solution was later mixed with the water in the tank. The advantage of making stock solution is two-fold. First, it ensures no lump-deposit of the particle. Secondly, using the stock solution is a very convenient way to replenish the particle concentration in case some particles settle down during the course of experimentation.

3.3.2 Illumination of the flow field

In the present experiments, a 50 mJ/pulse energy (wavelength 532 nm) Nd-YAG laser (New Wave Research Solo PIV) system was used as the illuminating source. The illumination should be short so that it does not cause blur or excessive reflection in the resulting image. Also, it should be long enough so that a majority of the particles can

move at least ½ of the interrogation area between two consequent laser pulses. Additionally, the illumination intensity must be such that it can illuminate each particle individually. The achievable repetition rate of the laser is not very high, so two lasers were operated simultaneously in straddle mode in conjunction with a TSI 610035 laserpulse synchronizer to get two laser pulses in a short time interval.

The beam from the laser was first passed through a spherical lens and then a cylindrical lens to generate a thin light sheet as shown in Figure 3.5. The spherical lens controls the thickness of the light sheet and the cylindrical lens controls the height of the sheet. The light sheet should be very thin to restrict the out-of-plane movement of the particles in the laser sheet. The thinnest portion of the laser sheet appears at the focal length of the lens and was approximately 1 mm. In the present study, a 500 mm focus spherical and -15 mm focus cylindrical lens was used. For measurement in the horizontal planes, the laser was placed at the side of the flume and, for the vertical measurement planes, the laser was placed at the bottom of the flume. Figure 3.5 illustrates the process of generation of the light sheet in a typical case.

3.3.3 Image recording

The reflected light from the particles was captured by a charged-coupled device (CCD) array in a double-exposure double-frame mode by a TSI Powerview plus 4MP camera. The charge-coupled sensors produce electrical charge proportional to the amount of incident light. The resolution of the camera is 2048 × 2048 pixels, implying that there are 2048 sensors in either direction. The incident light on the CCD array produces a

greyscale image. The intensity of the incident light at any pixel was discretized into 2^I intensity levels, where I is the number of bits of the camera. The camera was 12-bit, so the entire intensity range was discretized into 4096 levels. Level zero represent black and level 4096 represents white. Each of the CCD sensors produces electric charge according to the greyscale intensity. The two-dimensional array of the numbers was saved in a raw data format in the computer for further processing.

In all the experiments, 2000 images were recorded at each location, at a frequency of 1.04 Hz. The camera was fitted with either a 50 mm fixed or a 28-160 mm variable focal length micro-Nikkor lens to best view the region of interest. In addition, the distance of the camera from the object was adjusted manually to get the best possible view. Before each experiment, a steel ruler with minimum division of 1 mm was placed at the region of interest to calibrate the acquired image accordingly.

3.3.4 Image processing

The total area of each raw image was divided into several small areas called interrogation area (IA). The interrogation area should be small enough so that second order effects, such as high velocity gradient, or vorticity, would not affect it. Typical interrogation area size may be 16×16, 32×32 or 64×64 pixels. After the image was divided into a number of interrogation areas, either autocorrelation or cross-correlation method can be applied to find the displacement of any particular particle in that interrogation area. If the time interval between these two images is known, the velocity vector can be determined as

$$V(\vec{x},t) = \frac{\Delta S(x,t)}{\Delta t} \; ; \qquad\qquad\qquad\qquad\qquad\qquad\qquad (3.2)$$

where ΔS is the displacement of the particle and Δt is the time interval between two successive laser pulses. Since the time interval is known beforehand, evaluation of the displacement ΔS is required to estimate the velocity. A fast Fourier transform (FFT) based cross-correlation technique was applied to determine the displacement. A brief description of the method of finding the displacement is summarized below.

At this point of time, for each experiment, 2000 raw image pairs were saved in the computer. The first image contains information about the location of each particle, and the second image contains the information of particles which are moved a small distance in time Δt, according to the underlying flow behaviour. Tracking each particle requires enormous computational resources, so instead the movement of a group of particles contained in each interrogation area was analyzed. The intensity value contained in each of the interrogation area was cross-correlated with another image pair as

$$R_{II}(x,y) = \sum_{i=-K}^{K} \sum_{j=-L}^{L} I(i,j)I'(i+x,j+y) \; ; \qquad\qquad\qquad (3.3)$$

where I and I' are samples of the intensity value corresponding to each IA. Physically speaking, the interrogation area was shifted linearly in the second image with respect to the first image all over, without extending the edge of the image. By applying this technique on a range of shift ($-M \leq x \leq M$, $-N \leq y \leq N$), the final correlation plane of ($2M+1$, $2N+1$) was obtained. The cross-correlation function measures the extent of

61

statistical match between two images. The location of the peak of the correlation coefficient, compared to the initial location of the particles in the first image was taken as the particle displacement, ΔS.

Due to the huge requirement of computational resource for direct calculation of the cross-correlation coefficient, they were computed indirectly by FFT method. The FFT method operates based on the fact that the cross-correlation of two functions is the direct multiplication of the complex conjugate of the Fourier transform of these functions. The Fourier transform was applied to the discrete data by the FFT algorithm. Initially, FFT was applied to compute the two-dimensional FFT's of the images. Then the complex conjugate FFT's were multiplied and inverse-Fourier transformed to obtain the required correlation. In the present case, the correlation analysis was performed in two steps, initially, a 32×32 interrogation area was selected and the displacements were determined by FFT based cross-correlation analysis. Determining a rough estimate of the displacement from this course grid, the image was re-analyzed in a finer grid with a 16×16 interrogation area, with 50% overlapping. The second and final analysis yielded a velocity vector field of 127×127 vectors for each image. Figure 3.6 shows an example of the typical velocity vector field after processing. The actual spatial resolution of the processed velocity vector field this produced by process was mentioned in Table 3.2.

3.3.5 Removal and replacement of spurious vectors

It may happen that, during the cross-correlation procedure, a correlation peak was detected which may be due to the noise or some other experimental artifacts (for

example, body surface, noise from different sources), instead of the actual correlation peak. As a result of this wrong detection, a spurious vector may result in the velocity field. A typical spurious vector can be identified by either of the following two properties (Raffel et al. 1998):

- Their magnitude and direction of differs considerably from the surrounding neighbors.

- They often appear at the edge of the data field.

A typical image containing spurious vectors is shown in Figure 3.7. The spurious vectors are labeled as A-E. For a handful of images, manual checking and replacement is a feasible option. But, this is no longer possible if a large number of recordings have to be examined and evaluated and can only be performed by an automated algorithm. An ideal algorithm should comply with the following criteria (Raffel et al. 1998)

- The algorithm must ensure with a high degree of confidence that no questionable data is stored in the final PIV dataset.

- Questionable data should be rejected, if it can not be decided by the application of the algorithm that is valid or not.

Amongst different methods of detection of spurious vectors, a cellular neural network (CNN) based algorithm was found to perform superior compared to other methods (Liang et al. 2003). In this algorithm, the threshold is one of the most important parameter to

choose. Decreasing the threshold level makes the detection method more aggressive, i.e. it tends to tag valid vectors as spurious vector. The selection of a proper threshold is subjective and not always straightforward while dealing with a large amount of data. The variable threshold outlier technique (VCNN), proposed by Shinneeb et al. (2004) overcomes this subjectivity by calculating the threshold field from the velocity vector field itself. In this method, initially the CNN technique is applied to identify and replace the spurious vectors. From this replaced field, a new variable threshold field was estimated and was applied to the actual raw image to detect and replace the spurious vectors. The advantage of this method is the self-adjustment of the threshold value at different points of the flow-field depending on the velocity gradient. In the present experiments, VCNN method was applied to detect and replace spurious vectors from the processed velocity vector field. A brief discussion of the steps involved in this method is described below. More detailed treatise of this technique can be found in Shinneeb et al. (2004).

At each grid point of the PIV dataset, a weight function was determined by

$$W_{ij}^{u} = \max(-T_i^{u}, T_i^{u} - R_{ij}^{u}) ; \tag{3.4}$$

where T_i^{u} represents the threshold for u and R_{ij}^{u} indicates the absolute difference in the magnitude of u at grid points i and j,

$$R_{ij}^{u} = \left| u_i - u_j \right| . \tag{3.5}$$

Following this, the sum of the weight function at the ith grid was calculated as

$$S_{ij}^u = \sum_{j=1}^{n} W_{ij}^u \gamma_j^{k-1}.$$

(3.6)

Here n is the total number of neighboring grid points and γ is the state of the point (0 or 1) at the previous iteration. Initially, γ at all grid points were set to unity, implying a valid vector. Following the calculation of the sum, in the next iteration, the state γ at any grid point was set according to the following criterion

$$\gamma_i^k = 1 \text{ if } S_i^u \geq 0 \text{ and } \gamma_i^k = 0 \text{ if } S_i^u < 0.$$

(3.7)

Sometimes, a certain number of vectors may oscillate in between the states. After a certain number of iterations, they were labeled as spurious if they still continue to oscillate, in accordance to the second criterion of Raffel et al. (1998).

After the spurious vectors were identified by the aforementioned method, they were replaced by a Gaussian weighted vector, calculated as follows

$$u_i = \frac{\sum \alpha_{ij} u_j}{\sum \alpha_{ij}};$$

(3.8)

where $\alpha_{ij} = \exp\left(-\frac{1}{2}\left(\frac{L_{ij}}{\sigma}\right)^2\right)$.

Here σ is the width of the Gaussian filter and L_{ij} is the distance between the point i and j. Following this, the variable threshold field was calculated as

$$\tilde{T}_i^u = \frac{1}{n}\sum_{j=1}^{n}|u_i - u_j| + K$$

Here K is a constant and n is the number of neighbours. The threshold field was then filtered with a Gaussian filter as follows,

$$T_{ij}^u = \frac{\sum \alpha_{ij} \widetilde{T}_i^u}{\sum \alpha_{ij}}.$$

After this step, the same procedure as mentioned in (3.4) to (3.7) was followed, only instead of the constant threshold field the new variable threshold field was applied. The Matlab® code used to perform this function is given in Appendix B.

3.4 Proper orthogonal decomposition (POD)

The PIV data was analyzed using the proper orthogonal decomposition (POD) technique to educe the large-scale energetic structures in the flow. POD is a procedure which decomposes a signal into its modal base (Lumley, 1967). This method decomposes the flow field into a weighted linear sum of eigenfunctions which are representatives of the coherent structures present in the flow. Different types of coherent structures present in the flow gives rise to different eigenfunctions, and the largest eigenfunction corresponding to the largest eigenvalue represents the most energetic structure. In the present work, POD was performed by the method of snapshots proposed by Sirovich (1987). A brief mathematical description of the method is given below.

Following the calculus of variation, the fluctuating flow field can be projected onto an orthonormal basis by solving

$$\int_\Omega K(x,x')\zeta(x')dx' = \lambda\zeta(x) \; ; \tag{3.10}$$

66

where $K(x, x')$ is the two-point correlation function and λ is the eigenvalue. The kernel of the integral may be determined by

$$K(x,x') = \frac{1}{M}\sum_{m=1}^{M}\varphi^{(m)}(x)\varphi^{(m)}(x');$$

(3.11)

Here φ represents the fluctuation of the measured flow variable and M is the number of snapshots. The symmetric kernel can be represented by

$$\zeta(x) = \sum_{m=1}^{M}a_m\varphi^{(m)}(x);$$

(3.12)

where the constants a_m are to be determined. Substituting this into the original formulation,

$$\frac{1}{M}\sum_{m=1}^{M}\left[\int_{\Omega}\varphi^{(m)}(x')\zeta(x')dx'\right]\varphi^{(m)}(x) = \lambda\zeta(x).$$

(3.13)

The coefficients used to determine the eigenfunction $\varsigma(x)$ can be shown to originate from the eigenvectors of the inner product matrix C given by

$$C = [c_{mn}] = \frac{1}{M}\left[\left(\varphi^{(m)},\varphi^{(n)}\right)\right].$$

(3.14)

Sirovich (1987) showed that the eigenvalues of C are the same as those of the covariance matrix and the eigenfunctions can be determined directly from the eigenvectors as follows:

$$A_n = [a_{n1}, a_{n2}, \ldots \ldots a_{nM}];$$ (3.15)

while $\zeta_n = \sum_{m=1}^{M} a_{mn} \varphi^{(m)}$. In this manner, the orthonormal eigenfunctions can be viewed as

a combination of the snapshots of instantaneous flow fields, weighted by the

eigenfunctions of the corresponding coherent structure signature. After decomposing the

flow field into a number of eigenfunctions, corresponding to different modes of coherent

structures, it can be reconstructed back with the required amount of energy containing the

information of coherent modes that are chosen to reconstruct the flow field. In the present

work, the fluctuating velocity field was first decomposed into eigenfunctions, and then

they were reconstructed back with ~40% of fluctuating energy content. This particular

amount of energy was chosen to best represent the large-scale coherent structures of the

present flow condition and details are provided in a later section. The Matlab® code used

for this is mentioned in Appendix B.

3.5 Coherent structure identification algorithm

An automated algorithm was used to identify large-scale coherent structures in the

POD reconstructed velocity field, by a closed streamline based structure identification

algorithm, as described by Agarwal & Prasad (2002). This technique involves searching

for closed streamline in the POD reconstructed velocity field in a circular path around

any given point. The first step involves approximating a circle in the rectangular grid.

This was performed using Bresenham's algorithm for circle generation in a rectangular

grid (Rogers, 1997). A grid point was identified as the vortex center if it simultaneously satisfied the following criteria:

- Monotonic condition: At least a particular fraction of the velocity vectors in the surrounding circle-approximated grid points show monotonic variations.

- Threshold condition: At least a particular fraction of the velocity vectors in the surrounding circle-approximated grid points lies in a predefined limit of variation. The limit of variation at any point is set to be +/- 30° on both sided of the tangential line at that grid-point.

Once the vortex is identified, the circulation was calculated as follows,

$$\Gamma = \left(u_{POD} \Delta x + w_{POD} \Delta z \right);$$
(3.16)

Here u_{POD} and w_{POD} are the POD-reconstructed velocities in x and z directions, and Δx and Δz are the grid spacing in streamwise and transverse directions, respectively. The Matlab® code used for this is available in Appendix B.

Errors can arise from the use of the coherent structure identification algorithm. Firstly, the structure centre may not fall exactly on the grid point. In that case, instead of sub-grid interpolation this algorithm will identify the nearest grid point as the vortex center. Secondly, the structure may not be exactly circular as the algorithm assumes. Thirdly, due to the discrete nature of the data, the actual radius may not be the same as the identified radius. To assess the degree of compliance of the present structure identification algorithm, a random check of 50 snapshots was performed. The existence of the large-scale structures in those snapshots was assessed by the naked eye and was

compared with the output from the identification algorithm. A total of 132 large-scale structures were identified by the naked eye, whereas the algorithm reported 127 structures, which resulted in approximately 3.7% error in the total number of the structure identified. The typical uncertainty associated with three types of error sources mentioned above can be estimated as follows. The maximum error in locating the centre of a coherent structure is half of the grid interval which, in the worst case, does not exceeds 0.7 mm ($\approx 0.002D$). For the case of an elliptical or non-circular coherent structure, the present algorithm reports a circular structure with radius equal to the minor axis of the structure. While this does not affect the total count of the structures, it does underestimate the size of the structure. The error due to the approximation of the circle in rectangular grid decreases with increase in the size of the approximated circle, and was assumed to be small in the present case.

Table 3.1: Details of the preliminary experiment.

(a) Horizontal (x, z) fields-of-view				
FOV	**Location along x-axis (mm)**	**Image size (mm)**	**Spatial resolution (mm)**	**Time separation (msec)**
1	49.8	91.0 × 91.0	0.716	1.4
2	36.4	97.8 × 97.8	0.770	1.3
3	54.4	103.6 × 103.6	0.815	1.6
(b) Vertical (x, y) fields-of-view				
4	48.7	98.9 × 98.9	0.778	1.8

Table 3.2: Details of the final experiment series

	(a) Horizontal (x, z) fields-of-view			
FOV	Location along x-axis (mm)	Image size (mm)	Spatial resolution (mm)	Time separation (msec)
NB1	0.0765	90.93×90.93	0.715	0.7
NB2	7.4644	146.26×146.26	1.151	1.2
NB3	17.5533	145.24×145.24	1.143	1.2
MD1	-0.188	101.38×101.38	0.798	0.7
MD2	6.7143	156.73×156.73	1.234	1.2
MD3	17.139	153.21×153.21	1.206	1.2
NS1	-0.6192	103.82×103.82	0.817	0.7
NS2	6.6024	161.92×161.92	1.274	1.2
NS3	16.543	164.04×164.04	1.291	1.2

Table 3.3: Instrumentation used for the Particle Image Velocimetry measurement.

PIV camera	*TSI Powerview Plus 4MP*
Type	*Cross-correlation*
CCD chip	*12 bit resolution, greyscale*
Size	*2048×2048 pixel*
Mode	*Double-frame double exposure mode*
Typical time between frames	*1000 μs (detailed in Table 2)*
Lens	*AF Micro Nikkor*
Focal length	60 mm
Maximum aperture	$f\,2.8$
Frame rate	0.961
Personal computer: Intel P4 processor, 1 GB RAM, frame-grabber card, programmable timing unit, Windows XP Professional OS, INSIGHT ®3G software	
Tracer particles	
Material	*Hollow glass particle (Potters Industries)*

Diameter	*12 μm, 17 μm*
Specific Density	*1.1, 1.4*
Terminal velocity	*0.078 m/s, 0.015 m/s*
Illumination	
Laser	*New Wave Research SOLO PIV (Nd-YAG)*
Wavelength	*532 nm*
Power	*50 mJ/pulse*

Figure 3.1: A picture of the bluff body used in the experiment.

Figure 3.2: The open-channel flume in operation.
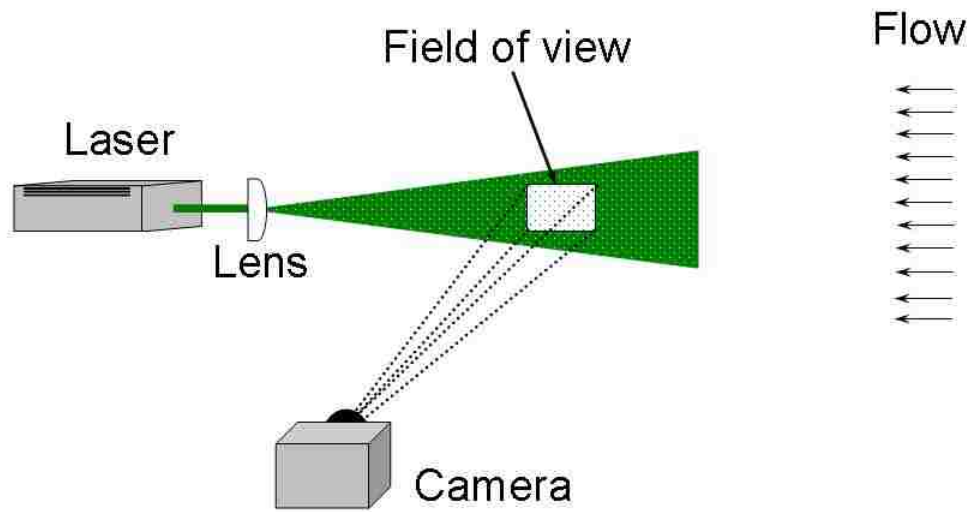
Figure 3.3: Schematic of the operating principle of a typical PIV system.
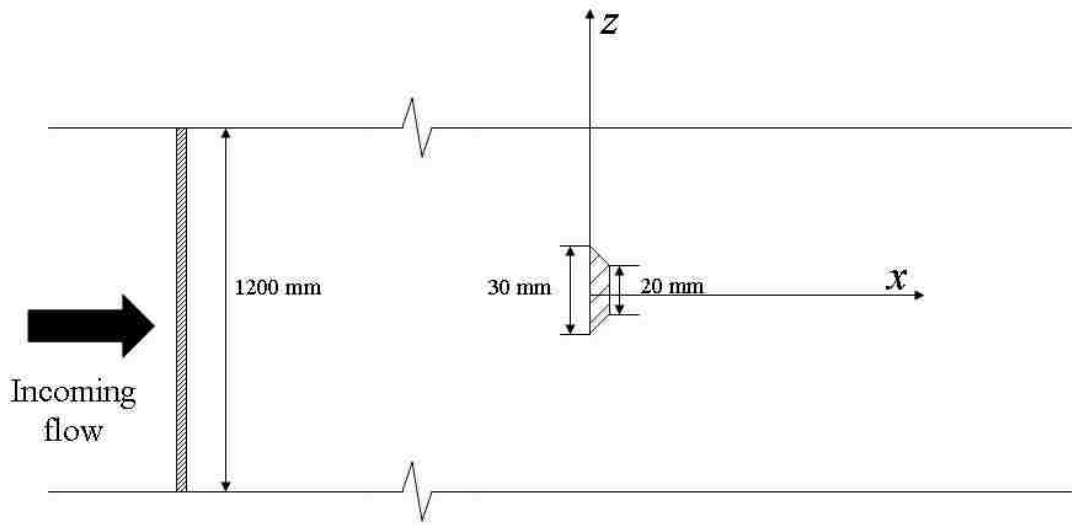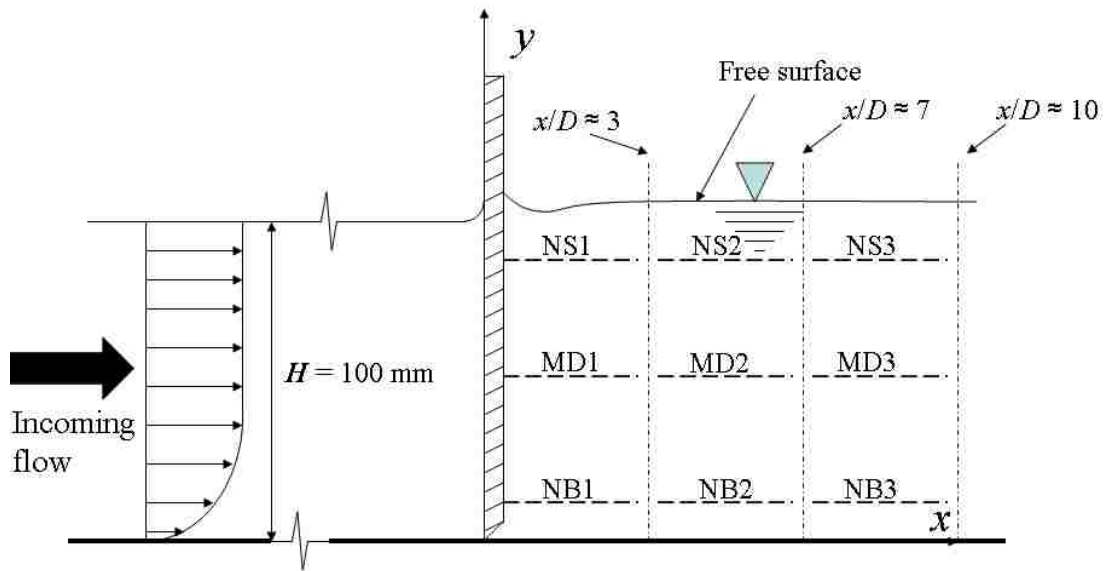
Figure 3.4: Schematic of the experimental setup (not to scale). The height of the body is 110 mm, and protrudes above the free surface.
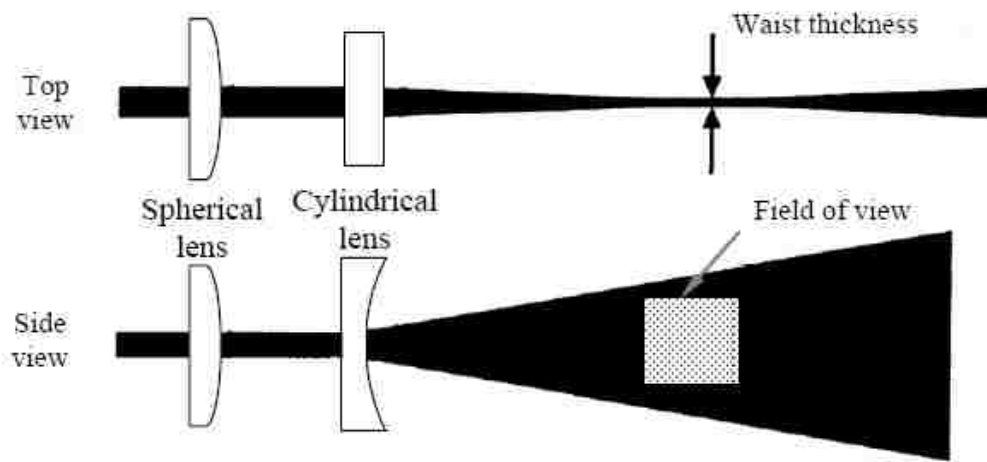
Figure 3.5: Schematics of the process of generation of the light sheet.
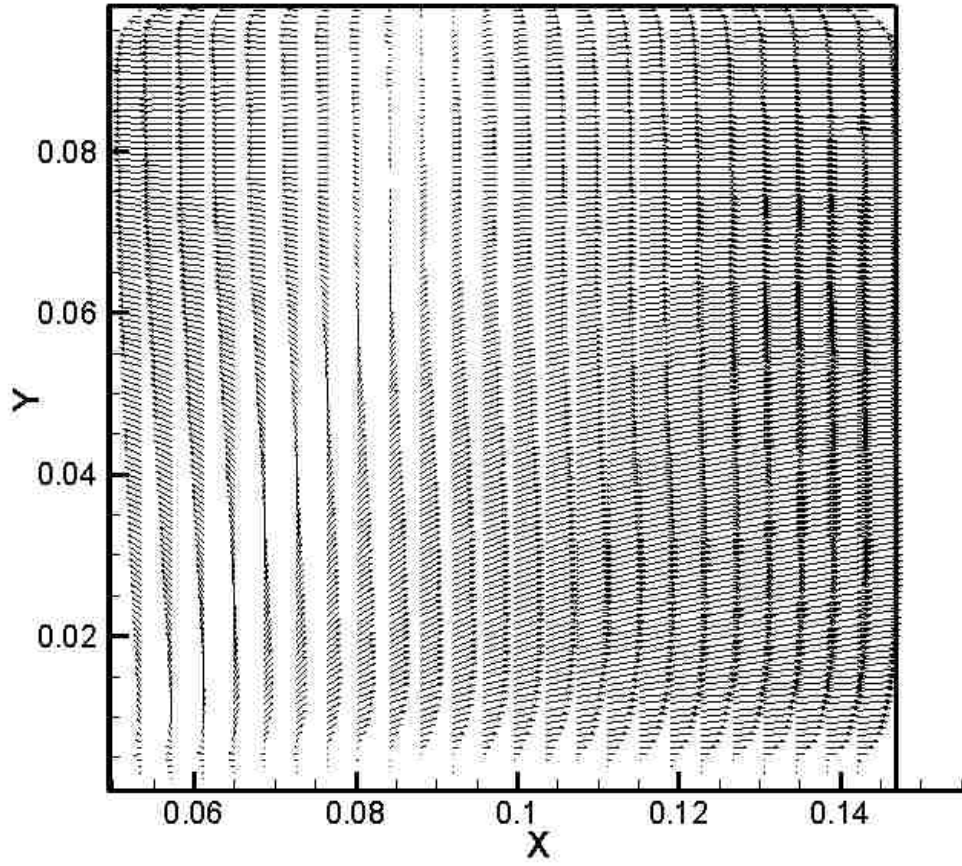
Figure 3.6: An example of the image after cross-correlation analysis.
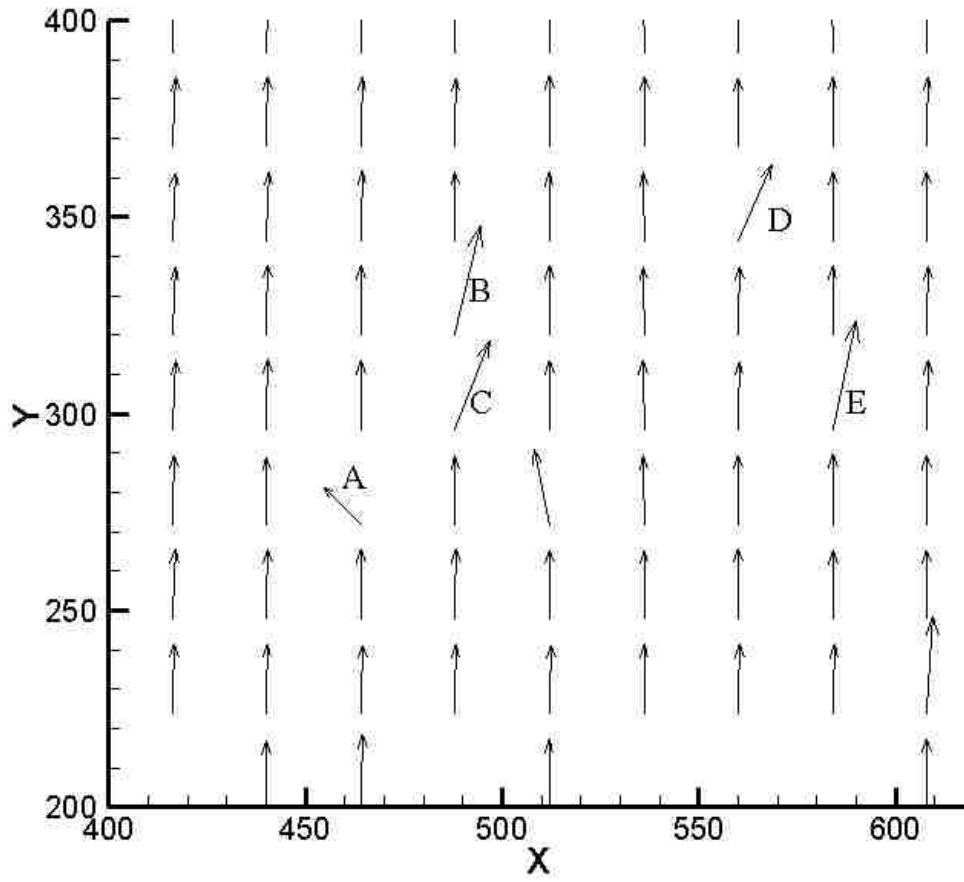
Figure 3.7: A sample field-of-view with spurious vectors. The spurious vectors are labelled as A-E.

Chapter 4
MEAN FLOW VARIABLES

4.1 General description

As mentioned earlier, a first set of experiments were carried out at a lower Reynolds number, based on the width of the body, $Re_D = 19,000$ and a stability number, $S = 0.0015$. This chapter is devoted to address vertical variation of the mean flow parameters of the shallow wake, at $x/D = 2.5$, 3.5 and 4.5. The present chapter starts with the quantification of the background channel flow information. Following that, the mean velocity field and the streamlines are examined. Comparison of the mean streamwise and transverse velocity components, the streamwise and transverse root-mean-square velocity and the Reynolds stress at different axial stations were performed. POD was also applied to expose the possible appearance of the coherent structures at the bed and free surface. This chapter concludes with specific conclusions, relevant to this section.

4.2 Approaching flow

The purpose of this section is to provide a comparison of the present data with well-documented channel flow results in order to validate the quality of the PIV data. For this reason, the velocity field of the channel flow was measured along the vertical mid-plane of the flume before inserting the bluff body. The mean freestream velocity (U_∞) of the channel flow was 0.19 m/s. The boundary layer thickness δ was estimated (based on $0.995 U_\infty$) to occupy ~80% of the shallow water layer H.

Although the resolution of the current PIV data is high, a few data points in the thin viscous sub-layer were missing. For this reason, a 6th order polynomial curve was used to fit the mean velocity profiles and generate the missing data points. The goodness-of-fit was assessed from the correlation coefficient of the least-square polynomial fit and found to be 0.9982. The displacement thickness (δ^*) and momentum thickness (θ) were then estimated by integrating the velocity data using Simpson's one-third rule and found to be 8.7 mm and 5.4 mm, respectively. The resulting shape factor was 1.6 and the Reynolds number based on the momentum thickness (Re_θ) was 986.

Figure 4.1 shows the mean velocity distribution in the channel flow in terms of the wall velocity U^+ ($= U/u_\tau$) and both inner y^+ ($= yu_\tau/v$) and outer y/H vertical axes. The data was fitted with the well-recognized logarithmic velocity profile (Pope, 2000). The present channel flow data was also compared with the experimental data of Balachandar & Bhuiyan (2007) for smooth channel flow at a Reynolds number, based on the depth of the flow, $Re_H = 51,000$. Both theoretical and experimental data exhibit good agreement with the present channel flow data. The deviation of the present PIV data for $y/H > 0.8$ may be attributed to the effect of the free surface on the velocity profile compared to the experimental unbounded case shown in the same figure. The friction velocity u_τ, defined as $\sqrt{\tau_w/\rho}$, was determined by the Clauser chart method (Clauser, 1954), which is based on the assumption that the velocity profile follows a universal logarithmic form in the overlap region of the boundary layer. In this study, the friction velocity u_τ was estimated to be 9.5 mm/s. The corresponding skin friction coefficient C_f, defined by $2\left(u_\tau/U_\infty\right)^2$,

was found to be 0.005. The viscous length scale l_v, defined as, (v/u_τ), (where v is the kinematic viscosity of the fluid) was estimated to be 0.1 mm, which is approximately seven to eight times smaller than the spatial resolution of the present data.

4.3 Mean velocity field of the wake flow

This section describes the mean velocity field of the shallow wake behind the bluff body. The stability parameter S of the current wake flow was estimated to be 0.0015. This result indicates that the bottom friction is not dominant compared to the effect of the free surface boundary as in extreme shallow cases (Shinneeb, 2006). At this particular stability parameter, the shallow wake is expected to be a vortex street type according to the classification of Chen & Jirka (1995). As illustrated by Balachandar et al. (1999), this region of the wake corresponds to deep-shallow wake.

4.3.1 Instantaneous streamline pattern

To have a clear perception of the differences in the three horizontal velocity fields of the wake flow, the streamline patterns of the mean velocity fields are shown in Figure 4.2. In these plots, the width of the body D (= 30 mm) is used as a normalizing length scale. Figure 4.2 show the existence of recirculation flow regions behind the bluff body, where the flow is in the positive x-direction at the outer edges of the fields-of-view and in the negative x-direction (reversed) near the vertical mid-plane ($z/D = 0$). In all cases, the wake appears almost symmetric about the x-axis. However, the size of the recirculation (wake) zones is different in the three fields. By comparing the three plots shown in Figure 4.2, it is clear that the size of the recirculation zones in the mid-depth plane ($y/H =$

0.51) shown in Figure 4.2(b) is much larger compared to the zones in the near-bed ($y/H =$ 0.10) and near-surface ($y/H = 0.76$) planes. The recirculation regions in the three cases appear to extend in the streamwise direction to $x/D \approx 2.5$, 4.0, and 3.3, corresponding to the horizontal velocity fields at $y/H =$ 0.10, 0.51, and 0.76, respectively. These differences are a clear indication of the three-dimensionality of the near-wake flow structure as a result of the distribution of the vortical structures throughout the water layer (see section 4.4). At this point, the length of the recirculation region can be compared with previous literature. Dong et al. (2006) experimentally determined the length of recirculation region for a circular cylinder of $H/D = 11.7$ at Re = 4,000 and 10,000 to be 1.47D and 0.78D, respectively. For a square cylinder, for aspect ratio $H/D = 10$, and Re = 15,000 the length of the recirculation region was found to be 0.6D (Nakagawa et al., 1999). Lyn et al. (1995) found this value to be 0.9D for a square-cylinder. The length of the recirculation region in the present investigation is the largest, probably due to the resistance of development of three-dimensional disturbances due to vertical confinement.

4.3.2 Velocity deficit parameter

The mode of instability of the current shallow wake can be assessed by defining the velocity deficit parameter (see Monkewitz 1988): $R = \left(\widetilde{u}_r - U_\infty\right)/\left(\widetilde{u}_r + U_\infty\right)$, where $\widetilde{u}_r$ is the reverse velocity in the recirculation zone measured at the vertical mid-plane ($z/D =$ 0), and U_∞ is the freestream velocity. Chen & Jirka (1995) reported R values for a shallow wake (generated by a cylinder) based on the maximum reverse velocity measured at the mid-depth plane. To illustrate the vertical variation of the recirculation zones in the

present data, the reverse velocity at the streamwise location $x/D = 2$ is used as a basis for the comparison, which represents the location of maximum value of $\tilde{u}_r$ for the mid-depth plane. It is found that $\tilde{u}_r$ = −0.014, −0.060, and −0.041, corresponding to the vertical locations y/H = 0.10, 0.51, and 0.76, respectively. According to the above relation, the corresponding values of velocity deficit parameter are R = −1.16, −1.92, and −1.55, respectively. Chen and Jirka (1995) reported R = −2.07 for the case of unsteady bubble and vortex street modes of a shallow wake, and R = −2.03 for the case of an unbounded wake. By comparing their values of R with the present data, it can be observed that the recirculation zone in the mid-depth plane (R = −1.92) seems to be more similar to the deep wake than the near-boundary planes.

4.3.3 Mean streamwise velocity profiles

More insight into the flow characteristics can be obtained by extracting the velocity profiles at specific downstream locations. Figure 4.3 shows the development of the mean streamwise velocity U profiles in the streamwise direction for the three horizontal planes (y/H = 0.10, 0.51 and 0.76). The velocity profiles are normalized by the mean streamwise velocity U_s (U_s = 0.147, 0.186 and 0.190 m/s, respectively) at the corresponding vertical location y/H of the channel flow without the body and plotted against the horizontal location z normalized by the width of the body D. In these figures, the velocity profiles are plotted at streamwise locations x/D = 2.5, 3.5 and 4.5. Note that only every second point of the velocity data is shown to avoid cluttering.

Figure 4.3 (a), (b), and (c) show that all velocity profiles in the three planes are generally symmetrical about the vertical mid-plane ($z/D = 0$). These figures also show that the behavior of the velocity profiles may be divided into two regions; inner and outer. The points that demarcate the inner region from the outer region (labeled P and Q) are located at $|z/D| = 0.74, 0.99$, and 0.97 which correspond to velocity fields shown in (a), (b), and (c), respectively. Point P and Q indicate the transverse locations where the slope of the curve changes sign. As mentioned earlier, due to limited transverse extent of the FOV, accurate estimation of the half-width of the wake is not possible, and the transverse extent of P and Q can be taken as the indication of the half-width. The longitudinal extent of the distance between P and Q shows the effect of bed and free surface on the transverse growth of wake. More about this can be found in section 5.3.5. The location of these points also illustrates that the largest wake occurs in the mid-depth case ($y/H = 0.51$). The corresponding magnitude of the normalized streamwise velocities at these points are $U/U_s = 0.86, 0.74$, and 0.70, respectively. The mean streamwise velocity U profiles in the inner region ($|z/D| \leq 0.74, 0.99$, and 0.97) demonstrate an increasing trend of the velocity in the streamwise direction with a corresponding decrease in the outer region.

4.3.4 Mean transverse velocity profiles

The mean transverse velocity W profiles for the three horizontal planes at $y/H = 0.10, 0.51$, and 0.76 are shown in Figure 4.4(a), (b), and (c), respectively. The velocity W and the horizontal locations z are also normalized by U_s and D, respectively. All figures

show that the velocity is inward towards the vertical mid-plane at all streamwise locations (x/D = 2.5, 3.5, and 4.5). The magnitude of the maximum velocity $|W/U_s|$ at x/D = 2.5 is approximately 0.25, 0.10 and 0.14, which occurs at $|z/D| \approx$ 0.91, 1.06, and 0.98, respectively. Figure 4.4(a) and (c) show that the velocity profiles of the near-bed and near-surface cases at x/D = 2.5 and 3.5 are almost similar, but the velocity profiles seem to decrease at x/D = 4.5. The maximum magnitude of the inward velocity towards the vertical mid-plane at x/D = 4.5 in these cases are $|W/U_s|$ = 0.16 and 0.10 located at $|z/D|$ = 0.82 and 0.90, respectively. In contrast to the above behavior, Figure 4.4(b) shows that the transverse inward flow in the mid-depth plane increased from x/D = 2.5 to 3.5, then became constant from x/D = 3.5 to 4.5.

To help the reader have a global view of the flow pattern under investigation, vector plots of the mean velocity field in the three horizontal planes are shown in Figure 4.5 superimposed by a color contour of the mean transverse velocity W/U_s. In summary, the above results indicate that the transverse velocity W/U_s profiles in the near-bed and near-surface planes developed faster than the velocity profiles in the mid-depth plane. In addition, the profiles in the near-bed case indicate that the inward flow is enhanced compared to the near-surface case. The differences between the near-bed and near-surface profiles may be attributed to the formation/distribution of secondary vortices that may be developed near the boundaries. This issue will be discussed in section 4.4.

4.3.5 Variation of the streamwise velocity in the central-plane of the wake

The variation of the mean streamwise velocity in the central-plane ($z/D = 0$) of the wake (U_c) with the streamwise distance x is shown in Figure 4.6. This figure shows three curves extracted from the horizontal velocity fields at vertical locations $y/H = 0.10$, 0.51 and 0.76, respectively. In this figure, the mean central velocity U_c (referred to as the central velocity hereafter) and the streamwise distance x are normalized by U_s and D, respectively. The central velocity U_c was obtained by fitting the horizontal profiles of the mean streamwise velocity U with a 10th order polynomial curve. Figure 4.6 illustrates that the streamwise location where the central velocity U_c becomes zero is at $x/D = 2.4$, 3.9, and 3.1 corresponding to $y/H = 0.10$, 0.51, and 0.76, respectively. U_c/U_s appears to vary linearly with x/D at a relatively high rate in the range $2.5 \leq x/D \leq 4.0$. However, U_c/U_s for the $y/H = 0.51$ case appears to vary at a much slower rate in the range $x/D \leq 2.5$ compared to the downstream rate. This is consistent with the relatively larger size of the recirculation zone at this vertical location compared to the other cases. Also, the rate of increase of U_c for the $y/H = 0.10$ and 0.76 cases becomes slower and non-linear for $x/D \geq 4.0$.

4.3.6 Half Width of the Wake

The half-width of wake $z_{0.5}$ is defined as the transverse location z where the velocity defect Δu ($= U - U_s$) equals half of the maximum velocity defect Δu_{max}. In this chapter, Δu_{max} is defined as ($U_c - U_s$), where U_s represents the streamwise velocity at a corresponding vertical location without the body and U_c is the central velocity.

Figure 4.7 shows the variation of the wake half-width $z_{0.5}$ with the streamwise distance x at three vertical locations $y/H = 0.10$, 0.51, and 0.76. Both half-width and the streamwise distance are normalized by the width of the bluff body D. The half width $z_{0.5}$ appears to be constant near the body for $y/H = 0.10$ and 0.51, then to spread non-linearly in the streamwise direction. The growth rate of the near-surface ($y/H = 0.76$) curve is also non-linear, but appears higher compared to the other curves at these locations. This figure illustrates that the streamwise velocity U profiles are narrower in the near-bed plane compared to the other planes (see Figure 4.3). Physically, the differences in the size of the recirculation zones may be explained by the differences in the entrainment rates (see Figure 4.4) as a result of the distribution of the vortical structures throughout the water depth (see Section 4.4).

4.3.7 Turbulent parameters

The development of the streamwise root-mean-square velocity U_{rms} in the streamwise direction x extracted from the horizontal velocity fields at $y/H = 0.10$, 0.51, and 0.76 are shown in Figure 4.8(a), (b), and (c), respectively. In these figures, U_{rms} is normalized by the upstream velocity U_{s} and x is normalized by the width of the bluff body D. Generally, the distribution of the U_{rms} velocity profiles in the three planes appear symmetrical about the vertical mid-plane ($z/D = 0$) with two distinct peaks.

Figure 4.8(a) shows the streamwise root-mean-square velocity U_{rms} profiles extracted from the near-bed plane ($y/H = 0.10$) at streamwise locations $x/D = 2.5$, 3.5 and 4.5. The peaks of $U_{\mathrm{rms}}/U_{\mathrm{s}}$ profiles at streamwise locations $x/D = 2.5$ and 3.5 are

approximately 0.39 and 0.35, respectively, which occurs at $|z/D| \approx 0.6$ and 0.5, while the minimum values are approximately 0.34 and 0.32. This figure demonstrates that, as the flow proceeds downstream, the magnitude of U_{rms} in the core region ($|z/D| < 1$) decreases with a relatively high rate until the profile becomes almost flat at $x/D = 4.5$ ($U_{\text{rms}}/U_{\text{s}} \approx$ 0.29). For the region $|z/D| > 1$, the change in $U_{\text{rms}}/U_{\text{s}}$ is negligible. Generally, the streamwise turbulence intensity U_{rms} tends to approach zero in the outer region of the wake flow.

Figure 4.8(b) shows that the relative streamwise rms velocity $U_{\text{rms}}/U_{\text{s}}$ profiles in the mid-depth plane ($y/H = 0.51$) are different compared to the profiles shown in Figure 4.8(a). Although the shape of the profiles consists of two off-axis peaks and a valley as in the previous case, the profile at $x/D = 2.5$ has a much larger valley than the previous case where the minimum magnitude occurs at $z/D = 0$. The peaks of this $U_{\text{rms}}/U_{\text{s}}$ profile are 0.36 which occur at $|z/D| \approx 0.9$, while the magnitude of the minimum value is 0.24. This distribution indicates that the recovery of the flow kinetic energy behind the bluff body is slower compared to the near-boundary planes. Further downstream, this figure shows that there is an increase in the streamwise rms velocity U_{rms} near the vertical mid-plane ($z/D = 0$) with a corresponding decrease of the peak values.

The profiles shown in Figure 4.8(c) illustrate the behavior of the streamwise rms velocity U_{rms} in the near-surface plane ($y/H = 0.76$). Although the peaks of the $U_{\text{rms}}/U_{\text{s}}$ profile at $x/D = 2.5$ is comparable to the previous cases at the same location ($U_{\text{rms}}/U_{\text{s}} \approx$ 0.39 at $|z/D| \approx 0.85$), the minimum value which occurs at $z/D = 0$ ($U_{\text{rms}}/U_{\text{s}} \approx 0.31$) is

91

smaller than the value shown in Figure 4.8(a), but larger than the value shown in Figure 4.8(b). This indicates that the recovery of U_{rms} in this plane is slower than the near-bed case, but faster than the mid-depth case. At locations farther downstream, the development of the U_{rms}/U_s profiles in the streamwise direction is similar to the near-bed case, where the off-axis peaks decrease while U_{rms} near $z/D = 0$ increases then decreases. The relative streamwise rms velocity U_{rms}/U_s at $x/D = 4.5$ appears to approach a flat shape in the core region ($|z/D| < 0.95$) with a magnitude equal to 0.29, and approaches zero in the outer region of the wake flow.

The relative transverse root-mean-square velocity W_{rms}/U_s profiles for the horizontal planes at $y/H = 0.10$, 051, and 0.76 are shown in Figure 4.9(a), (b), and (c). All profiles in these figures demonstrate a dome-type distribution. But the profiles extracted from the mid-depth ($y/H = 0.51$) and near-surface ($y/H = 0.76$) planes look broader than the near-bed profiles ($y/H = 0.10$). The profiles extracted from the near-bed and near-surface planes show that the profiles at $x/D = 2.5$ and 3.5 overlap in the core region ($|z/D| < 0.6$ and 0.8 for the $y/H = 0.10$ and 0.76 cases, respectively), while the profiles at $x/D = 3.5$ and 4.5 overlap in the outer region ($|z/D| > 0.6$ and 0.7, respectively). The peak values of the relative transverse turbulence intensity W_{rms}/U_s for the near-bed case are 0.58 at $x/D = 2.5$ and 3.5, and 0.50 at $x/D = 4.5$, while for the near-surface case are 0.47 at $x/D = 2.5$ and 3.5 and 0.44 at $x/D = 4.5$. This behavior indicates that there is an increase in W_{rms} in the streamwise direction from $x/D = 2.5$ to 3.5 (in the outer region), then W_{rms} in the core region ($|z/D| < 0.7$ and 0.9 for the $y/H = 0.10$ and 0.76 cases, respectively) decreases in the streamwise direction from $x/D = 3.5$ to 4.5.

The relative transverse turbulence intensity W_{rms}/U_s profiles shown in Figure 4.9(b) shows that there is an increase in W_{rms} in the streamwise direction by comparing the profiles at $x/D = 2.5$ and 3.5, then W_{rms} becomes constant as illustrated by the collapse of the profiles at $x/D = 3.5$ and 4.5. The values of W_{rms}/U_s at $z/D = 0$ are 0.31, 0.41, and 0.42 corresponding to streamwise locations $x/D = 2.5$, 3.5 and 4.5, respectively.

To summarize the behavior of the streamwise and transverse rms velocities discussed above, the distribution of turbulent kinetic energy K in the streamwise direction obtained from these components $K = \frac{1}{2}(U_{rms} + W_{rms})$ are shown in Figure 4.10. The turbulent kinetic energy K is normalized by the square of the upstream velocity $U_{upstream}$. Note that the relatively larger K/U_s^2 values shown in Figure 4.10(a) compared to the other cases, shown in (b) and (c), is because the upstream velocity U_s used to normalize the data was smaller (0.147). By comparing the three plots, it can be observed that there is an increase in K/U_s^2 in the mid-depth plane (in the region $|z/D| < 1$) from $x/D = 2.5$ to 3.5, while the other planes show a negligible change. From $x/D = 3.5$ to 4.5, the variation of K/U_s^2 is reversed, i.e. there is a decrease in the near-bed and near-surface planes (plots **a** and **c**) with a negligible change in the mid-depth plane (plot b). This behavior indicates that the turbulent energy is correlated in the three planes. In other words, there is transfer of energy throughout the water depth, which can be clarified by plotting the relationship between U_{rms} and W_{rms} along the central plane ($z/D = 0$). Figure 4.11 illustrates the variation of U_{rms}/W_{rms} in the streamwise direction x/D for the $y/H = 0.10$, 0.51, and 0.76

planes. The negligible increase of K/U_s^2 from $x/D = 2.5$ to 3.5 for the $y/H = 0.10$ and 0.76 planes shown in Figure 4.10(a) and (c) and the constant U_{rms}/W_{rms} ratio in Figure 4.11 indicate that both U_{rms} and W_{rms} are constant in this region. On the other hand, the increase of K/U_s^2 for the $y/H = 0.51$ plane shown in Figure 4.10(b) and the decrease of U_{rms}/W_{rms} in Figure 4.11 is a clear indication of the increase of U_{rms} with a higher rate compared to W_{rms} in this region (see also Figure 4.8b and Figure 4.9b). Further downstream ($x/D = 3.5$ to 4.5), it can be concluded from Figure 4.10 and Figure 4.11 that both U_{rms} and W_{rms} decrease in the $y/H = 0.10$ and 0.76 planes, while U_{rms} and W_{rms} for the $y/H = 0.51$ plane seem to be constant. This behavior indicates that there is a transfer of energy from the streamwise and transverse components in the near-boundary planes to the vertical component V_{rms} so as to maintain a constant U_{rms} and W_{rms} in the mid-depth plane. This observation is also supported by the behavior of the vortical structures that reside near the boundaries which direct flow towards the mid-depth plane(to be shown in section 4.4).

The Reynolds shear stress $<uw>/U_s^2$ profiles extracted from the horizontal planes at $y/H = 0.10$, 0.51, and 0.76 are shown in Figure 4.12(a), (b)**,** and (c)**,** respectively, at different streamwise locations. Figure 4.12(a) shows that the data extracted from the near-bed plane ($y/H = 0.10$) are symmetric about the vertical mid-plane ($z/D = 0$). It also shows that the Reynolds shear stress decreases in the streamwise direction. The maximum absolute values of $<uw>/U_s^2$ at $x/D = 2.5$, 3.5, and 4.5 are 0.089, 0.074, and 0.050, respectively, which are located at $z/D \approx \pm 0.55$. These results indicate that the

momentum exchange by the Reynolds stress is reduced in the streamwise direction because of the shallowness compared to the deep wakes (Williamson, 1996).

Figure 4.12(b) shows the variation of the Reynolds shear stress $<uw>/U_s^2$ profiles for the $y/H = 0.51$ plane. Consistent with the behavior of the transverse rms velocity profiles shown in Figure 4.9(b), Figure 4.10(b) shows that $<uw>/U_s^2$ increases then decreases in the streamwise direction, albeit the variation is small. The maximum absolute values of $<uw>/U_s^2$ at x/D = 2.5, 3.5, and 4.5 are 0.63, 0.72, and 0.61, respectively, which are located at $|z/D| \approx$ 0.94, 0.80, and 0.74. This behavior indicates that the horizontal momentum exchange has been slightly enhanced at these streamwise locations.

The Reynolds shear stress $<uw>/U_s^2$ profiles for the $y/H = 0.76$ plane (Figure 4.12(c)) show similar behavior as the profiles extracted from the near-bed plane (y/H = 0.10). The maximum absolute values of $<uw>/U_s^2$ are 0.089, 0.072, and 0.054, located at $|z/D|$ = 0.82, 0.84, and 0.86, respectively, corresponding to streamwise locations x/D = 2.5, 3.5, and 4.5.

4.4 Coherent structures

This section presents selected examples of large vortical structures in the wake of the bluff body educed by the proper orthogonal decomposition (POD) technique. The procedures may be summarized as follows. The instantaneous velocity fields were processed using the POD via the method of snapshots (Sirovich, 1987). Two thousand velocity fields were used in this process, which yielded a temporal correlation matrix of

size 2000 × 2000. A complete description of the implementation of the POD using the method of snapshots may be found in Shinneeb (2006). The number of modes used for the POD reconstruction in this paper was six including mode 0. Note that mode 0 represents a velocity field that resembles the mean velocity field. These POD reconstructed velocity fields provide a unique set of flow visualization results obtained by a quantitative technique since they include mode 0. In other words, it is not common to include mode 0 in the POD reconstruction since the structures cannot be exposed in most cases. In addition, the current results highlight the dynamics of large (energetic) structures in this flow while the small (less energetic) structures are filtered out, which adds to the quality of the results compared to conventional visualization. It should be pointed out that the time separation between two consecutive velocity fields was ~1 s. This time separation is too large to follow the same vortical structures in successive frames. However, some interesting features were captured. It should be pointed out that this work produced a large amount of data which cannot be presented here owing to space limitations. Consequently, only some selected examples will be presented in this section.

Figure 4.13 shows some selected examples of the large vortical structures extracted from the vertical mid-plane ($z = 0$) of the shallow bluff body flow. The streamwise x and vertical y axes are normalized by the water depth H. The total kinetic energy recovered in these fields was ~59.5%. This figure consists of three examples of streamline plots (a), (b), and (c) representing POD reconstructed velocity fields in order to highlight the features of the flow.

Figure 4.13(a) shows a vortical structure close to the free surface. This structure induces a strong backward flow being directed away from the free surface by a negative vertical velocity component (labeled E), and a forward flow being moved toward the free surface (labeled S). This behavior is very similar to the mechanism of the ejection and sweep events that occur near a solid wall. The flow direction of the ejection-like event (labeled E) suggests that the identified structure is a cross-section of a hairpin structure with two counter-rotating quasi-streamwise vortical elements. This observation is based on flow direction of the ejection-like event and the local maximum velocity as highlighted by the extracted velocity profile at $x/H = 0.65$ shown in the same plot. The quasi-streamwise vortical elements are known to exist in junction flows since horseshoe vortices wrap around the obstacle (Simpson, 2001). The streamline patterns in Figure 4.13(a) also shows an upward flow near the bed which seems to be thrust by a quasi-streamwise vortical element that resides near the bed. This example illustrates the interaction between induced flows by the structures that reside near the bed and the free surface. Another example is shown Figure 4.13(b). This figure shows a cross-section of a structure near the bed and a signature of a quasi-streamwise vortical element besides it (near the bed) which thrusts the flow upwards. In addition, there is a diverged downward flow that seems to be a result of a quasi-streamwise vortical element resides near the free surface.

An interesting feature can also be seen in Figure 4.13(c), which shows an element that appears as a thick vertical line. This element spans almost the entire water depth and extends close (and parallel) to the bed in the streamwise direction to $x/H \approx 0.75$. The

direction of the flow at the sides of this element indicates that it is a side-section of a vortical element which resembles a hairpin leg. However, the lower-lying portion of this element appears to reside ahead of the vertical portion of the element leg. Conversely, the hairpin vortex in a channel flow (without a bluff body) is supposed to be stretched in the streamwise direction according to velocity gradient in the boundary layer. This shape of the vortical element may be a result of the interaction of a hairpin vortex with quasi-streamwise elements that seem to be common in this kind of flow (see Simpson, 2001).

It should be mentioned that similar structures (to those exposed along $z/D = 0.0$) were also observed along the vertical plane at $z/D = 0.5$. Accordingly, they are not presented here because they would not add new information.

Figure 4.14, Figure 4.15 and Figure 4.16 show selected examples of the POD-reconstructed instantaneous velocity fields on the horizontal plane. The streamwise x and horizontal z locations are normalized by the width of the bluff body D. Each column in this figure shows three examples representing the velocity field in a horizontal plane at a specific vertical location. The total kinetic energy recovered (using the first six modes) was 90%, 86.7%, and 87.6% corresponding to horizontal velocity fields in planes at vertical locations $y/H = 0.10$, 0.51, and 0.76, respectively. In these plots, the streamline patterns are presented because the most useful information regarding the dynamics of the structures is apparent in these plots.

At first glance, all plots shown illustrate that the wake flow contains a large number of structures which makes the flow meander about the vertical mid-plane. The

meandering behavior was also predicted by the stability parameter S for this flow which suggests a lesser effect of the bed friction on the flow compared to the shear stress generated in the shear layer of the wake flow.

Plots (a) in Figure 4.14, Figure 4.15, and Figure 4.16 show that the vortical structures exist in pairs of opposite rotational sense. This suggests that the vortices are being shed from both sides of the bluff body. The vortical structures in these plots appear to undergo axial stretching generated by the surrounding flow with a corresponding horizontal compression as illustrated by the proximity of the streamlines at the edges of the vortices. In addition, the vortex pair shown in Figure 4.14(a) appears to consist of a circular vortex and a spiral vortex where the flow is spiraling into its center (see Perry & Steiner, 1987). Moreover, the vortex pairs shown in f Figure 4.15(a) and Figure 4.16(a) show similar configuration, but the flow is spiraling out of the spiral vortices in these examples. This configuration seems to be a characteristic feature of vortex pairs in shallow wakes.

Figure 4.14(b), Figure 4.15(b), and Figure 4.16(b) illustrate that the size of the vortices are relatively larger than the width of the bluff body. It appears that the vortices identified in the horizontal plane occupy more than double body width D. Furthermore, these plots show that the flow patterns are not symmetrical. They appear to meander like a sine wave about the vertical mid-plane. This behavior is due to the interaction of the vortices with the mean flow at either side of the vertical mid-plane.

Some interesting features about the interaction between the vortices are shown in Figure 4.14(c), Figure 4.15(c), and Figure 4.16(c). The plots in Figure 4.14(c) and Figure 4.15(c) show that the vortices are being compressed horizontally normal to the vertical mid-plane which could lead to merging of the two structures. Furthermore, the plot shown in Figure 4.15(c) illustrates the effect of stretching on the structures which appear elongated in the streamwise direction. The presence of two connected structures for z/D > 0 suggests the occurrence of the tearing process as a result of the vortex stretching by the instantaneous flow.

4.5 Conclusions

PIV measurements have been conducted to investigate the wake flow of a sharp-edged bluff body immersed in a shallow, smooth open channel flow. The purpose of the present chapter is to highlight the vertical variation of the wake turbulent flow field throughout the shallow water layer. The conclusions may be summarized as follows:

- The size of the recirculation zones in the mean velocity fields appears to be different at different vertical locations. It was found that the largest recirculation zone occurs in the mid-depth velocity field, while the smallest one occurs near the bed. This is a clear indication of the three-dimensionality of the near-wake flow. The differences in the wake size are attributed to the formation and distribution of the vortices (particularly the quasi-streamwise vortices) near the bed and the free surface, which are responsible for enhancing the entrainment (as shown in the

transverse velocity W profiles) and the consequent reduction in the size of the recirculation zones.

- The POD results show that the wake flow is rich with quasi-streamwise vortical elements that reside near the boundaries (bed and free surface). These elements were observed to thrust flow upwards from the bed and downwards from the free surface. This observation is consistent with the correlated distribution of energy throughout the water layer, which is attributed to the redistribution of the kinetic energy between the three velocity components (U_{rms}, V_{rms} and W_{rms}).

- The Reynolds stress $<uw>$ results indicate a reduction in the transverse momentum exchange near the boundaries as the flow moves in the streamwise direction, consistent with the reduction of the streamwise and transverse fluctuations reflected by U_{rms} and W_{rms} results. Furthermore, the transverse momentum exchange in the mid-depth plane has been enhanced in the streamwise direction.

- The POD results show the existence of structures near the free surface which induced flow similar to the ejection and sweep events that commonly occur near solid walls. The direction of the ejection-like event suggest that the shape of these structures is similar to the hairpin vortices with two counter-rotating quasi-streamwise vortical elements that usually exist near solid walls although the boundary conditions are different.

- The size of the vortices exposed on the horizontal plane appears to exceed 200% of the bluff body width (> 50% of the water depth) at these locations ($x/D < 5$). Similar observation was previously reported in the far-field region of a wake flow. In addition, these vortical structures undergo streamwise stretching and/or horizontal compression generated by the surrounding flow, which seems to be responsible for the occurrence of pairing and tearing processes.
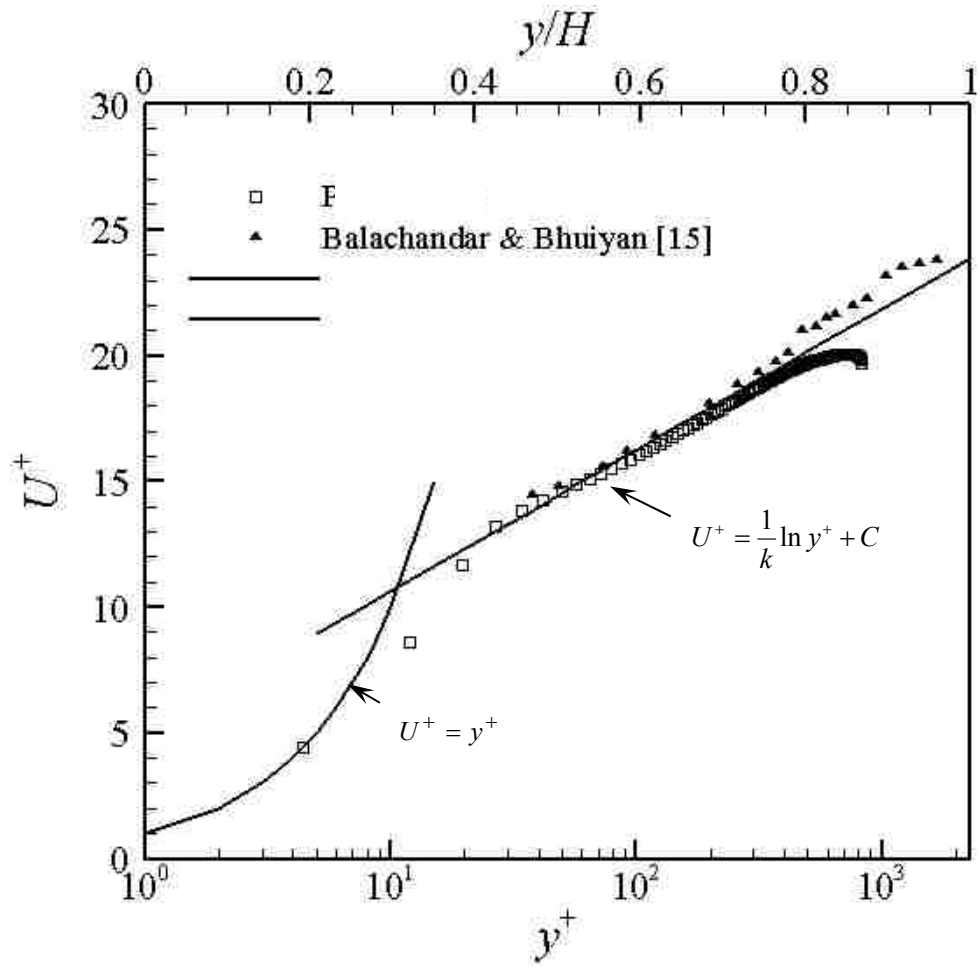
Figure 4.1: Mean streamwise velocity distribution of the smooth channel flow using inner coordinates.
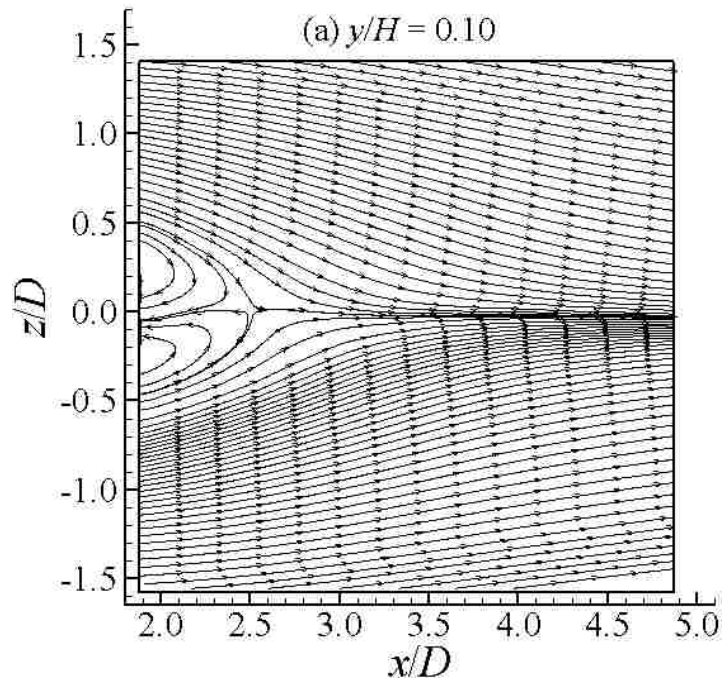
Figure 4.2: Streamline patterns of the mean velocity fields in the wake of the bluff body for three horizontal planes (a) $y/H = 0.10$, (b) $y/H = 0.51$, and (c) $y/H = 0.76$.
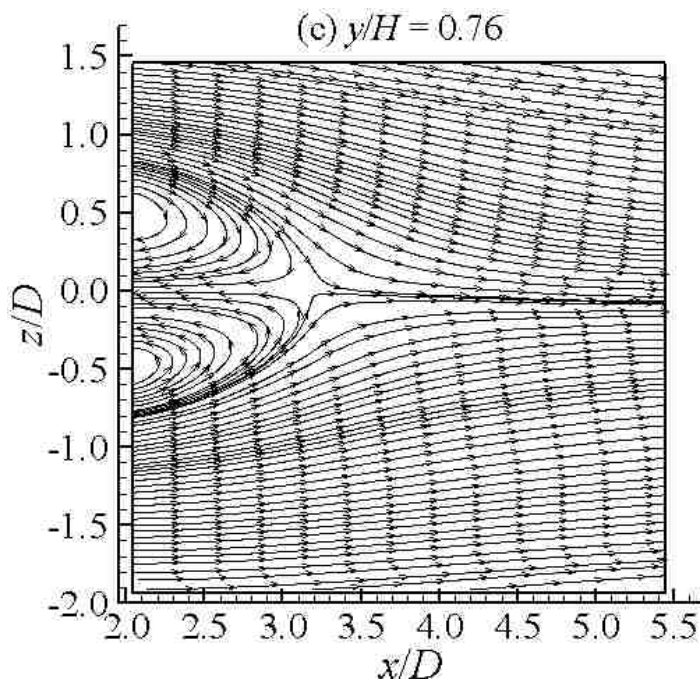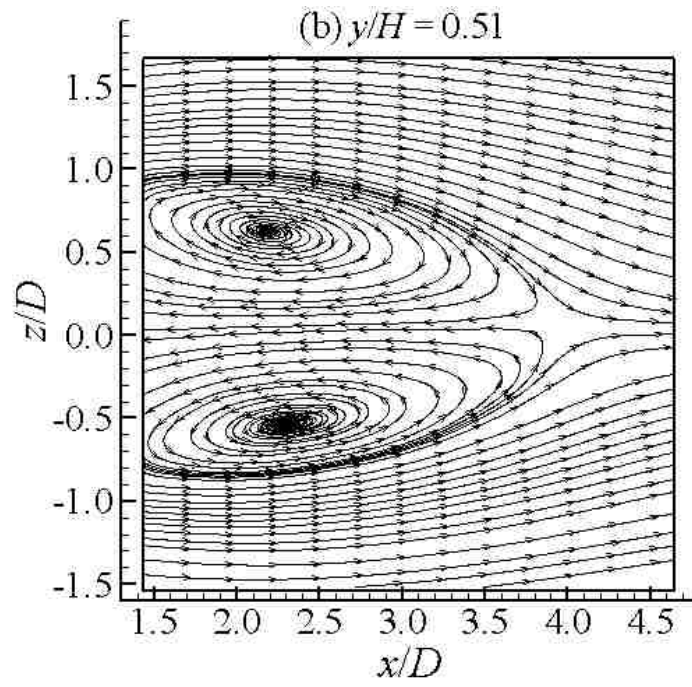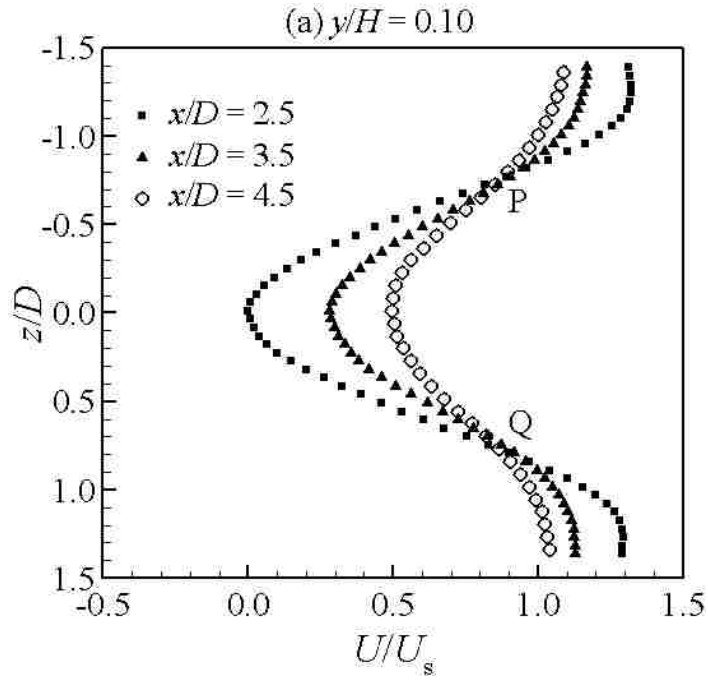
(b) $y/H = 0.51$

(c) $y/H = 0.76$

Figure 4.3: Development of the mean streamwise velocity U/U_s in the streamwise direction at different horizontal planes (a) $y/H = 0.10$, (b) $y/H = 0.51$, (c) $y/H = 0.76$.
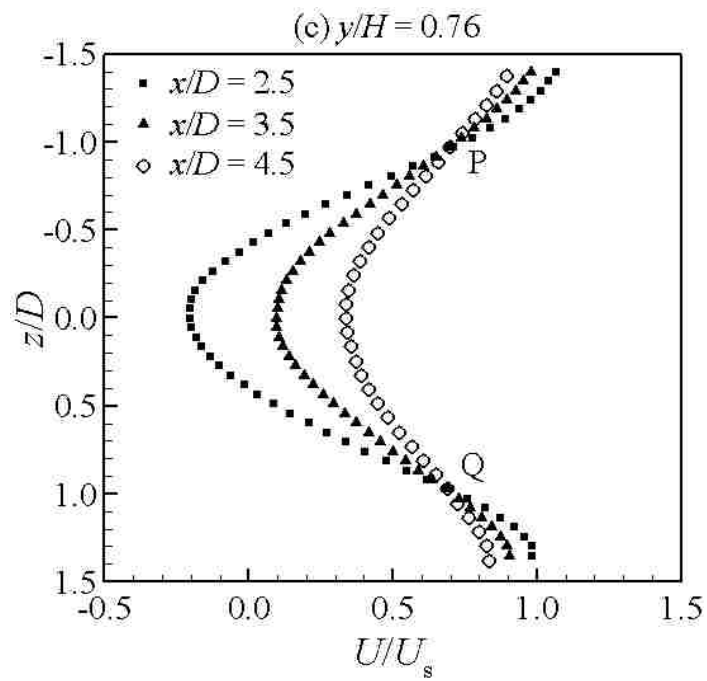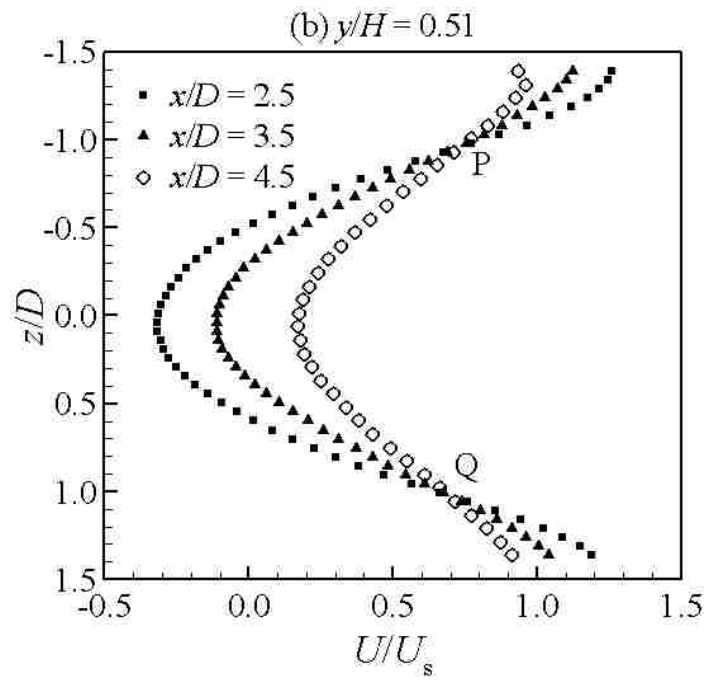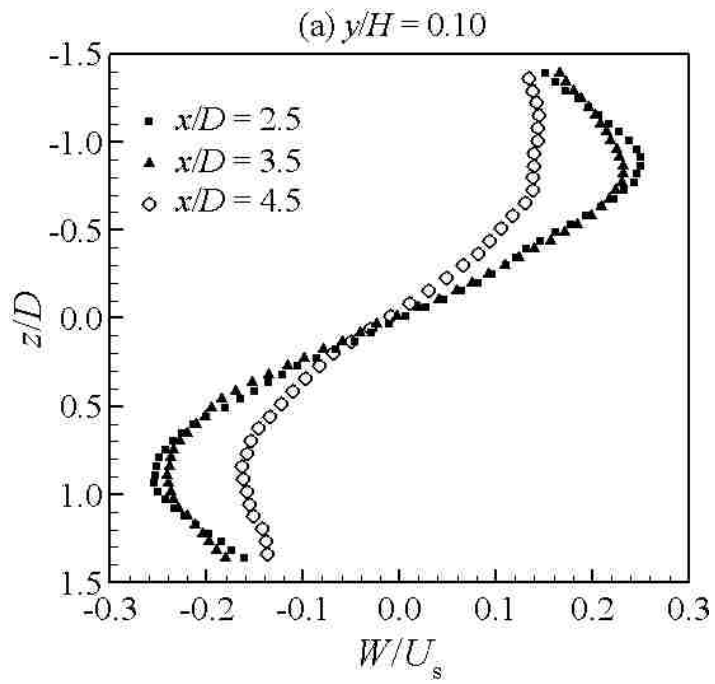
(b) $y/H = 0.51$

(c) $y/H = 0.76$

Figure 4.4: Development of the mean transverse velocity W/U_s in the streamwise direction at different horizontal planes (a) $y/H = 0.10$, (b) $y/H = 0.51$, and (c) $y/H = 0.76$.

(b) *y*/*H* = 0.51

(c) *y*/*H* = 0.76
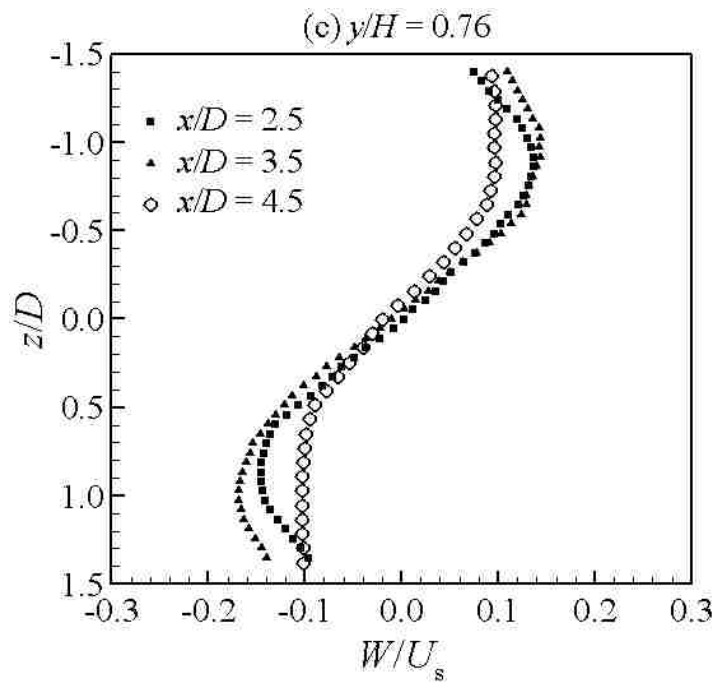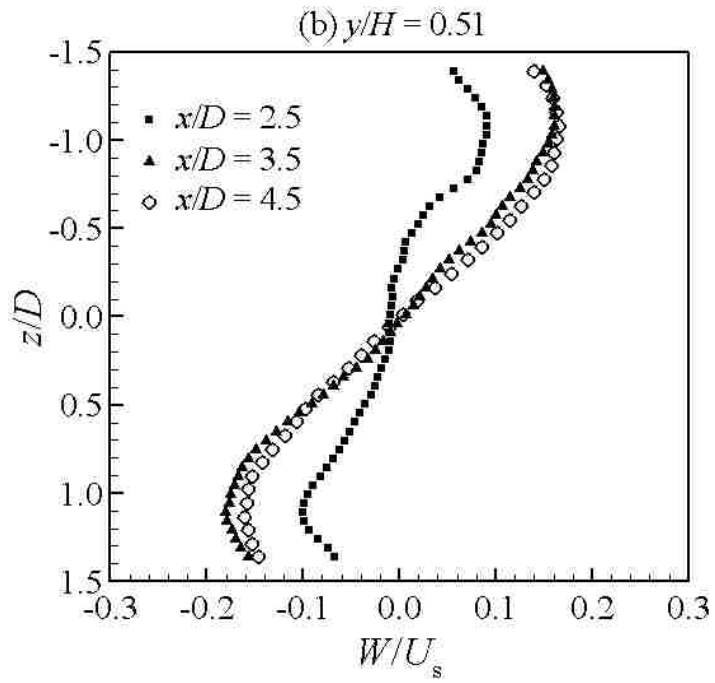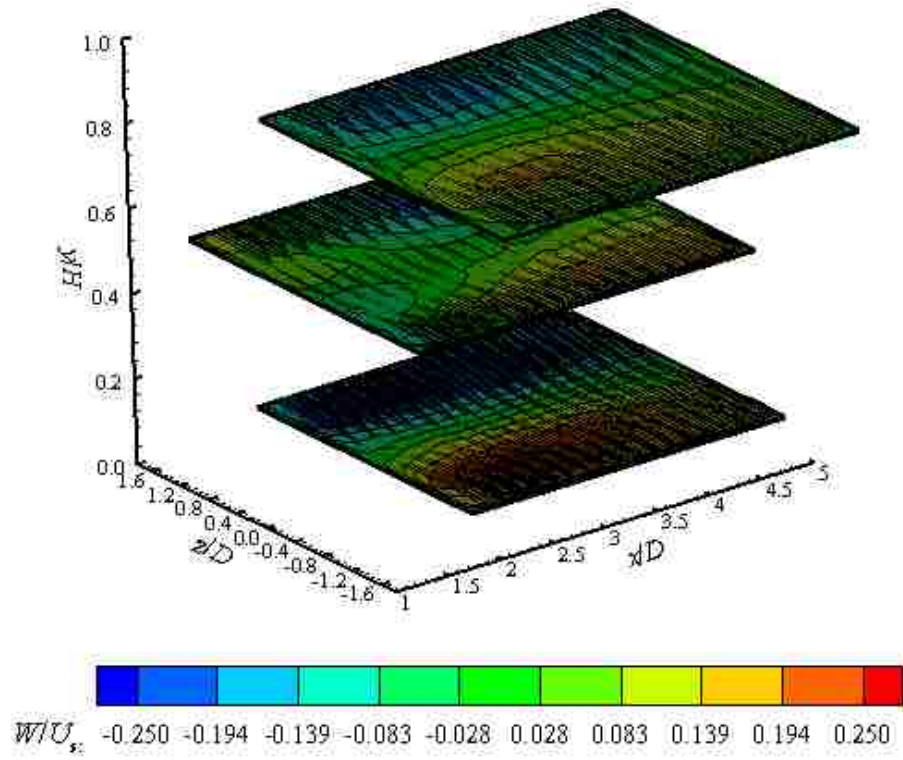
Figure 4.5: A vector plot representing the mean flow field in the three horizontal planes (y/H = 0.10, 0.51, and 0.76) superimposed by a color contour of the normalized mean transverse velocity W/U_s.
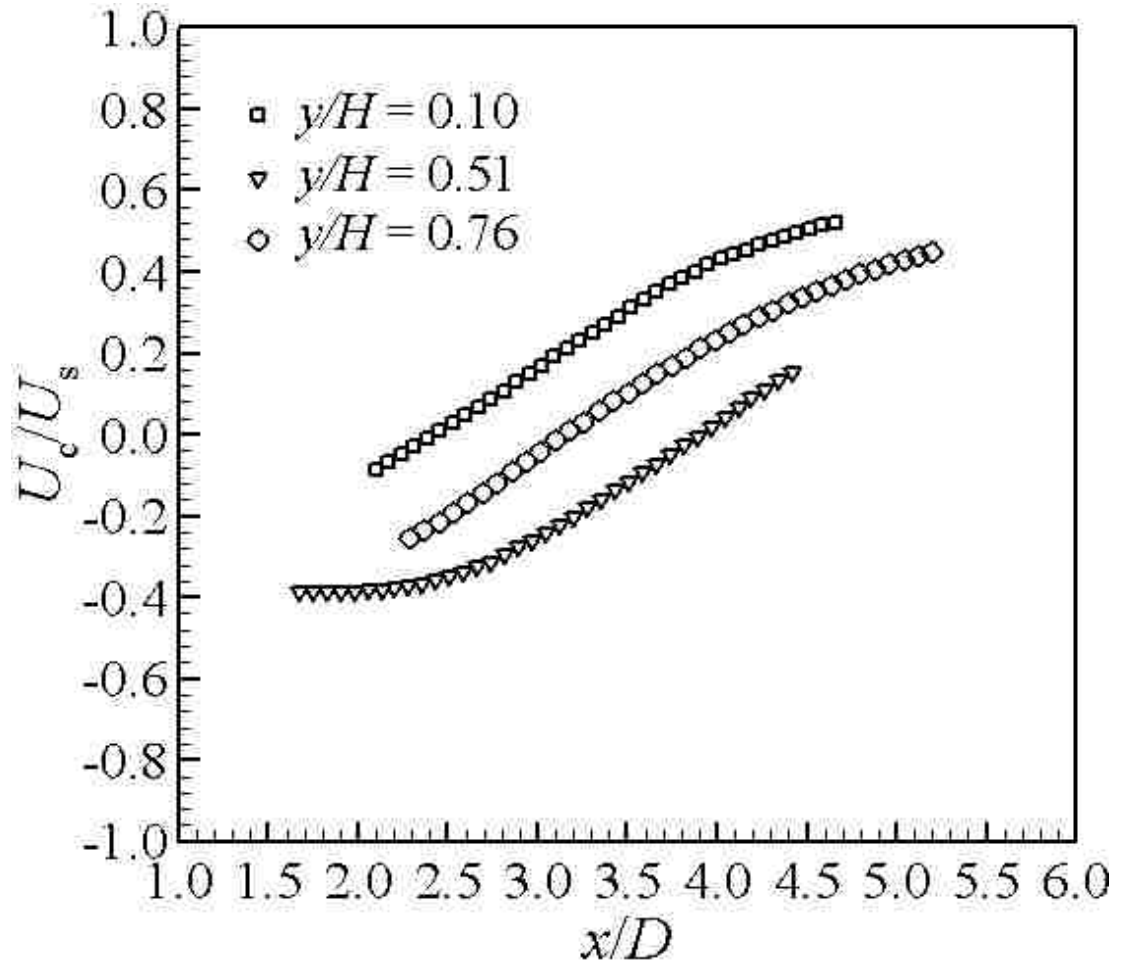
Figure 4.6: Variation of the normalized mean central velocity U_c/U_s with downstream distance.
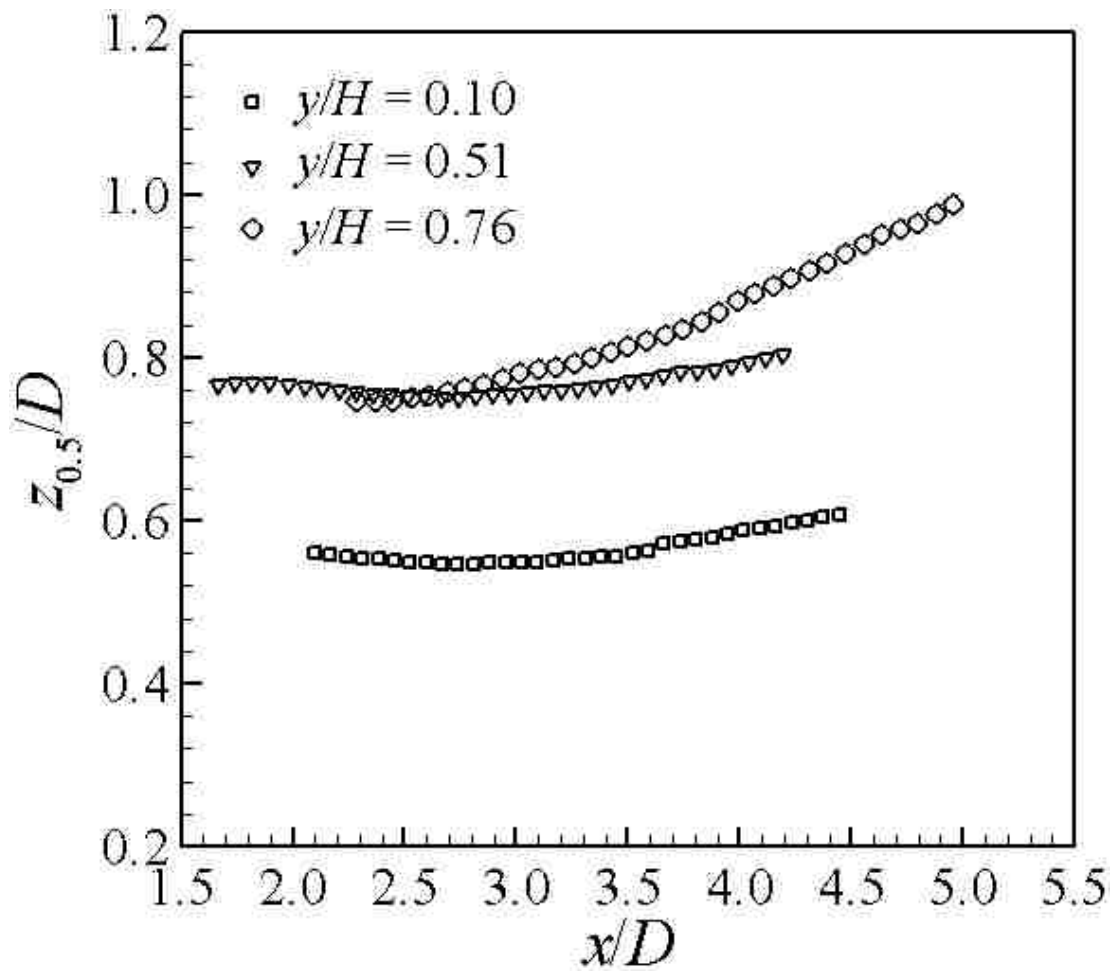
Figure 4.7: Variation of the wake half-width $z_{0.5}/D$ with downstream distance.
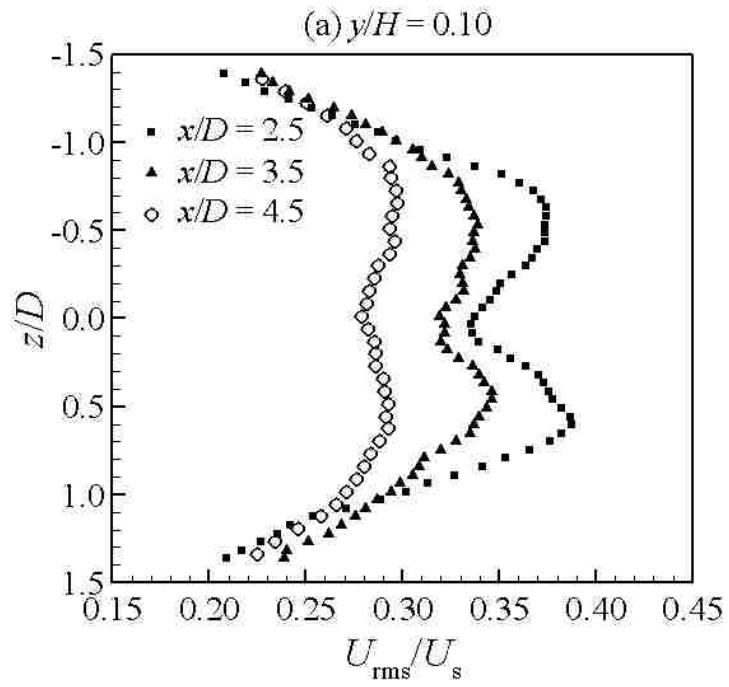
(a) $y/H = 0.10$

Figure 4.8: Development of the relative streamwise root-mean-square velocity U_{rms}/U_s in the normalized streamwise direction for horizontal planes at (a) $y/H = 0.10$, (b) $y/H = 0.51$, and (c) $y/H = 0.76$.

(b) $y/H = 0.51$

$x/D = 2.5$
$x/D = 3.5$
$x/D = 4.5$

(c) $y/H = 0.76$

$x/D = 2.5$
$x/D = 3.5$
$x/D = 4.5$
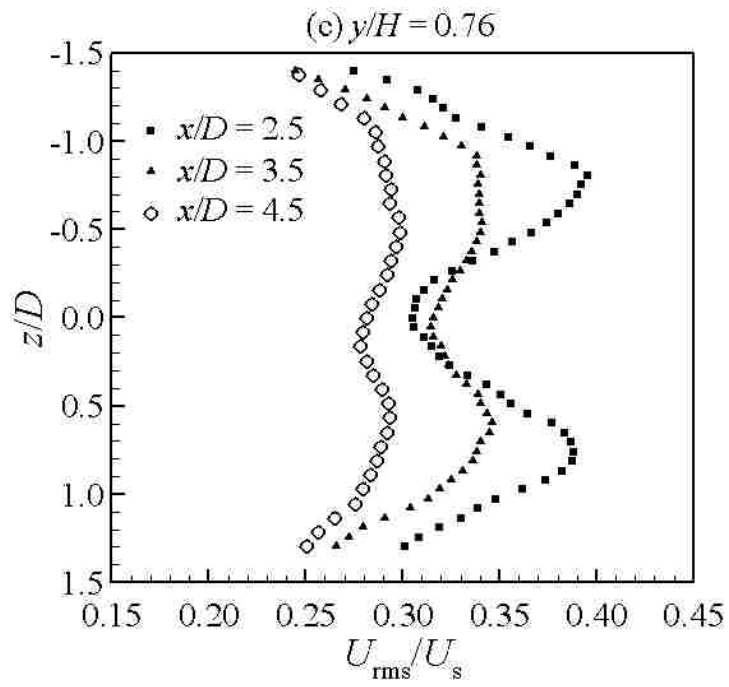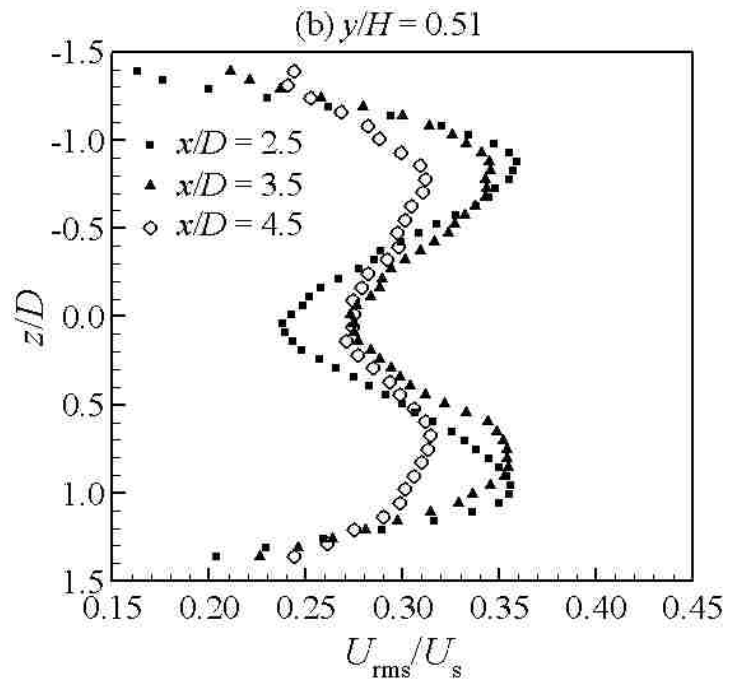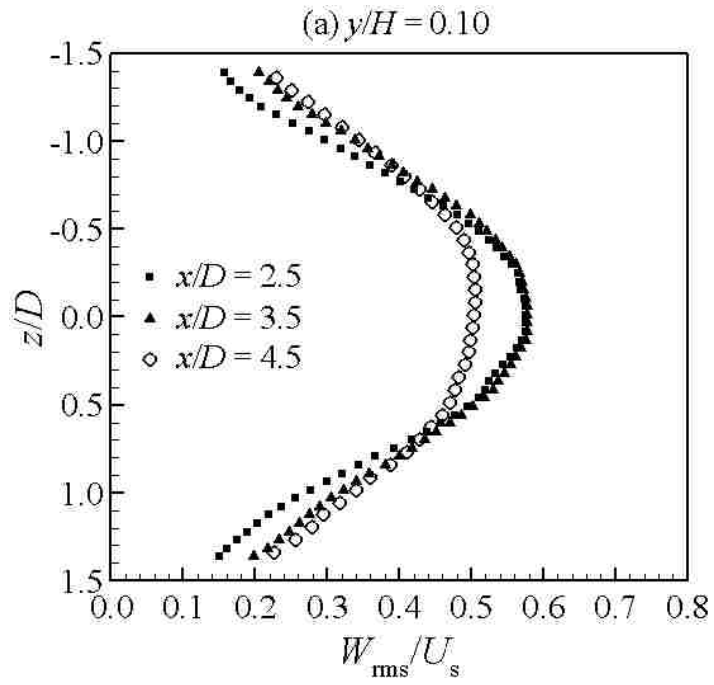
Figure 4.9: Development of root-mean-square transverse velocity W_{rms}/U_s in the streamwise direction for horizontal planes at (a) $y/H = 0.10$, (b) $y/H = 0.51$, (c) $y/H = 0.76$.
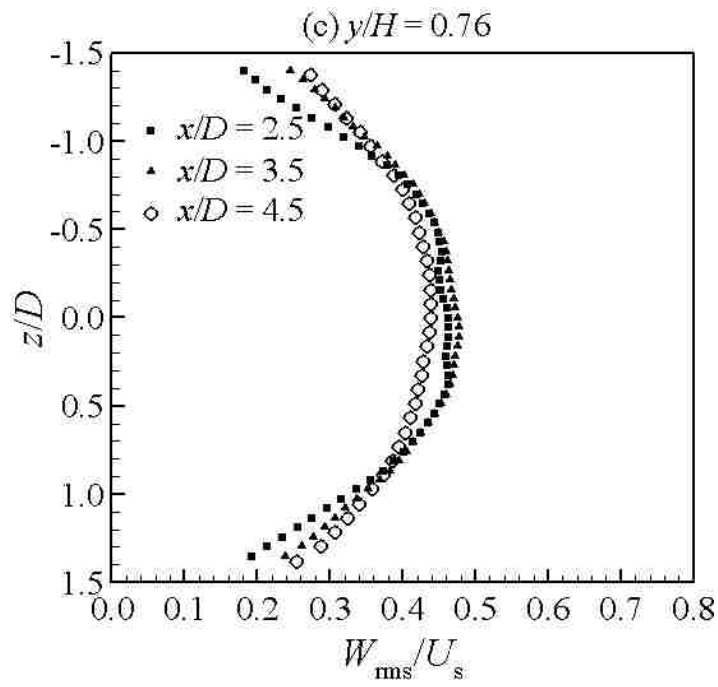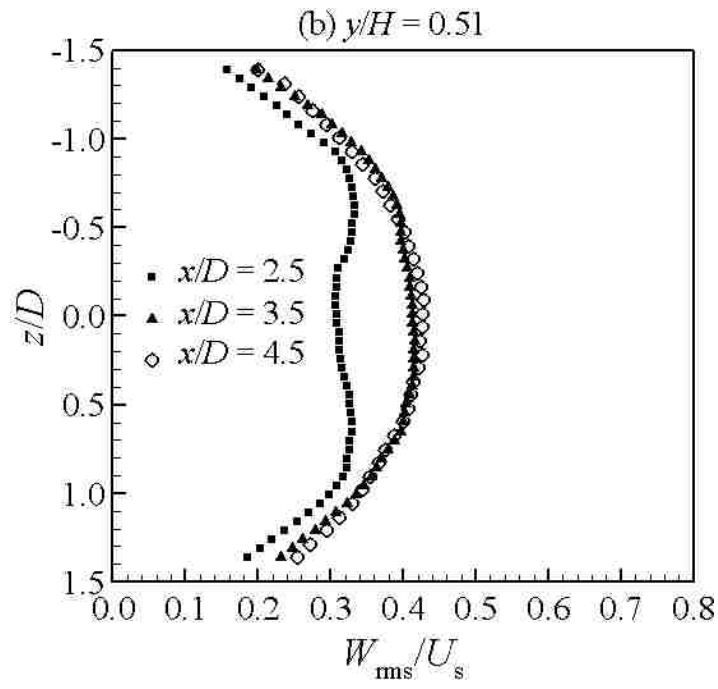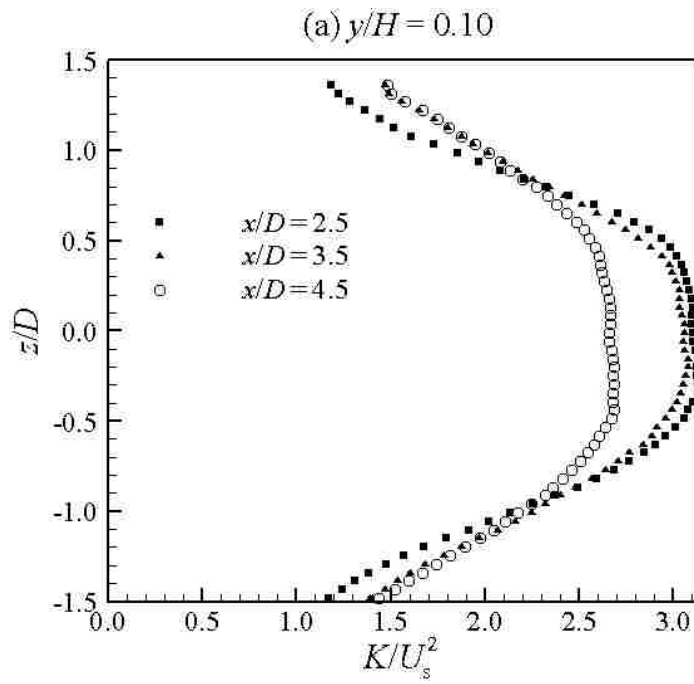
(b) *y/H* = 0.51

(c) *y/H* = 0.76

Figure 4.10: Development of turbulent kinetic energy K/U_s^2 in the streamwise direction for horizontal planes at (a) $y/H = 0.10$, (b) $y/H = 0.51$, (c) $y/H = 0.76$.

(b) $y/H = 0.51$

$x/D = 2.5$
$x/D = 3.5$
$x/D = 4.5$

z/D

K/U_s^2

(c) $y/H = 0.76$

$x/D = 2.5$
$x/D = 3.5$
$x/D = 4.5$

z/D

K/U_s^2

118
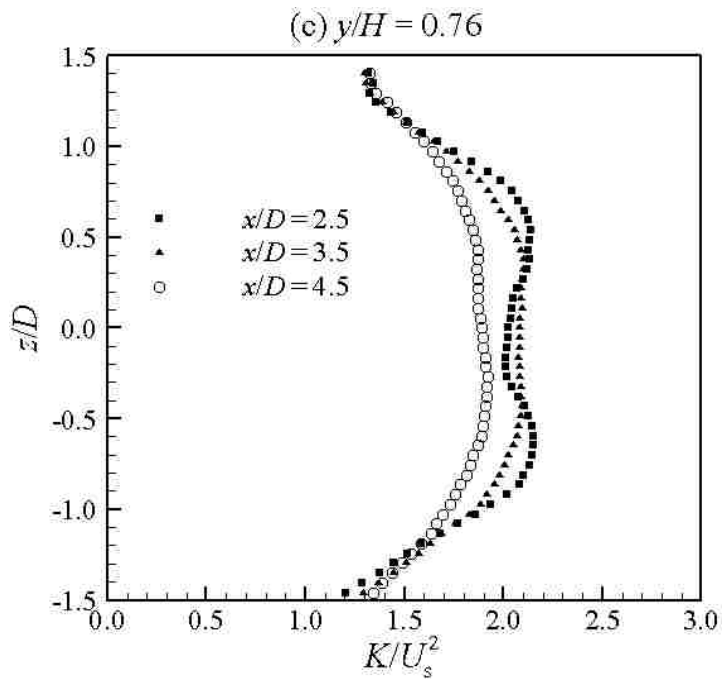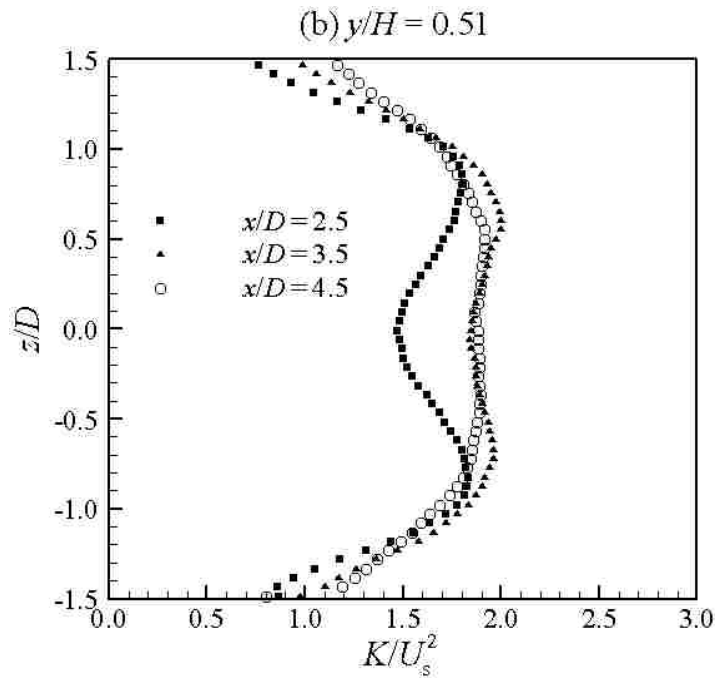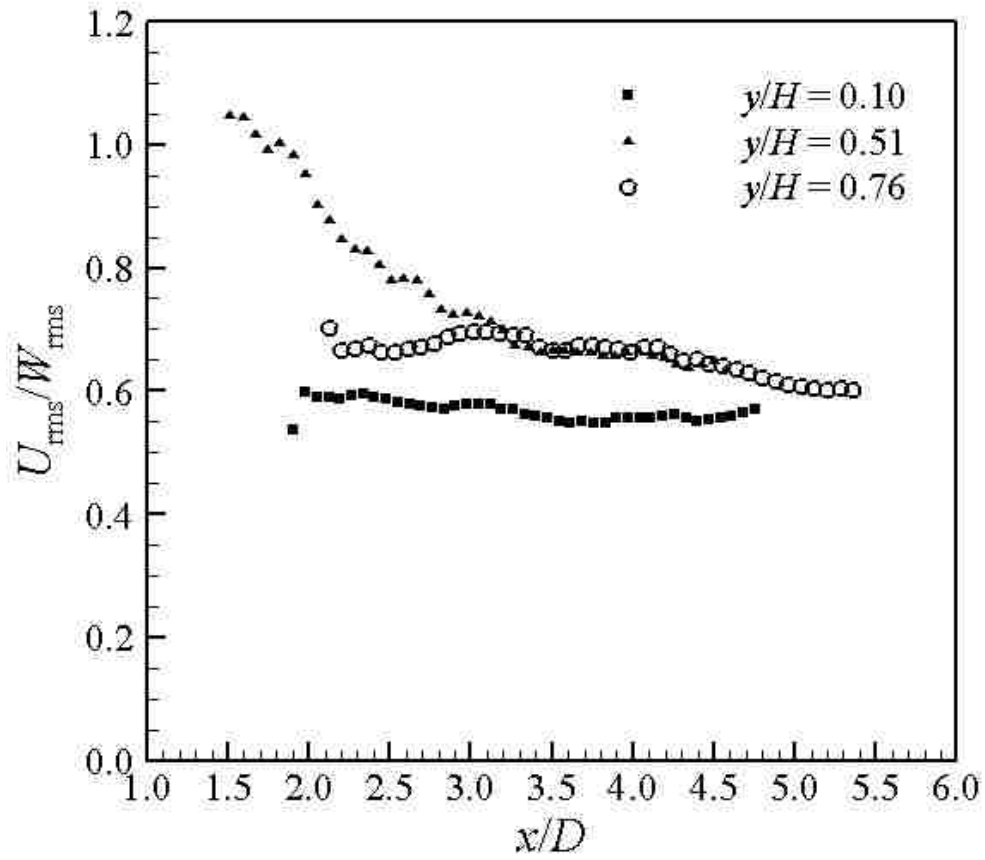
Figure 4.11: Variation of U_{rms}/W_{rms} in the streamwise direction. The three curves were extracted from the three horizontal planes along the vertical central plane ($z/D = 0$).
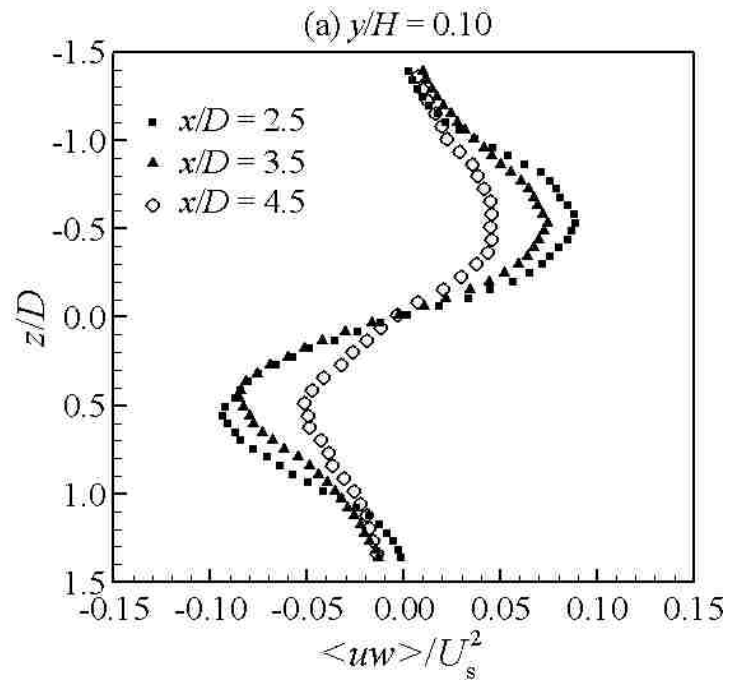
Figure 4.12: Development of Reynolds stress ($<uw>/U_s^2$) in the streamwise direction for horizontal planes at; (a) $y/H = 0.10$, (b) $y/H = 0.51$, (c) $y/H = 0.76$.

(b) $y/H = 0.51$

$x/D = 2.5$
$x/D = 3.5$
$x/D = 4.5$

z/D

$<uw>/U_s^2$

(c) $y/H = 0.76$

$x/D = 2.5$
$x/D = 3.5$
$x/D = 4.5$

z/D

$<uw>/U_s^2$
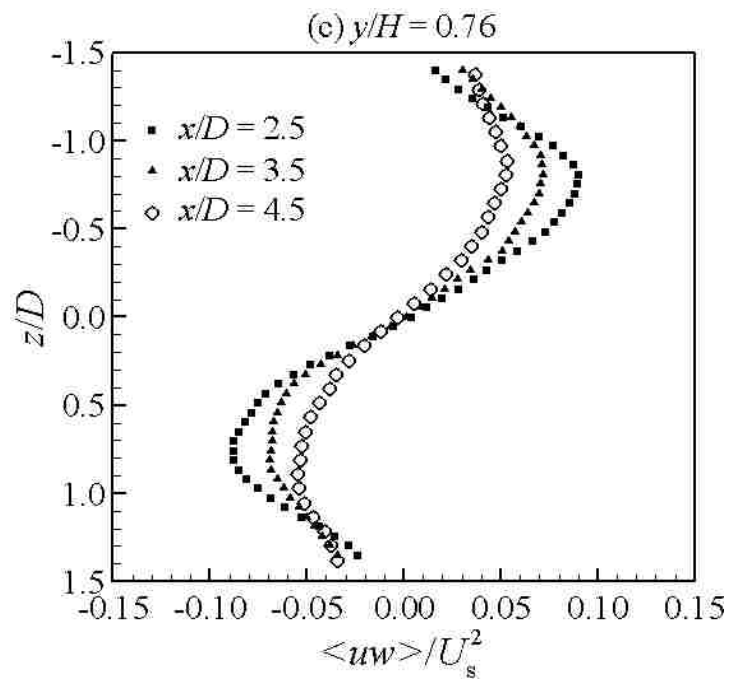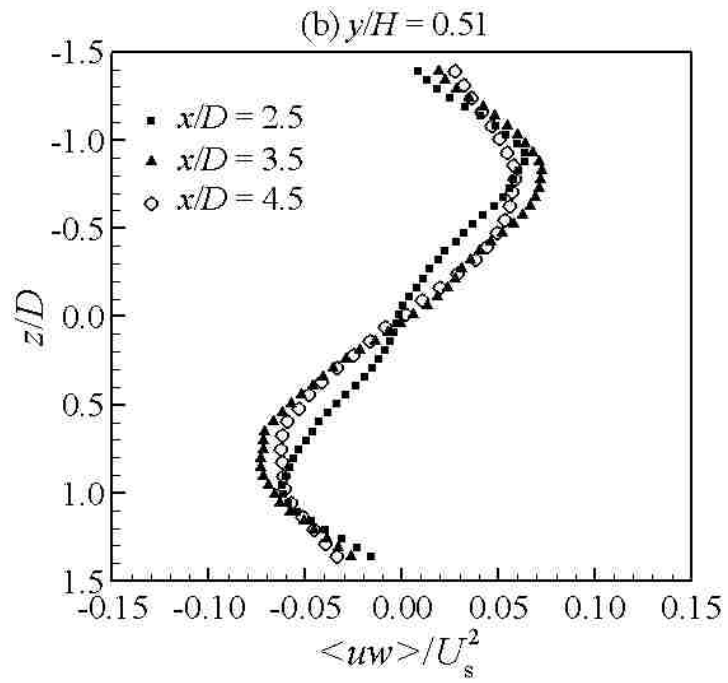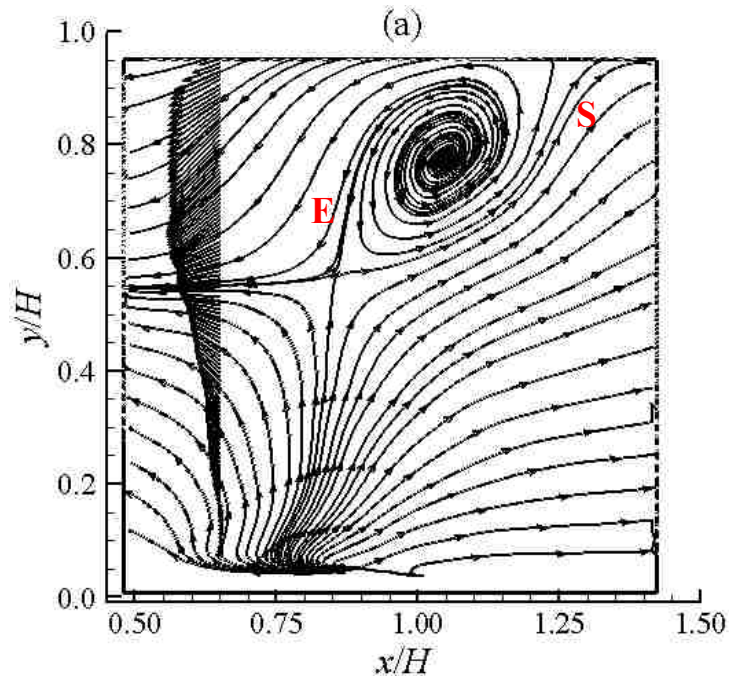
Figure 4.13: Three examples showing coherent structures identified on the mid-vertical plane by the POD technique.

(b)

(c)
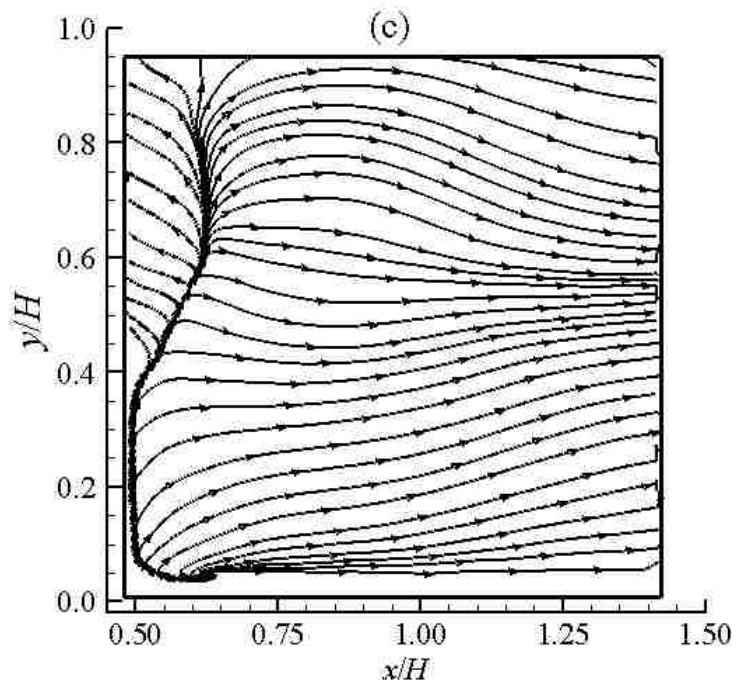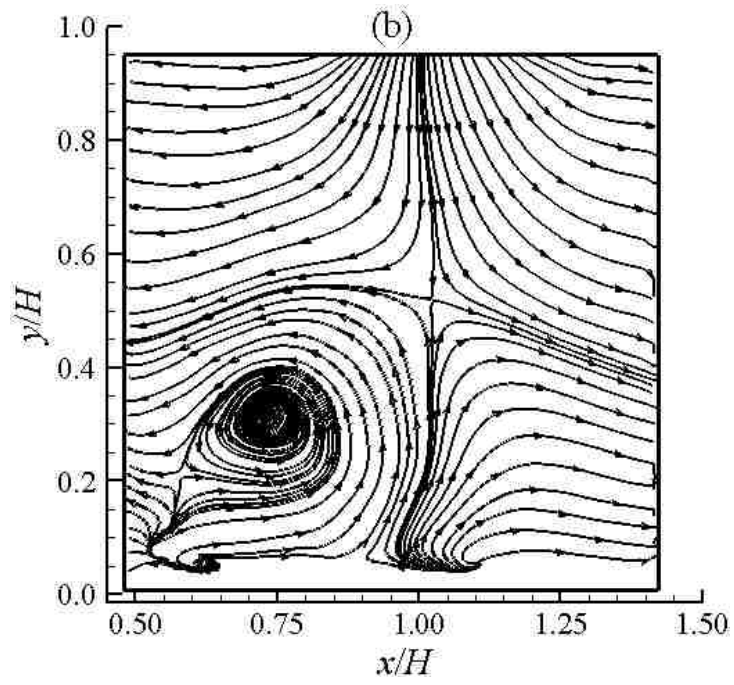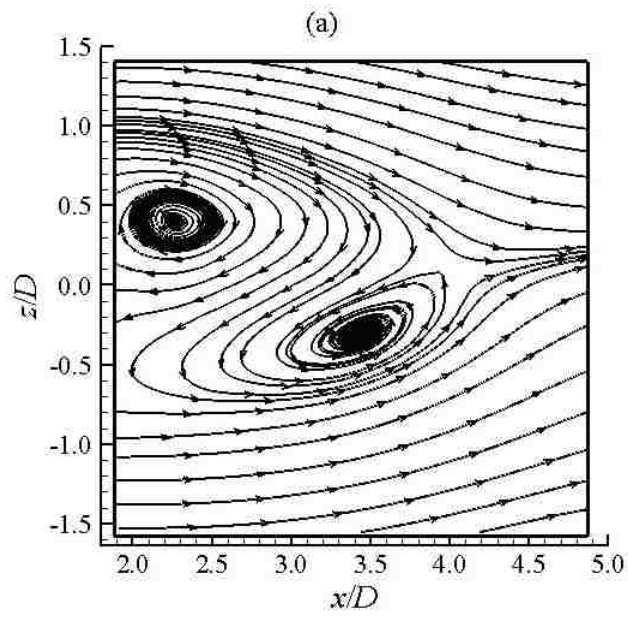
Figure 4.14: Examples of POD-reconstructed instantaneous velocity fields in the horizontal plane at $y/H = 0.10$.

(b)

(c)

125
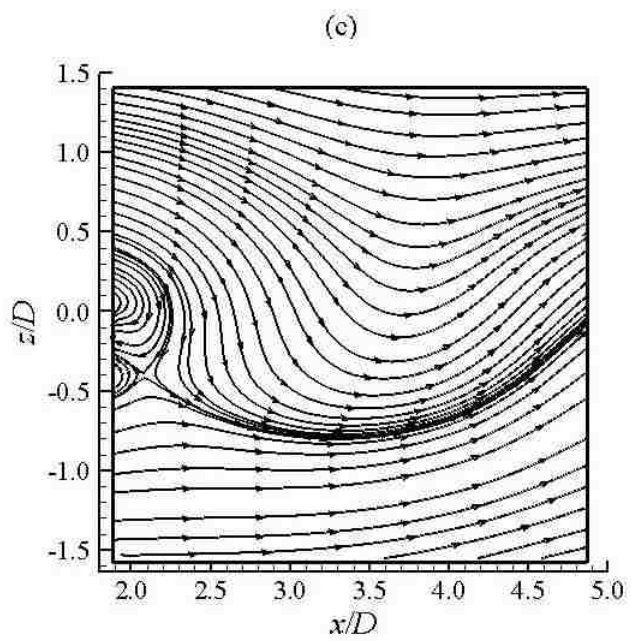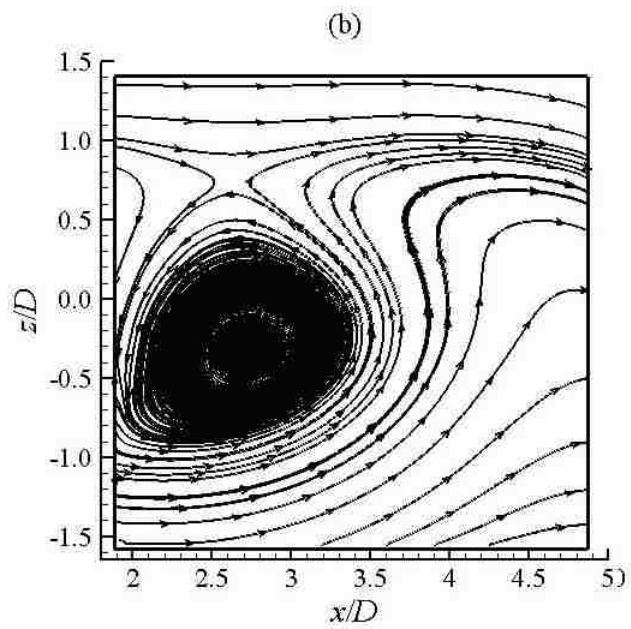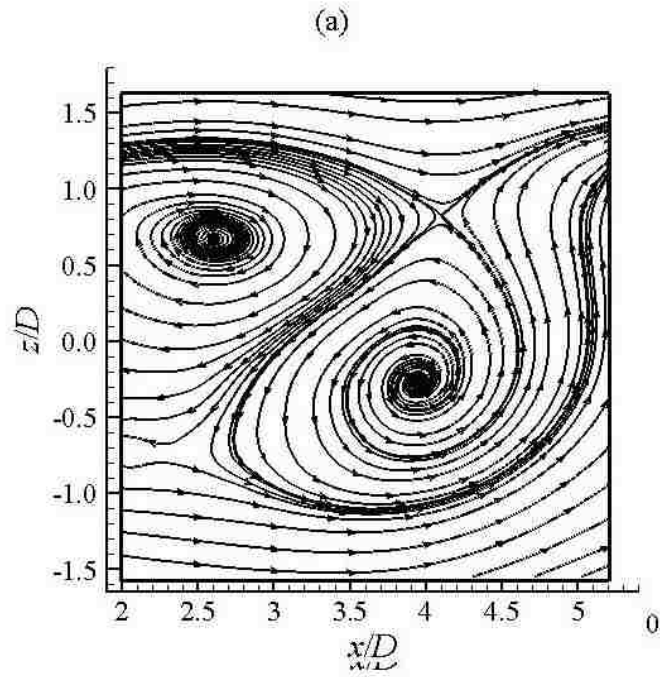
Figure 4.15: Examples of POD-reconstructed instantaneous velocity fields in the horizontal plane at $y/H = 0.51$.

(b)

(c)

127
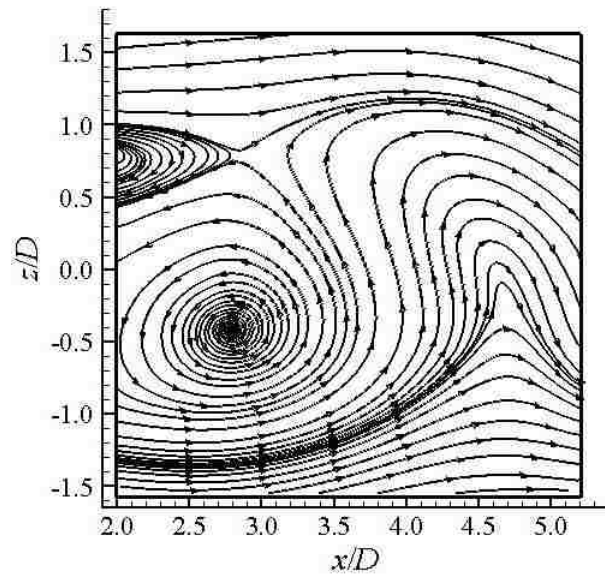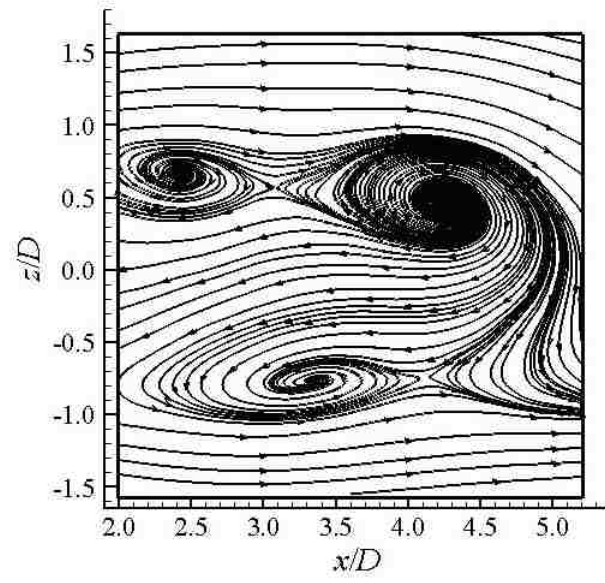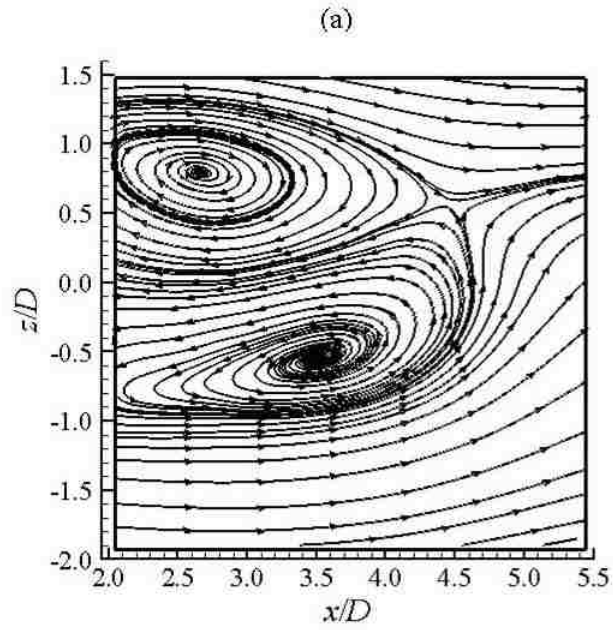
Figure 4.16: Examples of POD-reconstructed instantaneous velocity fields in the horizontal plane at $y/H = 0.76$.

(b)

(c)

129
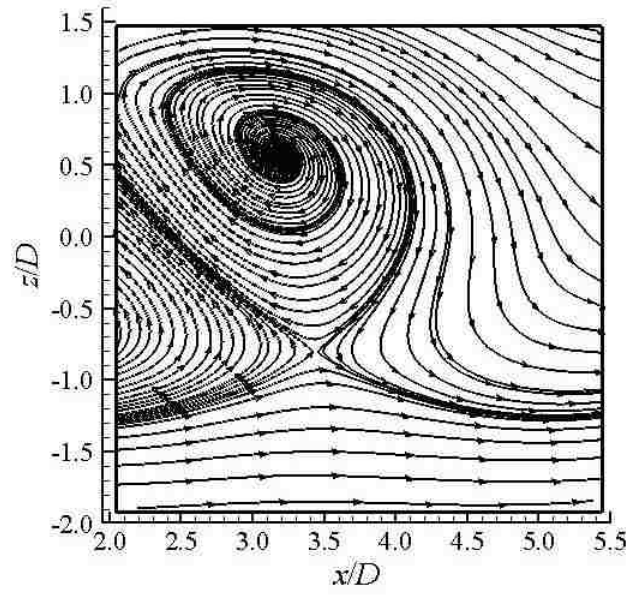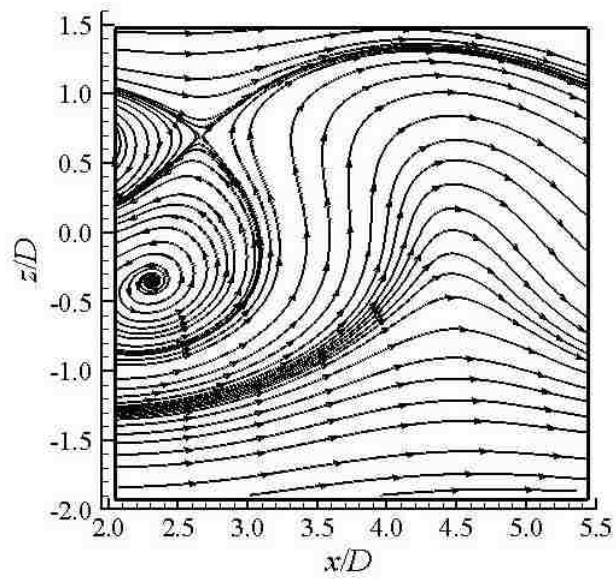
Chapter 5

GLOBAL VIEW OF FLOW PARAMETERS

5.1 General description

This chapter discusses the results obtained from the second set of experiments at a higher Reynolds number and a higher stability number. Unlike Chapter 2, this chapter discusses the flow parameters in a global sense using contour plots. Similar to the previous chapter, the discussion starts with the detail of the approaching flow, followed by the study of the mean flow parameters at different vertical locations. Consistent with the present aim of exposing the vertical variability of the wake flow, only results at the horizontal planes, at different elevations are discussed. Swirling strength analysis was also applied to the PIV dataset to track the variability of the vorticity at different vertical locations.

5.2 Approaching flow

Prior to conducting measurements downstream of the bluff body, measurements were obtained in the channel without the presence of the body to quantify the approaching flow velocity characteristics. The maximum velocity near the free surface was $U_\infty = 0.45$ m/s, and the Reynolds number based on the depth of flow and bluff body width were $Re_H = 45,000$ and $Re_D = 13,450$, respectively.The Froude number, Fr, was 0.45. The flow was turbulent and in the subcritical regime. The boundary layer thickness of the approaching flow is approximated to be 80 mm. The time-averaged velocity profile in the outer and inner coordinates is shown in Figure 4.1, and is compared with the

turbulent boundary layer data of Krogstad & Antonia (1994). The shape parameter of the boundary layer is approximated to be 1.27. In the inset of Figure 4.1, the velocity profile was fitted with the log-law and the friction velocity was computed via the Clauser plot technique (Clauser, 1954). The friction velocity and the skin-friction coefficient were estimated to be 19 mm/s and 0.084, respectively. In addition to the above mentioned measurement of the background flow in the vertical x-z plane, background flow measurements were performed in the horizontal y-z plane also at near-bed, mid-depth and near-surface locations. The time-averaged flow fields in the horizontal planes were fairly uniform over the whole measurement plane. The streamwise and transverse turbulent intensities u_{rms}/U_∞ and w_{rms}/U_∞ were approximately 0.067 and 0.048, respectively, at mid-depth horizontal plane. The value of the mean streamwise velocity from the horizontal plane matches well with the value of streamwise velocity in the vertical plane at the corresponding vertical locations.

5.3 Time-mean description of the flow

5.3.1 Streamwise velocity defect

The development of the streamwise velocity defect $U_{defect} = (U_{upstream} - U(x,y))$ of the wake normalized by the centerline velocity deficit $U_{c,defect} = (U_{upstream} - U(x,0))$ is plotted against the transverse distance, normalized by the local half-width, $z_{0.5}$ (Figure 5.2). The results are only shown at $x/D = 1$ and 5 at the near-bed, mid-depth and near-surface locations to reduce cluttering. The defect velocity profile is also compared with the data of Carmer (2005) and with the self-similar distribution for a deep flow wake.

131

The present data compares well with the experimental data of Carmer, and is reasonably close to the self-similar profile at $x/D = 5$. At any streamwise location, if one moves from the bed towards the free surface, change in the defect velocity profile is not significant. Close to the bluff body (at $x/D = 1$), a top-hat profile is observed at all vertical locations. As one moves from the peak of the velocity deficit towards the outer edge of the wake, the velocity defect attains a minimum value of -0.35 for the case of near-bed location at $x/D = 1$, due to flow acceleration. This value agrees well with the value of -0.36 reported by Tachie & Balachandar (2001) for the case of shallow wake flow behind a flat plate placed perpendicular to the flow.

5.3.2 Time averaged velocity field

The time-averaged velocity fields at the near-bed, mid-depth and near-surface vertical locations are shown in Figure 5.3. These fields were generated by averaging the history of the instantaneous velocity at each grid point for all 2000 snapshots. The presence of the bluff-body creates a pressure disturbance, and consequently, the flow directly approaching the object slows down and accelerates laterally around the body. Directly downstream of the body, a recirculation region is formed and momentum is fed continuously from the outer accelerating flow to the inner recirculation region. The gradual development of the recirculation region is evident in all the fields-of-view. However, the trend is different at different vertical locations. Firstly, the course of development of the transverse width of the recirculating region is different. Near the bed, close to the body, the transverse width of the recirculation region is decreasing monotonically with streamwise distance. At mid-depth, the transverse width decreases at

a slower rate than the near-bed location. Close to the surface, the transverse width increases till $x/D \approx 3.5$ and then starts decreasing. Secondly, close to the body, only at the near-bed location, streamwise directed positive velocity is observed till $x/D \approx 1.5$, and then the reverse flow region commences. For the other two vertical locations, the reverse flow (negative U) starts right after the body. Repeated experiments were performed to verify the existence of the streamwise positive velocity close to the bed, yielding the same result. The existence of this particular distribution of streamwise velocity is also evident in the time-averaged streamline plot of the downstream region of a shallow wake close to the bed in the investigation of Akilli & Rockwell (2002). In their study, a dye visualization technique was used to detect the possible existence of the three-dimensionality of flow downstream of a circular cylinder in a shallow flow. The spread of the dye clearly showed a three-dimensional rollup of the structures from the bed towards the free surface. In a dye visualization study of the fluid-structure interaction between a circular cylinder and a channel bed, Rao et al. (2004) demonstrated the same kind of upward rollup of spanwise vortices and subsequent interaction with the lateral shear layer at the mid-depth location. The streamwise positive velocity is a result of the induced velocity component due to this upward rollup phenomenon.

5.3.3 Instantaneous streamline pattern

The features of the time-averaged velocity can be best interpreted in conjunction with the corresponding time-averaged streamline pattern, shown in Figure 5.4. Once again, for each vertical location, three fields-of-views are combined. Care must be taken in interpreting these streamlines, since they are not actual streamlines, rather 'integrated

streamlines' based on the quasi-two-dimensional assumption of the flow field, as described by Perry and Steiner (1987). According to their kinematic study of the streamline topology, presence of the spiraling pattern in the 'integrated streamlines' indicates a three-dimensional flow, and outward and inward spiraling flow pattern indicates an unstable and stable focus, respectively. Close to the bed, a pair of inward spiraling stable foci at $x/D \approx 1.6$ and a saddle point at $x/D \approx 2.7$ is observed. Together with the saddle point and the foci, they resemble a topological structure, known as the owl face of the first kind (Perry & Steiner, 1987). The pair of foci and saddle point appears at all vertical locations. However, they are displaced downstream with increasing distance from the bed. At mid-depth location, the foci and saddle points are located at $x/D \approx 2$ and 4, respectively, whereas at the near-surface location, they are displaced to $x/D \approx 3.5$ and 5, respectively. It should be noted here that the nature of the foci change from stable, inward spiraling to unstable, outward spiraling from the near-bed to the near-surface location. The existence of the stable, inward spiraling focus was also reported by Akilli & Rockwell (2002), and Sau et al. (2003). In the present study the foci and the saddle points continue to exist at the mid-depth and the near-surface locations. Although Akilli & Rockwell (2002) reported the existence of the owl face of the first kind, they did not mention the location of the saddle point and foci, and therefore no direct comparison can be made with the present study. Interestingly, for the case of a circular cylinder, they identified almost same flow structure at near-bed location with significant positive streamwise velocity between to saddle points originating from the upward flow from the foci.

134

5.3.4 Centreline velocity deficit

The centreline velocity deficit, U_{sc} normalized with the freestream velocity U_s is shown in Figure 5.5. Typical uncertainty bars are included in the figure to indicate the typical uncertainties associated with this parameter. At $y/H = 0.10$, the effect of the positive streamwise velocity in the region $0 \leq x/D \leq 0.5$ is evident in the figure. At this vertical location, in the region $0.5 \leq x/D \leq 2.5$, the centreline deficit velocity increases, indicating a reverse transfer of momentum from recirculation region to accelerating flow region, but the wake starts recovering beyond $x = 2.5D$. At mid-depth, a mild reverse transfer of momentum can be observed for $x/D \leq 2.5$. At all three vertical locations, the wake starts recovering at approximately the same rate after $x/D \approx 2.5$. Beyond $x = 6.5D$, the recovery rate at the near-bed location becomes somewhat constant.

5.3.5 Wake half-width

The growth of the wake can be characterized by the half-width, $z_{0.5}$, which is defined as the transverse location where the mean velocity defect U_{defect} becomes one-half of the centreline velocity deficit $U_{defect,c}$. The downstream development of the wake half-width with the streamwise distance at the near-bed, mid-depth and near-surface vertical locations is shown in Figure 5.6. The shallow wake data of Tachie & Balachandar (2001) does not match exactly with the present data, but follows the same trend and lies within the range of the present data. The Reynolds number for the study of Tachie & Balachandar (2001) was 3900, an order of magnitude lower than the Reynolds number for the present experient. Lin at al. (1995) indicated that increase in the Reynolds number

of flow causes the flow structures downstream of a bluff body to shift in upstream direction. The deviation of the data of Tachie & Balachandar (1995) from the present data can be attributed mainly to the difference in the flow Reynolds number, since the data follows the same trend, but shifted downstream because of the prevailing Reynolds number. Close to the bed, a local contraction of the wake is observed at $x/D \approx 4$, but with increasing distance from the bed, the degree of contraction decreases. At mid-depth, the wake contracts mildly, but at the near-surface location, no contraction is observed. Following the contraction, the wake width increases with streamwise distance like a conventional deep wake. It should be mentioned here that for the case of a conventional deep wake, the wake half-width follows $x^{1/2}$ dependency. The variable degree of contraction of the wake clearly shows the damping effect of the bed friction on the wake half-width and its diminishing characteristic as a function of the distance from the bed. This finding is consistent with the result of Ingram & Chu (1987), that the bed friction arrests the growth of the wake in the transverse direction, thereby reduces the wake half-width. Nagretti et al. (2005) investigated the method of stabilization of a cylinder wake in shallow water by placing roughness element in the bed at the lateral edge of the shear layer as well as at the end of the recirculation bubble of the wake. The increased roughness was found to narrow the lateral extent of the cylinder wake significantly, thereby supporting the present hypothesis of the effect of bed friction.

5.3.6 Entrainment coefficient

The entrainment coefficient characterizes the spread and diffusion of the momentum flux in the transverse direction due to mixing. Following Ingram & Chu

(1987), the entrainment coefficient can be defined as the ratio of the transverse velocity at the transverse location corresponding to wake half-width, normalized by the mean freestream velocity. Figure 5.7 shows the variation of the entrainment coefficient α ($\alpha(x) = w(x,z_{0.5})/U_s$) with streamwise distance x/D. As rightly pointed out by Ingram & Chu (1987), the uncertainty associated with the computed entrainment coefficient can be large (~45 %) because of the smaller magnitude of transverse velocity and these plot should be interpreted carefully. The values of the entrainment coefficients are calculated separately at shear layers on both sides of the body at each downstream position and is averaged to get the representative value. A positive coefficient indicates entrainment into the wake and vice versa. At all vertical locations, the entrainment coefficient increases rapidly till $x/D \approx 4$, and then it starts to decrease. However, in the region $x/D \leq 4$, the entrainment coefficient is the highest at the near bed location, probably because of the fact that the presence of the horseshoe vortex helps to magnify the entrainment process between the wake flow and accelerating flow region. At the far-wake region, the entrainment coefficient tends to become zero asymptotically as the flow deficit decreases.

5.3.7 Turbulent fluctuations

The near-wake contour of the root-mean-square velocity (rms) in the streamwise direction normalized by U_s at the near-bed, mid-depth and near-surface vertical locations are shown in Figure 5.8. The transverse extent of the downstream field is loosely divided into two regions, for sake of discussion, as central ($|z/D| < 0.5$) and shoulder region ($|z/D| \geq 0.5$). From the near-bed to the mid-depth plane, around the shoulder region, the

137

value of u_{rms}/U_s decreases, but it increases mildly from the mid-depth to the near-surface location. The maximum magnitudes of the contours of u_{rms}/U_s always appear around the shoulder of the body and are 0.45, 0.35 and 0.35, respectively, at the near-bed, mid-depth and near-surface locations. Although the maximum value of the contour at the mid-depth and near-surface locations is the same, the contour is spread over a larger x/D. But in the central region downstream of the body, a different trend in the variation of u_{rms}/U_s is observed. As one moves from the near-bed to the near-surface location, the size of the contour u_{rms}/U_s = 0.15 grows, indicating that around the central region downstream of the body, at any particular x/D location, there is a decrease in the streamwise turbulence intensity from the near-bed to the mid-depth and near-surface plane. Also, the transverse locations of the peak magnitude approximately correspond to the location of the lateral shear layer as inferred from the half-width distribution. The contour of transverse root-mean-square velocity (w_{rms}/U_s) shown in Figure 5.9 also exhibits vertical variability. In the central region downstream of the body, between the near-bed and the mid-depth locations, the maximum value decreases. With increasing distance from the bed, any particular contour (e.g., 0.18 or 0.22) gets convected downstream. Around the shoulder region, there is also a slight decrease in magnitude of the transverse rms velocity with increasing distance from the bed.

More insight into the turbulent kinetic energy distribution can be gained by plotting the contour of the total turbulent kinetic energy, $k = \frac{1}{2}\left(\langle u'^2 \rangle + \langle w'^2 \rangle\right)$, where u' and w' indicate fluctuating velocity components in streamwise and transverse

138

directions, and $\langle \; \rangle$ represents time-averaging. The turbulent kinetic energy k is normalized by U_s^2. The contour of distribution at the near-bed, mid-depth and near-surface vertical locations are shown in Figure 5.10. At both the central and shoulder regions, monotonic increase of the magnitude of k/U_s^2 is observed from the near-bed to the near-surface location, but the degree of increase is different. For example, in the central region, the maximum value increases from 0.006 to 0.014 from the near-bed to the near-surface location, resulting in a 133% increase. The corresponding increase at the shoulder region is around 266%. Most interesting is the appearance of the high magnitude contour ($\sim$0.022) in between $2 \leq x/D \leq 3$ and $0.5 \leq |z/D| \leq 1.5$ at the near-surface location. This, in conjunction with Figure 5.8 and Figure 5.9, indicates that the turbulent kinetic energy is correlated in these three planes, and there is a redistribution of the turbulent kinetic energy between different directional components at these locations. For example, in the central region, the magnitude of u_{rms}/U_s and w_{rms}/U_s decreases from the near-bed to the near-surface location, whereas the magnitude of k/U_s^2 increases. Along the shoulder region, the decrease of u_{rms}/U_s and w_{rms}/U_s with distance from the bed is comparable to the decrease at the central region, but the increase of k/U_s^2 is very high compared to the central region. This observation indicates that the turbulent kinetic energy continuously redistributes itself between the streamwise, transverse and vertical components at the near-bed, mid-depth and near-surface vertical locations, and the degree of redistribution is different at different transverse locations. This redistribution of the turbulent kinetic energy was also demonstrated by Singha et al. (2009).

139

Figure 5.11 shows the pattern of the time-averaged vorticity $\omega_z D / U_s$ distribution at the near-bed, mid-depth and near-surface locations. The vorticity distribution is anti-symmetric with respect to the body and is consistent with the nature of shear-layer separation (i.e., positive for $z/D \leq 0$, and negative for $z/D \geq 0$). The length of the shear layer remains same for the near-bed and mid-depth locations (approximately 2.3D), but increases to approximately 2.9D at the near-surface location.

The overall pattern of the Reynolds stress as shown in Figure 5.12 is consistent with the result of Dong et al. (2007) in the near-wake region downstream of a circular cylinder. Mild change of the contour size can be observed from the near-bed to the near-surface location. At the same time the transverse locations of the peak of the Reynolds stress (shown by black dot) change from the near-bed to the near-surface location. At the near-bed location, they are situated at $z/D \approx 0.70$ and -0.78 respectively. At the mid-depth and near-surface locations, they are located at 0.82, -0.95; and 1.19, -1.23, respectively. Another distinguishing pattern is the appearance of the additional Reynolds stress contour (originating from $|z/D| \approx 0.8$ and extends up to $x/D \approx 1.2$ on both sides of the body) at the near-bed location due to the velocity fluctuations associated with the horseshoe vortex. It should be noted here that the sign of the Reynolds stress arising from the flow separation from the sides of the body, and that from the horseshoe vortex, are opposite to each other (the former is positive and later is negative for the case $|z/D| \leq 0$). Due to the horseshoe vortex, the streamwise component of vorticity (ω_x) would be negative for $|z/D| < 0$ and positive for $|z/D| > 0$. The mutually induced velocity close to

the bed would be directed outward from the centerline towards the ambient flow region, and therefore contributes to the opposite signed Reynolds stress. The separating shear layers from the sides of the body induce entrainment velocity and therefore have positive sign for $|z/D| < 0$, and vice versa. It should be mentioned here that the initial reverse transfer of momentum (see Figure 5.7) close to the bed, is probably an effect due to the result of the interaction of the horseshoe vortex with the flow. The additional contour noticed in the near-bed region due to the horseshoe vortex was also reported by Akilli & Rockwell (2002).

5.3.8 Evolution of flow pattern downstream of the bluff body

Based on the observations mentioned above, and with the help of the existing literature, a possible model of flow pattern downstream of the bluff body can be hypothesized. A schematic of the model highlighting the observations is shown in Figure 5.13. The flow is highly three-dimensional and exhibits a complex flow pattern due to the presence of the bed and free surface. Close to the bed, the presence of the horseshoe vortex system can be inferred from the additional Reynolds stress contour in Figure 5.12 and is highlighted in inset (a) of Figure 5.13. One would expect a pair of vortices (clockwise for negative z, and counterclockwise for positive z) close to the bed in the y-z plane due to the presence of the horseshoe vortex. This induces a velocity component pointing out from the centreline towards the ambient flow region very close to the bed. This will contribute towards the reverse transfer of momentum for $x/D \leq 0.5$, as seen in Figure 5.5(a). The presence of this pair of vortices in the y-z plane was experimentally demonstrated by Eibeck (1990) downstream of a circular cylinder and tapered cylinder.

141

He also concluded the presence of two large vortices (counterclockwise for negative z, and vice versa) in the streamwise vertical plane (y-z plane behind the body) inducing an upward flow along the center of the body. It is possible that the horseshoe vortex legs get dissipated prior to $x/D \approx 4$, but the large vortex pair remains. In the absence of a horseshoe vortex, the induced velocity because of the remaining vortex pair (counterclockwise for negative z, and vice versa) will contribute towards the contraction of the wake width at $x/D \approx 4$, as seen in Figure 5.6. Along the centreline downstream of the body at the near-bed location, flow goes towards the near-bed saddle point (see Figure 5.4 and inset (b) of Figure 5.13) and then directed away from the centreline upwards and in the transverse direction. Cohn & Koochesfahani (1989) reported the occurrence of an axial flow from the bed towards the free surface through the core of the vortex. Following the trend of the locations of the focus of instantaneous streamline topology in Figure 5.4, it can be concluded that this axial flow may not travel perpendicular to the bed, but at an angle. The upward flow reaches the free surface and, together with the sweep and ejection-like events at the surface (Singha et al. 2009) and the surface currents (Maheo, 1999), transfers the turbulent kinetic energy from this upward velocity component to the transverse and streamwise components. The surface currents, as pointed out by Maheo (1999), comprise of streamwise surface-parallel vortex structures at the near-surface vertical location. Streamwise structures of positive vorticity (counterclockwise if seen in negative x direction in y-z plane downstream of the body) originates for $z/D < 0$ and clockwise (if seen in negative x direction in y-z plane downstream of the body) structures appear at the $z/D > 0$ side. The mutually induced

outwardly directed velocity component from the wake towards the accelerated flow region is believed to contribute towards the widening of the wake width at the near-surface vertical location (see inset (c) of Figure 5.13). A schematic plot of the model flow pattern was indicated in Figure 5.13(b).

5.3.9 Swirling strength analysis

In an effort to study the vortex population and statistics, vortex identification and extraction from the instantaneous flow fields were carried out using a swirling strength analysis. Swirling strength analysis is a tool which can be utilized to identify vortical structures in a given flow field by computing the velocity gradient tensor T and its eigenvalue. Zhou et al. (1999) showed that the imaginary part of the eigenvalue (λ_i) of the local velocity gradient tensor quantified an embedded vortex in a given flow field. The advantage of swirling strength is that it is frame-independent since it uses the velocity gradient to identify local swirling motion. Also, it does not identify regions like shear layers, which may contain significant vorticity, but does not necessarily contain a vortex. The method is summarized as follows. The velocity gradient tensor of the present two-dimensional flow field can be computed as

$$T = \begin{bmatrix} \dfrac{\partial u}{\partial x} & \dfrac{\partial u}{\partial z} \\ \dfrac{\partial w}{\partial x} & \dfrac{\partial w}{\partial z} \end{bmatrix}. \tag{5.1}$$

The gradient terms were computed using a central differencing scheme, and only the imaginary part of the complex-conjugate eigenvalue was retained. Since, the original

swirling strength (λ_i) does not contain the information of the sense of rotation, it was multiplied with the sign of the local vorticity as follows,

$$\lambda_i(x,z) = \lambda_i(x,z)\frac{\omega_z(x,z)}{|\omega_z(x,z)|} \;; \tag{5.2}$$

where $\omega_z(x,z)$ is the instantaneous vorticity in the z-direction.

Figure 5.14 shows an example of the near-bed plane instantaneous and fluctuating velocity field, with the signed swirling strength contour superimposed. Dark shade represents positive swirling strength, while grey shade represents negative swirling strength. The advantage of the swirling strength technique is obvious from these plots. Being Galilean invariant, this technique yields the same result while applied to either instantaneous or fluctuating flow field. Also, it does not identify non-vortex regions which may contain significant vorticity (like the shear layer). For $z/D \le 0$, positive patches of swirling strength are observed to be dominant which is consistent with the sign of separation of the shear layer from the side of the body.

After calculating the signed swirling strength at each grid point of each snapshot, the fraction of time with positive ($T_{\lambda+}$), negative ($T_{\lambda-}$) and zero swirling strength is computed for each field-of-view and normalized by the total number of snapshots i.e., 2000. The transverse distributions of the fraction of positive and negative swirling strength at the near-bed, mid-depth and near-surface vertical locations at a few streamwise locations (x/D = 1, 3, 5 and 9) are shown in Figure 5.15 and Figure 5.16, respectively. At all vertical and streamwise locations, the peak of $T_{\lambda+}$ remains at $|z/D| < 0$,

and the peak of $T_{\lambda-}$ remains at $|z/D| > 0$. Therefore, the nature of the vortex shedding is not affected by the proximity to the bed, or the free surface. At any particular x/D, the distribution of $T_{\lambda+}$ and $T_{\lambda-}$ are almost mirror images of each other. Table 5.1 summarizes the approximate magnitude and the corresponding locations of the peaks of the time fraction of positive and negative swirling strengths. It is obvious from Table 5.1 that the magnitude of the peak does not change as a function of distance from the bed. However, the transverse location (z/D) of the peak changes at the near-bed, mid-depth and near-surface locations. From the bed towards the free surface, the transverse location of the peak shifts towards the outer accelerated flow region, except at streamwise locations close to the body ($x/D = 1$). This trend is consistent with the nature of vertical variability of the wake half-width. This is due to the fact that at any particular streamwise location, the major contribution of the swirling strength comes from the induced entrainment/ejection mechanism related to the separating shear layers from the sides of the body.

Furthermore, it may be useful to extract the information of the 'mean eddy' contributing towards the swirling strength on both sides of the body. The 'mean eddy' was found by conditionally averaging the swirling strength information from all 2000 snapshots. A threshold criterion was set for the identification of the vortex boundary as $|\lambda(x,z)| \geq 1.7\lambda_{rms}$. The choice of the threshold is somewhat subjective and iterative. Wu & Christensen (2006) had chosen a threshold of 1.5 for the identification of hairpin vortices in a turbulent boundary layer type of flow. In the present study, a range of

thresholds were attempted until the mean eddy became prominent in the conditional flow field.

Each instantaneous field is divided into positive and negative fields as follows:

$$\lambda_{pos}(x,z) = \lambda(x,z)$$
$$u_{pos}(x,z) = u(x,y) \; ; \qquad \text{if } \lambda(x,z) > 1.7\lambda_{rms} \; ; \qquad (5.3)$$
$$w_{pos}(x,z) = w(x,z)$$

or

$$\lambda_{neg}(x,z) = \lambda(x,z)$$
$$u_{neg}(x,z) = u(x,y) \; ; \qquad \text{if } \lambda(x,z) < -1.7\lambda_{rms} \; . \qquad (5.4)$$
$$w_{neg}(x,z) = w(x,z)$$

After using the aforementioned threshold, the negative and positive field was divided by the number of negative and positive signed swirling strength, respectively, at that particular grid point. The resulting positive mean eddy at the near-bed, mid-depth and near-surface locations is shown in Figure 5.17, respectively. The same for the resulting negative mean-eddy is shown in Figure 5.18. The location of the positive and negative mean eddy is in accordance with Figure 5.14. Close examination of the mean eddy leads to the following conclusions. Firstly, any particular contour (say e.g., +/- 300), grows in size as one moves from the bed towards the free surface. This is a consequence of the bed friction which opposes the spatial growth of vorticity contour and dissipates them faster at near-bed locations. Secondly, all the contours show a tendency of tilting towards the outer ambient flow region, with increasing distance from the bed. Thirdly, the contour of positive and negative conditioned eddy is found to be nearly symmetric,

indicating the fact that bed friction does not affect the nature of vortex shedding from the sides of the body.

The distribution function of the probability of appearance of the signed swirling strength along the centre, right ($z/D < 0$) and left ($z/D > 0$) behind the bluff-body are shown in Figure 5.19. Close to the bed, the swirling strength data is extracted from (0. 5D, 0), (0. 44D, 0. 8D) and (0. 44D, -0. 9D) locations. At the mid-depth and near-surface planes, the corresponding locations are (0. 5D, 0), (0. 48D, 0. 9D), (0. 37D, -0. 73D); and (0. 5D, 0), (0. 49D, 0. 95D), (0. 49D, -0. 82D), respectively. The locations of these points are shown as black dots in Figure 5.11, and they roughly correspond to the centreline, right and left shear layers. The probability of appearance of zero swirl strength at the central, left and right shear layers at the near-bed, mid-depth and near-surface vertical locations are 0.7, 0.8, 0.6; 0.68, 0.56, 0.56; and 0.69, 0.57, 0.62, respectively. These values are not represented in Figure 5.19. Also, the appearance of the zero swirling strength is not important from the perspective of the present study. At all vertical locations, most of the smaller, non-zero swirling strength are concentrated around the centre of the wake. However, the probability of finding smaller, non-zero swirling strength decreases with increasing distance from the bed. The range of the magnitude of the swirling strength is smaller at the near-bed location compared to mid-depth and near-surface locations. The bed friction helps to dissipate the vorticity rapidly close to the bed, and therefore the peak value of swirling strength remains low at the near-bed location. This is in accordance with the finding of Lin et al. (2003), who reported faster dissipation of vorticity for the shallow wake case, compared to the deep flow wake. The

range of the signed swirling strength magnitude is decreasing mildly from the mid-depth to the near-surface location. This is probably due to the appearance of structures parallel and close to the free surface, as found by Logory et al. (1996). The origin of these structures may contribute to the reduction of the swirling strength magnitude close to the free surface.

5.4 Conclusions

In this work, particle image velocimetry measurements are conducted to reveal the three-dimensionality of a wake, behind a sharp-edged bluff body immersed in shallow channel flow. The measurements were conducted up to $x = 10D$, at near-bed, mid-depth and near-surface vertical locations. The salient features can be summarized as follows:

- Although the stability parameter of the wake is small, there exists considerable effect of the bed friction and free surface on the wake flow. This is due to the fact that the background flow is maintained at a sufficiently shallow condition.

- The defect velocity profile does not reflect significant vertical variability. But the effect starts to appear in the axial development of the recirculation region downstream of the bluff body. The time-averaged shape of the recirculation region is found to depend on the distance from the bed. The 'instantaneous streamline' pattern is found to be unique at near-bed location and changes as a function of the distance from the bed. The recovery characteristic of the wake flow, quantified in terms of the centreline defect velocity, shows vertical variability of the aforementioned flow.

- The bed friction is found to arrest the transverse growth of the wake, and therefore reduces the half-width close to the bed. However, the damping effect of the bed weakens with increasing distance from the bed.

- Throughout the flow depth, signature of energy redistribution in the streamwise and transverse direction is evident in the contour plot of turbulent parameters. Additional contours of Reynolds stress close to the body at near-bed location appears because of the presence of the horseshoe vortex. The bed friction is also found to dissipate vorticity close to bed.

- Signed swirling strength is used to identify vortices from the instantaneous snapshots. The presence of the bed or free surface does not affect the nature of vortex shedding from the sides of the body. In addition to this, the fraction of time of appearance of positive and/or negative vorticity does not exhibit signs of vertical variability. However, the conditionally averaged mean eddy was found to be affected by the shallowness of the flow. The probability of finding larger swirling strength decreases close to the bed, probably due to the dissipative characteristic of the bed friction.
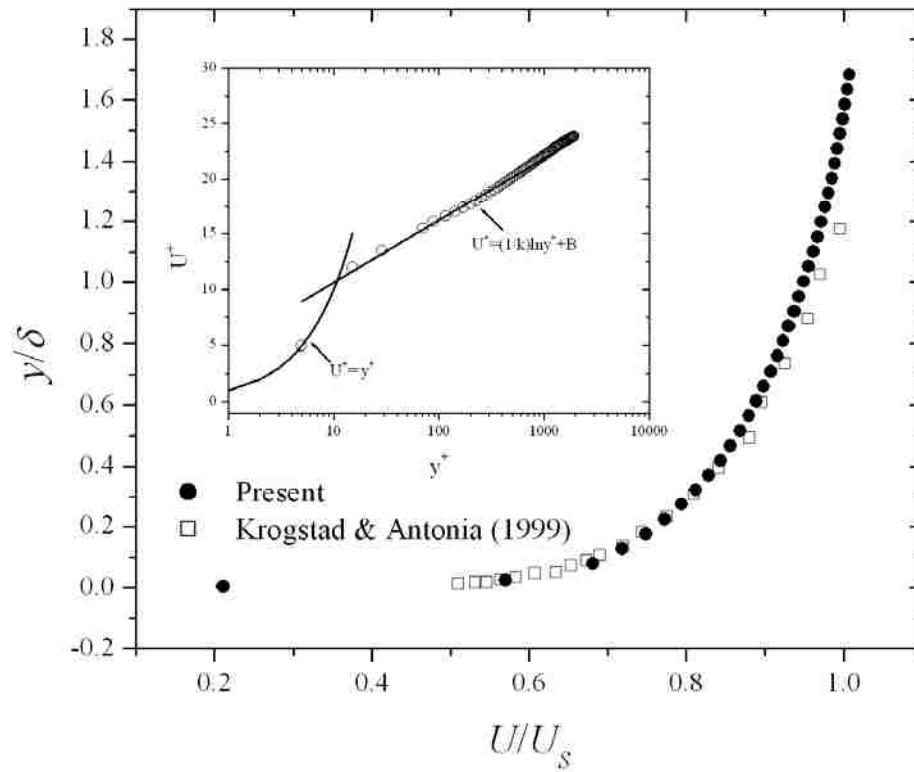
Figure 5.1: Mean streamwise velocity distribution of the approaching flow in the inner (inset) and outer coordinates. The solid lines in the inset correspond to the theoretical velocity profile at the viscous sublayer and logarithmic region of turbulent boundary layer.
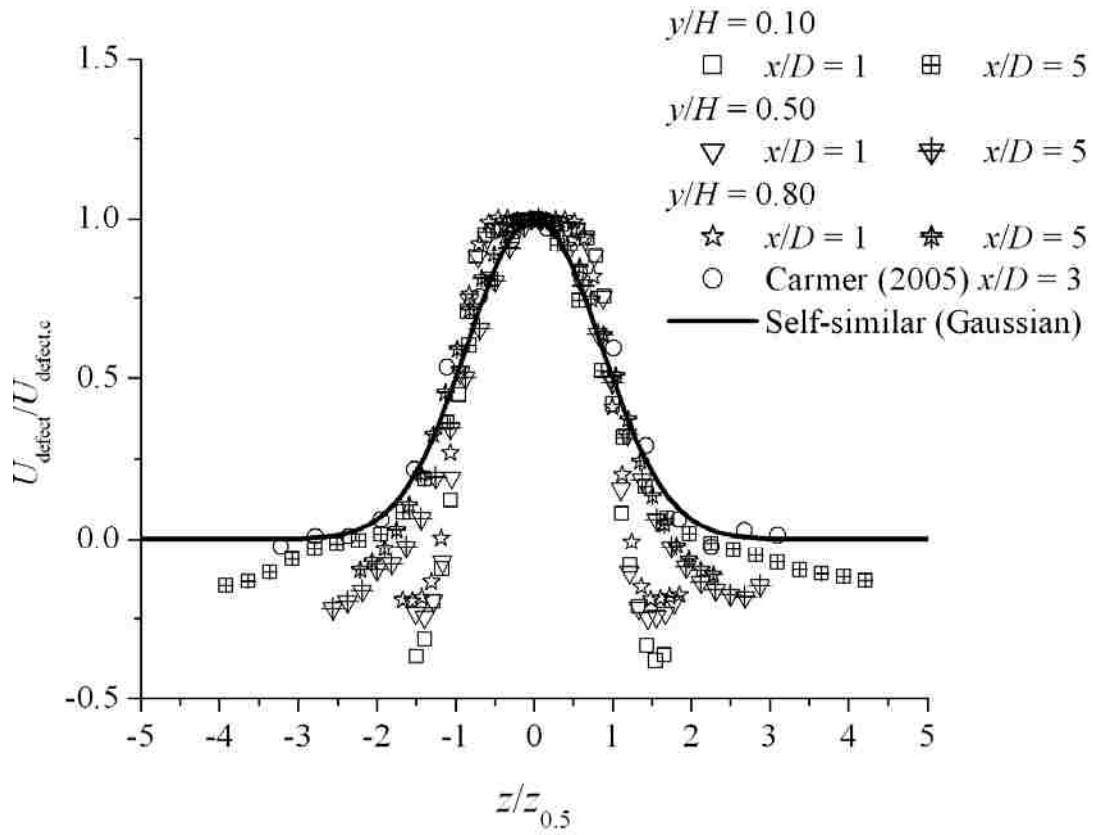
Figure 5.2: Transverse distribution of the streamwise velocity defect at near-bed (y/H = 0.10), mid-depth (y/H = 0.50) and near-surface (y/H = 0.80) vertical locations at streamwise distances x/D = 1 and 5, respectively from the trailing edge of the bluff body.
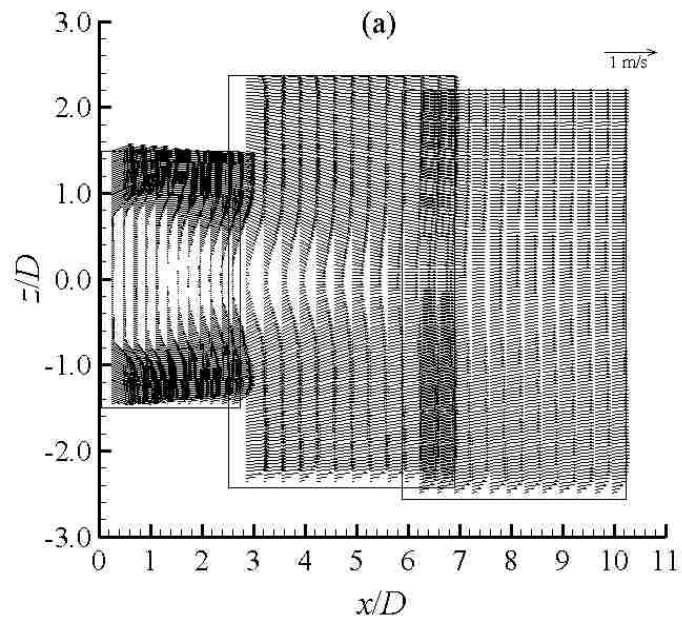
Figure 5.3: Time-averaged velocity field downstream of the bluff-body at (a) near-bed (y/H = 0.10), (b) mid-depth (y/H = 0.50) and (c) near-surface (y/H = 0.80) vertical locations. The unit reference vector is shown on top right.

(b)

(c)

153
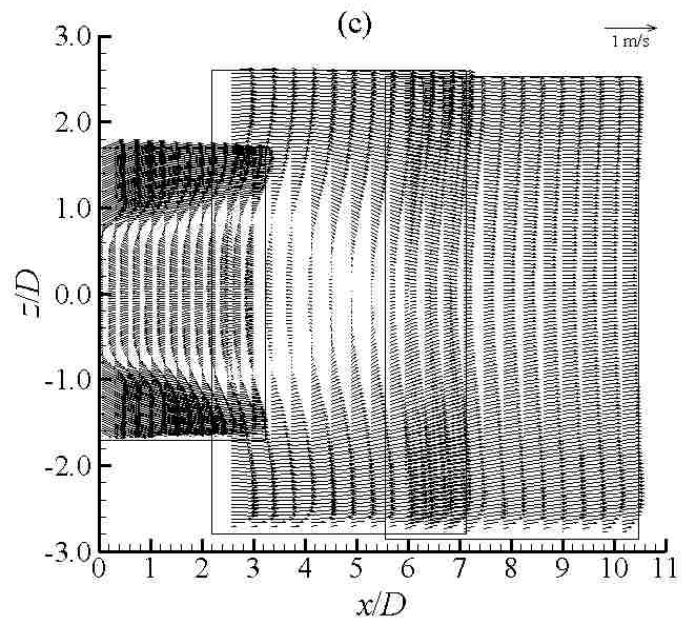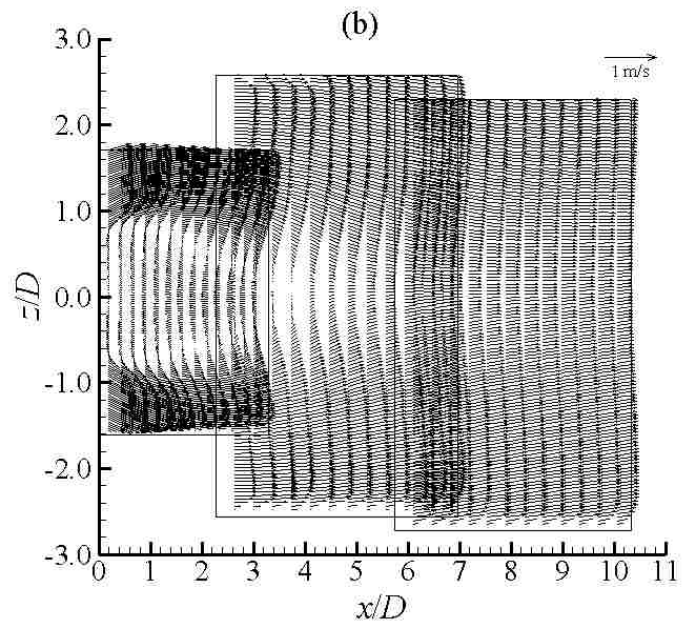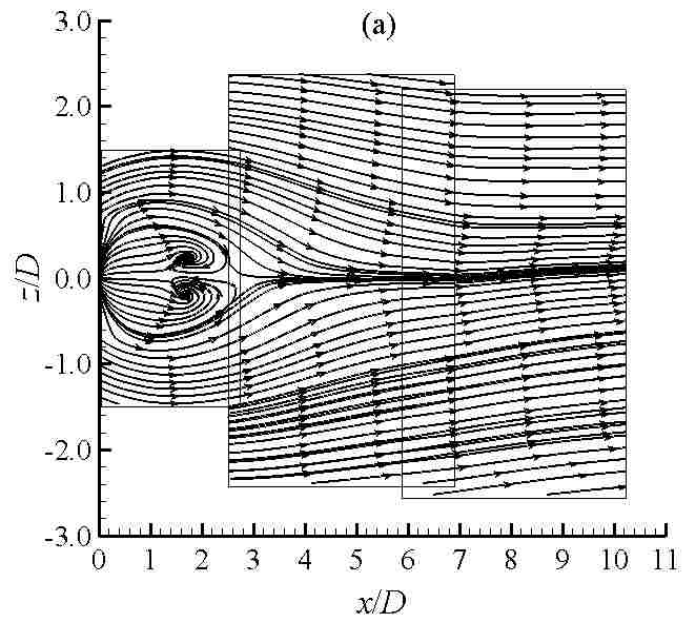
Figure 5.4: Time-averaged instantaneous streamline topology downstream of the bluff body at (a) near-bed (*y*/*H* = 0.10), (b) mid-depth (*y*/*H* = 0.50) and (c) near-surface (*y*/*H* = 0.80) vertical locations.

(b)

(c)

155
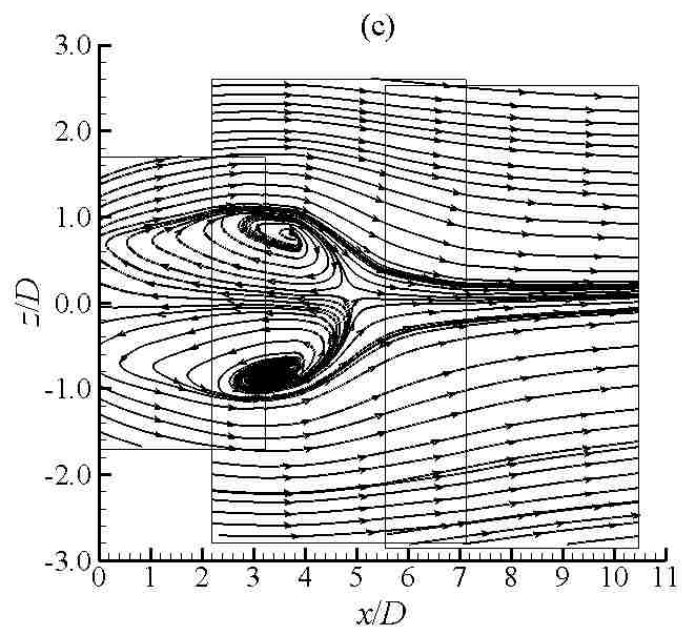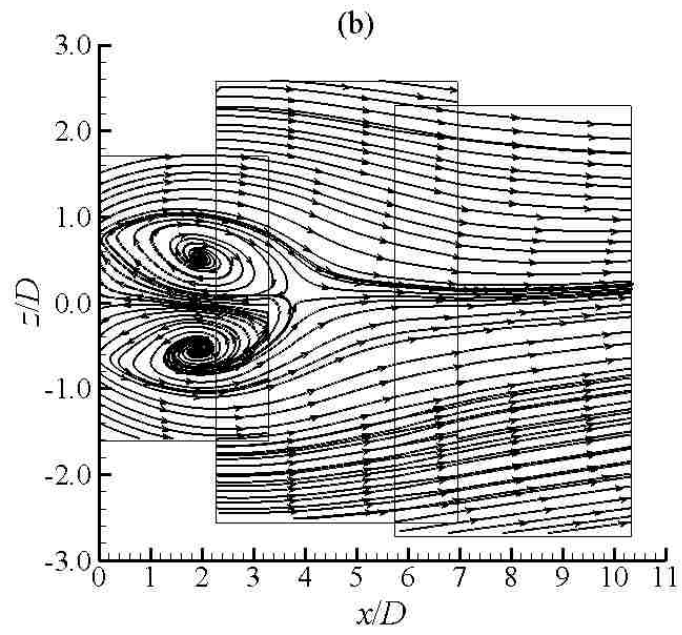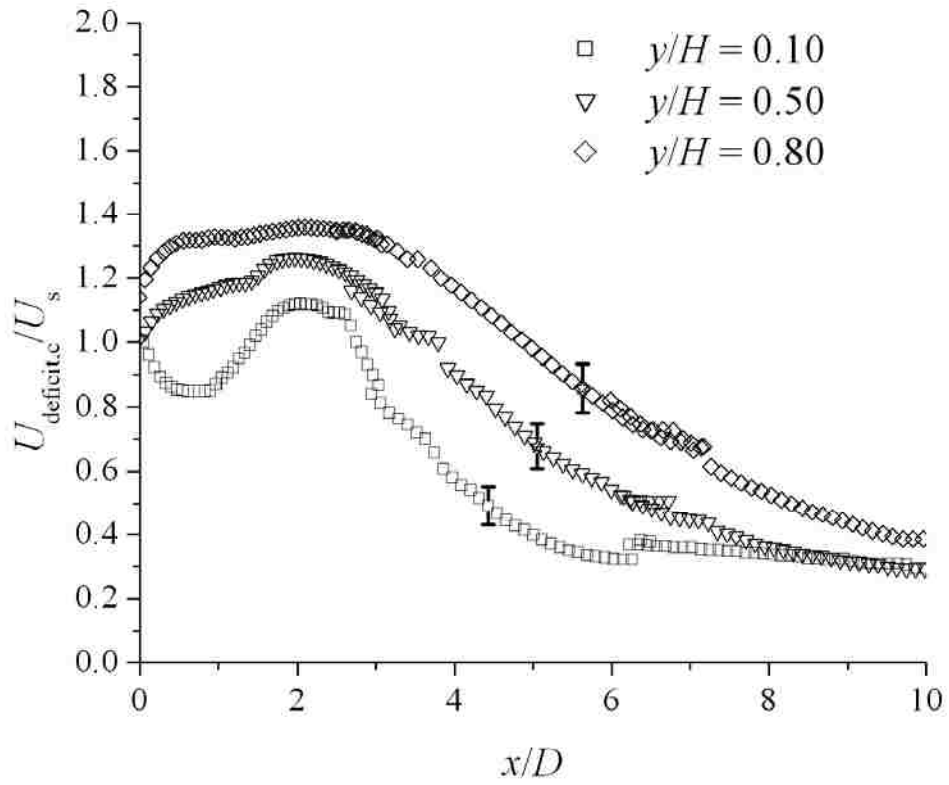
Figure 5.5: Downstream evolution of the centreline velocity deficit (U_{sc}) normalized by the freestream velocity (U_s) with the streamwise distance x/D, at near-bed ($y/H = 0.10$), mid-depth ($y/H = 0.50$) and near-surface ($y/H = 0.80$) vertical locations.
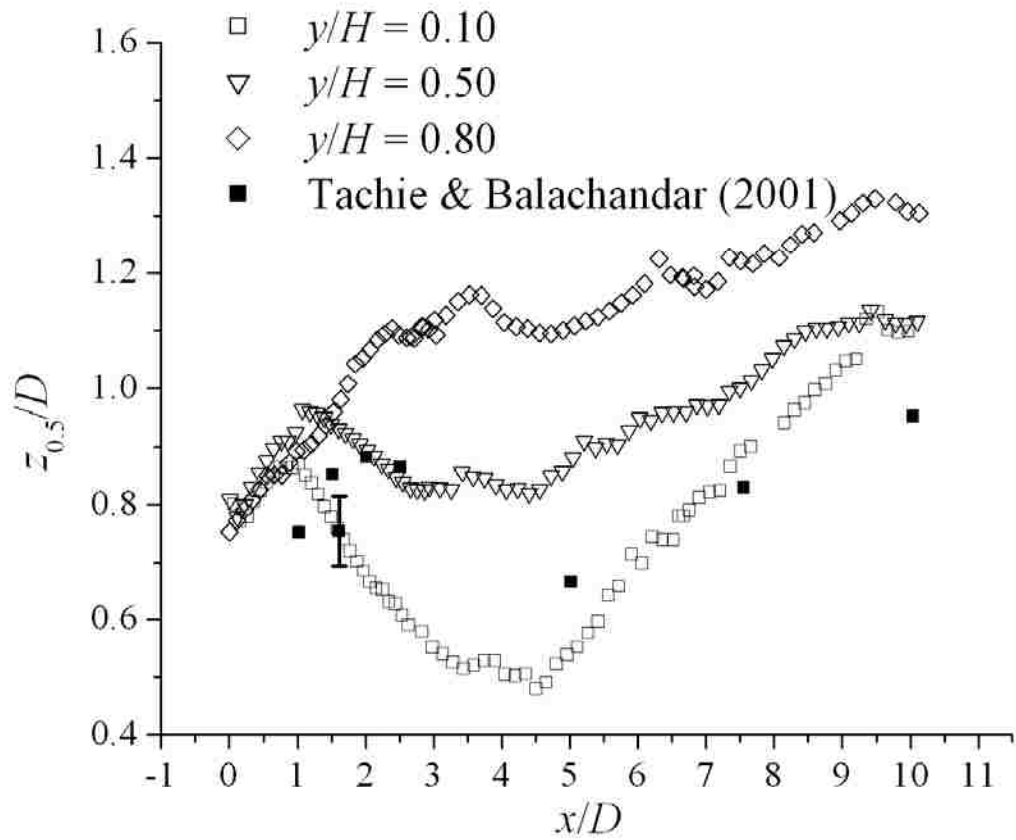
Figure 5.6: Downstream development of the normalized wake half-width with the streamwise distance x/D, at near-bed ($y/H = 0.10$), mid-depth ($y/H = 0.50$) and near-surface ($y/H = 0.80$) vertical locations.
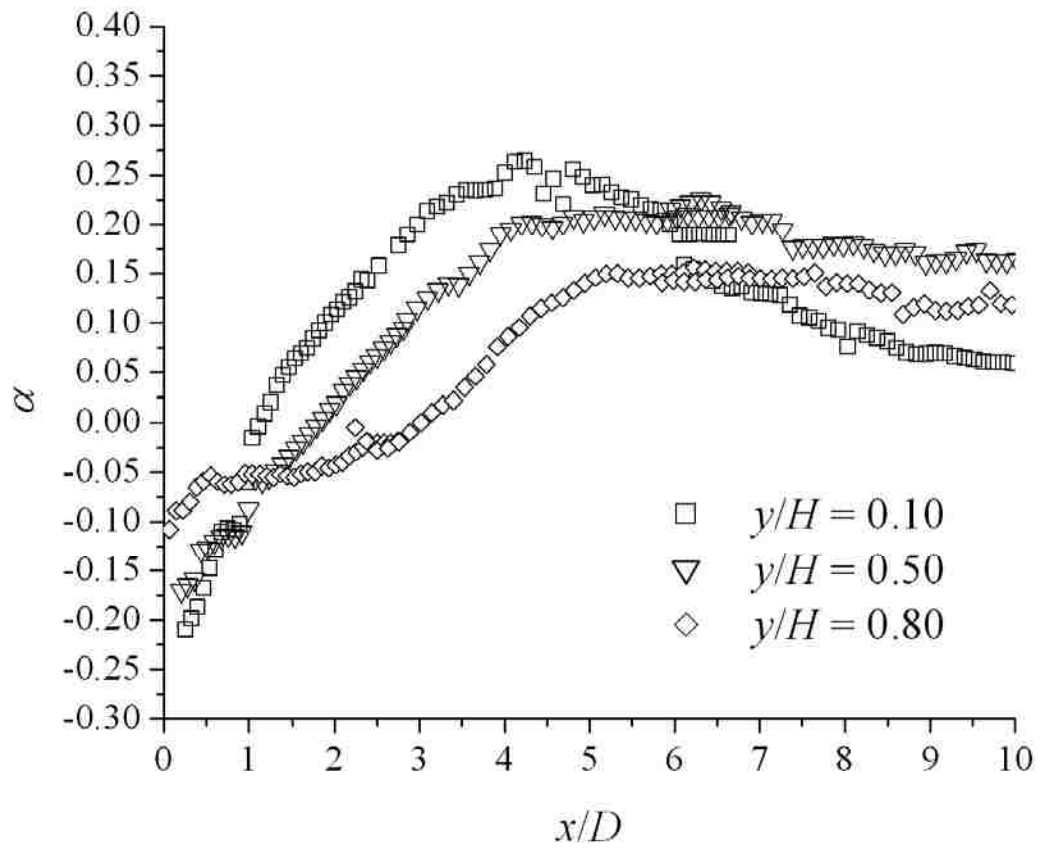
Figure 5.7: Downstream development of the entrainment coefficient with the streamwise distance x/D at near-bed ($y/H = 0.10$), mid-depth ($y/H = 0.50$) and near-surface ($y/H = 0.80$) vertical locations.
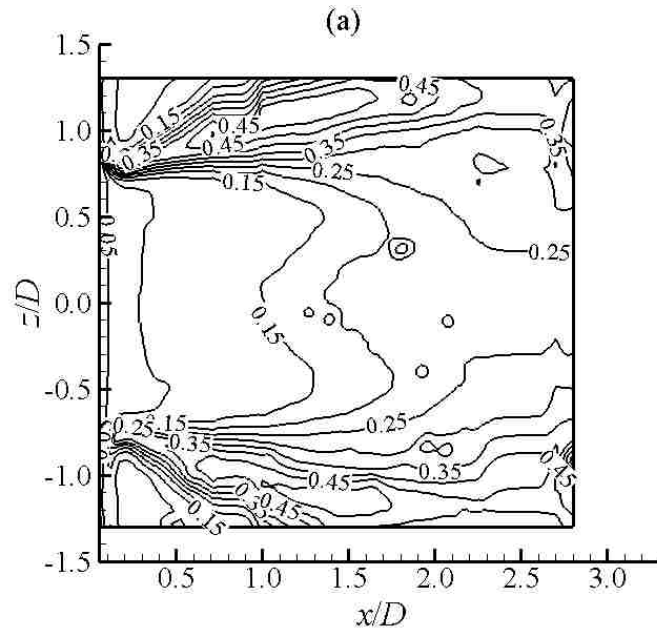
Figure 5.8: Comparison of the contours of root-mean square streamwise velocity (U_{rms}) normalized by U_s at (a) near-bed ($y/H = 0.10$), (b) mid-depth ($y/H = 0.50$) and (c) near-surface ($y/H = 0.80$) vertical locations.

159

(b)
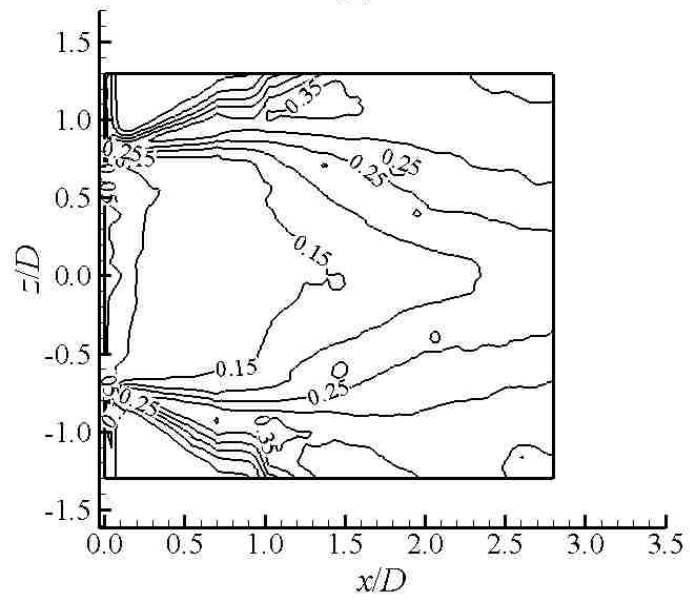
(c)
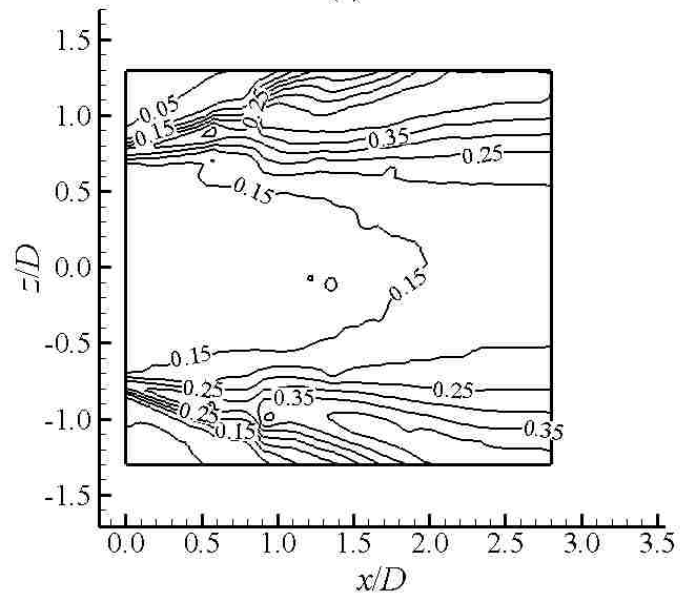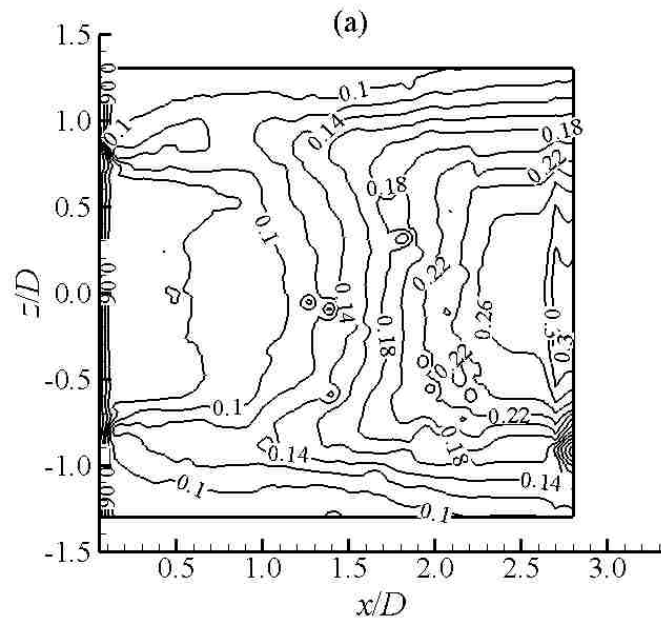
Figure 5.9: Comparison of the contours of root-mean square transverse velocity (W_{rms}) normalized by U_s at (a) near-bed ($y/H = 0.10$), (b) mid-depth ($y/H = 0.50$), and (c) near-surface ($y/H = 0.80$) vertical locations.

(b)
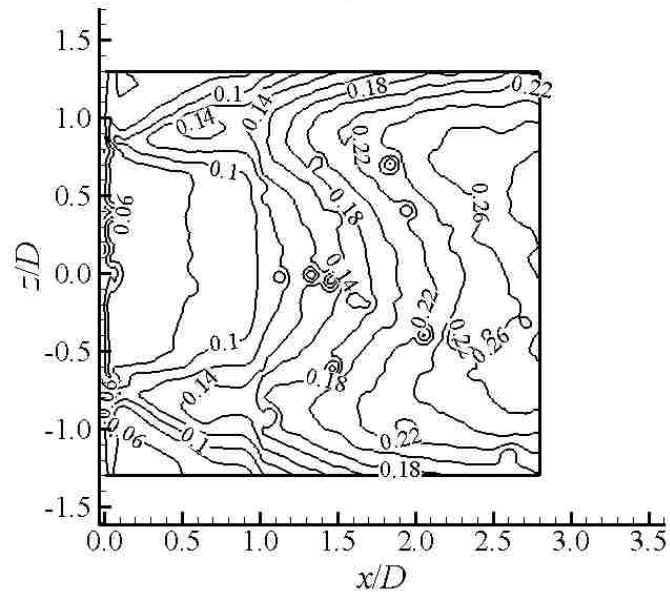
(c)
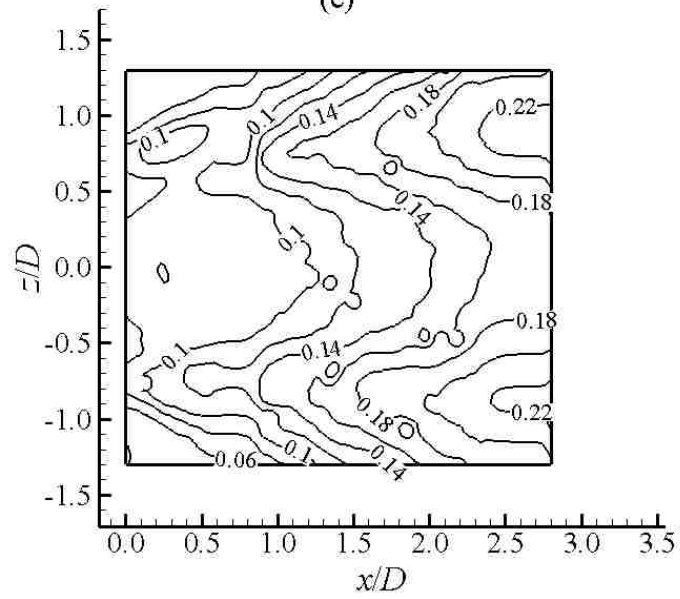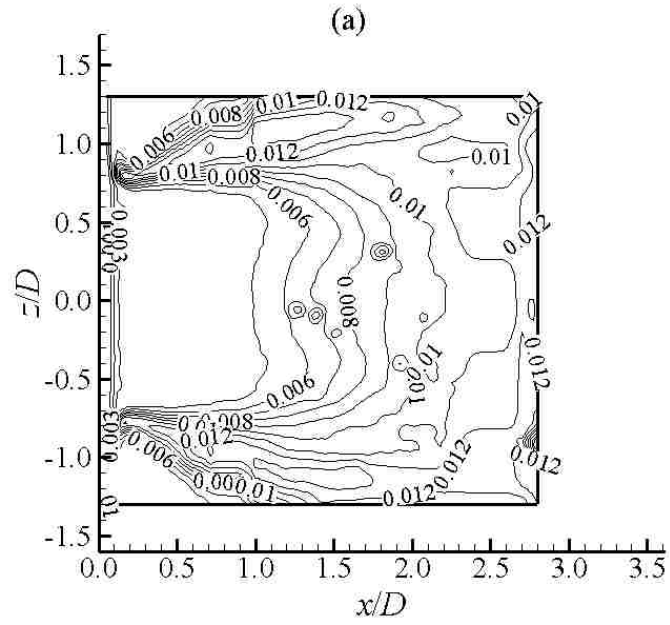
Figure 5.10: Comparison of the contours of turbulent kinetic energy (k) normalized by U_s^2 at (a) near-bed ($y/H = 0.10$), (b) mid-depth ($y/H = 0.50$), and (c) near-surface ($y/H = 0.80$) vertical locations.

(b)

(c)

164
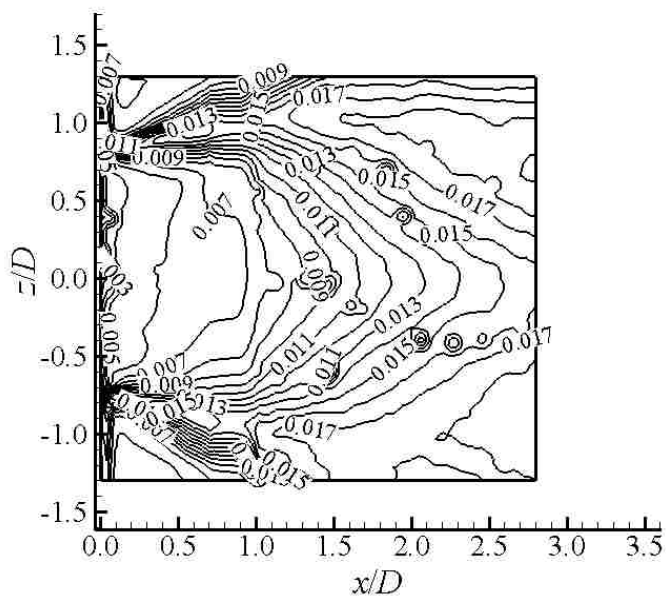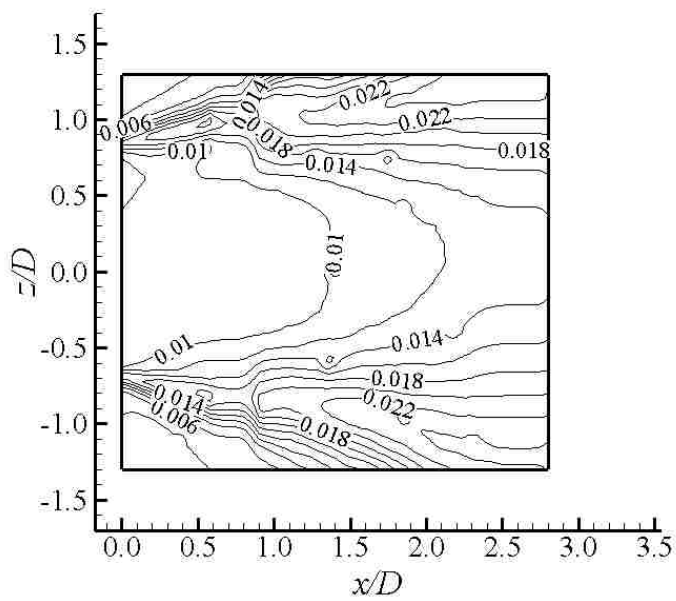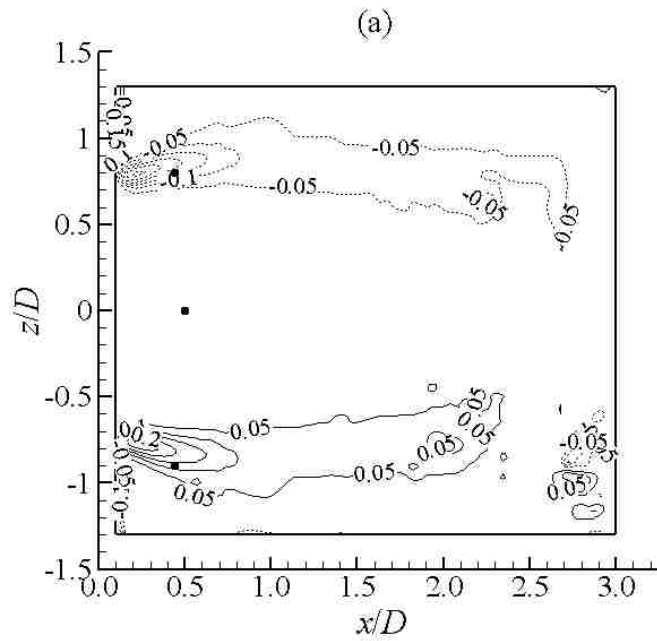
Figure 5.11: Comparison of the contours of normalized vorticity $\omega_z D / U_s$ at (a) near-bed (y/H = 0.10), (b) mid-depth (y/H = 0.50), and (c) near-surface (y/H = 0.80) vertical locations. The black dots correspond to the point of data extraction for Figure 5.19.

(b)

(c)

166
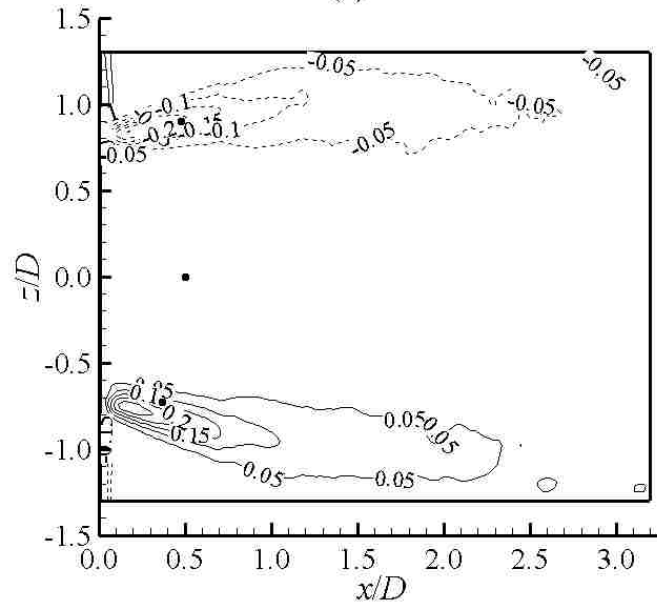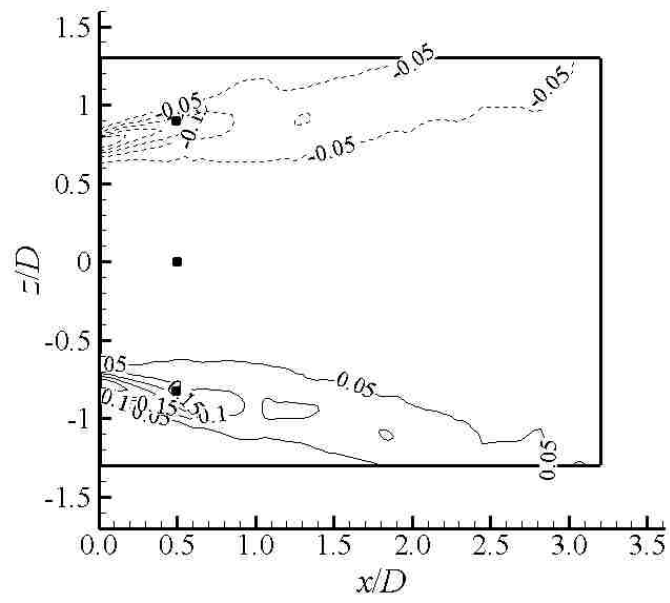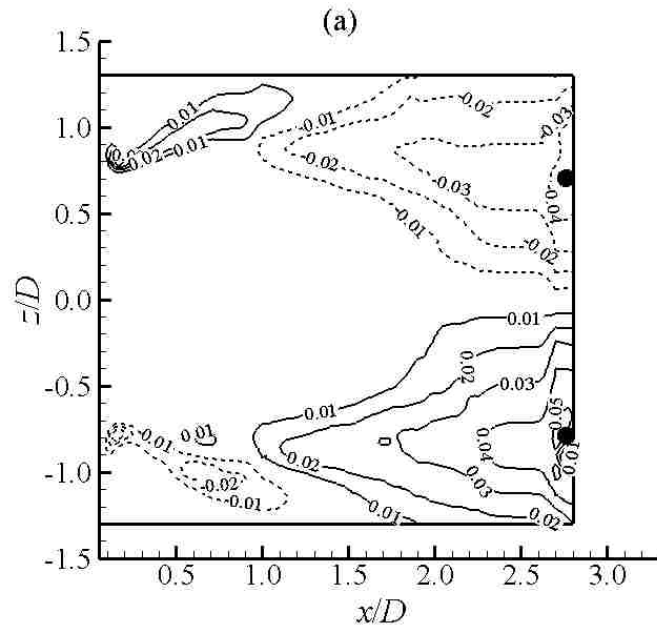
Figure 5.12: Comparison of the contours of normalized Reynolds stress $\langle u'w' \rangle / U_s^2$ at (a) near-bed ($y/H = 0.10$), (b) mid-depth ($y/H = 0.50$), and (c) near-surface ($y/H = 0.80$) vertical locations. The black dot represents the approximate location of the peak Reynolds stress.

(b)

(c)

168

(a)

Near-surface

Mid-depth

Near-bed

Near-bed
structure
$x/D = 1.6, 2.7$

Horseshoe
vortex
$x/D \leq 1.2$

Transverse velocity (m/s)

-0.18 -0.146 -0.112 -0.078 -0.044 -0.01 0.024 0.058 0.092 0.126 0.16
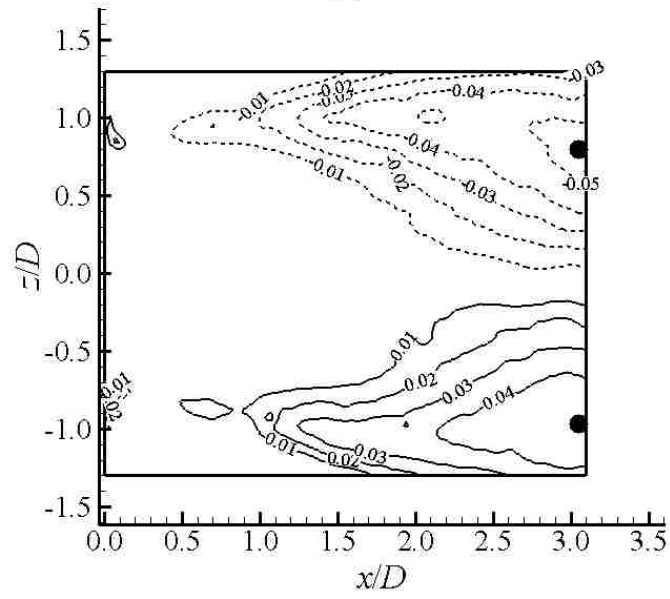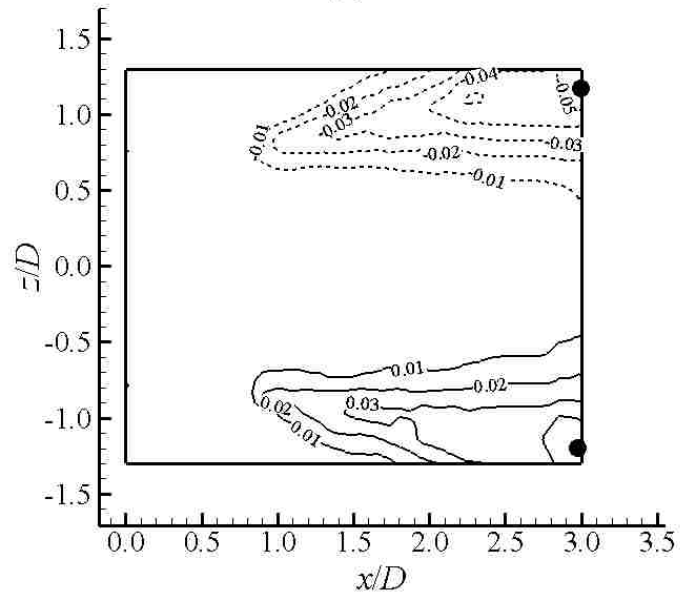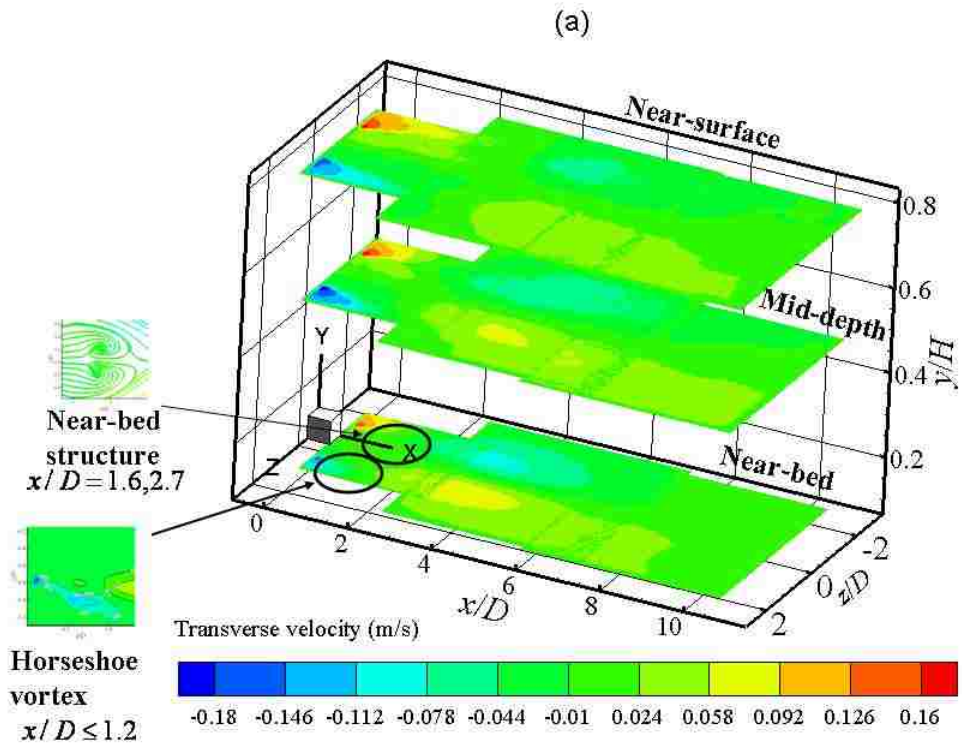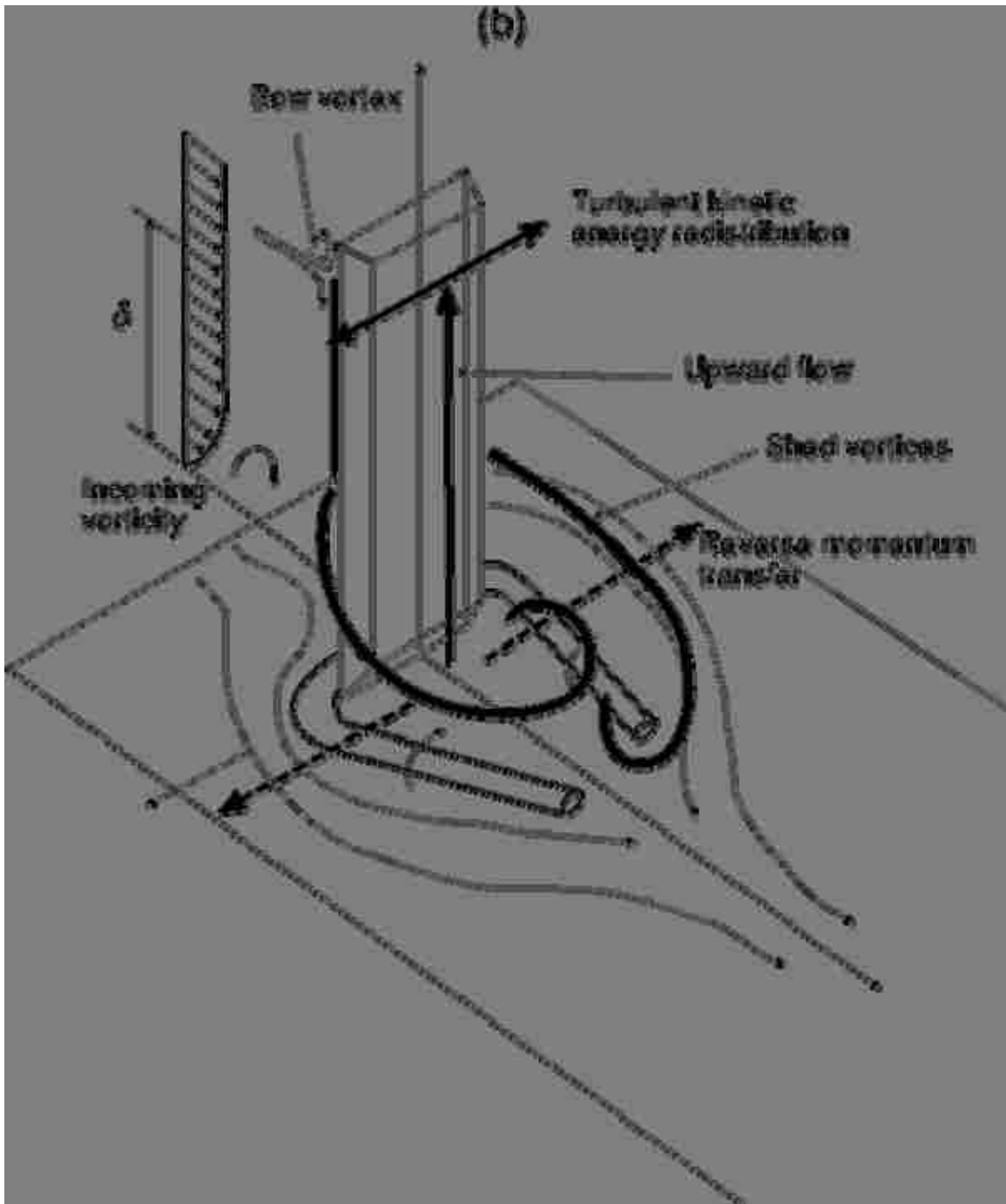
Figure 5.13: Schematic representations of the dynamics of flow at the near-wake region. Figure (a) indicates a concise plot of all flow features and figure (b) is a schematic of the model flow pattern.
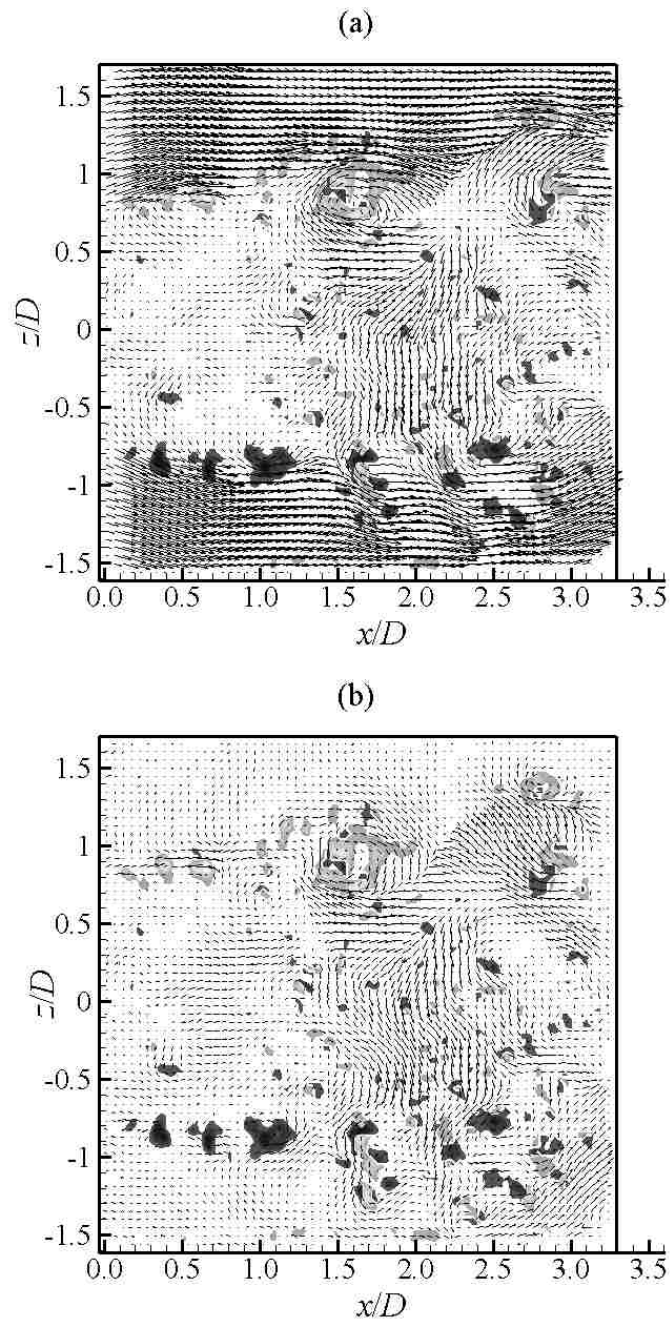
Figure 5.14: Typical (a) instantaneous and (b) fluctuating velocity field with patch of positive (dark shade) and negative (grey shade) swirling strength superimposed.

(a)
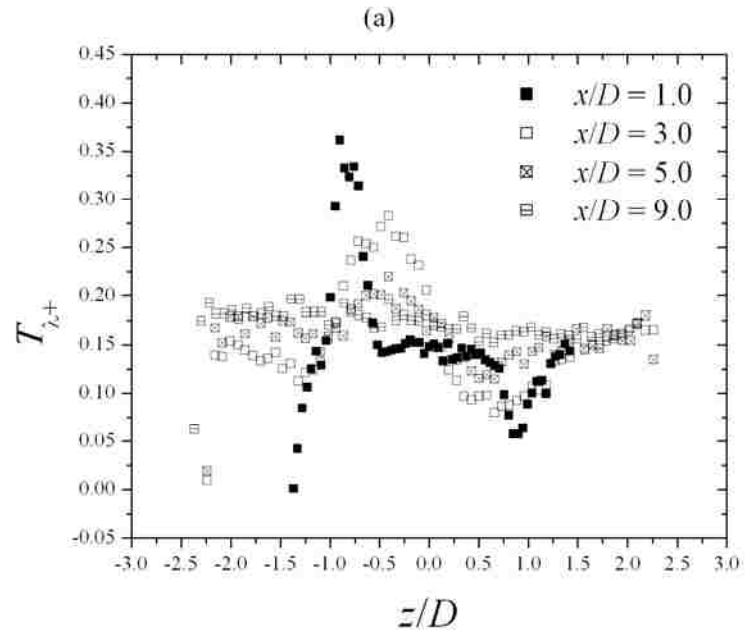
Figure 5.15: Fraction of time of positive swirling strength ($T_{\lambda+}$) at (a) near-bed ($y/H =$ 0.10), (b) mid-depth ($y/H = 0.50$) and (c) near-surface ($y/H = 0.80$) vertical locations at streamwise locations $x/D = 1.0, 3.0, 5.0$ and 9.0 respectively.

(b)

(c)
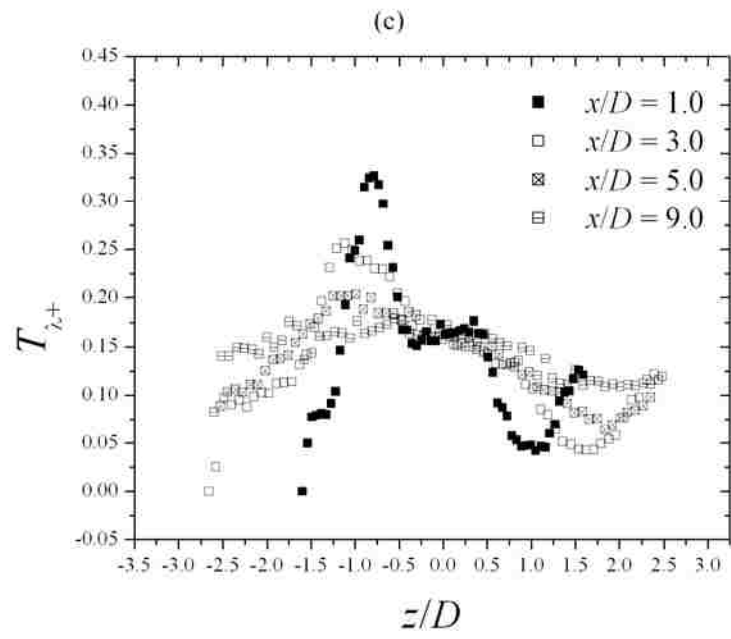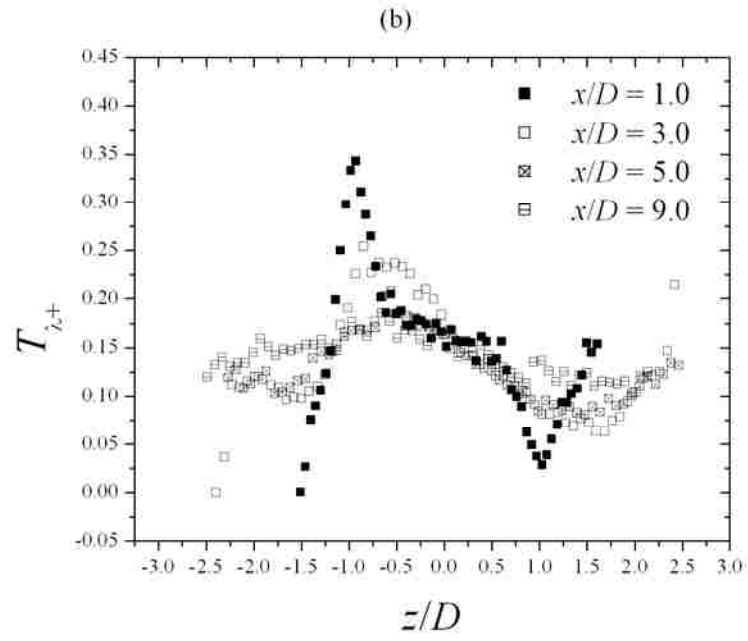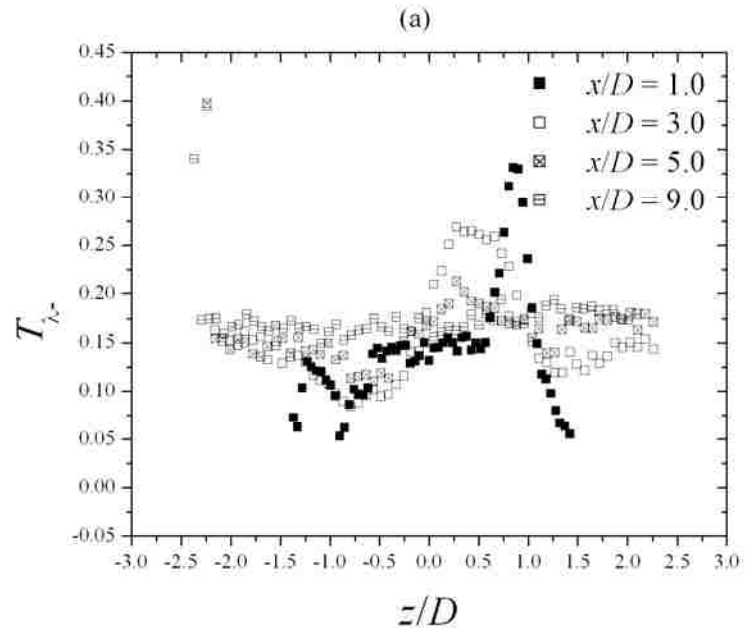
Figure 5.16: Fraction of time of negative swirling strength ($T_{\lambda-}$) at (a) near-bed ($y/H = 0.10$), (b) mid-depth ($y/H = 0.50$),and (c) near-surface ($y/H = 0.80$) vertical locations at streamwise locations $x/D = 1.0, 3.0, 5.0$ and 9.0 respectively.

(b)

(c)
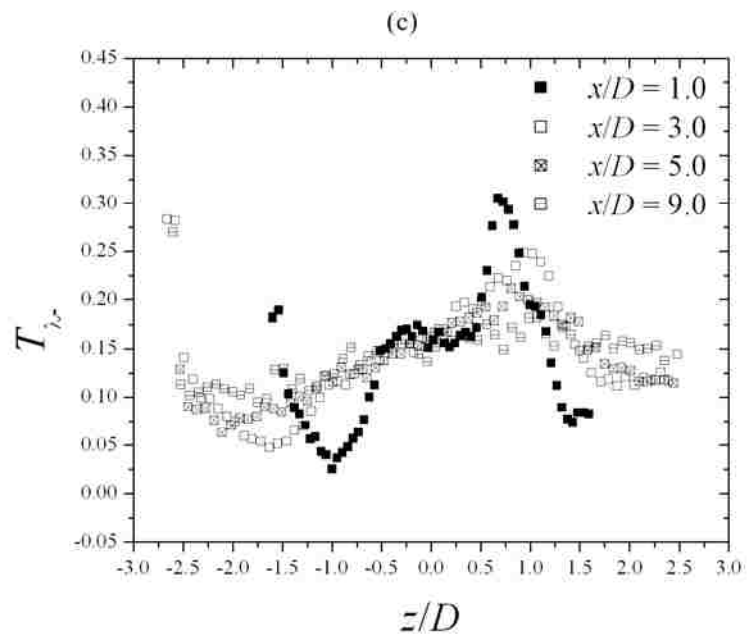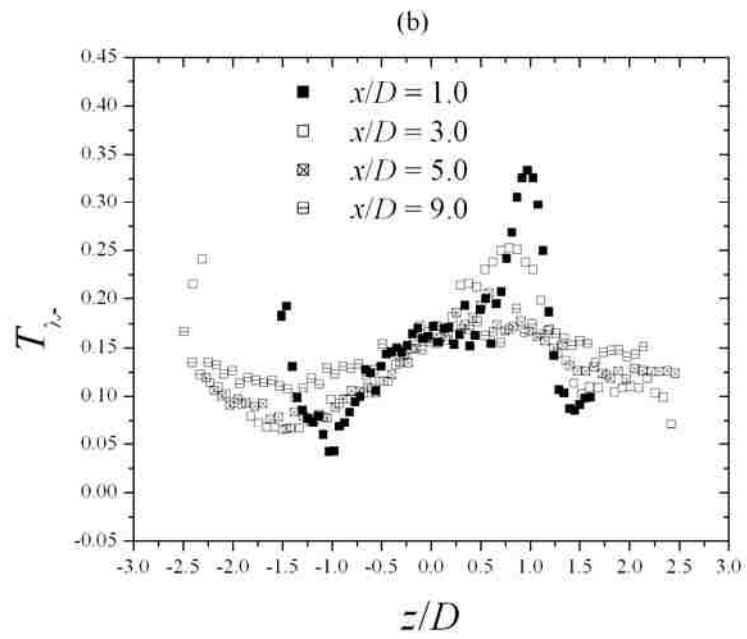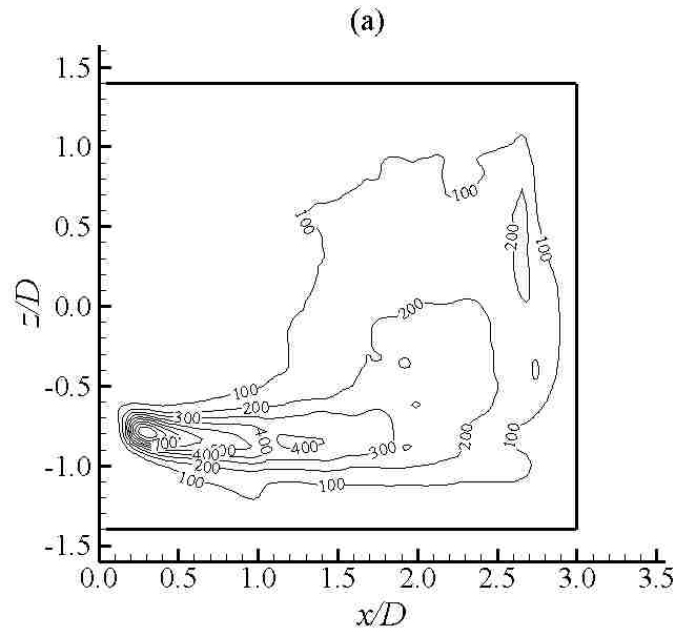
Figure 5.17: Mean positive eddy as found out by conditional averaging of the flow field, based on the sign of swirling strength at (a) near-bed ($y/H = 0.10$), (b) mid-depth ($y/H = 0.50$) and (c) near-surface ($y/H = 0.80$) vertical locations.

(b)
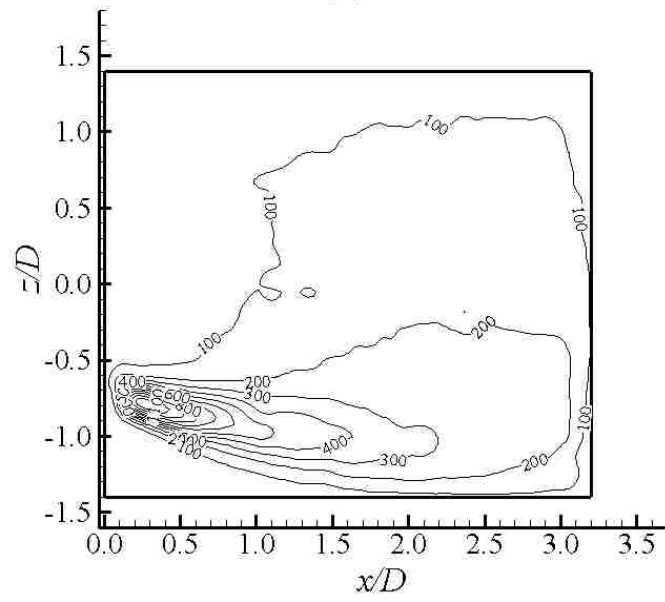
(c)
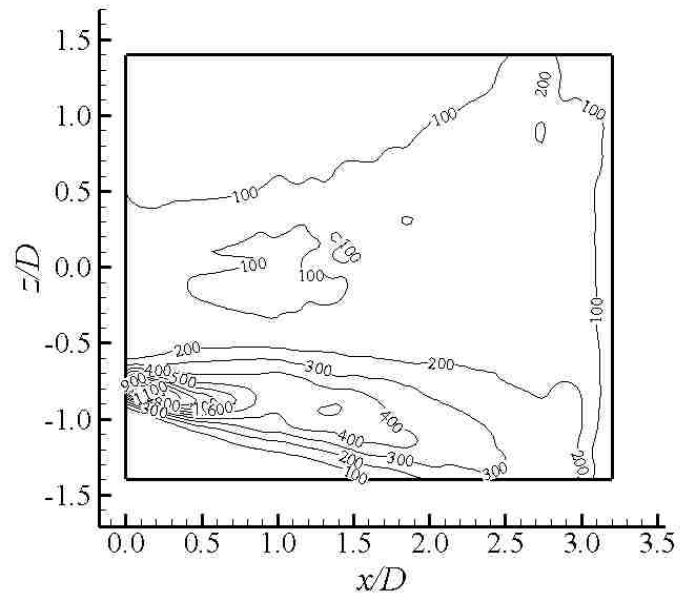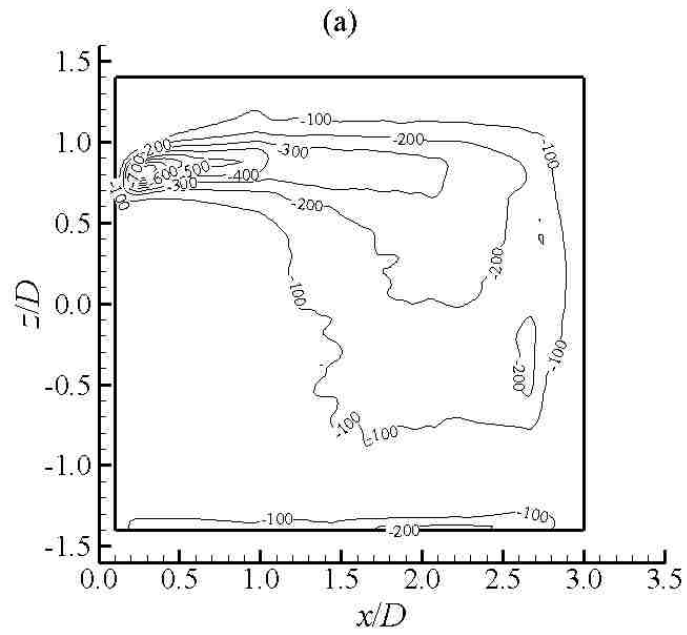
Figure 5.18: Mean negative eddy as determined by conditional averaging of the flow field, based on the sign of swirling strength at (a) near-bed ($y/H = 0.10$), (b) mid-depth ($y/H = 0.50$), and (c) near-surface ($y/H = 0.80$) vertical locations.

(b)

(c)

179
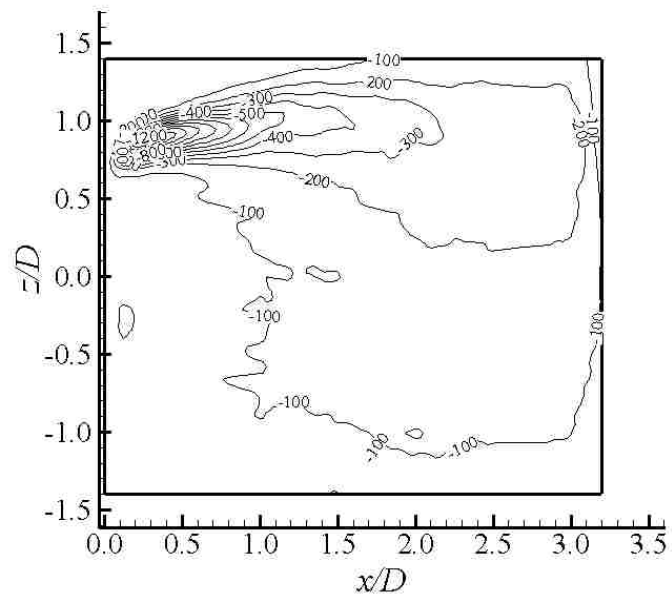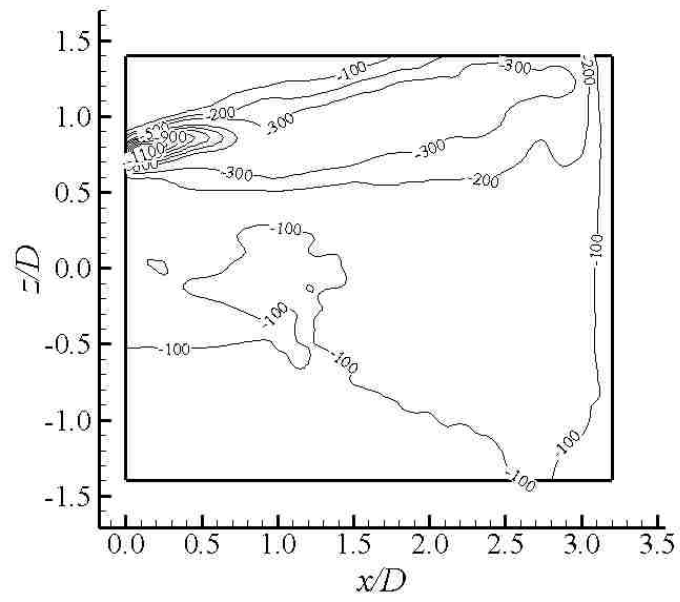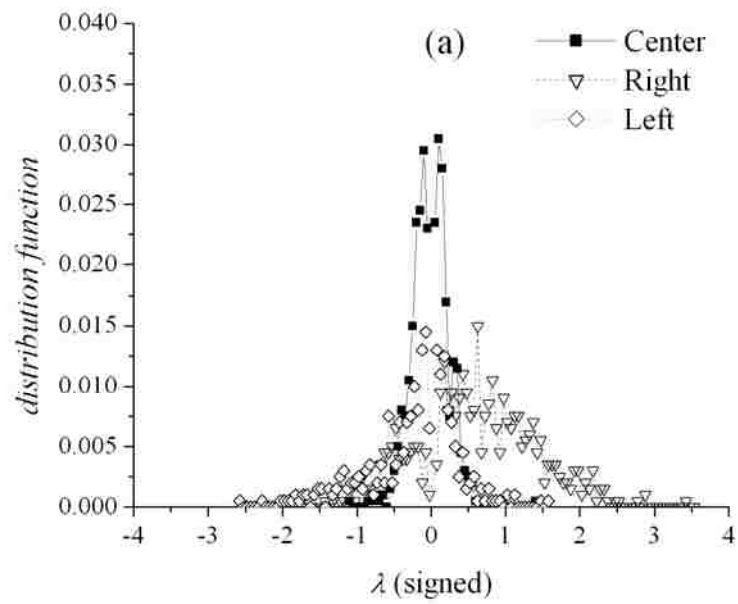
Figure 5.19: Distribution function of the signed swirling strength at (a) near-bed ($y/H =$ 0.10), (b) mid-depth ($y/H = 0.50$), and (c) near-surface ($y/H = 0.80$) vertical locations.
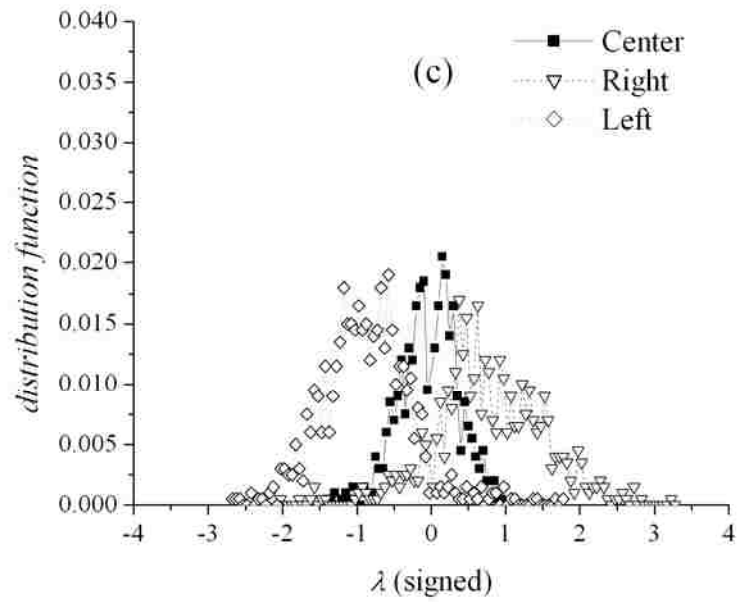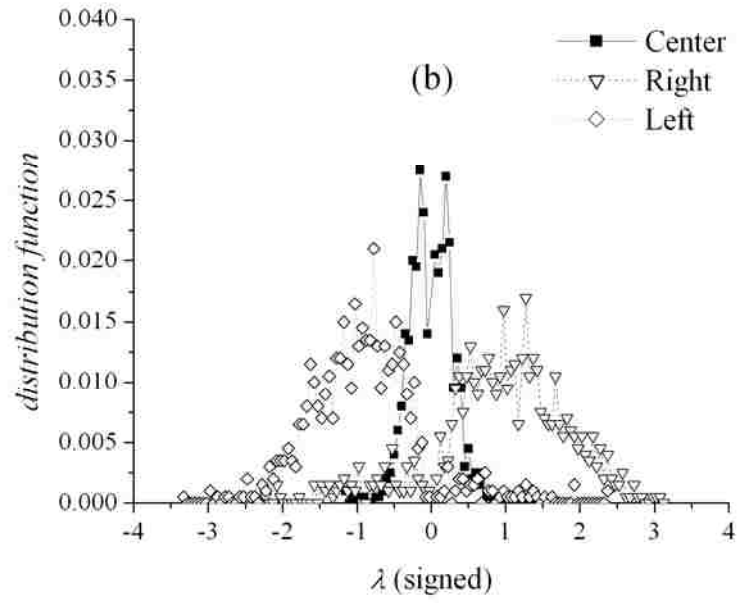
Table 5.1: Swirling strength data analysis

Streamwise location		Near-bed		Mid-depth		Near-surface	
		Maximum $(T_{\lambda+}, T_{\lambda-})$	z/D at maximum	Maximum $(T_{\lambda+}, T_{\lambda-})$	z/D at maximum	Maximum $(T_{\lambda+}, T_{\lambda-})$	z/D at maximum
1D	Negative	0. 33	0. 85	0. 33	0. 99	0. 33	0. 73
	Positive	0. 36	0. 90	0. 34	0. 93	0. 32	0. 81
3D	Negative	0. 26	0. 43	0. 25	0. 79	0. 25	0. 95
	Positive	0. 28	0. 41	0. 25	0. 87	0. 25	1. 09
5D	Negative	0. 22	0. 28	0. 20	0. 58	0. 21	0. 81
	Positive	0. 22	0. 43	0. 21	0. 56	0. 20	0. 98
9D	Negative	0. 19	0. 71	0. 19	0. 87	0. 18	1. 07
	Positive	0. 20	0. 60	0. 18	0. 67	0. 17	1. 2

Chapter 6

STATISTICS OF COHERENT STRUCTURES

6.1 General remarks

This chapter reports the result of education of coherent structures of the shallow wake flow. As mentioned earlier, the dynamics of the coherent structures plays an important role in influencing the characteristics of the shallow wake, and therefore, it is worth examining. Initially, POD was applied to the fluctuating velocity field and then it was reconstructed with ~ 40% of the fluctuating energy content. A closed-streamline based coherent structure identification algorithm was used to detect and extract information about the size, strength and sense of rotation of the structures. To this end, the distribution function of each of these parameters at near-bed, mid-depth and near-surface locations are presented.

6.2 Eduction of large-scale structures by POD

Before reconstructing the velocity field, the convergence of the eigenvalue of the correlation matrix needs to be verified. As discussed by Cazemier et al. (1998), the number of snapshots should be as large as possible for accurate estimation of the POD eigenfunctions. The effect of the number of snapshots on the computed values of modes 1 to 5 is shown in Figure 6.1. It is obvious that the computed eigenvalue does not depend on the number of snapshot for sample size more than 1000. All 2000 frames are used in this study for the reconstruction of each FOV.

The working principle of POD reconstruction is highlighted in Figure 6.2 using an instantaneous snapshot of the velocity field. The coherent structure is buried inside the mean flow field, so the instantaneous velocity field (Figure 6.2(a)) is not good for identification of the coherent structure. First, the Reynolds averaged flow field is subtracted from the snapshot to obtain the fluctuating velocity flow field (Figure 6.2(b)). POD decomposition and consequent reconstruction is carried out on the fluctuating flow field. Since the bulk of the turbulent kinetic energy is contained within the large-scale coherent structures, using a suitable cut-off percentage in the energy content for POD reconstruction will aid in reconstructing the velocity field where only the large-scale structure is exposed. This process of reconstruction can be continued using more energy, and eventually the original flow field can be retrieved if 100% energy is used for the reconstruction. But increasing the cut-off percentage of the energy content leads to inclusion of the small-scale structures and the information of the large-scale structure will be gradually lost. A typical signature of a clockwise structure can be seen in Figure 6.2(b), indicated by the rectangular area. But, the location and size of the structure is not very obvious because of the interacting small-scale structures. Figure 6.2(c) shows the POD reconstructed velocity field containing the first eight modes or ~ 40% of the fluctuating energy. Since POD reconstruction filters out the small-scale fluctuations, a large-scale structure can be clearly seen in Figure 6.2(c). The location of the centre and the size is shown by the black line in Figure 6.2(c). Another POD reconstructed snapshot, containing ~95% (1098 modes) energy is shown in Figure 6.2(d). This closely resembles the original fluctuating flow field in Figure 6.2(b) and is influenced by the small-scale

fluctuations. This shows that a suitable cut-off percentage of the energy content is important to successfully identify most of the large-scale structures present in the flow field.

Although important, unfortunately, there exists no particular choice for the cut-off energy to be used in the POD reconstruction, and it depends on the individual flow configuration. According to Citriniti & George (2000), choice of the cut-off energy is like using conditional sampling; only the threshold criterion is more rigorous, since it is based on statistics rather than observation. Perrin et al. (2006) used an energy cut-off value of ~60% for POD reconstruction to evaluate turbulent properties of a circular cylinder wake. Shinneeb et al. (2008), on the other hand, used ~ 40% of the fluctuating energy criterion to identify coherent structures at the far-field of an axisymmetric free jet. Figure 6.3 visualizes the effect of the choice of the energy cut-off percentage on the eduction of large-scale structures. The snapshot in Figure 6.3 is the same frame as in Figure 6.2 and the location of the large-scale structure shown in Figure 6.2 is indicated by a black-box (named C) in Figure 6.3(a). Figures 6.3(a), 6.3(b) and 6.3(c) are obtained by using ~35%, ~50% and ~80% cut-off energy, respectively. Figure 6.3(a) contains three counter clockwise (A, D and E) and two clockwise structures (B, C). The size of the structures A, B, C, D and E are approximately 1D, 0.55D, 0.35D, 0.2D and 0.2D, respectively. This figure also highlights one important aspect of the structure identification algorithm, i.e. it extrapolates the size of the identified structures lying around the edge of the field-of-view (for example, for the case of structures A, B). This would ensure smaller bias error associated with the identified size of the structures. Figure 6.3(b) also contains structures

185

A, B' (probably similar to structure B in Figure 6.3(a)), C and D, but not E. Although a weak signature of the structure E can be seen, as shown by the dotted line, it does not conform to the monotonic and threshold conditions of the algorithm. Most importantly, the size of the structures in Figure 6.3(b) is larger than that in Figure 6.3(a). The POD reconstruction with ~40% cut-off energy already shown in Figure 6.4 and is almost similar to Figure 6.3(b). In Figure 6.3(c), in addition to structures A and B, five smaller structures (D, E, F, G, H) of average size less than $0.08D$ appear. The size of structures A and B are reduced to $0.6D$ and $0.4D$, respectively, due to the masking effect of small-scale fluctuations. Most importantly, structure C completely disappears in Figure 6.3(c) and its probable location is shown by a black dotted circle. Therefore, it can be concluded that threshold greater than 50% cut-off energy starts to capture the small-scale fluctuations and the POD reconstructed velocity field does not represent the true information of the coherent structure. A cut-off energy content of less than 40% also fails to educe most of the possible large-scale coherent structures. Since the intention of the present study is to identify the large-scale structures only, the cut-off energy content of ~40% appears to be a good choice for POD reconstruction. Although ~50% cut-off energy content also produces almost similar results, ~40% cut-off energy is selected based on analyzing a large number of frames. In addition to this, this particular value of cut-off energy was chosen after careful manual checking of a large number of POD reconstructed velocity field.

6.3 Statistics of coherent structures

The approaching flow will form a boundary layer at the upstream face of the bluff

body and will separate in the form of vortex shedding from both sides the body. Because

of this, one would expect to observe more clockwise structures for $z/D > 0$ (upper portion

the wake axis) and more counterclockwise structures for $z/D < 0$ (lower portion the wake

axis). At each FOV, the identified structures are divided into two groups and their radius

is multiplied by the sign of the rotation. The sign of the structure is denoted as positive if

it is rotating clockwise and negative if it is counterclockwise. The distribution function

of the occurrence of the structures on both sides is shown in Figure 6.4. The bin size for

computing the distribution function is selected to be $0.8D$. Contrary to the general belief

mentioned earlier, the distribution functions for both sides of the wake axis look similar.

According to the classification of Chen & Jirka (1995), the present wake falls into the

category of vortex street (VS), and therefore meanders. At some instant the shed vortex

will be located in the region $z/D > 0$ and at another instant it may lie in the region $z/D <$

0. As a result, on an average, the distribution function on both sides of $z/D = 0$ looks

similar. Figure 6.4 in some sense also justifies the use of ~40% cut-off energy for POD

reconstruction, since the distribution function would not look similar unless majority of

the structures are identified successfully in the flow. Another point worth noting from this

figure is the size of the identified structures. Although most of the structures span less

than 10 grid points the maximum size of the identified structure is around 20 grid points,

which is approximately 70-80 mm. This is not surprising, since previous investigation

(Singha et al. 2009) revealed that the size of the large-scale structures may be as big as 200% of the width of the bluff body for the case of a shallow flow.

To further clarify the meandering nature of the wake, some typical POD reconstructed snapshots are shown in Figure 6.5. By observing an animation of 100 snapshots put together (not shown here), the wake can be seen to meander on either side of the $z/D = 0$ line. Figure 6.5(a)-(b) shows some of the POD reconstructed fluctuating flow field, with the vorticity contour superimposed. A solid circle indicates a clockwise structure and a dashed circle indicates a counterclockwise structure. In Figure 6.5(a), one clockwise structure is found at $z/D > 0$ and another counterclockwise structure is found at $z/D < 0$. Figure 6.5(b) shows a completely reverse case, where a counterclockwise structure is found at $z/D > 0$ and a clockwise structure is found at $z/D < 0$. As a cumulative effect of Figure 6.5(a) and Figure 6.5(b), the average distribution function of structure population computed in Figure 6.4 for $z/D > 0$ and $z/D < 0$ looks similar.

Table 6.1 summarizes the total number of structures identified in each fields-of-views (FOV), the cut-off percentage of fluctuating energy used for the POD reconstruction and the ratio of the clockwise (CW) to counterclockwise (CCW) structures. The ratio of the CW to CCW structures always remains close to unity and implies that the flow contains almost the same number of structures of each sense of rotation at every FOV. In the vertical direction, at station 1, the number of structures increases monotonically from the near-bed to the near-surface location. The number of structures decreases from NB2 (near-bed:station 2) to MD2 (mid-depth:station 2), and then again increases from MD2 to NS2 (near-surface:station 3) at station 2. At the station 3, the trend is completely reversed

compared to station 1; the number of identified structures decreases monotonically from NB3 to NS3. In the streamwise direction, at the near-bed location, the number of structure increases from station 1 to station 2 and then decreases from station 2 to station 3. But at all other locations (mid-depth and near-surface) the number of structures decreases monotonically with increase of x/D. The decrease in the number of structures in the streamwise direction is probably caused by the merging/pairing of two or more structures, as outlined by Chen & Jirka (1995).

In order to obtain a clearer perception of the physical size of the coherent structures, the identified structures are further subdivided into four groups based on the size, as $R/D < 0.2$, $0.2 < R/D < 0.5$, $0.5 < R/D < 0.7$, and $R/D > 0.7$. For sake of discussion, they are referred to as group 1, 2, 3 and 4. The fraction of the number of structures (N_f) belong to each group at all FOVs is tabulated in Table 6.2. At station 1, from NB1 to MD1, the increase in the total number of structure is mainly due to the increase in N_{f3} and N_{f4}, whereas N_{f1} decreases. This implies that statistically the probability of finding a larger structure is more at mid-depth than at near-bed location. Following the same reasoning, from MD1 to NS1, more structures of group N_{f2} and N_{f3} appear, but the probability of appearance of the largest size (group 4 structures) decreases. At station 2, although the total number of identified structures decrease from near-bed to mid-depth location, the fractions of identified structure in N_{f2} and N_{f3} increase. Similar to station 1, N_{f4} decreases from mid-depth to near-surface location at station 2 also. By analyzing the variation of the fraction of number in vertical direction, a number of trends can be observed (from Table 6.2): from near-bed to mid-depth the

189

fraction of number of coherent structures belonging to group 2 and 3 always increases. Also, close to the free surface, N_{f4} decreases consistently at all stations compared to the mid-depth location. Following the variation of the fraction in the streamwise direction, a clear indication of the merging process, mentioned above, can be observed in Table 6.2. With increase in streamwise distance, at near-bed, mid-depth and near-surface locations, N_{f1}, N_{f2} and N_{f3} decreases whereas N_{f4} increases. This indicates spatial growth of the coherent structures with streamwise distance. This observation, in conjunction with the fact that the number of identified coherent structures decreases in streamwise direction may be considered as a direct evidence of the merging phenomenon.

Additional insight can be gained by plotting the behaviour of the mean structure size (R_{mean}) and circulation (Γ_{mean}) in the axial direction (Figure 6.6). In this figure, the axial location x and the mean structure size R_{mean} are normalized with the width of the bluff body, D, while the circulation is normalized by DU, where U is the approach velocity. All FOV's are equally divided into 30 bins, resulting in approximately a 3-mm bin size in the streamwise direction. The size of the identified structures grows in the range $0 < x/D <$ 3 at all vertical locations. In the range, $x/D > 3$, the rate of increase of the size of the structure is slightly reduced. There is no trend of decrease in the size of the structure. This implies that the dissipation of the coherent structure only affects the number of structures, but not the size of the structures. The mean size of the coherent structures at all vertical locations increases with the streamwise distance, but the maximum size of structure ($R_{mean}/D \approx 1.4$) is detected at the mid-depth location. The rapid fall off in the size of the identified structures beyond $x/D = 9$ is perhaps due to the edge effect reducing

the ability of the identification algorithm to detect structures due to reduced number of available grid points. But, close to the surface, the mean size of the coherent structures decreases from $x/D \approx 7.5$, the reason for which cannot be attributed to the edge effect alone, but to the nature of the dynamics of the free surface. The variation of the mean circulation with the streamwise distance shown in Figure 6.6(b) also follows the same trend. The mean circulation of the identified structures increases monotonically till $x/D \approx$ 3 and increases at a reduced rate for $x/D > 3$. The free surface is found to not only resist the growth of the structures, but also reduce their strength. This along with the result presented in Table 6.2, leads one to conclude that the free surface may act as a weak-wall, tending to mildly reduce the size as well as the strength of the coherent structures.

Table 6.2 provides a measure of the number and size range of the structures. However, to track the location of the coherent structures, the transverse extent of the FOV downstream of the bluff body is divided into three regions; the central region $|z/D| <$ 0.3, the shear layer region, $0.3 < |z/D| < 0.7$ and the ambient flow region, $|z/D| > 0.7$. In general, the central region contains the recirculation region of the wake and the shear layer region contains the separated shear layer of the body. The ambient flow region represents the outer accelerating flow region. The fraction of occurrence of the coherent structures, sorted by size and strength, at near-bed, mid-depth and near-surface region, for stations 1, 2 and 3 are shown in Figures 6.7, 6.8 and 6.9, respectively. In each figure, the left column shows the distribution of the size and the right column shows the circulation. The top, middle and bottom row represents the near-bed, mid-depth and near-surface vertical locations, respectively. A number of observations can be drawn upon close

examination of the three figures. Firstly, the dominant location of the coherent structures is found to be constantly changing with y/H as well as x/D. At station 1, close to the bed, a majority of the coherent structures are agglomerated in the central region, and the ambient flow region contains negligible number of structures. However, at the near-surface location, the central region contains almost no structures, and they are mainly detected at the shear layer and ambient flow regions. With increase in the axial distance, at station 3, a different picture emerges. At station 3, at the near-bed location, most of the structures shift to the outer flow region, and the central region contains a negligible amount of structure. Again, at the near-surface location, most of the structures move to the central region. Secondly, it can be observed that larger structures are generally associated with larger circulation, and smaller structures have smaller value of circulation. This is consistent with the fact that for a constant approaching velocity, the circulation of the coherent structures should scale with the square of the radius of the structure, $\Gamma \propto R^2$. For example, a secondary peak in the function at $|\Gamma/UD| \approx 0.12$ can be observed at the central region due to these large-scale structures of size $R/D \approx 1.25$ at NB2. Thirdly, as mentioned earlier, the maximum range of the size of the structures is minimum at the bed, and maximum at the mid-depth location. At the near-surface location, the maximum size of the detected structures is lower than the mid-depth location, and higher than the near-bed location. Figures 6.7, 6.8 and 6.9 indicates that the range of the distribution function also follows the same trend as the size of the structures.

The reason for this transverse inhomogeniety of the location of the structures may be linked with the flow dynamics at the bed and free surface. Close to the bed, due to the

192

legs of the horseshoe vortex system, a pair of vortices can be detected in the streamwise *y-z* plane. Because of the associated vorticity of the approaching flow, this will appear as a clockwise vortex for *z/D* < 0 and counterclockwise vortex for *z/D* > 0 (if seen towards the negative *x* direction) and induces flow from the accelerated flow region towards the inner reverse flow region. This tends to push these coherent structures towards the central plane, at near-bed location, close to the body. Similarly, due to the existence of the surface currents (Maheo, 1999; Logory, 1996), the coherent structures get pushed towards the accelerated flow region at near-surface location. But the effect of both the horseshoe vortex and the surface currents are limited to only a few body-width lengths in the axial direction, and therefore with increasing axial distance, the structures tend to move and homogenize themselves in the transverse direction.

Assuming the circulation of coherent structure is a function of the freestream velocity (*U*), the characteristic width of the bluff-body (*D*) and the radius of the structure (*R*), dimensional analysis yields;

$$\left|\frac{\Gamma}{UD}\right| = k_c \left(\frac{R}{D}\right)^2 ; \tag{6.1}$$

where k_c is the constant of proportionality. This particular fitting is applied to the data obtained from all fields-of-view and the value of k_c is tabulated in Table 6.3. Figure 6.13 shows a typical fit at the field-of-view NS1. If the coherent structures are indeed following a rigid body motion, circulation should be proportional to the square of the radius of the structure. On one hand this fitting proves that the rotation of the structure is more like a rigid body rotation than a free vortex. It should be mentioned here that the

193

closed-streamline based structure identification does not check the radial variation of the tangential velocity as long as a closed streamline is found. In other word, the structure identification algorithm is independent of the nature (free or forced) of the structures. Lesser value of k_c represents either less circulation associated for the same size structure, or same circulation associated with larger size structure. Therefore, k_c can be thought of as a representation of the tangential velocity of the coherent structures. Clearly, k_c is a function of the downstream distance x/D. At all vertical locations, consistently, from station 1 to station 2, the value increases, and then decreases from station 2 to station 3. Although the trend is very clear and unambiguous, the exact reason for the variation may need further investigation and may not be clarified with the present dataset.

6.4 Conclusions

Particle image velocimetry measurements were conducted at near-bed, mid-depth and near-surface vertical locations downstream of a sharp-edged bluff body immersed in shallow channel flow. Proper orthogonal decomposition technique was used to extract the information about the coherent structures. A closed-streamline based structure identification algorithm was applied to identify and characterize the large-scale structures present in the flow field. Statistical analysis of the location, size and strength of the identified coherent structures was carried out to study the effect of downstream distance and the vertical confinement on the coherent structures. The distribution function of the size, location and strength of the identified structures were examined closely to reveal the interaction and development of the coherent structures.

The wake is found to contain a considerable number of coherent structures with both sense of rotation. The maximum size of the structures can be as large as twice the width of the bluff body. Close to the bed, the mean size of the structure is found to be a minimum, and increases at the mid-depth location. Again, close to the free surface, the size of the structure decreases mildly, compared to the near-bed location. The distribution function of the strength indicates that close to the bed, the strength of the structures is smaller than at the mid-depth location. This is because of the fact that the bed acts as a dissipative agent and consequently dissipates the vorticity rapidly compared to other locations. Similar to the previous observation, the free surface dampens the strength of the coherent structures. This may lead one to believe that the free surface imparts a 'weak-wall' effect on the coherent structures.

With increasing streamwise distance, the number of identified structure decreases and the mean-size increases, except at station 1. This is due to the spatial growth of the structures with streamwise distance, as well as the merging of several structures to generate a larger and stronger structure. This merging process was shown to contribute towards the inverse cascade (Kraichnan, 1967) phenomenon in shallow flows (Dracos et al. 1992). But the rate of merging is different at different distances from the bed, resulting in vertical variability in the size and strength of the identified structures.

The distribution function of the transverse location of the identified structures also exhibits the effect of the bed and the free surface. Close to the bed, due to the effect of the horseshoe vortex, all the coherent structures tend to reside in the central region. It has been shown earlier (Ingram & Chu, 1987; Singha at al. 2009) that the bed friction tends

to reduce the transverse extent of the wake, and this is one of the major reasons for agglomeration of the coherent structures at the central region at station 1. On the other hand, close to the free surface, due to the surface currents and energy transfer phenomenon (Logory et al. 1996; Maheo, 1999), all the coherent structures tend to get located at the ambient flow region. However, with streamwise distance, due to transverse movement of the coherent structures, they get homogenized. In this study, the coherent structures have been modeled with the associated circulation and the proportionality factor is found to be a function of streamwise distance as well as the distance from the bed. The constant of proportionality, in a statistical sense, represents the tangential velocity of the structures.
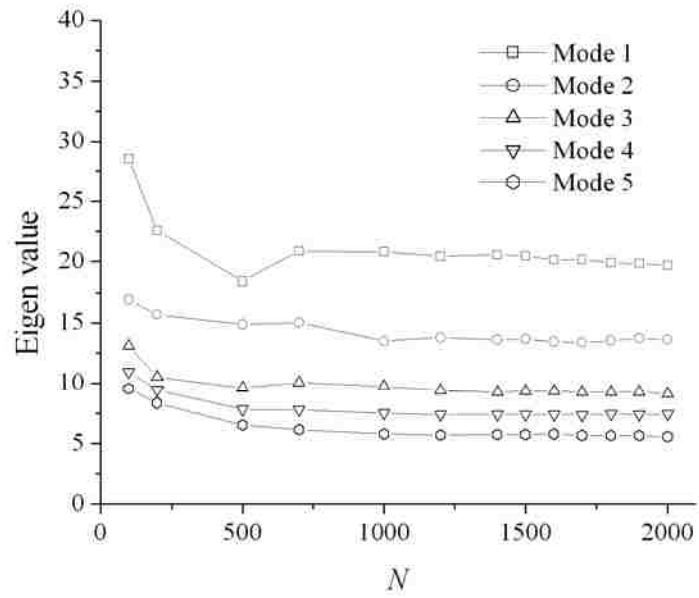
Figure 6.1: Effect of the number of snapshots on the convergence of the eigenvalue of the first five modes.
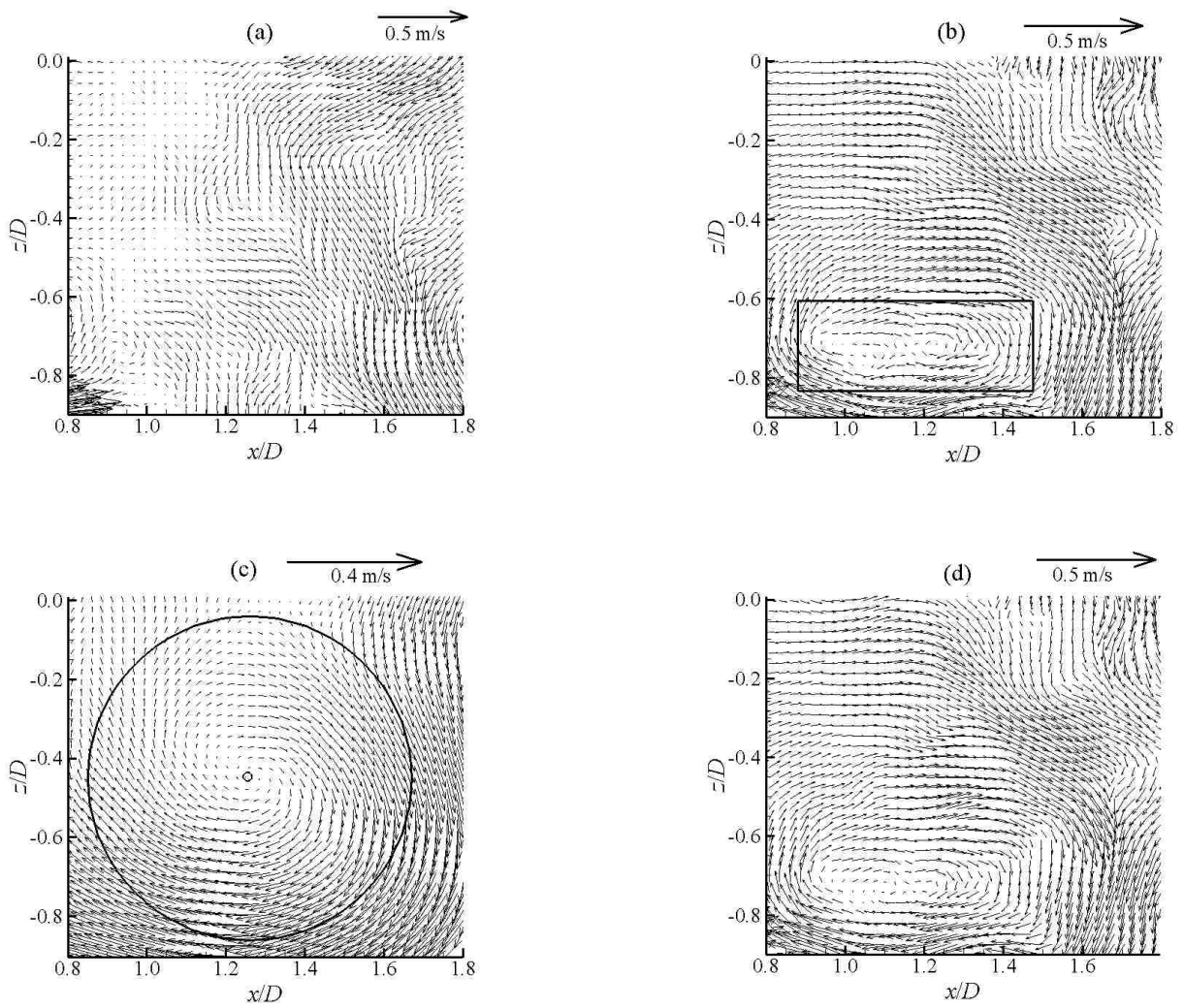
Figure 6.2: Example of (a) instantaneous, (b) fluctuating, (c) reconstructed (~40% energy), and (d) reconstructed (~95% energy) vector field.
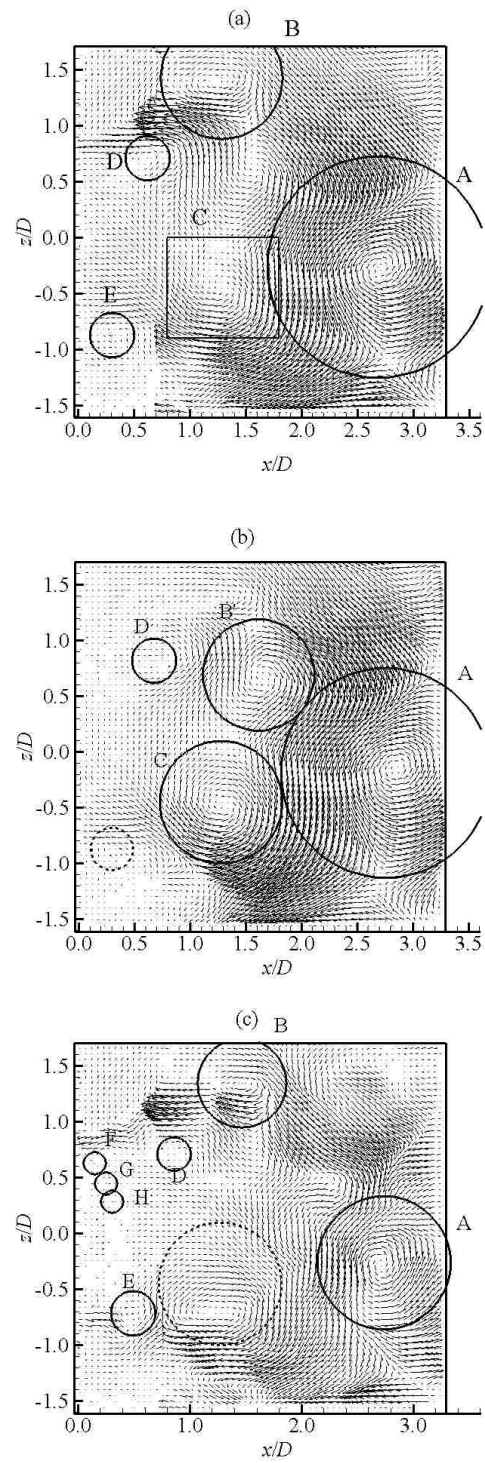
Figure 6.3: POD reconstructed velocity field for (a) modes 1-6 (~35% energy), (b) modes 1-15 (~50% energy) and (c) modes 1-99 (~80% energy).
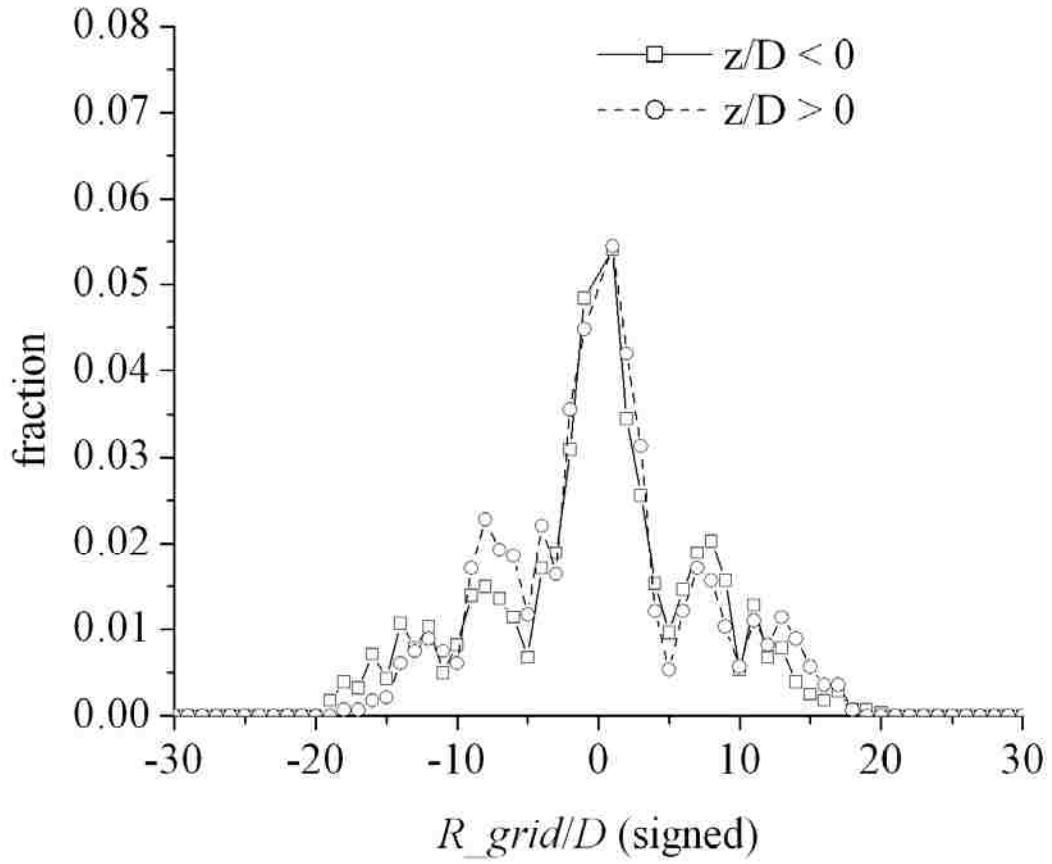
Figure 6.4: Distribution of number of identified structures on each sides of the wake, sorted by rotational sense.
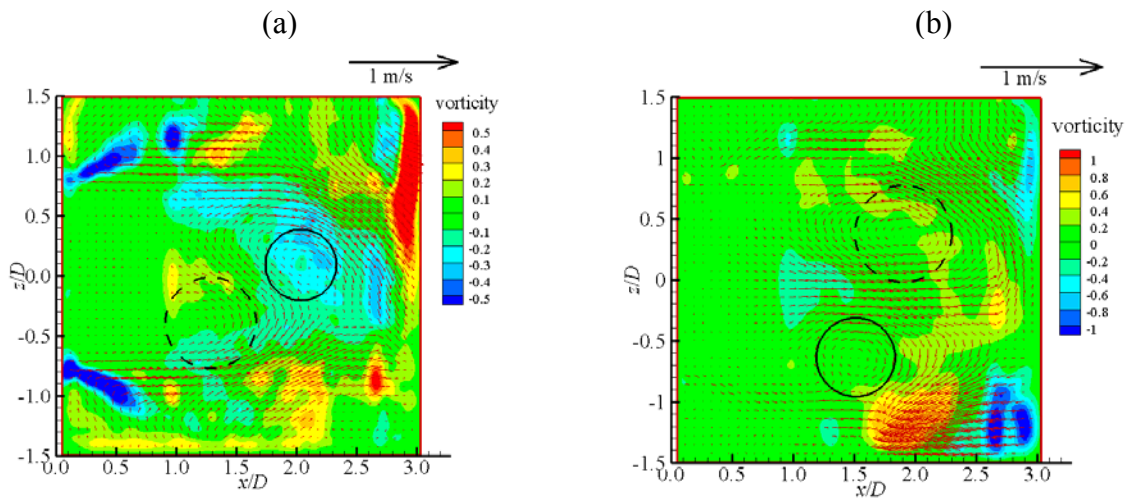
Figure 6.5: Some typical POD reconstructed FOV to highlight the meandering nature of the wake from NB1.
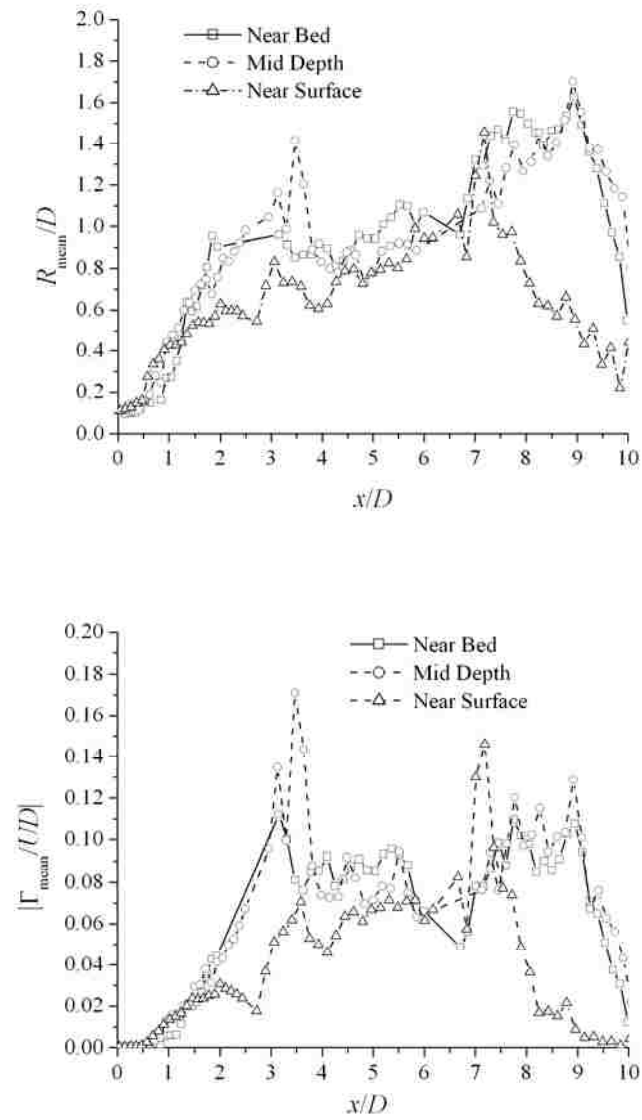
Figure 6.6: Variation of the mean size and circulation of the coherent structures with streamwise direction.
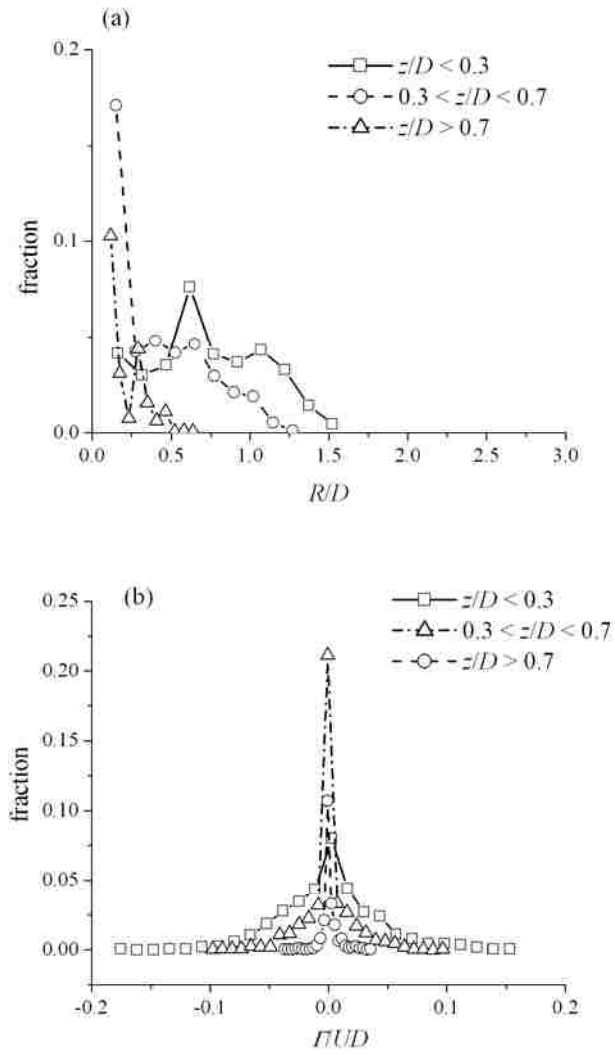
Figure 6.7: Distribution function of (a) size and (b) normalized circulation of the coherent structures at field-of-view NB1.
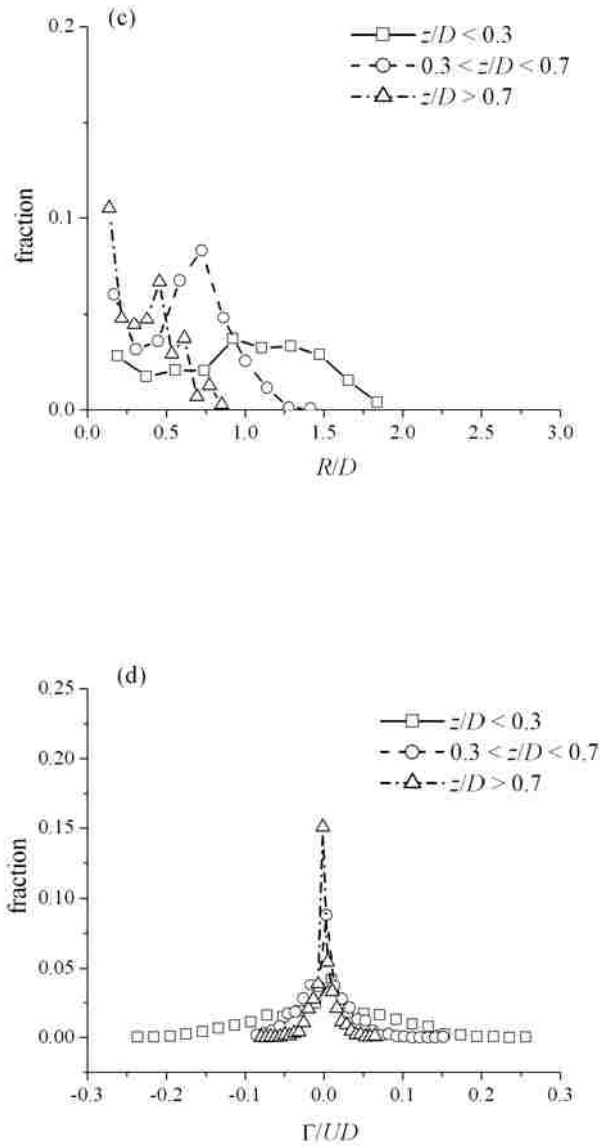
Figure 6.8: Distribution function of (c) size and (d) normalized circulation of the coherent structures at field-of-view MD1.
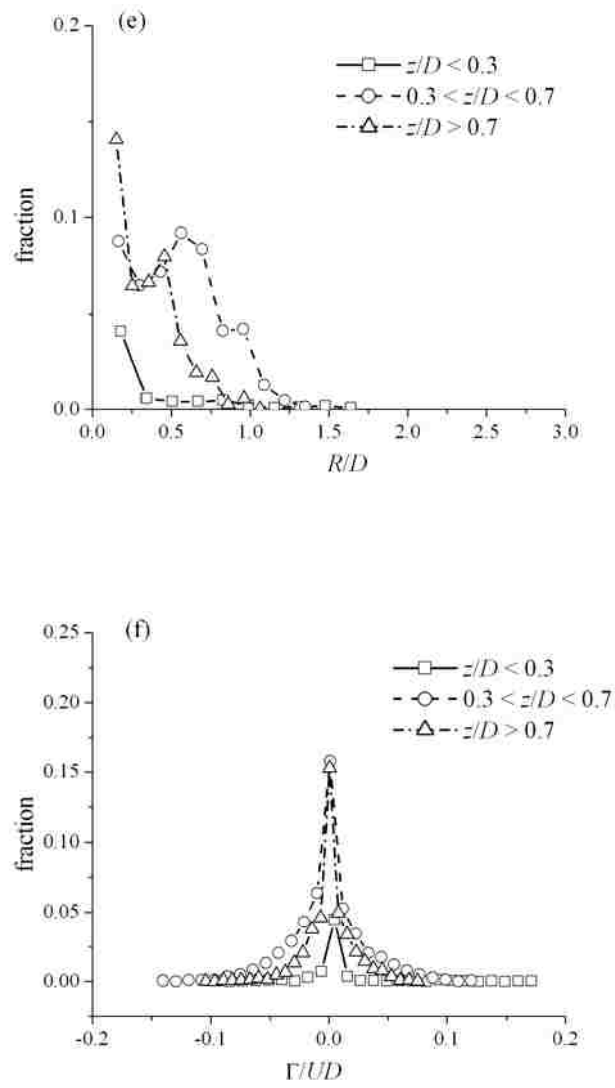
Figure 6.9: Distribution function of (e) size and (f) normalized circulation of the coherent structures at field-of-view NS1.
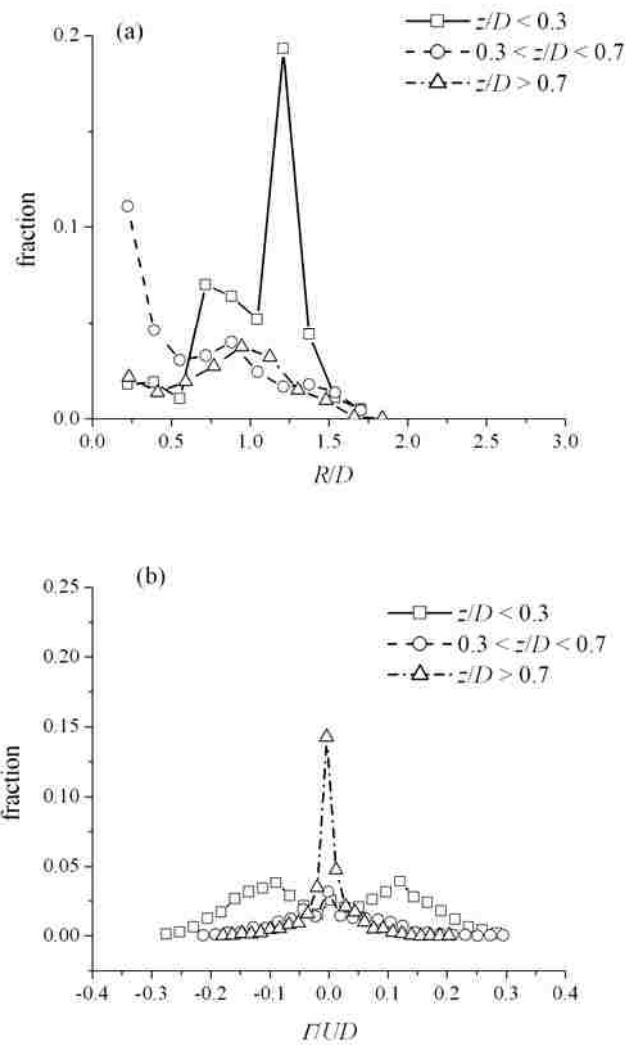
Figure 6.10: Distribution function of (a) size and (b) normalized circulation of the coherent structures at field-of-view NB2.
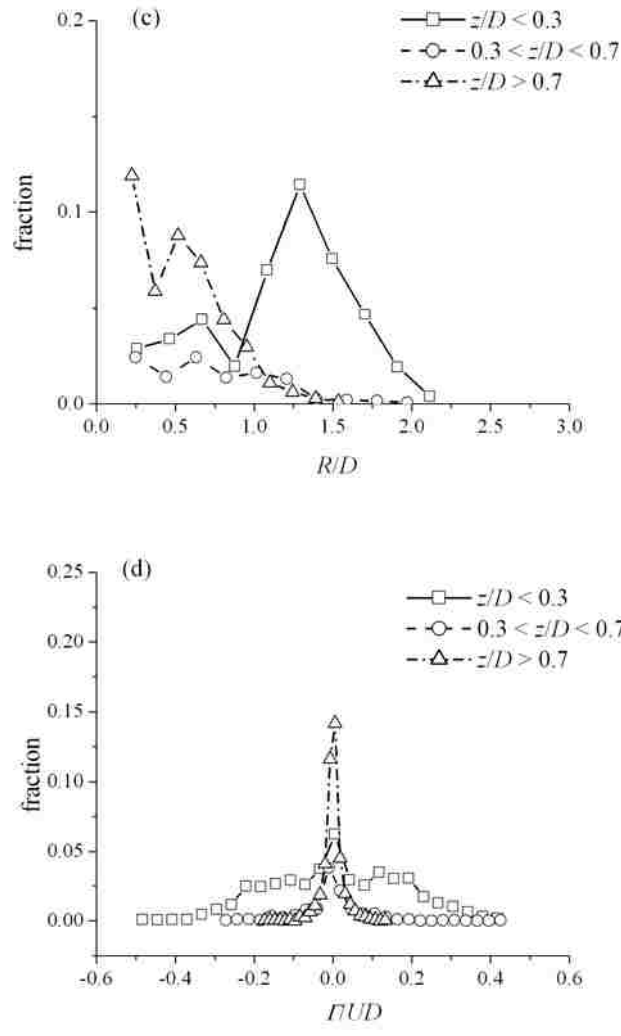
Figure 6.11: Distribution function of (c) occurrence and (d) normalized circulation of the coherent structures at field-of-view MD2.
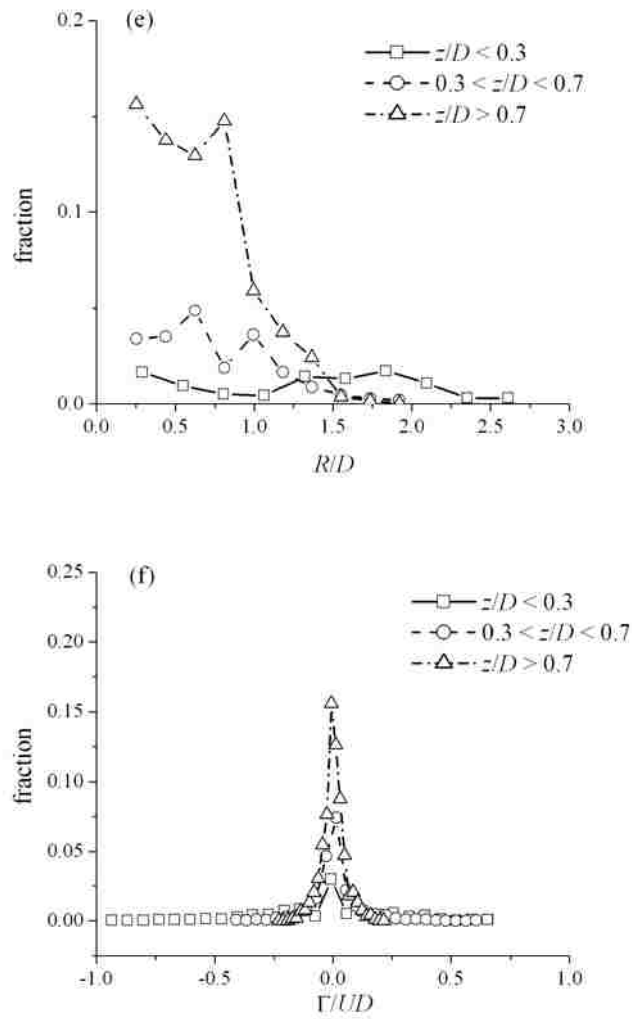
Figure 6.12: Distribution function of (e) size and (f) normalized circulation of the coherent structures at field-of-view NS2.
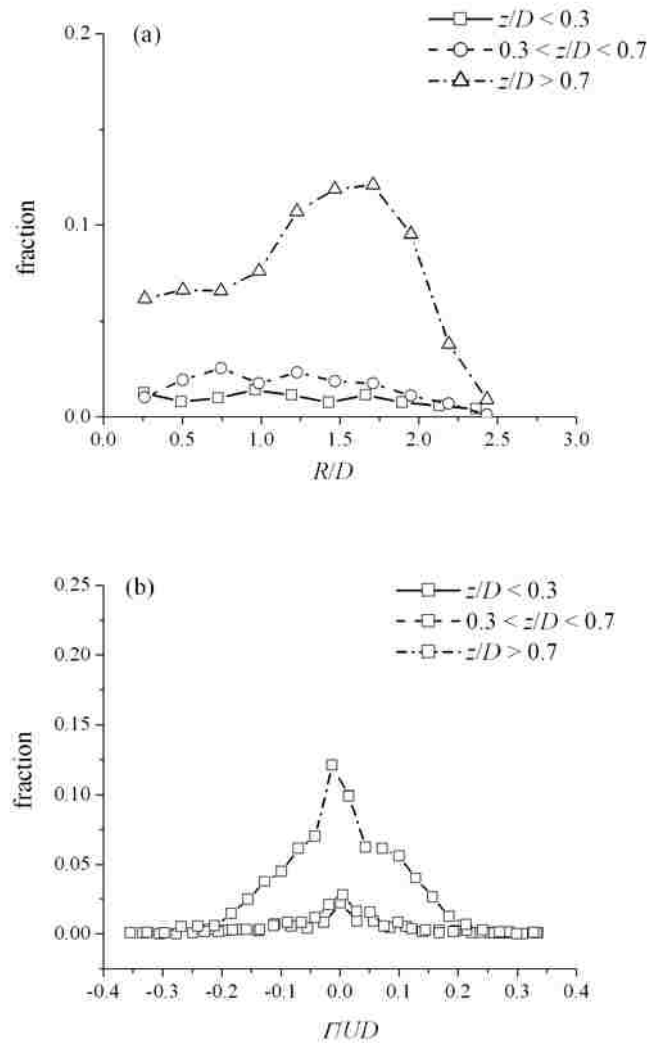
Figure 6.13: Distribution function of (a) size and (b) normalized circulation of the coherent structures at field-of-view NB3.
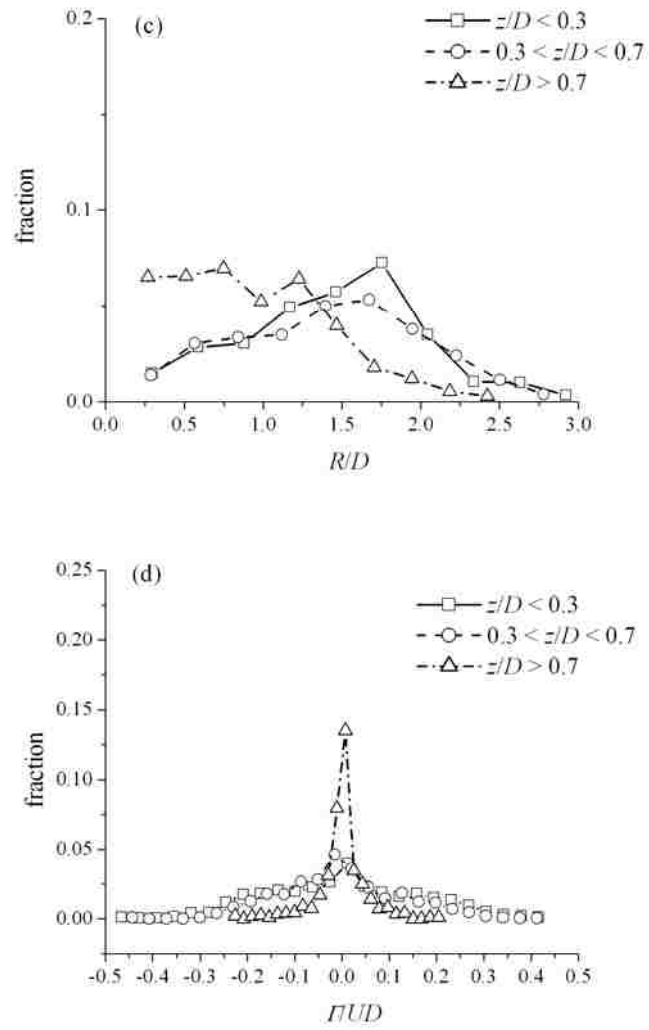
Figure 6.14: Distribution function of (c) size and (d) normalized circulation of the coherent structures at field-of-view MD3.
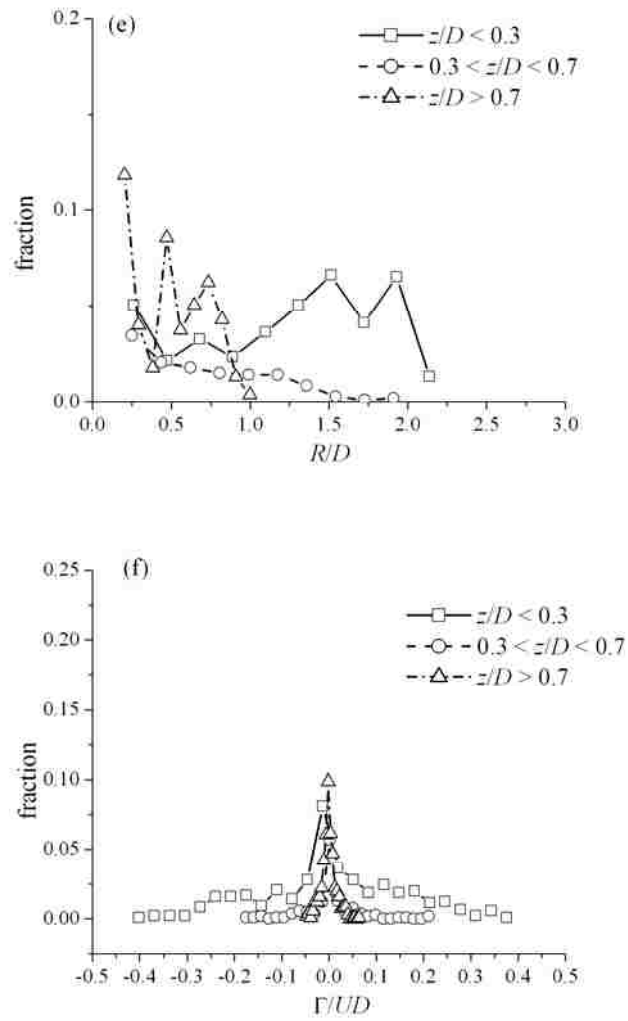
Figure 6.15: Distribution function of (e) size and (f) normalized circulation of the coherent structures at field-of-view NS3.

$$|\Pi/UD| = k(R/D)^2$$
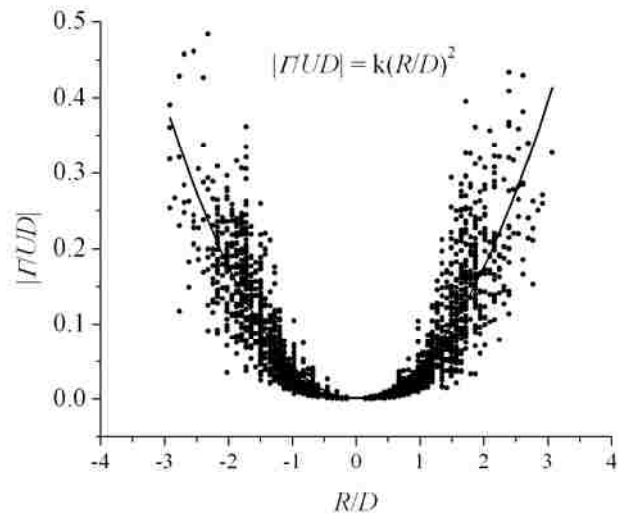
Figure 6.16: Modeling of circulation associated with the identified structures for a typical field of view (NS1).

Table 6.1: Summary of vortex identification in different field-of-views.

Field-of-view (FOV)		Location y/H	FOV size (mm)	Spatial resolution (mm)	Energy content of reconstructed field (%)	Number of vortices identified	N_{CW}/N_{CCW}
Station 1	NB1	0.10 $0 \leq x/D \leq 3$	90.9	0.715	39.9	2812	0.95
	MD1	0.50 $0 \leq x/D \leq 3$	101.3	0.797	39.8	3611	1.00
	NS1	0.80 $0 \leq x/D \leq 3$	103.8	0.817	40.7	3859	1.02
Station 2	NB2	0.10 $3 \leq x/D \leq 7$	144.8	1.14	40.1	3422	1.00
	MD2	0.50 $3 \leq x/D \leq 7$	153.2	1.21	41.0	2479	0.95
	NS2	0.80 $3 \leq x/D \leq 7$	164.0	1.29	40.5	2988	0.95
Station 3	NB3	0.10 $6 \leq x/D \leq 10$	145.2	1.14	40.6	2654	0.98
	MD3	0.50 $6 \leq x/D \leq 10$	153.2	1.21	41.2	2008	1.02
	NS3	0.80 $6 \leq x/D \leq 10$	164.0	1.29	39.0	1074	0.95

Table 6.2: Summary of the fraction of the number (N_f) of identified coherent structures at different fields-of-view.

Field-of-view (FOV)		$R/D < 0.2$ N_{f1}	$0.2 < R/D < 0.5$ N_{f2}	$0.5 < R/D < 0.7$ N_{f3}	$R/D > 0.7$ N_{f4}
Station 1	NB1	0.34	0.24	0.14	0.26
	MD1	0.23	0.25	0.18	0.32
	NS1	0.20	0.39	0.22	0.18
Station 2	NB2	0.08	0.16	0.07	0.67
	MD2	0.10	0.22	0.16	0.50
	NS2	0.08	0.29	0.15	0.46
Station 3	NB3	0.03	0.11	0.06	0.79
	MD3	0.04	0.10	0.09	0.75
	NS3	0.13	0.25	0.11	0.49

Table 6.3: List of k_c values

Field-of-view (FOV)	k
NB1	0.044
NB2	0.079
NB3	0.038
MD1	0.052
MD2	0.082
MD3	0.044
NS1	0.059
NS2	0.079
NS3	0.059

Chapter 7

CONCLUSIONS AND FUTURE RECOMMENDATIONS

7.1 Conclusions

This work has focused on exploring the vertical variability of a typical shallow wake generated in an open channel flow. The bluff body has fixed flow separation points and the effects of flow Reynolds number are minimized. The width of the body was 30 mm, and was immersed in the channel flow depth of 100 mm. The aspect ratio of the channel flow was 12, large enough to assume negligible effect of secondary currents. Two different sets of experiments were performed at freestream velocity of 0.19 m/s and 0.45 m/s, respectively.

Particle image velocimetry was used to measure the instantaneous flow velocities at three vertical locations downstream of the body, at near-bed, mid-depth and near-surface locations. Measurements were taken for a streamwise distance of 0-10D, where D is the width of the body. The mean velocity, turbulent intensity and Reynolds stress were compared at all these locations, to illustrate the vertical variability of the flow. The characteristic of the large-scale coherent structures were also investigated. The proper orthogonal decomposition method, in conjunction with a suitable structure identification scheme, was used to expose the coherent structures. The distribution function of the position, size and strength of these coherent structures were tabulated in Chapter 6. Each chapter was concluded with the specific conclusions drawn from each of them.

216

The negligible effect of Reynolds number can be inferred by comparing the result of first and second series of experiments, with Reynolds number Re = 19, 000 and 45, 000. For the first series of experiment, the location of saddle point at near-bed location was $x/D \approx 2.7$, whereas the location of the foci was indeterminate due to the size of field-of-view. For the second series of experiment, the location of saddle and foci are at $x/D \approx$ 2.7 and 1.6, respectively. Similarly, the location of the saddle points and foci at mid depth location for first and second series of experiments are $x/D \approx$ 2.4, 3.9 and 2, 4; respectively. At the near-surface location, the locations of the foci for first and second series of experiment are $x/D \approx$ 3.2 and 3.5, respectively. Plot 4.2-4.4 and 4.8-4.12 were reproduced from the second experiment, and they match closely enough to validate the conclusion from the first set of experiments.

From a global perspective, the main conclusions may be summarized as follows.

- Despite the small stability number, the wake profiles indicate considerable vertical variability and three-dimensionality. The effect of the background shallow open channel flow, perhaps, contributes to the variability.

- The size of the recirculation region, downstream of the body, shows a clear indication of the three-dimensionality and vertical variability of the wake flow under investigation. It was found that the size of the recirculation region is the largest at the mid-depth location, and smallest at the near-bed location. Again, at the near-surface region, the size of the recirculation region decreases, but not to the extent compared to the near-bed region.

- At the near-bed region, very close to the body, at $x/D < 0.5$, a small region of positive streamwise velocity can be observed. Usually, in the wake flow, momentum gets transferred from the outer accelerating flow region towards the inner recirculation region. But, because of the presence of this positive velocity, slight reverse transfer of momentum can be observed in this region.

- The shallow flow was shown to be rich in quasi-streamwise vortical elements at the boundaries, that is, the bed and the free surface. These structures were found to thrust flow from the boundary towards the flow domain, and therefore contribute to the drastic turbulent kinetic energy redistribution at the boundaries.

- It is well known that sweep and ejection events occur at the bed. But, events resembling them were also discovered at the free surface, which may contribute towards the near-surface flow physics.

- The defect velocity profile and the entrainment coefficient of the wake do not exhibit strong effect of the shallow condition. But, the axial variation of the half-width of the shallow wake was found to be affected significantly. The bed friction was found to arrest the transverse growth of the wake, but the friction effect dampens out with increasing distance from the bed.

- Close to the bed, the separated shear layers from the body were found to be slightly tilted towards the central plane, but at the mid-depth the tendency decreases. Again, at the free surface, a completely reverse trend was observed the shear layers tend to tilt outward towards the accelerating flow region.

218

- The instantaneous streamline pattern shows signature of the owl-face of the first kind, and the locations of saddle point and foci at different vertical locations were consistent.

- Signature of the legs of the horseshoe vortex can be found at the near-bed location, till $x/D < 1.0$, and that contributes towards increased momentum transfer at the bed.

- Swirling strength analysis was performed to identify vortex cores from the instantaneous flow fields, and the results indicate negligible effect of the bed or freesurface towards the vortex shedding of the flow. Also, the time fraction of the signed swirling strength does not show signature of vertical variability, but the transverse location of the maximum swirling strength changes with increasing distance from the bed. Close to the bed, the bed friction was found to dissipate the vorticity more quickly than at the mid-depth or near-surface region.

- POD was applied successfully to extract the information about the coherent structures. The size of the structures was found to exceed 200% of the body width or 50% of the depth of flow. The characteristics match well with the previously documented information about two-dimensional coherent structures. The uniqueness of the method of eduction used in the present study is its robustness.

- Evidence of the pairing/tearing process of the two-dimensional coherent structures was also observed in the POD reconstructed flow field.

- Due to the meandering nature of the wake (note that the present shallow wake falls in the category of vortex street) the distribution function of of the clockwise and counterclockwise structures on both sides of the wake looks similar.

- The size of the identified coherent structures monotonically increases in the streamwise direction at all vertical locations. This, along with the fact that the number of identified coherent structures decreases in the streamwise direction, is a direct indication of the merging of two or more structures to generate a stronger larger size structure. This observation was also supported by the axial variation of the mean strength of the coherent structures.

- The size of the identified structures exhibit vertical variability. The size of the structures was smallest at the near-bed location, but increases at the mid-depth location. Again, at the near-surface location there is a slight decrease of the size of the identified structures. Statistically speaking, the probability of finding a larger structure is higher at the mid-depth location than at the near-bed and surprisingly, at near-surface. This may suggests that the free-surface may be modeled as a 'weak wall'.

- The distribution function of the identified structures also exhibits proof of vertical variability. Near the body, close to the bed, they are agglomorate at the central region. Close to the body, at the near-surface location, a majority of the structures were identified at the accelerated flow region. But, with increase of the

streamwise distance, this inhomogeneity tends to smooth out and the distribution function starts to look similar.

- For all the identified coherent structures, it was found that the larger structures are associated with higher circulation and smaller structures are associated with smaller circulation. The non-dimensional circulation was found to be directly proportional to the square of the non-dimensional size of the structure, and the constant of proportionality was found to be a function of the streamwise distance.

7.2 Recommendations for future work

The present experimental work tried to shed some light on the behaviour of the shallow wake. But, as expected, this work also raised several questions. Some recommendations for the future work are as follows

- A full-fledged computational work is needed to complement the present work.

- The dynamics of the coherent structures are not quantified beyond 10D. Further experimental analysis would be needed to throw light on the dynamics of the coherent structures in the far-wake region.

- Another important aspect of this study can be complemented by concentration measurement using Planer Laser Induced Flouriscence to correlate the role of the coherent structures in mass transfer. This would help to design effective discharge systems in shallow lakes and rivers.

- The coherent structure identification code should be modified to take into account the eccentricity of the coherent structures. A good starting point may be a swirling strength based algorithm.

References

Adrian, R. J., Particle imaging techniques for experimental fluid mechanics, Ann. Rev. Fluid. Mech. 23, pp 263-304, 1991.

Adrian, R. J., Hairpin vortex organization in wall turbulence, Phys. Fluids., 19, pp 041301-16, 2007.

Agarwal, A., Prasad, A. K., Properties of vortices in the self-similar turbulent jet, Exp. Fluids., 33**,** p 565-577**,** 2002.

Akilli, H., Rockwell, D., Vortex formation from a cylinder at shallow flow, Phys. Fluids, 14, pp 2957-2967, 2002.

Anthony, D. G., Willmarth, W. W., Turbulence measurements in round jet beneath a free surface, J. Fluid Mech, 243, pp 699-720, 1992.

Balachandar, R. Bhuiyan, F., Higher-order moments of velocity fluctuations in an open channel flow with large bottom roughness, J. Hyd. Engg., 133, pp.77-87, 2007.

Balachandar, R., Tachie, M. F., Chu, V. H., Concentration profiles in shallow turbulent wakes, J. Fluids Engg., 121, pp 34-40, 1999.

Balachandar, R., Ramachandran, S., Tachie, M. F., Characteristic of shallow turbulent near wakes at low Reynolds number, J. Fluids Engg., pp 302-308, 2000.

Tachie, M. F., Balachandar, R., , Shallow wake generated on smooth and rough surfaces, Exp. Fluids., 30, pp 467-474, 2001.

Barbarutsi, S., Chu, V. H., Experimental study of turbulent mixing layers in shallow open channel flow, Technical Report 85-1, McGill University, 1985.

Blackwelder, R. F., Kovasznay, L. S. G., Time scales and correlations in a turbulent boundary layer, Phys. Fluids. 15, pp 1545-1555, 1972.

Bonnet, J. P., Delvillie, J., Glauser, M. N., Antonia, R. A., Bisset, D. K., Cole, D. R., Fiedler, H. E. Garem. J. H., Hilberg, D., Jeong, J., Kevlahan, N. K. R., Ukeiley, L. S., Vincendeau, E., Collaborative testing of eddy structure identification methods in free turbulence shear flows, Exp. Fluids, 25, pp 197-225, 1998.

Carmer, C. F. V., Shallow turbulent wake flows: Momentum and mass transfer due to Coherent Structures, PhD Dissertation, Hydromechanics Lab, University of Karlsruhe, 2005.

Carmer, C. F. V., Jirka, G. H., On turbulent and transport in shallow wake flows, IAHR Conference, Beijing, 2001.

Cazemier, W., Verstappen, R. W. C. P., Veldman, A E. P., 1998, Proper orthogonal decomposition and low dimensional models for driven cavity flows, Phys. Fluids., 10, 1998.

Chen, D., Jirka, G. H., Experimental study of plane turbulent wakes in a shallow water layer, 16, Fluid Dyn. Res., pp 11-41, 1995.

Chen, D., Jirka, G. H., Linear instability analyses of turbulent mixing layers and jets in shallow water layers, J. Hyd. Res., 36, 1998.

Chu, V. H., Wu, J. H., Khayat, R. E., Stability of turbulent shear flows in shallow channels, Proceedings of 20th IAHR Congress, Moscow, 1983.

Citriniti, N. R., George, W. K., Mixing character and meandering mechanism of a plane jet bounded in shallow water layer, IUTAM Symposium on simulation and identification of organized structures in flows, Lyngby, Denmark, 1997.

Clift, R., Grace, J. R., Weber, M. E., Bubbles, drops and particles, Academic Press, London, 1978.

Clauser, F., 1954, Turbulent boundary layers in adverse pressure gradient, J. Aero. Sci., 21, pp 91-108, 1954.

Cohn, R. K., Koochesfahani, M. M., Effect of boundary conditions on axial flow in a concentrated vortex core, Phys. Fluids, 5, pp 280-290, 1993.

Davenport, W. J., Simpson, R. L., Time-dependent and time-averaged turbulence structure near the nose of a wing-body junction, J. Fluid Mech., 210, pp 23–55, 1990.

Dommermuth, D. G., The initialization of vertical free surface flows, J. Fluids Engg., 116, pp 95-102, 1994.

Dong, S., Karniadakis, G. E., Ekmerci, E., Rockwell, D., A combined direct numerical simulation-particle image velocimetry study of turbulent near-wake, J. Fluid Mech., pp 185-207, 2007.

Dracos, T., Gigor, M., Jirka, G. H., Plane turbulent jets in a bounded fluid layer, J. Fluid Mech., 214, pp 587-614, 1992.

Eibeck, P. A., An experimental study of the flow downstream of a circular cylinder and tapered cylinder, J. Fluids Engg., 112, pp 393-401, 1990.

Falco, R. E., Coherent motions in the outer region of the turbulent boundary layer, Phys. Fluids., 20, pp 124-142, 1977.

Fu, H., Rockwell, D., Shallow wake past a cylinder: transitional phenomenon at low Reynolds number, J. Fluid Mech, 540, pp 675-697, 2005a.

Fu, H., Rockwell, D., Shallow flow past a cylinder: control of near wake, J. Fluids. Mech., 539, pp 1-24, 2005b.

Goldburg, W. I., Rutgers, M. A., Wu, X. I., Experiments on turbulence in soap-films, Physica A, pp 340-349, 239, 1997.

Gupta, R., Kumar S., Banerjee, S., Characteristics of attached vortices in free surface channel flows, 12th US National Congress of Applied Mechanics, Washington, 1994.

Hammache, M., Gharib, M., An experimental study of parallel and oblique vortex shedding from circular cylinder, J. Fluid Mech., 232, pp 567-590, 1991.

Handler, R. A., Swean, T. F. Jr., Leighton R. I., Swearingen, J. D., Length scale and energy balance for turbulence near a free surface, AIAA J., pp 311-320, 1993.

Head, M. R., Bandyopadhyay, P. R., New aspects of turbulent boundary-layer structures, J. Fluid. Mech., 107, pp 297-265, 1981.

Holmes, P., Lumley, J. L., Berkooz, G., Turbulence, Coherent structures, Dynamical Systems and Stability, Cambridge University Press, 1996.

Hunt, J. C. R., Graham, J. M. R., Free stream turbulence in near plane boundaries, J. Fluid Mech., 84, pp 209-235, 1978.

Hussain, A. K. M. F., Coherent structures - reality and myth, Phys. Fluids, 26, pp 2816-2850, 1983.

Ingram, R. G., Chu, V. H., Flow around islands in Rupert bay: An investigation of the bottom friction effect, J. Geophys. Res., 92, pp 14521-14523, 1987.

ITTC, Uncertainty analysis: particle image velocimetry, International Towing Tank Conference, 2008.

Jirka, G. H., Large scale flow structures and mixing processes in shallow flows, J. Hyd. Res., 39, pp 567-573, 2001.

Jirka G. H., Uijttewaal W. S. J., Shallow Flows, Taylor & Francis Group, London, 2004.

Kanda, S., Linden, A. P., Interaction of quasi-horizontal jet in bounded domains, Shallow flows, Taylor & Francis Group, London, 2004.

Kline, S. J., Robinson, S. K., Quasi-coherent structures in the turbulent boundary layer, Part I: Status report on a community wide summary of the data, in *Near Wall Turbulence*, Ed. Kline, S. J., Afgan, S. H., Hemisphere, New York, 1989.

Komori, S., Ueda, H., Ogino, F., Misushina, T., Turbulence structures and transport mechanism at the free surface in an open channel flow, Int. J. Heat Mass Transfer, 25, pp 513-521, 1982.

Komori, S., Nagaosa, R., Murakami, Y., Chiba, S., Ishii, K., Kuwahara, K., Direct numerical simulation of three-dimensional open channel flow with zero shear gas-liquid interface, Phys. Fluids, 5, pp 115-123, 1993.

Kraichnan, R., Inertial ranges in two-dimensional turbulence, Phys. Fluids, 10, pp 1417-1428, 1967.

Krogstad, P. A., Antonia, R. A., Structure of turbulent boundary layers on smooth and rough walls, J. Fluid Mech., 277, pp 1-21, 1994.

Lam, K., Banerjee, S., On condition of steak formation in a bounded turbulent flow, Phys. Fluids., 4, pp 306-312, 1992.

Liang, D, Jiang, C., Li, Y., Cellular neural network to detect spurious vectors in PIV data, Exp. Fluids, 34, pp 52-62, 2003.

Lin. J. C., Townfighi, J., Rockwell, D., Instanteneous structure of the near-wake of a circular cylinder: on the effect of Reynolds number, J. Fluids and Structures, 9, pp 409-418, 1995.

Lin, J. C., Ozgoren, M., Rockwell, D., Space-time development of the onset of a shallow −water vortex, J. Fluid Mech., 485, pp 33-66, 2003.

Logory, R. M., Hirsa, A., Anthony, D. G., Interaction of wake turbulence with a free surface, Phys. Fluids, 8, pp 805-815, 1996.

Lyn, D. A., Einav, S., Rodi, W., Park, J. H., A laser-Doppler velocimetry study of the ensamble-averaged characteristics of the turbulent near wake of a square cylinder, J. Fluid Mech., 304, pp 285-319, 1995.

Lumley, J. L., The structures of inhomogeneous turbulent flows, Atmos. Turb. Radio Wake Propg., pp 166-178, 1969.

Maheo, P., Free Surface Turbulent Shear Flow, PhD Dissertation, California Institute of Technology, 1999.

Monkewitz, P. A., The absolute and convective nature of instability in two- dimensional wakes at low Reynolds numbers, Phys. Fluids, 31(5), pp 999-1006, 1998.

Nagretti, M. E., Scott, S. A., Rummel, A. C., Jirka, G. H., Stabilization of cylinder wakes in shallow water flows by means of roughness elements: an experimental study, Exp. Fluids., 38, pp 403-414, 2005.

Nakagawa, S., Nitta, K., Senda, M., An experimental study on unsteady turbulent near wake of a rectangular cylinder in channel flow, Exp. in Fluids, 27, pp 284-294, 1994.

Nezu, I. and Nakagawa, H., *Turbulence in Open Channel Flows,* IAHR Monograph, A. A. Balkema, Rotterdam, The Netherlands, 1993.

Nikora, V., Nokes, R., Veale, W. Davidson, M, Jirka G. H., Large scale turbulent structure of uniform shallow free-surface flows, Environ. Fluid Mech., 7 pp 159-172, 2007.

Okoamoto, K., Nishio, S., Saga, T., Koboyashi, T., Standard images for particle image velocimetry, J. Meas. Sci. Tech., 11, pp 685-691, 2000.

Pan, Y., Banerjee, S., Numerical study of free surface turbulence in channel flow, Phys. Fluids., 7, pp 1649-1663, 1995.

Perrin, R., Braza, M., Cid, E., Cazin, S., Moradei, F., Barthet, A., Sevrain, A., Hoarau, Y., Near-wake turbulence properties in the high Reynolds number incompressible flow around a circular cylinder measured by two- and three-components PIV, Flow Turb. Comb., 77, p 185-204, 2006.

Perry, A. E., Chong, M. S., Topology of flow patterns in vortex motions and turbulence, Applied Scientific Research, 54 (3/4), pp 357-374, 1994.

Perry, A. E., Steiner, T. R., Large scale vortex structures in turbulent wakes behind bluff bodies: 1. Vortex formation process, J. Fluid Mech., 174, p 233-265, 1987.

Pope, S.B., *Turbulent flows*, Cambridge University Press, 2000.

Pokrajac, D., Campbell, L.J., Nikora, V., Manes, C., McEwan, I., Quadrant analysis of persistent spatial velocity perturbations over square-bar roughness., Exp. in Fluids*, 42, pp 413-423, 2007.

Raffel, M., Willart, C., Kompenhans, J., Particle Image Velocimetry: A practical guide, Springer-Verlag, Berlin, Germany, 1998.

Ramberg, S. E., The effect of yaw and finite length upon the vortex wakes of stationary and vibrating circular cylinder, J. Fluid Mech., 128, pp 81-107, 1983.

Rao, S. K., Sumner, D., Balachandar, R., A visualization study of fluid structure interaction between a circular cylinder and channel bed, J. Visualization, 7, pp 187-199, 2004.

Robinson, S. K., Coherent motions in the turbulent boundary layer, Ann. Rev. Fluid Mech., 23, pp 601-639, 1991.

Rogers, D. F., *Procedural elements for computer graphics*, McGraw Hill, 1997.

Roshko, J., Perspective on bluff-body aerodynamics, J. Wind Eng Ind. Aero., 49, p 79-100, 1993.

Roussinova, V. Shinneeb, A-M., and Balachandar, R. (2008). Investigation of fluid structures in a smooth open channel flow using proper orthogonal decomposition (POD), Under review at J. Hyd. Engg., 2008.

Sau, R. R. Hwang, Tony, W. H. S. ,Yang W. C., Interaction of trailing vortices in the wake of a wall-mounted rectangular cylinder, Phy. Rev. E., 68, pp 1-15, 2003.

Scorer, R. S., *Experimental Aerodynamics*, Ellis Horwood Limited, Chichester, 1978.

Shen, L., Zheng, X, Yue, D. K. P., Triantafyllou, G. S., The surface layer for free surface turbulent flow, J. Fluid Mech., 386, pp 167-221, 1999.

Shen, L., Triantafyllou, G. S., Yue, D. K. P., Turbulent diffusion near a free surface, J. Fluid Mech., 407, pp 145-166, 2000.

Shinneeb, A. M., Bugg, J. D., Balachandar, R., variable threshold outlier identification in PIV data, Measurement Sc. And Tech., 15, pp 1722-1732, 2004.

Shinneeb, A. M., Confinement effects in shallow water jets, PhD dissertation, University of Saskatchewan, 2006.

Shinneeb, A. M., Bugg, J. D., Balachandar, R., Quantititive investigation of vertical structures in the near-exit region of an axisymmetric turbulent jet, J. of Turbulence, 9, pp 1-20, 2008.

Simpson, R. L., Junction flows, Ann. Rev. Fluid. Mech., 33, pp 415-443, 2001.

Singha, A., Shinneeb, A-M, Balachandar, R., PIV-POD investigation of the wake of a sharp-edged flat bluff body immersed in a shallow channel flow, J. Fluids. Engg., 131, p 021202-1-12, 2009.

Sirovich, L., Turbulence and the dynamics of coherent structures. Part I: Coherent structures, Quarterly of Applied Math., XLV(3), pp. 561-571, 1987.

Tachie, M. F., Scalar Transport in Intermediate Two-dimensional Turbulent Wakes, M. A. Sc. Thesis, University of Saskatchewan, 1997.

Theodorsen, T., The structures of turbulence, 50th *Jahre Grenzschictforschubg*, Ed. H Gortier, W. Tolmien, Friedrich Vieweg & Sohn, Braunschweig, 1995.

Uijtewaal, W. S. J., Tukker, T., Development of quasi-two-dimensional structures in shallow free surface mixing layer, Exp. Fluids, 24, pp 192-200, 1998.

Umeda, S., Yang, W.J., Comparison of wake flows behind square and square circular cylinders, J. Flow Visualization and Image Processing, 8, pp 69-79, 2001.

Van Dyke, M., An Album of Fluid Motions, Parabolic Press, Stanford, CA, 1982.

Visualization Society of Japan, Handbook of particle imge velocimetry, Morikita publishing (Japanese), 2002.

Vriend, H. J. D., Complex flows in civil and environmental engineering, Shallow flows, ed: Jirka, G. H., Uijttewaal, W. S. J., Taylor and Francis, 2004.

Walker, D. T., Johnston, V. G., Observation of turbulence near the free surface in the wake of a model ship, dynamics of bubbles and vortices near a surface, Ed. Sahin, I, Tryggvasan, ASME, AMD 119, 1991.

Walker, D. T., Leighton, R. I., Garza-Rios, L. O., Shear free turbulence near a flat free surface, J. Fluids Mech., 320, pp 19-51, 1996.

Wang, H. F., Zhou, Y., Chen, C. K., Lam, K. S., Effect of initial conditions on interaction between a boundary layer and a wall mounted finite length cylinder wake, Phys. Fluids. 18, pp 065106-11, 2006.

Wei, T., Smith, C. R., Secondary vortices in the wake of circular cylinder, J. Fluid. Mech., 169, pp 513-533, 1986.

Williamson, C. H. K., Vortex dynamics in the wake of cylinders, Fluid Motions, ed. Green, S. I., pp 155-234, 1995.

Williamson, C. H. K., Vortex dynamics in the cylinder wake, Ann. Rev. Fluid Mech., pp 477-539, 1996.

Willart, C. E., Gharib, M., The interaction of modulated vortex pairs with free surface, FED Vol 101, Free Surface Turbulence, 25-36, ASME, 1994.

Wolonski, E., Imberger, J., Heron, M. L., Island wakes in shallow coastal waters, J. Geophys. Res., 89, pp 10533-10569, 1984.

Wu, Y., Christensen, K. T., Population trends of spanwise vortices in wall turbulence, J. Fluid Mech., 568, pp 55-76, 2006.

Zheng, C., Shen, L., Yue, D. K. P., The mechanism of vortex connection at a free surface, J. Fluids Mech, 384, pp 207-241, 1999.

Zhou, J., Adrian, R. J., Balachandar, S., Kendall, T. M., Mechanism for generating coherent packets of hairpin vortices in channel flow, J. Fluid Mech., 387, pp 353-396, 1999.

Zdravkovich, M., Flow Around Circular Cylinder, Volume 1, Oxford University Press, New York, 1997.

Appendix A

Uncertainty Estimates of Velocity Measurement

7.3 Uncertainty estimates of measurement

The overall measurement accuracy of a typical PIV image depends on a variety of processes, starting from the recording of images to the analysis of images. As the PIV system is composed of different subsystems, the estimate of the individual uncertainty associated with each of these subsystem are need to be evaluated. The absolute error in the estimate can be decomposed into two components – systematic error and the residual error. The systematic error arises due to the inadequacy of the statistical method of cross-correlation in the evaluation of the PIV recording, such as use of an inappropriate subpixel peak estimator. The second type of error, the residual error, remains in the system even if all the systematic errors from the measurement have been removed.

The guideline of uncertainty analysis of PIV dataset was proposed by the Visualization Society of Japan (VSJ, 2002). Based on this procedure, a guideline of the estimation of the uncertainty of PIV dataset was put forward by the International Towing Truck Conference (ITTC, 2008). In the present case, the uncertainty analysis was carried out according to the procedure pointed out by the guideline.

For the procedure, the field-of-view MD2 was selected. The uncertainty estimates from all other fields-of-view was expected to be same order of magnitude. The estimation of each of the error sources is briefly described below. The principle of PIV measurement can be described by the following equation (ITTC, 2008).

234

$$u = \alpha \left(\frac{\Delta x}{\Delta t} \right) + \delta u \, ; \tag{A.1}$$

where α, Δx, Δt are the magnification factor, displacement of the particle image, and time interval of the successive images, respectively. This equation is essentially the same as equation (3.1), only the extra term of δu comes into play. The magnification factor was determined by the calibration prior to the experiment. The PIV data analysis process depends on the visualization of the flow field by tracer particles and there is always a certain lag between the response of the tracer particles and the actual flow. These uncertainties consolidate into a parameter δu. In the next section, the sources of uncertainty in each of these four parameters are examined individually and the propagation of the total uncertainty was found out. The typical values of the uncertainties associated with the calculation are tabulated in Table 7.1, Table 7.2 and Table 7.3. In these tables, $u(x_i)$, $c_{i,}$ and u_c denote the typical unit uncertainty of the variable x_i, the sensitivity coefficient of the uncertainty of that particular variable and the cumulative uncertainty as a result of the sources as mentioned in the i-list. In all the cases, the expression of the sensitivity coefficient was borrowed from the guideline, as mentioned above. In the present context, only a short summary of the error source was mentioned. Detail definition of each source of error can be found in the guide.

7.3.1 Error in calibration, α

The sources of the error in the calibration are as follows:

7.3.1.1 Image distance of the reference point

The distance of the reference points were measured on the image plane. If the position of the reference point was detected from a single point, the typical uncertainty band will be 0.7 pixels. The sensitivity of the uncertainty was given as 3.84×10^{-4} mm/pixels^2.

7.3.1.2 Physical distance from the reference point

The uncertainty of the physical length of the reference point also affects the accuracy of the magnification factor. In a present case, a steel ruler was used, and the maximum uncertainty can be estimated to be 0.002 m.

7.3.1.3 Image distortion

The image could be affected by the aberration of the lens and the associated uncertainty. The distortion of the image would be less than 0.5% of the total length, that is $0.005L_r = 4$ pixels. The sensitivity coefficient of the estimate can be estimated to be 1.41×10^{-4} mm/pixels^2.

7.3.1.4 Distortion in the CCD device

It was assumed that there was no distortion in the CCD device and as a result, it did not contribute towards any uncertainty.

7.3.1.5 Ruler position

The position of the light sheet and the calibration ruler can be different. In that case, the maximum uncertainty was estimated to be 0.5 mm. The sensitivity coefficient is estimated to be 2.87×10^{-4} 1/pixel.

7.3.1.6 Ruler parallelism

Ideally, the ruler should be perpendicular to the camera axis. But, practically, it was always at an angle with the camera axis. The maximum misalignment was estimated to be 5^0, and the sensitivity coefficient can be estimated to be 0.011 mm/pixel.

7.3.2 Error in displacement of the particle image, Δx

The sources of the error in the displacement of the particle image are as follows:

7.3.2.1 Laser power fluctuation

The spatial and temporal fluctuations of the laser sheet will affect the detection and computation of the correlation peak in the PIV recording. If the experiment is very well controlled, the uncertainty due to this may be limited to 1/10 of the particle diameter. The sensitivity coefficient was estimated to be 13.06 pixels/mm.

7.3.2.2 Optical distortion by CCD

It is assumed that there was no optical distortion in the CCD device.

7.3.2.3 Normal viewing angle

If the illumination plane is not perpendicular to the camera axis, this could affect the velocity measurement. The angle is estimated to be maximum 5^0 off the normal and the sensitivity coefficient is 0.011 pixels/mm.

7.3.2.4 Mismatching error

In the pixel unit analysis, mis-matching of the paired particle can take place. Large errors can be detected by comparing the vector with the surrounding vectors, and replacing them. This is the step of spurious vector detection as discussed in section 3.3.5. The typical uncertainty due to this error can be estimated by preparing an artificial image (Okamoto et al., 2000), and was estimated to be about 0.2 pixels.

7.3.2.5 Sub-pixel analysis

The uncertainty of the subpixel analysis depends on a number of factors, like the size of the tracer particle, noise level of the image and particle concentration. In a conservative way, the uncertainty due to this was estimated to be 0.03 pixels (Okomoto et al., 2000).

7.3.3 Error in the time interval, Δt

The sources of the error in the estimation of time interval are as follows:

7.3.3.1 Delay generator

The delay generator controls the pulse timing and the uncertainty of that was 1×10^{-9} seconds, as found from the manual.

7.3.3.2 Pulse timing accuracy

The laser pulse has some extent of uncertainty associated with it. The typical uncertainty band, as found from the manual was 5×10^{-9} seconds.

7.3.4 Error in δu

The sources of the error in δu are as follows:

7.3.4.1 Particle trajectory

The particle trajectory depends on the local velocity gradient and the acceleration of the flow. When the tracer particle was assumed to follow the flow faithfully, the error due to the particle trajectory was 0.01% of the total velocity. For the maximum velocity of 0.45 m/s, the uncertainty was $0.45\times1000\times0.0001 = 0.045$ mm/s.

7.3.4.2 Three-dimensional effect

The out-of plane velocity vector also contributes towards the total uncertainty. When the out-of-plane velocity was assumed to be 1% of the total flow, the uncertainty can be estimated to be 0.73 mm/s.

7.3.5 Error in the measurement location, x

The sources of the error in the measurement location, x are as follows:

7.3.5.1 Centre position of the correlation area

The centre position of the correlation area was defined in terms of the grid, and the maximum uncertainty can be 0.5 grid point.

7.3.5.2 Nonuniformity of tracer particle density

The flow velocity was identified with the displacement of the particle. This estimation can be affected by non-uniform density of the tracer particle. The possibility of bias error due to this was maximum ¼ of the correlation area size.

7.3.6 Error in the measurement time, t

The error in the measurement time would come from the delay generator and from the error in the pulse.

7.4 Summary of uncertainty calculation

The individual uncertainty sources and the total uncertainty of the instantaneous velocity is shown in Table 7.3. The total uncertainty of the instantaneous velocity is estimated to be 14.32 mm/sec, or 3.18%. The typical uncertainty in the measurement of the displacement and time interval are 0.3366 mm and 5.09×10^{-9} seconds, respectively.

Table 7.1: Uncertainty estimates from different sources.

Parameter	Category	Error source	$u(x_i)$ (unit)	C_i (unit)	$C_i\,u(x_i)$	u_c
α (mm/pixel)	Calibration	Reference image	0.7 (pixel)	3.84×10^{-4} mm/pixel^2	2.68×10^{-4}	0.00115
		Physical distance	0.02 (mm)	1.22×10^{-3} (1/pixel)	2.44×10^{-5}	
		Image distortion by lens	4 (pixel)	1.41×10^{-4} (mm/pixel^2)	5.64×10^{-4}	
		Image distortion by CCD	0 (pixel)	0	0	
		Ruler position	0.5 (mm)	2.87×10^{-4} (1/pixel)	1.435×10^{-4}	
		Parallelism	0.087 (rad)	0.011 (mm/pixel)	9.57×10^{-4}	
ΔX (pixel)	Acquisition	Laser power fluctuation	0.0017 (mm)	13.06 (pixel/mm)	0.0222	0.203

		Image distortion by CCD	0	0	0	
		Normal view angle	0.087 (rad)	0.011 (mm/pixel)	9.57×10^{-4}	
	Reduction	Mismatching error	0.2 (pixel)	1.0	0.2	
		Sub-pixel analysis	0.03 (pixel)	1.0	0.03	
Δt (sec)	Acquisition	Delay generator	1×10^{-9} (sec)	1.0	1×10^{-9}	5.09×10^{-9}
		Pulse time	5×10^{-9} (sec)	1.0	5×10^{-9}	
δu (mm/s)	Experiment	Particle trajectory	0.045 (mm/s)	1.0	0.045	0.731
		Three-dimensional effect	0.73 (mm/s)	1	0.73	

Table 7.2: Summary of uncertainty for the instantaneous velocity.

Parameter	Error source	$u(x_i)$ (unit)	C_i (unit)	$C_i \, u(x_i)$
α	Magnification factor	0.00115 (mm/pixel)	5880 (pixels/sec)	6.672
ΔX (pixel)	Image displacement	0.203 (pixel)	62.33 (mm/pixel/sec)	12.65
Δt (sec)	Image interval	5.09×10^{-9} (sec)	0.6	3.05×10^{-9}
δu	Experiment	0.731 (mm/s)	1	0.731
Combined uncertainty			14.32 (mm/s)	

Table 7.3: Summary of uncertainty of the estimate of displacement and time.

Parameter	Category	Error source	$u(x_i)$ (unit)	C_i (unit)	C_i $u(x_i)$
X_s, X_e	Acquisition	Digital error	0.5 (pixel)	0.0748 (mm/pixel)	0.0374
		Non-uniformity of distribution	4.0 (pixels)	0.0748 (mm/pixel)	0.2992
X_0	Calibration	Origin correlation	2.0 (pixel)	0.0748 (mm/pixel)	0.1496
			Combined uncertainty	0.3366 mm	

Parameter	Category	Error source	$u(x_i)$ (unit)	C_i (unit)	C_i $u(x_i)$

t_s, t_c	Acquisition	Delay generator	1×10^{-9} (sec)	1	1×10^{-9}
		Pulse time	5×10^{-9} (sec)	1	5×10^{-9}
			Combined uncertainty		5.09×10^{-9} (sec)

Appendix B

MATLAB® codes

7.5 General comments

Analysis of the PIV data files in a multi-step process. Appropriate Matlab ® scripts are developed for these steps. The Matlab ® scripts used in the present work are described here.

7.6 Variable outlier rejection code

```matlab
% This file will read all the VEC files from the experiments and convert
% them into data files containing the coordinates and velocity vector
% written.
clear all
close all
FileName=input('File Name','s');
SortExtn=input('Sort order extension','s');
Nfile=input('Number of files');
Nvec=input('Number of vectors');
CTh=input('Constant threshold');
VTH=input('Variable threshold');
NeuronC=input('Neuron connectivity for CCNN (r)');
Fwidth=input('Input gaussian filter width for vector replacement');
NeuronV=input('Neuron connectivity for VCNN (r)');
StartFile=input('Start file number');
Edge=input('Location of nearest edge of the body');
delT=input('Time seperation in seconds');
FOV=input('Size of field of view in m');
H=2*16;  %Gaussian signal width = 2gridpoints
% String header to write in the output data files
str1='VARIABLES=X,Y,U,V,flag';
str2='ZONE I=          127J=          127F=POINT';
str=strvcat(str1,str2);

%--------------------------------------------------------------------------
----
%           READING OF THE .VEC FILES
%--------------------------------------------------------------------------
----
for k=StartFile:StartFile+Nfile-1
    if (k < 10)
        title_num=['00000',int2str(k)];
        title=[FileName,title_num,'.',SortExtn,'.','VEC']
```

246

```
        [Xpixel Ypixel Upixel Vpixel CHC]=textread(title,'%f %f %f %f
%f','delimiter',',','headerlines',1);
        data=[Xpixel Ypixel -1.0*Upixel Vpixel];
    end

    if (k < 100 & k >=10)
        title_num=['0000',int2str(k)];
        title=[FileName,title_num,'.',SortExtn,'.','VEC']
        [Xpixel Ypixel Upixel Vpixel CHC]=textread(title,'%f %f %f %f
%f','delimiter',',','headerlines',1);
        data=[Xpixel Ypixel -1.0*Upixel Vpixel];
    end

    if (k < 1000 & k >= 100)
        title_num=['000',int2str(k)];
        title=[FileName,title_num,'.',SortExtn,'.','VEC']
        [Xpixel Ypixel Upixel Vpixel CHC]=textread(title,'%f %f %f %f
%f','delimiter',',','headerlines',1);
        data=[Xpixel Ypixel -1.0*Upixel Vpixel];
    end


    if (k < 10000 & k >= 1000)
        title_num=['00',int2str(k)];
        title=[FileName,title_num,'.',SortExtn,'.','VEC']
        [Xpixel Ypixel Upixel Vpixel CHC]=textread(title,'%f %f %f %f
%f','delimiter',',','headerlines',1);
        data=[Xpixel Ypixel -1.0*Upixel Vpixel];
    end

    if (k < 100000 & k >= 10000)
        title_num=['0',int2str(k)];
        title=[FileName,title_num,'.',SortExtn,'.','VEC']
        [Xpixel Ypixel Upixel Vpixel CHC]=textread(title,'%f %f %f %f
%f','delimiter',',','headerlines',1);
        data=[Xpixel Ypixel -1.0*Upixel Vpixel];
    end


%------------------------------------------------------------------------
----
%           READING OF THE .VEC FILES COMPLETED
%------------------------------------------------------------------------
----


%------------------------------------------------------------------------
----
%           OUTLIER REJECTION
%------------------------------------------------------------------------
----
%           Outlier rejection by CNN method (constant threshold)
```

247

```
%----------------------------------------------------------------------
----
    veldata=data;

    Xpixel=reshape(veldata(:,1),Nvec,Nvec);
    Ypixel=reshape(veldata(:,2),Nvec,Nvec);
    Upixel=reshape(veldata(:,3),Nvec,Nvec);
    Vpixel=reshape(veldata(:,4),Nvec,Nvec);


    Xraw=reshape(veldata(:,1),Nvec,Nvec);
    Yraw=reshape(veldata(:,2),Nvec,Nvec);
    Uraw=reshape(veldata(:,3),Nvec,Nvec);
    Vraw=reshape(veldata(:,4),Nvec,Nvec);

    % CNN method based on U velocity
    % Initial state of neuron set to 1
    flag(1:Nvec,1:Nvec)=1.0;

    gammaPreviousU(1:Nvec,1:Nvec)=1.0;
    gammaPreviousV(1:Nvec,1:Nvec)=1.0;

    gammaPresentU(1:Nvec,1:Nvec)=1.0;
    gammaPresentV(1:Nvec,1:Nvec)=1.0;

    MaxIter=100; %Maximum number of iterations
    disp('Performing CCNN check');
    for Iter=2:MaxIter
        Nflip_count=0.0;
        Nflip(1:Nvec,1:Nvec)=0;  %Nflip = 0 (good vector) 1 (bad
vector)
        Noutlier(Iter)=0;
        for j=1:Nvec
            for i=1:Nvec
                SumU=0.0;
                SumV=0.0;
                for jj=j-NeuronC:j+NeuronC
                    for ii=i-NeuronC:i+NeuronC
                        if (ii == i & jj == j) continue; end;
                        if (ii < 1 | jj < 1) continue; end;
                        if (ii > Nvec | jj > Nvec) continue; end;
                        Ru=abs(Upixel(i,j)-Upixel(ii,jj));
                        Rv=abs(Vpixel(i,j)-Vpixel(ii,jj));

                        Wu=max(-CTh,CTh-Ru);
                        Wv=max(-CTh,CTh-Rv);

                        SumU=SumU+Wu*gammaPreviousU(ii,jj);
                        SumV=SumV+Wv*gammaPreviousV(ii,jj);
                    end  %Closing jj loop
                end  % Closing ii loop
```

248

```matlab
        if(SumU < 0 | SumV < 0)
            gammaPresentU(i,j)=0.0;
            gammaPresentV(i,j)=0.0;
            Noutlier(Iter)=Noutlier(Iter)+1;
            flag(i,j)=0.0;
        else
            gammaPresentU(i,j)=1.0;
            gammaPresentV(i,j)=1.0;
            Noutlier(Iter)=Noutlier(Iter);
            flag(i,j)=1.0;
        end

        % Flagging unexpected high/low value vectors
        if(Upixel(i,j) > 500 | Vpixel(i,j) > 500)
            flag(i,j)=0.0;
            Upixel(i,j)=0.0;
            Vpixel(i,j)=0.0;
            Noutlier(Iter)=Noutlier(Iter)+1;
        end

        UDif(i,j)=abs(gammaPreviousU(i,j)-gammaPresentU(i,j));
        VDif(i,j)=abs(gammaPreviousV(i,j)-gammaPresentV(i,j));

        if (UDif(i,j) == 1 | VDif(i,j) == 1)
            Nflip(i,j)=1;
        else
            Nflip(i,j)=0;
        end


        % After 20 iterations flag flipping vectors as zero

        if (Iter > 20 & Nflip(i,j) == 1)
            flag(i,j)=0.0;
            Noutlier(Iter)=Noutlier(Iter)+1;
        end


    end % Closing i loop
end % Closing j loop


% Convergence criterion
% Counting Nflip
for i=1:Nvec
    for j=1:Nvec
        if(Nflip(i,j) == 1)
            Nflip_count=Nflip_count+1;
        end
    end
```

```matlab
            end

        gammaPreviousU(1:Nvec,1:Nvec)=gammaPresentU(1:Nvec,1:Nvec);
        gammaPreviousV(1:Nvec,1:Nvec)=gammaPresentV(1:Nvec,1:Nvec);

        if(abs(Noutlier(Iter)-Noutlier(Iter-1)) <= 0.01*Nvec*Nvec)
            disp('CNN method converged');
            break;
        end


    end % Closing loop for Iter

    for i=1:Nvec
        for j=1:Nvec
            if(Nflip(i,j) == 1)
                flag(i,j)=0.0;
                Noutlier(Iter)=Noutlier(Iter)+1;
            end
        end
    end

    disp('Final Outlier vectors'); (Noutlier(Iter)/(Nvec*Nvec))*100
    if(Iter == MaxIter)
        disp('CCNN method failed to converge, exit forcefully');
    end



    % ----------------------------------------------------------------
-------
    %    Replacing outlier vectors identified by CCNN
    % ----------------------------------------------------------------
-------

    disp('Replacing spurious vectors by Gaussian technique');
    for j=1:Nvec
        for i=1:Nvec
            sum1=0.0;
            sum2=0.0;
            sum3=0.0;

            if (flag(i,j) == 0)
                for ii=i-Fwidth:i+Fwidth
                    for jj=j-Fwidth:j+Fwidth

                        if(ii < 1 | jj < 1)
                            continue;
                        end

                        if(ii > Nvec | jj > Nvec)
                            continue;
```

```matlab
                            end

                            uT=Upixel(ii,jj);
                            vT=Vpixel(ii,jj);
                            delx=Xpixel(ii)-Xpixel(i);
                            dely=Ypixel(jj)-Ypixel(j);
                            R=sqrt(delx.^2+dely.^2);
                            Gauss=exp(-(0.5*(R/H)^2));

                            sum1=sum1+Gauss*flag(ii,jj);
                            sum2=sum2+Gauss*uT*flag(ii,jj);
                            sum3=sum3+Gauss*vT*flag(ii,jj);

                    end  % Closing jj loop
                end % Closing ii loop
                if (sum1 == 0)
                    Upixel(i,j)=0.0;
                    Vpixel(i,j)=0.0;
                end
                if (sum1 ~= 0)
                    Upixel(i,j)=sum2/sum1;
                    Vpixel(i,j)=sum3/sum1;
                end

            end % Closing flag if loop

        end % Closing i loop
    end % Closing j loop


    % ----------------------------------------------------------------
-------
    %  Outlier rejection by variable threshold
    % ----------------------------------------------------------------
-------
    % Calculating the threshold field
    disp('Calculating the threshold field');
    for j=1:Nvec
        for i=1:Nvec
            SumU=0.0;
            SumV=0.0;
            count=0;
            for jj=j-NeuronV:j+NeuronV
                for ii=i-NeuronV:i+NeuronV
                    if (ii == i & jj == j)
                        continue;
                    end
                    if(ii < 1 | jj < 1)
                        continue;
                    end
                    if(ii > Nvec | jj > Nvec)
                        continue;
```

251

```matlab
                        end
                        SumU=SumU+abs(Upixel(i,j)-Upixel(ii,jj));
                        SumV=SumV+abs(Vpixel(i,j)-Vpixel(ii,jj));
                        count=count+1;
                    end  %Closing jj loop
                end  % Closing ii loop
                if(SumU == 0)
                    VThu(i,j)=0;
                end

                if(SumU ~= 0)
                    VThu(i,j)=SumU/count;
                end

                if(SumV == 0)
                    VThv(i,j)=0;
                end

                if(SumV ~= 0)
                    VThv(i,j)=SumV/count;
                end
            end % Closing i loop
        end % Closing j loop


    % ----------------------------------------------------------------
--------
    % Smoothing the threshold field
    %-----------------------------------------------------------------
--------
    disp('Smoothing the threshold field');
    for j=1:Nvec
        for i=1:Nvec
            sum1=0.0;
            sum2=0.0;
            sum3=0.0;

            for ii=i-NeuronV:i+NeuronV
                for jj=j-NeuronV:j+NeuronV

                    if(ii < 1 | jj < 1)
                        continue;
                    end

                    if(ii > Nvec | jj > Nvec)
                        continue;
                    end

                    delx=Xpixel(ii)-Xpixel(i);
                    dely=Ypixel(jj)-Ypixel(j);
                    R=sqrt(delx.^2+dely.^2);
                    Gauss=exp(-(0.5*(R/H)^2));
                    sum1=sum1+Gauss;
```

252

```matlab
                    sum2=sum2+Gauss*VThu(ii,jj);
                    sum3=sum3+Gauss*VThv(ii,jj);

                end   % Closing jj loop
            end % Closing ii loop
            if (sum1 == 0)
                VThu(i,j)=0.0;
                VThv(i,j)=0.0;
            end
            if (sum1 ~= 0)
                VThu(i,j)=sum2/sum1;
                VThv(i,j)=sum3/sum1;
            end

        end % Closing i loop
    end % Closing j loop

    VThu(1:Nvec,1:Nvec)=VThu(1:Nvec,1:Nvec)+VTH;
    VThv(1:Nvec,1:Nvec)=VThv(1:Nvec,1:Nvec)+VTH;


    % -----------------------------------------------------------------
----
    % Clearing variables
    % -----------------------------------------------------------------
----
    clear Xpixel Ypixel Upixel Vpixel;
    clear gammaPreviousU gammaPreviousV;
    clear gammaPresentU gammaPresentU;
    clear flag;
    clear UDif VDif;
    clear Nflip Noutlier;
    clear SumU SumV sum1 sum2 sum3 count;
    clear Ru Rv Wu Wv;




    % -----------------------------------------------------------------
--------
    %   Outlier rejection with the threshold field
    % -----------------------------------------------------------------
--------
    flag(1:Nvec,1:Nvec)=1.0;

    gammaPreviousU(1:Nvec,1:Nvec)=1.0;
    gammaPreviousV(1:Nvec,1:Nvec)=1.0;

    gammaPresentU(1:Nvec,1:Nvec)=1.0;
    gammaPresentV(1:Nvec,1:Nvec)=1.0;

    disp('Performing VCNN check');
    for Iter=2:MaxIter
```

```
Nflip_count=0.0;
Nflip(1:Nvec,1:Nvec)=0;   %Nflip = 0 (good vector) 1 (bad
vector)
Noutlier(Iter)=0;
for j=1:Nvec
    for i=1:Nvec
        SumU=0.0;
        SumV=0.0;
        for jj=j-NeuronV:j+NeuronV
            for ii=i-NeuronV:i+NeuronV
                if (ii == i & jj == j) continue; end;
                if (ii < 1 | jj < 1) continue; end;
                if (ii > Nvec | jj > Nvec) continue; end;
                Ru=abs(Uraw(i,j)-Uraw(ii,jj));
                Rv=abs(Vraw(i,j)-Vraw(ii,jj));

                Wu=max(-VThu(ii,jj),VThu(ii,jj)-Ru);
                Wv=max(-VThu(ii,jj),VThu(ii,jj)-Rv);

                SumU=SumU+Wu*gammaPreviousU(ii,jj);
                SumV=SumV+Wv*gammaPreviousV(ii,jj);
            end  %Closing jj loop
        end  % Closing ii loop

        if(SumU < 0 | SumV < 0)
            gammaPresentU(i,j)=0.0;
            gammaPresentV(i,j)=0.0;
            Noutlier(Iter)=Noutlier(Iter)+1;
            flag(i,j)=0.0;
        else
            gammaPresentU(i,j)=1.0;
            gammaPresentV(i,j)=1.0;
            Noutlier(Iter)=Noutlier(Iter);
            flag(i,j)=1.0;
        end

        % Flagging unexpected high/low value vectors
        if(Uraw(i,j) > 500 | Vraw(i,j) > 500)
            flag(i,j)=0.0;
            Uraw(i,j)=0.0;
            Vraw(i,j)=0.0;
            Noutlier(Iter)=Noutlier(Iter)+1;
        end

        UDif(i,j)=abs(gammaPreviousU(i,j)-gammaPresentU(i,j));
        VDif(i,j)=abs(gammaPreviousV(i,j)-gammaPresentV(i,j));

        if (UDif(i,j) == 1 | VDif(i,j) == 1)
            Nflip(i,j)=1;
        else
            Nflip(i,j)=0;
        end
```

```matlab
                % After 20 iterations flag flipping vectors as zero

                if (Iter > 20 & Nflip(i,j) == 1)
                    flag(i,j)=0.0;
                    Noutlier(Iter)=Noutlier(Iter)+1;
                end


            end % Closing i loop
        end % Closing j loop

        % Convergence criterion
        % Counting Nflip
        for i=1:Nvec
            for j=1:Nvec
                if(Nflip(i,j) == 1)
                    Nflip_count=Nflip_count+1;
                end
            end
        end

        if(abs(Noutlier(Iter)-Noutlier(Iter)) < 0.005*Nvec*Nvec)
            disp('VCNN method converged');
            break;
        end


        gammaPreviousU(1:Nvec,1:Nvec)=gammaPresentU(1:Nvec,1:Nvec);
        gammaPreviousV(1:Nvec,1:Nvec)=gammaPresentV(1:Nvec,1:Nvec);

    end % Closing loop for Iter

    disp('Final Outlier vectors'); (Noutlier(Iter)/(Nvec*Nvec))*100
    if(Iter == MaxIter)
        disp('VCNN method failed to converge, exit forcefully');
    end

    % -----------------------------------------------------------------
----
    %    Replacing outlier vectors identified by VCNN
    % -----------------------------------------------------------------
----

    disp('Replacing spurious vectors by identified by VCNN');
    for j=1:Nvec
        for i=1:Nvec
            sum1=0.0;
            sum2=0.0;
            sum3=0.0;
```

```matlab
            if (flag(i,j) == 0)
                for ii=i-Fwidth:i+Fwidth
                    for jj=j-Fwidth:j+Fwidth

                        if(ii < 1 | jj < 1)
                            continue;
                        end

                        if(ii > Nvec | jj > Nvec)
                            continue;
                        end

                        uT=Uraw(ii,jj);
                        vT=Vraw(ii,jj);
                        delx=Xraw(ii)-Xraw(i);
                        dely=Yraw(jj)-Yraw(j);
                        R=sqrt(delx.^2+dely.^2);
                        Gauss=exp(-(0.5*(R/H)^2));

                        sum1=sum1+Gauss*flag(ii,jj);
                        sum2=sum2+Gauss*uT*flag(ii,jj);
                        sum3=sum3+Gauss*vT*flag(ii,jj);

                    end  % Closing jj loop
                end % Closing ii loop
                if (sum1 == 0)
                    Uraw(i,j)=0.0;
                    Vraw(i,j)=0.0;
                end
                if (sum1 ~= 0)
                    Uraw(i,j)=sum2/sum1;
                    Vraw(i,j)=sum3/sum1;
                end

            end % Closing flag if loop

        end % Closing i loop
    end % Closing j loop

    % ----------------------------------------------------------------
----
    %Filtering the final field
    % ----------------------------------------------------------------
----

    disp('Filtering final field');
    for j=1:Nvec
        for i=1:Nvec
            sum1=0.0;
            sum2=0.0;
```

```
            sum3=0.0;

            for ii=i-Fwidth:i+Fwidth
                for jj=j-Fwidth:j+Fwidth

                    if(ii < 1 | jj < 1)
                        continue;
                    end

                    if(ii > Nvec | jj > Nvec)
                        continue;
                    end

                    uT=Uraw(ii,jj);
                    vT=Vraw(ii,jj);
                    delx=Xraw(ii)-Xraw(i);
                    dely=Yraw(jj)-Yraw(j);
                    R=sqrt(delx.^2+dely.^2);
                    Gauss=exp(-(0.5*(R/H)^2));

                    sum1=sum1+Gauss*flag(ii,jj);
                    sum2=sum2+Gauss*uT*flag(ii,jj);
                    sum3=sum3+Gauss*vT*flag(ii,jj);

                end  % Closing jj loop
            end % Closing ii loop
            if (sum1 == 0)
                Uraw(i,j)=0.0;
                Vraw(i,j)=0.0;
            end
            if (sum1 ~= 0)
                Uraw(i,j)=sum2/sum1;
                Vraw(i,j)=sum3/sum1;
            end


            end % Closing flag if loop

        end % Closing i loop
    end % Closing j loop




    % -----------------------------------------------------------------
----
    % Converting pixel to mm/m
    % -----------------------------------------------------------------
----

    PixelEq=FOV/2048;
    Xraw=2048-Xraw+1;
    X=Xraw.*PixelEq;
```

```matlab
Y=Yraw.*PixelEq;
U=Uraw.*PixelEq/delT;
V=Vraw.*PixelEq/delT;

X=Edge+X;
Y=Y;

X=reshape(X,Nvec*Nvec,1);
Y=reshape(Y,Nvec*Nvec,1);
U=reshape(U,Nvec*Nvec,1);
V=reshape(V,Nvec*Nvec,1);
flag=reshape(flag,Nvec*Nvec,1);
write=[X Y U V flag];




%----------------------------------------------------------------
--------
% Final output
% ----------------------------------------------------------------
--------

if (k < 10)
    title_num=['00000',int2str(k)];
    titleout=[FileName,title_num,'.',SortExtn,'.','dat'];
end

if (k < 100 & k >= 10)
    title_num=['0000',int2str(k)];
    titleout=[FileName,title_num,'.',SortExtn,'.','dat'];

end

if (k < 1000 & k >= 100)
    title_num=['000',int2str(k)];
    titleout=[FileName,title_num,'.',SortExtn,'.','dat'];

end


if (k < 10000 & k >= 1000)
    title_num=['00',int2str(k)];
    titleout=[FileName,title_num,'.',SortExtn,'.','dat'];

end

if (k < 100000 & k >= 10000)
    title_num=['0',int2str(k)];
    titleout=[FileName,title_num,'.',SortExtn,'.','dat'];
end

fnam=titleout
```

258

```matlab
        dlmwrite(fnam,str,...
            'delimiter','');
        dlmwrite(fnam,write,...
            'delimiter',' ',...
            '-append');

end %end of loop for filenumber

disp('The End');
```

7.7 Code for ensemble averaging of PIV dataset

```matlab
% This code will read the data files processed by outlier rejection
code
% and find out the average quantities of them.
clear all
close all
FileName=input('File Name','s');
SortExtn=input('Sort order extension','s');
Nfile=input('Number of files');
Nvec=input('Number of vectors');
StartFile=input('Start file number');
str1='VARIABLES=X,Y,U,V';
str2='ZONE I=          127J=          127F=POINT';
str=strvcat(str1,str2);

% --------------------------------------------------------------------
----
% Reading files
% --------------------------------------------------------------------
----
Umean=0.0;
Vmean=0.0;
Urms=0.0;
Vrms=0.0;
stress=0.0;
FileCount=0;

for k=StartFile:StartFile+Nfile-1
    if (k < 10)
        title_num=['00000',int2str(k)];
        title=[FileName,title_num,'.',SortExtn,'.','dat']
        [X Y U V]=textread(title,'%f %f %f
%f','delimiter',',','headerlines',2);
    end

    if (k < 100 & k >=10)
```

```matlab
        title_num=['0000',int2str(k)];
        title=[FileName,title_num,'.',SortExtn,'.','dat']
        [X Y U V]=textread(title,'%f %f %f
%f','delimiter',',','headerlines',2);
    end

    if (k < 1000 & k >= 100)
        title_num=['000',int2str(k)];
        title=[FileName,title_num,'.',SortExtn,'.','dat']
        [X Y U V]=textread(title,'%f %f %f
%f','delimiter',',','headerlines',2);

    end


    if (k < 10000 & k >= 1000)
        title_num=['00',int2str(k)];
        title=[FileName,title_num,'.',SortExtn,'.','dat']
        [X Y U V]=textread(title,'%f %f %f
%f','delimiter',',','headerlines',2);
    end

    if (k < 100000 & k >= 10000)
        title_num=['0',int2str(k)];
        title=[FileName,title_num,'.',SortExtn,'.','dat']
        [X Y U V]=textread(title,'%f %f %f
%f','delimiter',',','headerlines',2);
    end

    FileCount=FileCount+1;
    Umean=Umean+U;
    Vmean=Vmean+V;

end

Umean=Umean./FileCount;
Vmean=Vmean./FileCount;

% -----------------------------------------------------------------------
----
% Calculating the flactuations field
% -----------------------------------------------------------------------
----

for k=StartFile:StartFile+Nfile-1

    if (k < 10)
        title_num=['00000',int2str(k)];
        title=[FileName,title_num,'.',SortExtn,'.','dat']
        [X Y U V]=textread(title,'%f %f %f
%f','delimiter',',','headerlines',2);
```

```matlab
        end


    if (k < 100 & k >=10)
        title_num=['0000',int2str(k)];
        title=[FileName,title_num,'.',SortExtn,'.','dat']
        [X Y U V]=textread(title,'%f %f %f
%ff','delimiter',',','headerlines',2);
    end


    if (k < 1000 & k >= 100)
        title_num=['000',int2str(k)];
        title=[FileName,title_num,'.',SortExtn,'.','dat']
        [X Y U V]=textread(title,'%f %f %f
%f','delimiter',',','headerlines',2);


    end


    if (k < 10000 & k >= 1000)
        title_num=['00',int2str(k)];
        title=[FileName,title_num,'.',SortExtn,'.','dat']
        [X Y U V flag]=textread(title,'%f %f %f
%f','delimiter',',','headerlines',2);
    end


    if (k < 100000 & k >= 10000)
        title_num=['0',int2str(k)];
        title=[FileName,title_num,'.',SortExtn,'.','dat']
        [X Y U V]=textread(title,'%f %f %f %f
%f','delimiter',',','headerlines',2);
    end


   Uflac=U-Umean;
   Vflac=V-Vmean;

   Urms=Urms+Uflac.^2;
   Vrms=Vrms+Vflac.^2;
   stress=stress+Uflac.*Vflac;


end

Urms=sqrt(Urms./FileCount);
Vrms=sqrt(Vrms./FileCount);
stress=sqrt(stress./FileCount);

DataMean=[X Y Umean Vmean];
DataRms=[X Y Urms Vrms stress];

TitleMean='MeanVelocity.dat';
dlmwrite(TitleMean,str,...
        'delimiter','');
    dlmwrite(TitleMean,DataMean,...
```

```matlab
        'delimiter',' ',...
        '-append');




TitleRms='RmsVelocity.dat';
dlmwrite(TitleRms,str,...
        'delimiter','');
    dlmwrite(TitleRms,DataRms,...
        'delimiter',' ',...
        '-append');
```

7.8 Proper orthogonal decomposition

7.8.1 POD decomposition

```matlab
clear all
close all
% ------------------------------------------------------------------------
----
% File inputs
% ------------------------------------------------------------------------
----
FileName=input('File Name','s');
SortExtn=input('Sort order extension','s');
Nfile=input('Number of files');
Nvec=input('Number of vectors');
StartFile=input('Start file number');


% ------------------------------------------------------------------------
----
% Reading data files
% ------------------------------------------------------------------------
----
[X Y Umean Vmean flag]=textread('MeanVelocity.dat','%f %f %f %f
%f','delimiter',',','headerlines',2);
for i=StartFile:StartFile+Nfile-1
    if (i < 10)
        title_num=['00000',int2str(i)];
        title=[FileName,title_num,'.',SortExtn,'.','dat']
        [X Y U V flag]=textread(title,'%f %f %f %f
%f','delimiter',',','headerlines',11);
        U_flac=U-Umean;
        V_flac=V-Vmean;
    end

    if (i < 100 & i >=10)
        title_num=['0000',int2str(i)];
```

```matlab
        title=[FileName,title_num,'.',SortExtn,'.','dat']
        [X Y U V flag]=textread(title,'%f %f %f %f
%f','delimiter',',','headerlines',11);
        U_flac=U-Umean;
        V_flac=V-Vmean;
    end

    if (i < 1000 & i >= 100)
        title_num=['000',int2str(k)];
        title=[FileName,title_num,'.',SortExtn,'.','dat']
        [X Y U V flag]=textread(title,'%f %f %f %f
%f','delimiter',',','headerlines',11);
        U_flac=U-Umean;
        V_flac=V-Vmean;

    end


    if (i < 10000 & i >= 1000)
        title_num=['00',int2str(k)];
        title=[FileName,title_num,'.',SortExtn,'.','dat']
        [X Y U V flag]=textread(title,'%f %f %f %f
%f','delimiter',',','headerlines',11);
        U_flac=U-Umean;
        V_flac=V-Vmean;
    end

    if (i < 100000 & i >= 10000)
        title_num=['0',int2str(k)];
        title=[FileName,title_num,'.',SortExtn,'.','dat']
        [X Y U V flag]=textread(title,'%f %f %f %f
%f','delimiter',',','headerlines',11);
        U_flac=U-Umean;
        V_flac=V-Vmean;
    end
    veldata(:,i)=[U_flac;V_flac];
end % End of loop for filename

 cord=[X Y];
% -------------------------------------------------------------------
% Manipulating the data
% -------------------------------------------------------------------
disp('Manupulating tha data');
velflac=veldata;
%-------------------------------------------------------------------
----
% Calculating covariance matrix
% -------------------------------------------------------------------
----
disp('Calculating covariance matrix');
R = (velflac'*velflac)/Nfile;
```

```matlab
% ----------------------------------------------------------------------
----
% Calculating eigen values
% ----------------------------------------------------------------------
----
disp('Calculating eigen values');
[V Lambda]=eig(R);
%-----------------------------------------------------------------------
----
% Arrenging the eigen values in ascending order
%-----------------------------------------------------------------------
----
disp('Arranging eigenvalues in ascending order');
[C D]=sort(diag(Lambda));
lengthC=length(C);


%-----------------------------------------------------------------------
----
% Setting the smallest eigen value to zero
% ----------------------------------------------------------------------
----
disp('Setting smallest eigenvalue as zero');
C=C(lengthC:-1:1);
D=D(lengthC:-1:1);
C(lengthC)=0;
V=V(:,D);


%-----------------------------------------------------------------------
----
% Energy associated with each of the eigen mode
%-----------------------------------------------------------------------
----
disp('Calculation of energy associated with each eigen modes');
totalenergy=sum(C(1:lengthC));
energy=(C./totalenergy);
energy=energy.*100;
cumenergy(1)=energy(1);
for i=2:Nfile
    cumenergy(i)=cumenergy(i-1)+energy(i);
end
mode=1:size(energy);
energydata=[mode' energy cumenergy'];
dlmwrite('Modalenergy.dat',energydata);

disp('Mode number  Energy(%)   Cumulative energy(%)');
energydata
plot(energydata(:,1),energydata(:,3),'d');
xlabel('Mode');
ylabel('Cumulative energy');

save flac_velocity.mat velflac;
save eigenvectors.mat V;
save cord.mat X Y
```

```
disp('code ended');
```

7.8.2 POD reconstruction

```
clear all
close all

% ------------------------------------------------------------------------
----
% File Input
% ------------------------------------------------------------------------
----
FileName=input('File Name','s');
SortExtn=input('Sort order extension','s');
Nfile=input('Number of files');
Nvec=input('Number of vectors');
StartFile=input('Start file number');
Fmode=input('Starting mode');
Nmode=input('Ending mode');
str1='VARIABLES=X,Y,Upod,Vpod';
str2='ZONE I=          127J=          127F=POINT';
str=strvcat(str1,str2);
% ------------------------------------------------------------------------
----
% Loading relevant data
% ------------------------------------------------------------------------
----
disp('Reading data files');
load flac_velocity.mat;
load eigenvectors.mat;
load cord.mat
%-------------------------------------------------------------------------
----
% Reconstruction of the eigen functions
%-------------------------------------------------------------------------
----
disp('Reconstruction of eigen functions');
phi=velflac*V;
phi=phi(:,1:Nmode);
%-------------------------------------------------------------------------
----
% calculating the time-dependent coefficient
%-------------------------------------------------------------------------
----
disp('Calculating the time dependent coefficient');
for i=Fmode:Nmode
    for j=1:Nfile
        a(j,i)=sum(phi(:,i).*velflac(:,j))./sum(phi(:,i).*phi(:,i));
    end
end
```

```matlab
%------------------------------------------------------------------------
% Reconstructing the velocity field
%------------------------------------------------------------------------
disp('Reconstructing the velocity field');
for k=1:Nfile
    for i=1:2*Nvec*Nvec
        velrecons(i,k)=sum(a(k,1:Nmode).*phi(i,1:Nmode));
    end
end


%------------------------------------------------------------------------
% Restructuring the velocity field back
%------------------------------------------------------------------------
for k=1:Nfile
    urecons(:,k)=velrecons(1:Nvec*Nvec,k);
    vrecons(:,k)=velrecons(Nvec*Nvec+1:2*Nvec*Nvec,k);
end


%------------------------------------------------------------------------
% Writing data into files

for i=StartFile:StartFile+Nfile-1
if (i < 10)
        title_num=['00000',int2str(i)];
        titleout=['POD',FileName,title_num,'.',SortExtn,'.','dat'];
    end

    if (i < 100 & i >= 10)
        title_num=['0000',int2str(i)];
        titleout=['POD',FileName,title_num,'.',SortExtn,'.','dat'];

    end

    if (i < 1000 & i >= 100)
        title_num=['000',int2str(i)];
        titleout=['POD',FileName,title_num,'.',SortExtn,'.','dat'];

    end


    if (i < 10000 & i >= 1000)
        title_num=['00',int2str(i)];
        titleout=['POD',FileName,title_num,'.',SortExtn,'.','dat'];

    end
```

```matlab
    if (i < 100000 & i >= 10000)
        title_num=['0',int2str(k)];
        titleout=['POD',FileName,title_num,'.',SortExtn,'.','dat'];
    end

    fnam=titleout
    write=[X Y urecons(:,i) vrecons(:,i)];
    dlmwrite(fnam,str,...
        'delimiter','');
    dlmwrite(fnam,write,...
        'delimiter',' ',...
        '-append');
end
```

7.9 Closed streamline based structure identification code

7.9.1 Main code

```matlab
clc
clear all
close all
% ----------------------------------------------------------------------
----
% File input
Nvec=127;
ThLimit=60;
Rmax=20;
PixelEq=0.000765;
FileName=input('File Name','s');
SortExtn=input('Sort order extension','s');
Nfile=input('Number of files');
StartFile=input('Start file number');
% ----------------------------------------------------------------------
----
for i=StartFile:StartFile+Nfile-1
    if (i < 10)
        title_num=['00000',int2str(i)];
        title=[FileName,title_num,'.',SortExtn,'.','dat']
        titleout=[FileName,title_num,'.',SortExtn,'.','mcr'];
        [X Y U V]=textread(title,'%f %f %f
%f','delimiter',',','headerlines',2);
    end

    if (i < 100 & i >=10)
        title_num=['0000',int2str(i)];
        title=[FileName,title_num,'.',SortExtn,'.','dat']
        titleout=[FileName,title_num,'.',SortExtn,'.','mcr'];
        [X Y U V]=textread(title,'%f %f %f
%f','delimiter',',','headerlines',2);
```

```matlab
        end

    if (i < 1000 & i >= 100)
        title_num=['000',int2str(k)];
        title=[FileName,title_num,'.',SortExtn,'.','dat']
        titleout=[FileName,title_num,'.',SortExtn,'.','mcr'];
        [X Y U V]=textread(title,'%f %f %f
%f','delimiter',',','headerlines',2);

    end

    if (i < 10000 & i >= 1000)
        title_num=['00',int2str(k)];
        title=[FileName,title_num,'.',SortExtn,'.','dat']
        titleout=[FileName,title_num,'.',SortExtn,'.','mcr'];
        [X Y U V]=textread(title,'%f %f %f
%f','delimiter',',','headerlines',2);
    end

    if (i < 100000 & i >= 10000)
        title_num=['0',int2str(k)];
        title=[FileName,title_num,'.',SortExtn,'.','dat']
        titleout=[FileName,title_num,'.',SortExtn,'.','mcr'];
        [X Y U V]=textread(title,'%f %f %f
%f','delimiter',',','headerlines',2);
    end

    X=reshape(X,Nvec,Nvec);
    Y=reshape(Y,Nvec,Nvec);
    U=reshape(U,Nvec,Nvec);
    V=reshape(V,Nvec,Nvec);
    Xmin=X(1,1);
    Ymin=Y(1,1);
    Xmax=X(Nvec,Nvec);
    Ymax=Y(Nvec,Nvec);
    % ----------------------------------------------------------------
--------
    % Identifying vortices (CW sense = 1)(CCW sense = -1)
    % ----------------------------------------------------------------
--------
    disp('Finding vortices');
    VCount=0;
    for Ic=1:Nvec
        for Jc=1:Nvec
            for Rad=3:Rmax
                flag=0;
                [XPold YPold Countold]=ApproxCircle(Ic,Jc,Rad);
                for N=1:Countold
                    if(XPold(N) < 1 | YPold(N) <1 | XPold(N) > Nvec |
YPold(N) > Nvec)
                        flag=1; %error
                    end
```

268

```matlab
                    end
                    if(flag == 0)
                        Count=Countold;
                        for i=1:Count
                            XP(i)=XPold(i);
                            YP(i)=YPold(i);
                            UP(i)=U(XP(i),YP(i));
                            VP(i)=V(XP(i),YP(i));
                        end

[VortexCW]=VOR_CW(Ic,Jc,Count,XP,YP,UP,VP,ThLimit,Rad);

[VortexCCW]=VOR_CCW(Ic,Jc,Count,XP,YP,UP,VP,ThLimit,Rad);
                        if(VortexCW == 1)
                            VCount=VCount+1;
                            cord(VCount,1)=X(Ic,Jc);
                            cord(VCount,2)=Y(Ic,Jc);
                            cord(VCount,3)=Rad*PixelEq;
                            cord(VCount,4)=1;
                            cord(VCount,5)=Ic;
                            cord(VCount,6)=Jc;
                            cord(VCount,7)=Rad;
                        end
                        if(VortexCCW == 1)
                            VCount=VCount+1;
                            cord(VCount,1)=X(Ic,Jc);
                            cord(VCount,2)=Y(Ic,Jc);
                            cord(VCount,3)=Rad*PixelEq;
                            cord(VCount,4)=-1;
                            cord(VCount,5)=Ic;
                            cord(VCount,6)=Jc;
                            cord(VCount,7)=Rad;
                        end
                    end
                end
            end
        end
    end
    if(VCount == 0)
        continue;
    end

    FirstList=cord;
    FirstCount=VCount;
    % -----------------------------------------------------------------
--------
    % Deleting small vortices
    % -----------------------------------------------------------------
--------
    for N=2:FirstCount
        if(FirstList(N,1) == FirstList(N-1,1) & FirstList(N,2) ==
FirstList(N-1,2) & FirstList(N,4) == FirstList(N-1,4))
            FirstList(N-1,3)=0;
        end
```

```matlab
    end

    SecondCount=0;
    for N=1:FirstCount
        if(cord(N,3) ~= 0)
            SecondCount=SecondCount+1;
            SecondList(SecondCount,:)=FirstList(N,:);
        end
    end




    % ----------------------------------------------------------------
--------
    % Deleting overlapping vortices
    % ----------------------------------------------------------------
--------

    for Point=1:SecondCount-1
        for N=Point+1:SecondCount
            CCD1=(SecondList(Point,1)-SecondList(N,1))^2;
            CCD2=(SecondList(Point,2)-SecondList(N,2))^2;
            CCD=sqrt(CCD1+CCD2);
            R1=SecondList(Point,3);
            R2=SecondList(N,3);
            if(CCD <= R1 | CCD <= R2 & SecondList(N,4) ==
SecondList(Point,4))
                if(R1 < R2)
                    SecondList(Point,3)=0;
                end

                if(R1 > R2 & SecondList(N,4) == SecondList(Point,4))
                    SecondList(N,3)=0;
                end

                if(R1 == R2 & SecondList(N,4) == SecondList(Point,4))
                    Ufirst=U(SecondList(Point,5),SecondList(Point,6));
                    Vfirst=V(SecondList(Point,5),SecondList(Point,6));
                    Ufirst_resultant=sqrt(Ufirst^2+Vfirst^2);

                    Usecond=U(SecondList(N,5),SecondList(N,6));
                    Vsecond=V(SecondList(N,5),SecondList(N,6));
                    Usecond_resultant=sqrt(Usecond^2+Vsecond^2);
                    if(Ufirst_resultant > Usecond_resultant)
                        SecondList(Point,3)=0;
                    else
                        SecondList(N,3)=0;
                    end
                end
            end
        end
```

```matlab
            if(CCD > R1 & CCD > R2 & CCD <=(R1+R2) & SecondList(N,4) ==
SecondList(Point,4))

SecondList(Point,1)=0.5*(SecondList(Point,1)+SecondList(N,1));

SecondList(Point,2)=0.5*(SecondList(Point,2)+SecondList(N,2));
                SecondList(Point,3)=0.5*(R1+R2);
                SecondList(Point,4)=SecondList(Point,4);
                SecondList(N,3)=0;
            end

        end
    end

    ThirdCount=0;
    for N=1:SecondCount
        if(SecondList(N,3) ~=0)
            ThirdCount=ThirdCount+1;
            ThirdList(ThirdCount,:)=FirstList(N,:);
        end
    end




    % -----------------------------------------------------------------
--------
    % Calculating circulation
    % -----------------------------------------------------------------
--------
    for N=1:ThirdCount
        [XV YV
Count]=ApproxCircle(ThirdList(N,5),ThirdList(N,6),ThirdList(N,7));
        circx=0;
        circy=0;
        for i=1:Count
            XVOR(i)=X(XV(i),YV(i));
            YVOR(i)=Y(XV(i),YV(i));
            UVOR(i)=U(XV(i),YV(i));
            VVOR(i)=V(XV(i),YV(i));
        end

        for i=1:Count-1
            circx=circx+0.5*(UVOR(i)+UVOR(i+1))*(XVOR(i+1)-XVOR(i));
            circy=circx+0.5*(VVOR(i)+VVOR(i+1))*(YVOR(i+1)-YVOR(i));
        end

        circ(N)=circx+circy;
    end
    data_write=[ThirdList(:,1:4) circ'];

    %-----------------------------------------------------------------
-------
```

```matlab
    %Writing the macro file
    %----------------------------------------------------------------
-------
    fnam=titleout;
    StrHeader='#!MC 1100';
    dlmwrite(fnam,StrHeader,...
        'delimiter','');
    for i=1:ThirdCount
        line2='$!ATTACHGEOM';
        line3='GEOMTYPE = CIRCLE';
        line3a='LINETHICKNESS=0.4';
        line4='ANCHORPOS';
        line5='{';
        line6=strcat('X = ',num2str(ThirdList(i,1)));
        line7=strcat('Y = ',num2str(ThirdList(i,2)));
        line8='}';
        if(ThirdList(i,4) == -1)
            line8a='COLOR = CUSTOM3';
        end
        if(ThirdList(i,4) == 1)
            line8a='COLOR = CUSTOM36';
        end
        line9='RAWDATA';
        line10=num2str(ThirdList(i,3));
        line11='$!ATTACHGEOM';
        line12='GEOMTYPE = CIRCLE';
        line13='ANCHORPOS';
        line14='{';
        line15=strcat('X = ',num2str(ThirdList(i,1)));
        line16=strcat('Y = ',num2str(ThirdList(i,2)));
        line17='}';
        line18='COLOR = BLACK';
        line19='ISFILLED = YES';
        line20='FILLCOLOR = BLACK';
        line21='RAWDATA';
        line22='0.0006';


content=strvcat(line2,line3,line3a,line4,line5,line6,line7,line8,line8a
,line9,line10,line11,line12,line13,line14,line15,line16,line17,line18,l
ine19,line20,line21,line22);

        dlmwrite(fnam,content,...
            'delimiter','',...
            '-append');
    end

    dlmwrite(FileName,data_write,'-append');

    clear X Y U V
    clear i
    clear VCount Ic Jc
    clear Rad
```

```
    clear XP YP UP VP
    clear cord Point N
    clear FirstCount FirstList
    clear SecondCount SecondList
    clear ThirdCount ThirdList
    clear data_write
    clear circ
    disp('Vortex identification completed');
end %end for filename loop
```

7.9.2 Approximation of circle in rectangular grid(Bresenham's algotithm)

```
 function [XPoint YPoint Count] = ApproxCircle(Ic,Jc,R);
% ---------------------------------------------------------------------
----
% Identification of neighbouring points
% ---------------------------------------------------------------------
----
theta=0:10:360;
x=Ic+R.*cos(theta*pi/180);
y=Jc+R.*sin(theta*pi/180);


% ---------------------------------------------------------------------
----
% Bresenham circle generation
% For Reference see Procuremental elements for computer graphics
%                   David F Rogers
% ---------------------------------------------------------------------
----
if(R == 1)

    XPoint(1)=Ic+R;
    YPoint(1)=Jc+R;

    XPoint(2)=Ic+R;
    YPoint(2)=Jc;

    XPoint(3)=Ic+R;
    YPoint(3)=Jc-R;

    XPoint(4)=Ic;
    YPoint(4)=Jc-R;

    XPoint(5)=Ic-R;
    YPoint(5)=Jc-R;
```

```
    XPoint(6)=Ic-R;
    YPoint(6)=Jc;

    XPoint(7)=Ic-R;
    YPoint(7)=Jc+R;

    XPoint(8)=Ic;
    YPoint(8)=Jc+R;

    Count=8;

end

if (R ~=1)
% First Quadrant
x_i=0;
y_i=R;
theta_i=2*(1-R);
Limit=0.0;
Count=1;
Xpoint1(Count)=x_i;
YPoint1(Count)=R;
while (y_i > Limit)
    Count=Count+1;
    if (theta_i < 0)
        delta=2*(theta_i+y_i)-1;
        if (delta <= 0)
            % Move horizontally
            x_i=x_i+1;
            theta_i=theta_i+(2*x_i)+1;
        else
            % Move diagonally
            x_i=x_i+1;
            y_i=y_i-1;
            theta_i=theta_i+(2*(x_i-y_i))+2;
        end

    elseif (theta_i > 0)
        delta_prime = 2*(theta_i-x_i)-1;
        if(delta_prime <= 0)
            % move diagonally
            x_i=x_i+1;
            y_i=y_i-1;
            theta_i=theta_i+(2*(x_i-y_i))+2;
        else
            % mode vertically
            y_i=y_i-1;
            theta_i=theta_i-(2*y_i)+1;
        end

    elseif (theta_i == 0)
```

```matlab
        % move diagonally
        x_i=x_i+1;
        y_i=y_i-1;
        theta_i=theta_i+(2*(x_i-y_i))+2;
    end
    XPoint1(Count)=x_i;
    YPoint1(Count)=y_i;
end
%For the fourth quadrant
XPoint4=XPoint1;
YPoint4=-YPoint1;
length4=length(XPoint1);
XPoint4=XPoint4(length4-1:-1:1);
YPoint4=YPoint4(length4-1:-1:1);


% For the third quadrant
XPoint3=-XPoint1;
YPoint3=-YPoint1;
length3=length(XPoint3);
XPoint3=XPoint3(2:1:length3);
YPoint3=YPoint3(2:1:length3);


% For the scond quadrant
XPoint2=-XPoint1;
YPoint2=YPoint1;
length2=length(XPoint2);
XPoint2=XPoint2(length2-1:-1:2);
YPoint2=YPoint2(length2-1:-1:2);


% Collectinig all points
XPoint=[XPoint1 XPoint4 XPoint3 XPoint2];
XPoint=XPoint';

YPoint=[YPoint1 YPoint4 YPoint3 YPoint2];
YPoint=YPoint';
Count=length(XPoint);

% Shift the discrete circle
XPoint=XPoint+Ic;
YPoint=YPoint+Jc;

end
```

7.9.3 Detection of a clockwise structure

```matlab
    function [VortexCW]=VOR_CW(Ic,Jc,Count,XP,YP,UP,VP,ThLimit,Rad);
```

```matlab
% ------------------------------------------------------------------------
% Generating points in the neighbourhoood
% ------------------------------------------------------------------------
ThCountCW=0;
for i=1:Count
    theta(i)=(atan2(VP(i),UP(i)))*(180/pi);
    if(theta(i) > 0)
        theta(i)=theta(i)-360;
    end
end
% ------------------------------------------------------------------------
% Checking threshold condition
% ------------------------------------------------------------------------
XDif=XP-Ic;
YDif=YP-Jc;
slopeCW=(atan2(-XDif,YDif))*(180/pi);
for i=1:Count
    if(slopeCW(i) > 0)
        slopeCW(i)=slopeCW(i)-360;
    end
end

slopeCW(1)=0;

for N=1:Count
    if(theta(N) < (slopeCW(N)+ThLimit) & theta(N) >= (slopeCW(N)-
ThLimit))
            ThCountCW=ThCountCW+1;
    end
end


% ------------------------------------------------------------------------
% Checking monotone condition
%-------------------------------------------------------------------------
thetaDIFF=diff(round(theta));
positive=0;
negative=0;
for i=1:length(thetaDIFF)
    if(sign(thetaDIFF(i)) == 1)
        positive=positive+1;
    end

    if(sign(thetaDIFF(i)) == -1)
        negative=negative+1;
    end
```

```matlab
end



if(ThCountCW > 0.75*Count & abs(negative) >= 0.75*Count)
    VortexCW=1;
else
    VortexCW=0;
end
```

7.9.4 Detection of counterclockwise structure

```matlab
    function [VortexCCW]=VOR_CCW(Ic,Jc,Count,XP,YP,UP,VP,ThLimit,Rad);
% ------------------------------------------------------------------------
----
% Generating points in the neighbourhoood
% ------------------------------------------------------------------------
----
ThCountCCW=0;
for i=1:Count
    theta(i)=(atan2(VP(i),UP(i)))*(180/pi);

end

XDif=XP-Ic;
YDif=YP-Jc;
slopeCCW=(atan2(XDif,-YDif))*(180/pi);
slopeCCW(1)=180;


% ------------------------------------------------------------------------
----
% Checking threshold condition
% ------------------------------------------------------------------------
----
for N=1:Count
    if(theta(N) < (slopeCCW(N)+ThLimit) & theta(N) >= (slopeCCW(N)-
ThLimit))
        ThCountCCW=ThCountCCW+1;
    end
end
% ------------------------------------------------------------------------
----
% Checking Monotone condition
% ------------------------------------------------------------------------
----

thetaDIFF=diff(round(theta));
positive=0;
```

```matlab
negative=0;
for i=1:length(thetaDIFF)
    if(sign(thetaDIFF(i)) == 1)
        positive=positive+1;
    end

    if(sign(thetaDIFF(i)) == -1)
        negative=negative+1;
    end
end




if(ThCountCCW > 0.75*Count & abs(negative) > 0.75*Count)
    VortexCCW=1;
else
    VortexCCW=0;
end
```

7.10 Calculation of swirling strength from PIV dataset

```matlab
% This code reads data files and compute the swirling strength and
write
% new files with pre-phase "SWIRL"
clear all
close all
% -----------------------------------------------------------------------
----
% File Input
% -----------------------------------------------------------------------
----
FileName=input('File Name','s');
SortExtn=input('Sort order extension','s');
Nfile=input('Number of files');
Nvec=input('Number of vectors');
StartFile=input('Start file number');
str1='VARIABLES=X,Y,U,V,swirl';
str2='ZONE I=         127J=          127F=POINT';
str=strvcat(str1,str2);

for i=StartFile:StartFile+Nfile-1
    if (i < 10)
        title_num=['00000',int2str(i)];
        title=[FileName,title_num,'.',SortExtn,'.','dat']
        titleout=['SWIRL',FileName,title_num,'.',SortExtn,'.','dat'];
        [X Y U V]=textread(title,'%f %f %f
%f','delimiter',',','headerlines',2);
    end

    if (i < 100 & i >=10)
```

```matlab
        title_num=['0000',int2str(i)];
        title=[FileName,title_num,'.',SortExtn,'.','dat']
        titleout=['SWIRL',FileName,title_num,'.',SortExtn,'.','dat'];
        [X Y U V]=textread(title,'%f %f %f
%f','delimiter',',','headerlines',2);

    end

    if (i < 1000 & i >= 100)
        title_num=['000',int2str(i)];
        title=[FileName,title_num,'.',SortExtn,'.','dat']
        titleout=['SWIRL',FileName,title_num,'.',SortExtn,'.','dat'];
        [X Y U V]=textread(title,'%f %f %f
%f','delimiter',',','headerlines',2);
    end


    if (i < 10000 & i >= 1000)
        title_num=['00',int2str(i)];
        title=[FileName,title_num,'.',SortExtn,'.','dat']
        titleout=['SWIRL',FileName,title_num,'.',SortExtn,'.','dat'];
        [X Y U V]=textread(title,'%f %f %f
%f','delimiter',',','headerlines',2);

    end

    if (i < 100000 & i >= 10000)
        title_num=['0',int2str(i)];
        title=[FileName,title_num,'.',SortExtn,'.','dat']
        titleout=['SWIRL',FileName,title_num,'.',SortExtn,'.','dat'];
        [X Y U V]=textread(title,'%f %f %f
%f','delimiter',',','headerlines',2);
    end

    X=reshape(X,Nvec,Nvec);
    Y=reshape(Y,Nvec,Nvec);
    U=reshape(U,Nvec,Nvec);
    V=reshape(V,Nvec,Nvec);
    delx=X(2,1)-X(1,1);
    dely=Y(1,2)-Y(1,1);
    for i=2:Nvec-1
        for j=2:Nvec-1
            ux(i,j)=(U(i+1,j)-U(i-1,j))/(2*delx);
            vx(i,j)=(V(i+1,j)-V(i-1,j))/(2*delx);
            uy(i,j)=(U(i,j+1)-U(i,j-1))/(2*dely);
            vy(i,j)=(V(i,j+1)-V(i,j-1))/(2*dely);
            temp=[ux(i,j) uy(i,j);vx(i,j) vy(i,j)];
            temp_eigen=eig(temp);
            lambda(i,j)=imag(temp_eigen(1,1));
        end
    end
    lambda(1,1:Nvec)=0.0;
```

```matlab
        lambda(Nvec,1:Nvec)=0.0;
        lambda(1:Nvec,1)=0.0;
        lambda(1:Nvec,Nvec)=0.0;
        lambda=reshape(lambda,Nvec*Nvec,1);
        X=reshape(X,Nvec*Nvec,1);
        Y=reshape(Y,Nvec*Nvec,1);
        U=reshape(U,Nvec*Nvec,1);
        V=reshape(V,Nvec*Nvec,1);
        write=[X Y U V lambda];

        fnam=titleout

        dlmwrite(fnam,str,...
            'delimiter','');
        dlmwrite(fnam,write,...
            'delimiter',' ',...
            '-append');
        clear X Y U V ux vx uy vy lambda;
end % End of loop for filename
```

Appendix C

Copyright permissions

7.11 Figure 2.5

```
----------------------------------------------------------------------
Dear Dr. Singha:

Thank you for requesting permission to reproduce material from American
Institute of Physics publications.

Permission is granted – subject to the conditions outlined below – for
the
following:

Logory, R. M., Hirsa, A., Anthony, D. G., Interaction of wake turbulence
with a
free surface, Phys. Fluids. 8, pp 805-815, 1996.
Figure 5(a)

To be used in the following manner:

Reproduced in a review article and also included as part of your
dissertation
for submission to the University of Windsor.

1. The American Institute of Physics grants you the right to reproduce
the
material indicated above on a one-time, non-exclusive basis, solely for
the
purpose described. Permission must be requested separately for any
future or
additional use.

2.  This permission pertains only to print use and its electronic
equivalent,
including CD-ROM or DVD.

3.  The following copyright notice must appear with the material (please
fill
in the information indicated by capital letters): "Reprinted with
permission
from [FULL CITATION]. Copyright [PUBLICATION YEAR], American Institute
of
Physics."
Full citation format is as follows: Author names, journal title, Vol. #,
Issue
#, Page #, Year of publication.
For an article, the copyright notice must be printed on the first page
of the
article or book chapter.  For figures, photographs, covers, or tables,
the
notice may appear with the material, in a footnote, or in the reference
list.
```

281

4. This permission does not apply to any materials credited to sources other
than the copyright holder.

5. If you have not already done so, please attempt to obtain permission from
at least one of the authors. The author's address can be obtained from the
article.

Please let us know if you have any questions.

Sincerely,
Susann Brailey

~~~~~~~~~~~
Office of the Publisher, Journals and Technical Publications
Rights & Permissions
American Institute of Physics
Suite 1NO1
2 Huntington Quadrangle
Melville, NY 11747-4502
516-576-2268   TEL
516-576-2450   FAX
rights@aip.org

>>> <arindam@uwindsor.ca> 2/17/2009 3:58 PM >>>
Dear Sir

Would you please grant permission for the following.
The details of the paper is as follows:

Logory, R. M., Hirsa, A., Anthony, D. G., Interaction of wake turbulence
with a free surface, Phys. Fluids. 8, pp 805-815, 1996.
I need permission to reuse Figure 5(a) for a review paper and my
dissertation.
Thanks

Arindam
Arindam Singha
PhD candidate
University of Windsor
Windsor, ON, Canada.
Phone: (519) 253 3000 (x 2546)

----- Forwarded by Arindam Singha/University of Windsor on 02/17/2009
03:55 PM -----

From:
"Amir H. Hirsa" <hirsaa@rpi.edu>
To:
<arindam@uwindsor.ca>
Cc:
<rambala@uwindsor.ca>, "'Anthony, Douglas G AMRDEC'"
<Douglas.Anthony@us.army.mil>
Date:
02/17/2009 03:42 PM
Subject:
RE: copyright permission to use one figure

Dear Arindam:

Thanks for writing and your interest in that paper of ours. I don?t have a
problem with you using that figure, but you need the permission of AIP
(American Institute of Physics) to use a figure from one of their
journals. The good thing is that they routinely grant such requests.

Good luck with your research.

Cheers
amir

Amir H. Hirsa, Professor and Associate Head for Graduate Studies; Dept.
Mechanical, Aerospace & Nuclear Engineering
      also
Professor, Howard P. Isermann Dept. Chemical & Biological Engineering
(joint appointment)
Rensselaer Polytechnic Institute
Troy, NY 12180-3590
tel. (518) 276-6997
Email: hirsaa@rpi.edu
webpage: www.rpi.edu/~hirsaa

From: arindam@uwindsor.ca [mailto:arindam@uwindsor.ca]
Sent: Tuesday, February 17, 2009 3:09 PM
To: hirsaa@rpi.edu
Cc: rambala@uwindsor.ca
Subject: copyright permission to use one figure

Dear Prof. Hirsa

I am Arindam Singha, a PhD student in University of Windsor. I would like
to use Figure 5(a) from the paper, "Interaction of wake turbulence with
free surface' Physics of Fluids, 1996 in my dissertation as well as a
review paper to be submitted for possible publication.
I would like to ask permission to use the aforementioned figure.
Thanks
Arindam

Arindam Singha
PhD candidate
University of Windsor
Windsor, ON, Canada.
Phone: (519) 253 3000 (x 2546)

7.12 Figure 2.6

Fine by me, Arindam.
Regards,
---Patrice

Patrice Maheo

```
M)  415.377.6536
E)  pmaheo@yahoo.com
```

Dear Arindam,

It is fine with Professor Gharib. Please contact Dr. Maheno to see if it is fine with him. His email is pmaheo@yahoo.com.

Please let us know his response and thank you for contacting us.

Warmest Regards,

Martha

Martha Salcedo

Assistant to Professor

Mory Gharib

Caltech

1200 E California Blvd.

MC: 205-45

Pasadena, CA 91125

Location: 205 Guggenheim

Office: (626) 395-4450

Fax: (626) 577-5258

msalcedo@caltech.edu

http://www.gharib.caltech.edu

7.13 Figure 2.4

Journals Publications Specialist

Dear Arindam,

It has took me some time to find copyright notice. The aerial photos in
Rupert Bay were obtained from Energy, Mines and Resource Canada, Survey
and Mapping Branch in 1986. Ingram at the time was collecting field data
in the Rupert Bay area. We have "non-exclusive" use.

I assume that it will be ok to use the photo if you mention reproduction
from the JGR paper, or get clearance from JGR.

I am looking forward to reading your thesis. Regards,

Vincent H. Chu

Professor
Department of Civil Engineering and Applied Mechanics
McGill University
817 Sherbrooke Street West
Montreal, Quebec, Canada H3A 2K6

_____

From: arindam@uwindsor.ca [mailto:arindam@uwindsor.ca]
Sent: Tue 2/17/2009 10:03 AM
To: Vincent H. Chu, Prof.
Cc: rambala@uwindsor.ca
Subject: copyright permission

Dear Professor Chu

First of all I would like to thank you for agreeing to be the external
examiner for my dissertation. I would like to request permission to use
Figure 5 from the paper, 'Flow around islands in Rupert Bay: An
investigation of the bottom friction effect' (Journal of Geophysical
Research, Vol 92, 1987) in my dissertation as well as in a review paper
that would be submitted for publication.
I would be grateful if you would give me the permission to use the
aforementioned figure.
Thank you for your help.

Arindam

Arindam Singha
PhD candidate
University of Windsor
Windsor, ON, Canada.
Phone: (519) 253 3000 (x 2546)

7.14 Figure 2.9

Dear Arindam:

Feel free to use the figures you requested.

Please extend my best regards to Ram.

Regards

Mark

arindam@uwindsor.ca wrote:

Dear Dr. Tachie

I am Arindam Singha, PhD student under the supervision of Dr. Balachandar. I would like to use figure B6.1 and B7.1from your masters thesis (scalar transport in intermediate two-dimensional turbulent wakes) in my dissertation as well as a review paper, that is going to be submitted for publication.

I would like to sought permission for the use. I would really appreciate if you could let me use the mentioned figure.

Thanks

Arindam

Arindam Singha

PhD candidate

University of Windsor

Windsor, ON, Canada.

Phone: (519) 253 3000 (x 2546)

7.15 Published article

COPYRIGHT 'TRANSFER ‘E

FORM .ı.,rt6"ıC / ' *D* 1r41011(1

Publishing Three Park Avenue *New* York, NY FAX `212-591-7060; 212-591-7292` E-Mail:

PAPER NUMBER: FE-07-1433

TITLE: PIV-POD investigation of the wake of a sharp-edged flat bluff body immersed in a shallow channel flow

AUTHOR(s): Arindam Singha, AbdulMonsif Shinneeb, Ram Balachandar

PAPER OFFERED FOR FIRST PUBLICATION IN:

Journal publication: Journal of Fluids Engineering

1. OWNERSHIP OF RIGHTS.

(A). Please check the box below next to the applicable provision.

You acknowledge that ASME has specially ordered and commissioned the Paper as a work made for hire and accordingly, ASME is the "author" of the Paper for purposes of copyright laws. If it is determined that the Paper is not a work made for hire, then you hereby irrevocably assign to ASME forever, as of the date of creation, all worldwide rights in the Paper, including all United States and foreign copyrights (and extensions of them), and all other proprietary rights in the Paper. You shall promptly sign and deliver to ASME any instruments of transfer or other documents which ASME may reasonably request to further effect and enforce ASME's ownership of the Paper and you hereby irrevocably appoint ASME as your attorney-in-fact to sign and deliver any of those documents that you fail or refuse to sign or deliver.

(Note: If you created the Paper during the course of your employment or independent contractor agreement or received a grant to fund your Paper, please review applicable company, institutional and grant policies and your employment/independent contractor agreement to determine if your employer or another third party owns or exclusively licenses some or all nghts m your Paper. I f you do not own the rlghts in the Paper, then the copyright owner should sign this agreement instead of you.)

d You wrote the Paper within the scope of your employment by the U.S. Government or the Paper is otherwise in the public domain and the Paper includes a copyright notice identiQing those portions of the Paper that are protected by copyright (if any) and those portions in the public domain.

(Note: I f you are a United States federal employee who created the Paper within the scope of your official duties, then the Paper is in the public domain and you should check the second box above. I f you are a U.S. federal employee who created the Paper outside the scope of your employment, then you own the copyright in the Paper despite your federal employee status and may check the first box above, unless you previously transferred these rights to another party, in which case that copyright owner should sign this agreement instead of you.)

(B). You also (i) grant ASME the right to use your name, and your likeness and biographical information (if applicable) in connection with the Paper, and (ii) waive all rights generally known as moral rights in the Paper, to the extent they can be waived, under any existing or future law of any jurisdiction. You reserve all patent rights in the Paper's patentable subject matter (if any).

2. PERMITTED USES. Notwithstanding the transfer of rights described in Section 1(A) (if applicable), ASME grants you, your successors and heirs a non-exclusive, worldwide, royalty-free right to: (A) reproduce, distribute, publicly display and publicly perform the Paper or excerpts from it solely within your company or organization in print format or electronically via a restrlctedaccess internal Web site (e.g., intranet or non-publicly-accessible LANIWAN) available only to members of your company or organization (e.g., employees, staff, faculty and enrolled students and not to the general public, including alumni); and (B) create derivative works (but not translations) from the Paper, provided appropriate credit is given to Paper authors, sources and to ASME as the Paper's publisher. You may credit ASME and the Journal of Fluids Engineering as the Paper's flrst publisher only when exercis~ngth e rights set forth in Section 2(A) above with respect to the final ASME-published form of the Paper (i.e., the Paper must include ASME's conference header, Paper number and the appropriate copyright notice). You may not deposit your Paper in a publicly accessible archive (whether print or electronic) that permits users to copy and distribute its contents without first contacting ASME for permission.

3. REPRESENTATIONS AND WARRANTIES. You represent and warrant the following:

(A). this Paper represents (check one):

d h efi rst publication of

the first publication of an original compilation of information

original material or from a number of sources as specifically noted by footnotes and/or

bibliography;

(B). you have full power and authority to make and perform your obligations under this Agreement;

(C), you have the right to make the assignment of rights to ASME in Section 1(A) (if applicable), and if the Paper contains excerpts from other copyrighted material (including without limitation any diagrams, photographs, figures or text), you have acquired in writing all necessary rights from third parties to include those materials in the Paper, and have provided appropriate credit for that third-party material in footnotes or in a b~bliography;

(D), all statements contained in the Paper purporting to be facts are true or supported by reasonable scientific research;

(E). the Paper does not contain any defamatory or libelous material and does not infringe any third party's copyright, patent, trade secret or other proprietary rights and does not violate the right of privacy or publicity of any third party or otherwise violate any other applicable law;

(F). if the Paper was produced in the course of your employment by or contractual relationship with the U.S. Government and/or contains classified material, it has been cleared for public release through public affairs channels and you have indicated those approvals and clearances on the Paper;

(G). the Paper is not subject to any prior claim, encumbrance or agreement and is not under consideration for publication elsewhere; and

(H). you have cited in the acknowledgements all third parties who have participated significantly in the Paper's technical aspects.

4. AUTHOR OBLIGATIONS AND ACKNOWLEDGEMENTS:

(A). I f ASME publishes the Paper for a conference, you or one of your co-authors will register and pay any applicable fees for that conference and present the Paper to your fellow conference attendees.

(B). I f ASME publishes the Paper in a journal, you will pay (i) any applicable excess-page charges and, (ii) if your Paper requires the inclusion of four-color artwork in a print journal publication, applicable charges for printing in four-color.

(C). You will comply with the length requirements for your Paper indicated in the ASME Publishing Policies available at

http://www.asme.org/Publications/ConfProceedings/Author/Author~Resources.cfm, which are incorporated in this Agreement.

(D). You acknowledge that (i) all print and electronic copies of the Paper submitted to ASME become ASME's physical property regardless of whether ASME publishes the Paper; (ii) you are responsible for ensuring the accuracy of your research and the Paper's content; (iii) ASME has the right to edit your Paper; (iv) ASME is not obligated to publish your Paper; (v) statements and opinions advanced in your Paper are yours and not those of ASME; and (vi) ASME is not responsible for any of your expenses incurred in connection with preparing the Paper or attending meetings to present it, nor will ASME pay you any financial compensation if it publishes your Paper.

5. ASME OBLIGATIONS; TERMINATION: I f ASME decides to publish the Paper, ASME will provide appropriate credit to the author(s) of the Paper in all copies of the Paper in any format, but ASME's failure to do so will not constitute a material breach of this Agreement. I f ASME decides not to publish your Paper, it will notify you in writing, which notice may be given by email. This Agreement, including all of ASME's rights in your Paper, terminates upon your receipt of that written notice, and you are thereafter free to offer the Paper for publication elsewhere.

6. GENERAL PROVISIONS: This Agreement, together with the ASME Publishing Policies available at http://www.asme.org/Publications/ConfProceedings/Author/AuthorResources.cfm, which are incorporated in this Agreement, sets forth the entire agreement between you and ASME and supersedes all prior or contemporaneous negotiations, understandings and representations, whether oral or written, between us concerning your Paper. This Agreement may not be amended or modified except in a written instrument signed by you and ASME. A waiver of any term or condition or breach of this Agreement must be In writing, and no such waiver constitutes a waiver of any other term or condition or of any later breach of this Agreement. This Agreement inures to the benefit of and is binding upon ASME and you and our respective successors and heirs and ASME's assigns. You may not assign this Agreement or delegate any of your obligations, in whole or in part, to any third party. Any assignment in violation of this provision is null and void. ASME reserves the right to assign this Agreement in its sole discretion. This Agreement may be executed in counterparts, each of which will be deemed an original and all of whlch together constitute one

and the same instrument. Signatures sent by facsimile transmission and scanned executed agreements in pdf format sent by email transmission are each valid and binding.

7. GOVERNING LAW: This Agreement is governed by and should be construed in accordance with the laws of the State of New York, United States of America, applicable to agreements made and performed there, without regard to its conflicts of law principles. Any claim, dispute, action or proceeding relating to this Agreement may be brought only in the applicable state and federal courts in the State and County of New York, and you expressly consent to personal jurisdiction and venue in any of those courts and will not object to such jurisdiction on the ground of forum non conveniens or otherwise.

IMPORTANT: Your Paper will not be published unless this Agreement is signed by you and any other copyright owner(s) and returned to ASME with your Paper. No proxies allowed (ORIGINAL SIGNATURES of each author or copyright owner ONLY).

CORRESPONDING AUTHOR OR COPYRIGHT OWNER

AbdulMonsif Signature :

Name : Shinneeb Date :

Affiliation: WUninivdesrosrit y Of Title : Post-doctoral Fellow

Address : Department of Civil and Environmental Engineering City : Windsor

State : ON Zip Code : N9B 3P4 Country : Canada

(519) 253-

Phone : 3000 ext. Fax : (519) 971-3686 Email : sh~nneeb@uw~ndsor.ca

2546

CO-AUTHORS

Arindam

Name : Singha Signature : Date :

\

Affiliation: WUninivdesrosri ty Of Title : Graduate student

¨

Department of Mechanical Engineering 401 Sunset

Address : Avenue City : Windsor

- --

State : ON Zip Code : N9B 3P4 Country : Canada

(519) 253-

Phone : 3000 Fax : (519) 971-3686 Email : singha2@uwindsor.ca

Ext.2546

Ra m

Name : Balachandar Signature :

University of

Oat" : $J-$ 17, W

Affiliation: Windsor

Department of Civil and Environmental Engineering

Address : 401 Sunset Avenue City : Windsor

State : ON Zip Code : N9B 3P4 Country : Canada

(519) 253-

Phone : 3000 ext. Fax : (519) 971-3686 Email : rambala@uwindsor.ca

5029

VITA AUCTORIS

Arindam Singha was born in 1981 in Chandan Nagar, West Bengal, India. He earned his Bachelor of Engineering in Mechanical Engineering from Bengal Engineering and Science University (formerly, Bengal Engineering College) in 2002. He earned his Masters of Engineering in Aerospace Engineering from Indian Institute of Science, Bangalore, India in 2004. Arindam Singha is currently enrolled as a PhD candidate in the Mechanical, Materials and Automotive Engineering department at the University of Windsor and expecting to graduate in Winter, 2009.